UNCLASSIFIED

AD NUMBER

AD825617

NEW LIMITATION CHANGE

TO

Approved for public release, distribution unlimited

FROM

Distribution authorized to U.S. Gov't. agencies and their contractors; Critical Technology; MAY 1967. Other requests shall be referred to Air Force Cambridge Research Lab., Hanscom Field, MA.

AUTHORITY

AFCRL ltr, 22 Dec 1971

THIS PAGE IS UNCLASSIFIED

AFCRL-68-[illegible]
MAY 1968
UNCLASSIFIED STATEMENT #2 UNLIMITED

This document is subject to special export controls and each transmittal to foreign governments or foreign nationals may be made only with prior approval of [illegible]

AIR FORCE CAMBRIDGE RESEARCH LABORATORIES
L. G. HANSCOM FIELD, BEDFORD, MASSACHUSETTS

Proceedings of the Third Symposium on the Plasma Sheath - Plasma Electromagnetics of Hypersonic Flight

Volume II. Electrical Properties of Shock-Ionized Flow Fields

W. ROTMAN
H. MOORE
R. PAPA
J. KENNON
Editors

DDC
JUL 25 1968
A

OFFICE OF AEROSPACE RESEARCH
United States Air Force

356

825617

AFCRL-67-0280 (Volume II)
MAY 1967
SPECIAL REPORTS, NO. 64 (II)



MICROWAVE PHYSICS LABORATORY PROJECT 4642

AIR FORCE CAMBRIDGE RESEARCH LABORATORIES

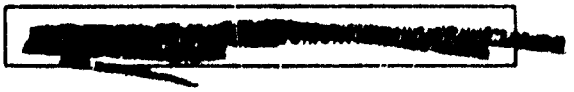
L. G. HANSCOM FIELD, BEDFORD, MASSACHUSETTS

Proceedings of the Third Symposium on the Plasma Sheath - Plasma Electromagnetics of Hypersonic Flight

Volume II. Electrical Properties of Shock-Ionized Flow Fields

W. ROTMAN
H. MOORE*
R. PAPA
J. LENNON
Editors

*Lowell Technological Institute Research Foundation, Lowell, Mass.



OFFICE OF AEROSPACE RESEARCH
United States Air Force



Best
Available
Copy

Abstract

This volume is a collection of the unclassified papers presented at the Third Symposium on the Plasma Sheath – Plasma Electromagnetics of Hypersonic Flight. This symposium consisted of the review of progress in reentry communication studies during the three year period since the prior meeting. The program of this symposium on plasma electromagnetics of hypersonic flight involves a wide range of scientific disciplines, including electromagnetics, aerodynamics, aerothermochemistry, plasma dynamics, electronics, and high-temperature phenomena. The papers were selected to explore as many of these facets of research, including the results of laboratory, flight, and system tests, as time permitted.

Contents:

The Papers in this volume are from the sessions directed by Dr. Ronald Row, Sylvania Electric Products, Inc., Waltham, Mass., and Dr. Romayne F. Whitman, Lockheed Missiles and Space Co., Sunnyvale, California.

I. RESEARCH APPROACHES TO THE PROBLEM OF REENTRY COMMUNICATIONS BLACKOUT by Huber and Sims 1

II. ESTIMATES OF NONEQUILIBRIUM IONIZATION PHENOMENA IN THE INVISCID APOLLO PLASMA SHEATH by Dunn, Daiber, Lordi, and Mates 35

III. THE EFFECT OF GLIDE RE-ENTRY SHOCK INDUCED IONIZATION ON THE COMMUNICATION SYSTEM OF THE ASSET VEHICLE by Krause 95

IV. THE USE OF LANGMUIR PROBES IN DIAGNOSING IONIZED FLOW FIELDS by Scharfman, Bredfeldt, Guthart, and Morita 125

V. ANTENNA BREAKDOWN IN A HYPERSONIC RE-ENTRY ENVIRONMENT by Epstein 169

VI. ELECTROMAGNETIC WAVE PROPERTIES IN A NONLINEAR, ANISOTROPIC, TIME-DEPENDENT PLASMA MEDIUM by Papa 203

VII. EFFECTS OF RE-ENTRY AND SPACE ENVIRONMENTS ON ANTENNA BREAKDOWN by Chown, Taylor, Vance, Nanevicz, and Morita 271

VIII. A MATHEMATICAL MODEL FOR PREDICTING RF INTERFERENCE EFFECTS IN ROCKET EXHAUST PLUMES by Pergament and Calcote 309

I. RESEARCH APPROACHES TO THE PROBLEM OF REENTRY COMMUNICATIONS BLACKOUT

By Paul W. Huber and Theo Sims

NASA Langley Research Center
Langley Station, Hampton, Va.

ABSTRACT

In order to significantly reduce the constraints on radio-link systems due to reentry blackout, it is necessary to define accurately the extent of the blackout region and to develop methods for reducing its extent. The achievement of these goals will, however, require considerable improvement in knowledge of chemical-kinetics plasma processes, of boundary layers and separated plasma flows with ablation contamination, and of em-wave propagation from plasma covered antennas.

Research efforts directed toward the improved understanding of fundamental plasma processes and em-wave propagation are described. It is shown that certain aspects of the problem are accessible to simulation in ground facilities and that small-scale flight experiments and piggyback experiments can be useful for supplementing knowledge in those areas not obtainable on the ground. Based on projected research efforts, significant improvement in the required knowledge should be forthcoming. Generalized blunt-body reentry blackout bounds, as based on state-of-the-art knowledge, are presented. It is shown that reentry blackout extent for a given body can be minimized through the choice of signal frequency and antenna location. Factors influencing antenna location include the configuration and type of separated plasma fluid, as well as the nonequilibrium nature of the inviscid and boundary-layer flow.

L-4591

INTRODUCTION

Almost everyone is familiar with the fact that the reentry communications problem is caused by the high concentration of free electrons which are generated in the flow regions around reentry vehicles.[1] It is also generally understood that, for a large reentry vehicle, a communications blackout typically occurs when the electron concentration in the plasma near an antenna reaches or exceeds a certain critical number which corresponds to the given signal frequency - that is, when $N_e \approx N_{e,cr}$ where $N_{e,cr} \sim f^2$. Based solely on this criterion, therefore, two obvious directions for the reduction or circumvention of the problem are indicated: (1) increase the signal frequency to a point where its critical electron value will clearly be higher than the plasma value, and/or (2) lower the plasma electron concentration by modifying the plasma (for example, by injecting a material which accelerates electron depletion). These two directions are, in fact, the most usable ones within the present state of the art[2,3,4] even though there are other possibilities.

In any case, before mission designers can compute the magnitude of signal loss caused by the plasma, can define the points in the reentry at which the signal will be lost, or can evaluate the magnitude of alleviation required to avoid the signal loss, two parts of the problem must be understood: (1) specification of the plasma electron concentration (based on flow-field knowledge), and (2) determination of the electron concentration which can be tolerated for a given vehicle and antenna (based on electromagnetic-wave-propagation knowledge).[5] Both of these electron concentration levels must be determined quantitatively, since the magnitude of the signal loss generally increases with the magnitude of their difference.

In this paper, research and state of knowledge regarding the properties of the fluids about blunt reentry bodies are discussed, and the implications of these fluids on the communications problem are indicated. It is also shown that flight experiments can be very useful for study of plasma and em-wave propagation problems in regimes not accessible to ground simulation.

SYMBOLS

C_p	pressure coefficient
d_b	body diameter, ft
f	signal frequency, cps
H	fluid enthalpy
k_r	recombination rate constant
M	any third body
N_e	electron concentration, cm^{-3}
$N_{e,cr}$	critical electron concentration, $\frac{f^2}{8.06 \times 10^7}$, cm^{-3}
p_s	vehicle stagnation pressure
s	distance along streamline
s^*	distance along streamline to first point where $N_e = N_{e,eq}$
u	fluid velocity, fps
X	any neutral species
Δ_{ns}	shock-wave standoff distance at nose
ρ	fluid density

Subscripts:

a	antenna
eq	equilibrium

stagnation point or nose flow

free stream

REENTRY PLASMA CONFIGURATION

Figure 1 is a schematic representation of continuum flow-field regions near typical reentry bodies and illustrates the fact that several distinctly different types of plasma may be present. The outer region (between the shock wave and viscous layers) consists of inviscid air which is first compressed and heated by a strong bow shock wave, at which time free electrons are produced. When this fluid expands around the vehicle, some of the electrons and ions recombine, but, in general, this flow is never in complete chemical equilibrium.

There is a viscous boundary-layer region close to the body surface where fluid is decelerated from the inviscid flow velocity to zero velocity at the surface. There may be additional electron production within the layer, or there may be primarily recombination, depending upon the aerodynamics involved. Due to the ablation of surface material during reentry, this fluid may furthermore be a reacting mixture of air and ablation products. As in the case of the inviscid plasma, the boundary-layer plasma is generally not in equilibrium.

The inner plasma region (between the free-shear layer and the rear-body surfaces) is one of viscous separated fluid which is composed of boundary-layer air "contaminated" with ablation material from the heat shield. This separated mixture recirculates in the base-flow region and is finally scavenged into the wake. Because of the long dwell time of this fluid, the separated plasma is likely to approach equilibrium.

Depending upon the aspect angle, attitude, and roll orientation of the reentry vehicle, signal propagation from an antenna on the body will be through both the inviscid plasma and one of the viscous plasma regions. It will never be through a viscous region only, or the inviscid region only. Since the general problem involves propagation through all these plasmas, it is therefore necessary to determine the electron concentration in each type of plasma.

INVISCID PLASMA PROPERTIES

For determination of the inviscid-flow plasma properties, it is necessary to consider the finite rates at which changes in chemical composition occur with respect to flow rates. Figure 2 is a reentry chemical-kinetics map which helps to illustrate this. The shaded areas represent boundaries of ionic chemical-kinetics regimes for blunt bodies of from 1 foot to 12 feet in diameter, where the upper edge of an area (high-altitude edge) is the boundary for the largest (12-foot-diameter) body.

Only at altitudes above or below those within the reentry map is it permissible to ignore the rates at which ionic reactions occur. For example, at very high altitudes where the fluid density is very low and reaction rates are very slow, there is negligible production of electrons during the flow-dwell time over the vehicle ("negligible" herein means $N_e \lesssim 10^9$ cm^{-3}, which value is the highest tolerable value for VHF transmission frequencies) and therefore the rate values are not important. At altitudes below the lowest boundary, reaction rates are very fast in relation to flow rates because of the high fluid densities and, again, the actual values of the rates may be ignored since complete equilibrium may be assumed.

For large portions of typical reentry trajectories, however, the values of the reaction rates cannot be ignored. In the altitude range between the upper two boundaries shown, the reaction rates, although somewhat slow, are by no means negligible, and both the production processes and recombination processes are nonequilibrium. At altitudes below the next to highest boundary, the electron concentration in the high-density nose region may approach, or be somewhat above, the complete equilibrium value before expanding around the body, although the neutral species may be still short of equilibrium. The expanding body flow is - again - one of nonequilibrium recombination. At altitudes below the next to the lowest shaded area (note the reduced extent along the velocity scale), the ionic chemistry in the aft flow may approach local equilibrium (ions in equilibrium with the local nonequilibrium neutral species)* although the value of the electron concentration is not the complete equilibrium value. Complete equilibrium is achieved only below the lowest altitude boundary where three-body recombinations of the atoms are no longer frozen.

The map is also divided into velocity regimes because the number and types of ionic reactions which can occur in the flow field are a function of the flow enthalpy. In the lowest velocity regime, A, 90 percent or more of the ions produced in the flow field are molecular ions; the ion-production

*Since this boundary is a result of faster two-body recombination, it does not extend into the high-velocity, atomic-ion regime. However, if three-body ionic recombination involving electrons as the third body is found to be fast,[6] this bound may extend into the high-velocity regime.

processes are atom-atom and the recombination processes are of the two-body dissociative type. Both processes must be treated using finite rates. The principal ionic reaction is

$$N + O + 2.77 \text{ ev} \rightleftarrows NO^+ + e^- \qquad (1)$$

In the highest velocity regime of the map, C, a completely different situation exists - essentially all the ions produced are atomic ions and recombinations occur only by slow three-body processes, namely

$$O^+ + e^- + M \rightleftarrows O + M + 13.61 \text{ eV} \qquad (2)$$

$$N^+ + e^- + M \rightleftarrows N + M + 14.54 \text{ eV} \qquad (3)$$

where M is any third body. Two-body recombination processes are largely excluded in this regime (even considering charge transfer) since the appropriate molecular species represent less than 10 percent of the ionic species. Because the three-body processes are slow at typical reentry fluid-density levels, it is therefore often correct to assume that very few of the ions produced at the nose of the vehicle recombine in the subsequent expanded body flow (i.e., frozen ionic recombination). Hence, the electron concentrations will be very high in this regime. The production processes are also different in this regime due to the importance of the direct electron impact ionizations at high enthalpy. These ionizations are

$$e^- + X + E \rightleftarrows X^+ + e^- + e^- \qquad (4)$$

where X is any of the neutral species (atomic or molecular) and E is the required energy.

In the middle velocity regime, B, both molecular and atomic ions are present in the plasma, and a class of reactions called charge transfers becomes very important in both the production and recombination aspects of the flow, even though these reactions directly produce no net change in the ionization level. Their importance lies in the fact that the charge transfers are fast relative to other ionic processes and provide an indirect path for the production and depletion of atomic ions, which is more rapid than direct ionization and recombination of atomic species at these velocities. For example, the dominant ionization and recombination processes in this regime are

$$N + O + 2.77\ eV \rightleftarrows NO^+ + e^- \qquad (1)$$

$$N + N + 5.84\ eV \rightleftarrows N_2^+ + e^- \qquad (5)$$

$$O + O + 6.96\ eV \rightleftarrows O_2^+ + e^- \qquad (6)$$

By the transfer of charge from these molecular ions to the atoms O and N, significant "production" of atomic ions can take place within typical nose-flow dwell times. Perhaps even more important is the reverse of this process (charge transfer from atomic ions to molecular species), since a path is provided for the finite-rate depletion of electrons in the expanded flow by means of two-body dissociative recombination. Without this path, the atomic ions might be frozen because of slow three-body recombination. Since the dominant two-body recombination is $NO^+ + e^-$ in this velocity regime, as well as in regime A, the dashed line shown represents the point at which the NO concentration in the equilibrium nose flow equals the atomic-ion concentration. This is another way of saying that s two-body recombination path

is available for all the ions produced. The charge transfer path referred to actually consists of a large group of reactions (20 or more), in some only charge is transferred and in others a simultaneous transfer of charge and exchange of atoms occurs.[7]

The real problem in regard to the reentry chemical-kinetics picture is that many of the important reaction-rate constants and their temperature dependencies are not well known. In fact, the currently estimated uncertainties in rates are so large in the medium- and high-velocity regimes that the overall uncertainties in the flow-field electron concentrations amount to factors of from 10 to 30. It is obvious that much improvement in this knowledge is required if plasma computations are to be made with confidence in these regimes.

INVISCID PLASMA SIMULATION

A logical place to study plasma processes is in ground facilities, where attempts can be made to simulate the reentry flow (or at least to isolate some of the significant processes of the reentry flow) and to measure changes in ionic concentration. One of the most useful classes of facilities for this purpose is the shock tunnel and shock tube.

Shock tunnel.- In figure 3, the reentry simulation capabilities of present shock tunnels are shown superimposed on the reentry chemical-kinetics map of figure 2. Two methods in current use are illustrated: complete simulation and stagnation streamline simulation. The upper shaded area represents the complete simulation method in which the reflected shock flow of a shock tube is expanded through a hypersonic nozzle to ambient flight conditions u_∞ and ρ_∞. The high stagnation enthalpy conditions in the shock tube permit such an expansion. A model can be mounted in this

flow and measurements can be made. There are, however, several limitations to this method. Because extremely high shock-tube pressures are required, there is a structural limit to the operating range as indicated by the line labeled "high-pressure limit." Furthermore, the expanded nozzle flow does not duplicate the ambient air composition due to nonequilibrium recombination in the nozzle. Because of this nonequilibrium, the clearly valid simulation range is in a lower altitude regime wherein the nose flow can reach equilibrium as in the flight situation. The complete simulation method is useful, however, for studies in the low-velocity reentry regime.[8,9]

Stagnation streamline simulation, as shown by the lower shaded area, is accomplished by expanding the reflected shock-tube flow through a nozzle which is shaped to duplicate the expansion of a vehicle flow-field streamline (to a Mach number of approximately 4) which originates at, or near, the stagnation point. The flight total enthalpy H_s and vehicle stagnation pressure p_s (not free-stream stagnation pressure) must be duplicated in order to permit the simulation. The change in fluid properties along the "streamline" is studied by use of tunnel instrumentation. The primary constraint on this scheme is the large wall boundary layer which develops at the low densities (low Reynolds numbers) required to simulate a flow-field streamline at the higher reentry altitudes. The line in figure 3 labeled "low-pressure limit" indicates the approximate altitude simulation limit due to this constraint. If all the significant reactions were two-body, then the results could be applied also at the higher altitudes by using the binary scaling criterion[10] wherein nonequilibrium effects are duplicated at different altitudes for $\rho_\infty s$ = Constant at a given flight velocity (s = distance along streamline to a given value of $C_p/C_{p,s}$).

Unfortunately, this is not the case for the low-altitude portions of reentry (high fluid density). In spite of this limitation, however, the method is a very useful one for reentry chemical-kinetics study, since many of the important recombination reactions are thus made accessible. Investigations using this simulation are currently being carried out at the Cornell Aeronautical Laboratory.[6]

Also shown in figure 3 are the reentry paths of small-scale flight-research vehicles used in Project RAM (radio attenuation measurement) at the Langley Research Center of NASA.[5] These are shown to illustrate an experimental approach which provides the capability for plasma and em-wave propagation studies in the reentry areas not accessible to ground simulation.

Shock tube.- The incident shock-wave flow of a shock tube (the flow before reflection or expansion occurs) can be used for study of nonequilibrium production processes. Results of these investigations have application to high-altitude reentry flow in the bow shock region. (Note that normal shocks can be used to simulate the vehicle oblique-shock flow as well.) Since the bow shock region is the principal region for electron production, such studies can yield valuable information about reentry blackout points. Figures 4 and 5 illustrate the nature of the correlation. Note that a finite distance, s^*, is required in the flow behind the shock for the electron concentration to first reach a value which corresponds to the final equilibrium value. (This is not complete equilibrium since the neutral species are generally not in equilibrium dissociation at this point. The overshoot which usually occurs in N_e beyond this point is, in fact, the result of such a condition.) The increase with distance of electron concentration behind the shock is shown in figure 5. For this discussion, the overshoot

and the return to complete equilibrium can be ignored. The curve for 23,000-fps flight velocity is based on results given by Lin and Teare,[7] and the curve for high flight velocity ($u > 35{,}000$ fps) is assumed on the basis that electron impact ionization will yield an increase in production rate in the later stages of production.

If (see fig. 4) a typical flow distance in the bow shock region - say Δ_{ns}, the shock standoff distance - is large compared to s^*, the required equilibrium ionization distance, then the flow will certainly come to ionic equilibrium before expanding around the body. However, if the ionization distance becomes very large relative to the standoff distance, as at high altitudes where rates are slow, then the fluid may be far short of ionic equilibrium at the start of the expansion. Since all the production processes are two-body, and the competing three-body recombination processes (for example, neutral atom recombination) can be neglected under conditions short of equilibrium production[10] (again note that at the first point where $N_e = N_{e,eq}$, the fluid is generally short of full equilibrium), it is permissible to use the binary scaling criterion previously mentioned. This criterion was used to establish the boundary for "equilibrium" nose ionization given in figure 2 - that is, the point where $2\Delta_{ns} = s^*$. ($2\Delta_{ns}$ was used as the typical nose flow distance, and $s^* = s^*(u_\infty)$ at an altitude of 250,000 ft was taken from shock-tube results[7] along with extrapolation to higher velocity.)

By making some additional assumptions, the foregoing nonequilibrium shock wave results are used to approximately determine initial reentry blackout points without making complete finite-rate calculations - which are laborious. The first assumption is that, in the flow-expansion region,

ionic recombination is frozen at altitudes above the nose equilibrium boundary shown in figure 2. This assumption is valid except for cases in the medium- and low-velocity regimes where the value of N_e is high enough at the start of the expansion to allow significant two-body recombination to occur. The reason for this restriction can be seen from the following relation for two-body electron depletion:

$$\frac{dN_e}{ds} = -\frac{k_r(N_e)^2}{u} \tag{7}$$

where k_r is the reverse rate (for example, eq. (1)) and u is the local fluid velocity. For typical values of k_r and u, the highest allowable N_e for which frozen ionic recombination can be assumed is about 10^{11} cm^{-3}. The second assumption is one of similarity of the frozen ionic expansion, that is, the ratio $N_{e,a}/N_{e,s}$ is invariant with altitude and dependent only on $C_{p,a}/C_{p,s}$, the pressure-coefficient ratio at the antenna. This assumption can be shown to be a reasonably good one.

The following additional steps are then used to complete the determination of a blackout point: (a) At the altitude corresponding to equilibrium N_e at the nose (fig. 2) the electron concentrations at the nose* and at the antenna location are found. (The latter N_e is found by means of a frozen flow expansion from $C_p = C_{p,s}$ to $C_p = C_{p,a}$). (b) As a result of the second assumption above, the ratio $N_{e,a}/N_{e,s}$ has the same value at the equilibrium nose altitude and at the blackout altitude. Since $N_{e,a}$ at the blackout altitude is equal to $N_{e,cr}$ for the signal, it follows that,

*The N_e restriction doesn't apply here, since this is merely a fictitious step in the procedure.

$$\frac{N_{e,cr}}{(N_{e,a})_{eq.\ alt.}} = \frac{(N_{e,s})_{B.O.\ alt.}}{(N_{e,s})_{eq.\ alt.}} \tag{8}$$

(c) Using curves such as shown in figure 5, the nose flow distance ratio, s/s^*, is found which corresponds to the electron concentration ratio on the right-hand side of equation (8) above. The distance, s, in this ratio then represents the fraction of the nose flow distance at the equilibrium altitude which grows to the full nose flow distance at the blackout (nonequilibrium production) altitude.

(d) From binary scaling ($\rho_\infty s$ = Constant) of the above nose flow distance ratio, the blackout altitude is then found by determining the altitude at which ambient air density is equal to $(\rho_\infty)_{B.O.\ alt.}$ in the following equation:

$$\frac{s}{s^*} = \frac{(\rho_\infty)_{B.O.\ alt.}}{(\rho_\infty)_{eq.\ alt.}} \tag{9}$$

The application of this method, for example to Mercury-Atlas or Gemini-Titan orbital reentry, yields a VHF blackout altitude of about 313,000 feet, as compared with experimental values of 308,000 to 318,000 feet. The computed blackout altitude is not sensitive to the choice of $2\Delta_{ns}$ as a typical nose flow distance, although the equilibrium nose altitude boundary is sensitive.

Experimental studies of nonequilibrium production chemistry behind shock waves are being carried out by several research groups, including those at Avco-Everett Research Laboratory and Cornell Aeronautical Laboratory. Improved production rate knowledge in the high-velocity regime (electron impact production) is, of course, needed for proper assessment of reentry plasma properties.

BOUNDARY-LAYER PLASMA

As in the case of inviscid plasma, determination of the reentry boundary-layer plasma properties involves consideration of the finite rates at which changes in chemical composition occur. The problem is more complex, however, because the nonequilibrium chemistry includes - in addition to the air species - also the species resulting from reaction of ablation products with the air. Furthermore, the fluid mechanics part of the problem is complicated by the necessity for inclusion of effects due to diffusion, heat conduction and viscosity, which are usually negligible in the inviscid problem. Nevertheless, comprehensive analyses of reentry boundary-layer plasma have been made.[11,12,13,14] In general, the results of studies such as these indicate that this plasma region is of importance in reentry communications primarily for pointed or long slender bodies at low altitudes - say, below 120,000 ft - and for antennas located on the aft parts of the bodies. In such cases, the boundary-layer region is the primary site for electron production and - due to the finite rates involved - this production occurs well back from the nose region (on the order of 10 ft or more). Small amounts of alkali impurities in the ablation material are shown to cause large increases in the boundary-layer electron concentration over that for clean air. On the other hand, the electron concentration in the boundary layer must go considerably higher than $N_{e,cr}$ to cause blackout, since this layer is generally thin in relation to a signal wavelength.

The boundary-layer plasma is less important in blunt body reentry communications for several reasons. First, the inviscid plasma is much thicker for blunt bodies due to the much larger fraction of the flow which passes through the strong bow shock front. Next, due to the lower Mach number in

the external flow for blunt-body flow fields, the peak temperature in the boundary layer is not as high relative to the inviscid flow temperature and does not occur as close to the wall.

SEPARATED FLOW PLASMA

Current knowledge regarding separated flow plasma properties is not very refined, although great strides are being made.[15] In order to determine, at least grossly, the possible importance of this plasma region in reentry communications, electromagnetic-wave-propagation results from flights involving separated regions have been studied. For this purpose, results from the Mercury-Atlas reentries have been used, because the separated region completely surrounds the antennas.

Shown in figure 6 are the effective values of flow-field electron concentration as deduced from the propagation results, along with computed values based on several assumed plasma models. The symbols represent the electron concentrations required to produce the observed attenuations when using a plane-wave, slab model of the propagation. (It is interesting that the C-band propagation is such a sensitive diagnostic tool. The electron concentration must be between about 2×10^{11} and 4×10^{11} in order to give attenuation without blackout.) Note, first of all, that the finite-rate inviscid-flow theoretical model (plasma properties along a streamline expanded from the nose region to the antenna region) does not provide a reasonable correlation in the peak N_e part of the reentry, although it appears to be good otherwise. This lack of correlation cannot be attributed to the rate-knowledge uncertainty, so that one must conclude that this plasma was not the significant one for attenuation during the peak N_e

period. A 25 reaction system was used in this model. It is interesting to note that the peak N_e region appears to be flattened; this is a result of increased two-body recombination at the higher values of N_e (see eq. (7)), since there is a sufficiently long dwell time along the streamline (to the rearward antenna location) for this action to be very effective. For this same reason, a rearward antenna location is preferred over a more forward location, and larger bodies - within certain limitations - are preferred over smaller bodies.

The results obtained from a separated plasma model are, however, seen to be much closer to the experimental results. Two principal assumptions are used in this model: (1) the separated fluid is in complete equilibrium, and (2) the effective enthalpy of the fluid is 0.70 of the stagnation fluid enthalpy. By using these assumptions, along with the pressure for the separated flow, the electron concentrations are readily calculated. The first assumption should be a reasonable one since the fluid dwell time in this low-velocity, recirculating region is long; whereas the second assumption is rather arbitrary. It should be noted, however, that the assumed value of $0.70H_s$ for the effective fluid enthalpy is not unreasonable in the light of current knowledge,[16] and the correlation shown in figure 6 is not obtained when using higher or lower assumed values.

In order to obtain good correlation also with the data near the peak heating period of the reentry, the additional assumption is made that ablation impurities are present in the separated fluid during this period. It is assumed that alkali impurities (sodium or potassium) are present in the separated fluid at a peak mole fraction of a little more than 10^{-5} during peak heating. These impurities would be present, of course, due to

impurities in the original ablation heat shield before it is vaporized and dissociated. Because the temperature in this fluid region is high, the alkali particles (i.e., the ionizable particles) are assumed to be in atomic form (unreacted). Again, the ablation impurity assumptions are arbitrary but are in line with current knowledge of separated flow ablation contamination.

It can be concluded from the comparisons shown in figure 6 that, although other combinations of assumed enthalpy and impurity level might also correlate the results, there are strong indications that the separated flow plasma is the significant one for attenuation during the peak N_e part of the reentry.

REENTRY BLACKOUT BOUNDS

By application of the plasma concepts previously discussed, estimates of the reentry blackout bounds for large blunt bodies can be made. The additional qualification involved is that the pertinent plasma layer be of sufficient thickness such that blackout occurs at the point, $N_e = N_{e,cr}$. This is believed to be generally the case for blunt bodies of the size, $d_b \gtrsim 1$ ft. Such estimates have been made and are shown in figure 7 for three signal frequencies and two body sizes. For general applicability, the estimates have been made for the body flow condition, $0.01 < C_p/C_{p,s} < 0.02$, which is representative of aft antenna locations on blunt reentry bodies. The separated plasma bounds are shown only where they are higher (higher N_e than the inviscid), but it should be noted that in some cases - for example, the VHF calculations - the bounds for separated and for inviscid plasma are very close (as in fig. 6). For cases where propagation is through both

types of plasma (depending on attitude, aspect angle, and roll orientation) the higher of the bounds must, of course, be used.

It is seen, first of all, from the inviscid results shown that the VHF boundaries are the highest of the three frequencies and that the larger body has the higher of the two bounds for this frequency and for the other frequencies in the high-velocity regime. The latter result is due to the larger flow distance available for electron production at the nose along with the nearly frozen recombination in the expansion. It is to be noted next that there is a marked reversal in the body size versus altitude comparison as well as a sharp dip in some of the inviscid bounds at velocities around 26,000 or 27,000 ft/sec. These effects result from the relatively fast two-body ionic recombinations which are dominant in the expanding flow at velocities below these values (refer to the two-body - or N_e limiting - velocity boundary shown in fig. 2). At these lower velocities, the larger bodies have the lower bounds because there is more flow time available in the expansion for this recombination to be effective. It is to be noted, furthermore, that because this recombination has an $(N_e)^2$ dependency (see eq. (7)), the dip is much more pronounced for the X-band bounds because of the higher $N_{e,cr}$ involved. In fact, no dip at all is seen in the VHF bounds because the N_e is too low for the recombination to be significant. The blackout boundary for the smaller body at S-band shows no dip because the flow distance is insufficient for recombination at this value of $N_{e,cr}$. In the case of X-band, the shorter flow length is seen to be nearly as effective as the longer one, due to the strong influence of the N_e limiting effect. These results point up the importance of providing sufficient flow length (by using an aft antenna location, for example) at S-band

frequencies to minimize blackout, and of the use of higher signal frequencies, such as X-band, when the flow length cannot be as long.

The separated flow bounds shown have no body size identification since equilibrium flow was assumed for this plasma. It is interesting to note from these results that, at X-band, the separated flow plasma increases blackout for both body sizes in the lower velocity regime, while at S-band, it increases the blackout for the larger body size only. This latter effect is, however, seen to be a very detrimental one. The separated plasma with ablation result is shown only for the S-band frequency since the calculated N_e's for such a plasma are typically below 10^{12} cm^{-3} (that required to influence X-band). There is no significant ablation occurring at the reentry conditions corresponding to the VHF boundaries shown.

Several other remarks can be made regarding the results shown in figure 7. No bounds are shown due to boundary-layer plasma because for large blunt bodies in the continuum flow regime this plasma is not generally a determining one for bounds such as shown, although it must certainly be considered in attenuation estimates. While bounds for pointed or long slender bodies are not presented, boundary-layer plasma knowledge for such bodies does suggest the desirability of forward antenna locations to minimize the attenuation and blackout at low altitudes, which is the reverse of the blunt-body inviscid result. In any case, the results of present reentry plasma knowledge in regards to the communication problem point up the need for employment of other means (such as material addition) to reduce the blackout region for large blunt bodies in the super-orbital reentry regime where blackout is extensive.

In order to improve on estimates such as these, three-dimensional flow-field calculations coupled with improved chemical-kinetics knowledge is necessary for the inviscid flow.[6] Much improvement is also needed in knowledge of the fluid mechanics and chemistry of separated air flows with contamination. Even with the improved plasma knowledge, the electromagnetic-wave-propagation problem must be better understood for antenna configurations in close proximity to plasmas[17] and for propagation involving unsymmetrical plasma configurations.

CONTINUING RESEARCH EFFORT

In order to provide a more reliable basis for the design and planning of reentry communications of spacecraft in the higher velocity earth regimes, as well as for planetary entry, the Langley Research Center (LRC) is continuing its research in these problem areas. The program (Project RAM) has already contributed much to the understanding and reduction of blackout as a result of fundamental research in the areas of plasma processes and electromagnetic-wave propagation.[1,5,17,18,19]

The program involves the use of ground facilities and small-scale flight experiments, supplemented by outside contracts, and the continuing research will have a direct bearing on reentry communications. For example, diagnostic instrumentation (reflectometers[19] and Langmuir probes) on RAM C-B will provide basic plasma data in a regime which cannot be simulated in ground facilities. Furthermore, the most promising method for reduction of blackout for a mission such as Apollo - that of material addition - was conceived and flight demonstrated[3] in the RAM program, and will be further refined in the continuing effort. Demonstration of this scheme for a manned reentry was accomplished in the GT-3 mission.[20] It is interesting to note

that, although this experiment involved injection of material into the inviscid flow, the results also suggest the importance of the separated plasma.[16]

Research on wave propagation through plasmas and on the effects of plasmas on antenna performance has resulted in significant advances in knowledge.[1,5,17] The results are, in fact, unique in having provided quantitative propagation data under specifiable flight plasma conditions.

As a result of this program and of work contributed by other research organizations in these categories, it is believed that the reentry communications blackout can be more closely delineated and by the employment of certain physical modifications can indeed be greatly reduced.

CONCLUDING REMARKS

The following points are believed to represent a reasonable assessment of the reentry communications blackout picture as based on current knowledge and projected research:

1. The fluid properties in the inviscid- and viscous-flow regions about the reentry vehicles must be more precisely defined in order to determine quantitatively the extent of or to design means to alleviate the reentry communications blackout.

2. Improved chemical-kinetics knowledge is required to properly define the inviscid plasma.

3. An improved understanding of the separated plasma flow, boundary-layer plasma, and of the effects of ablation impurities in these flows is also required.

4. As a result of continuing research in ground facilities and with small-scale flight experiments it is expected that the more important

refinements needed in inviscid and viscous plasma knowledge, as well as improved understanding of em propagation from plasma-covered antennas, will be forthcoming.

5. In order to minimize blackout effects during reentry, communications frequencies in the X-band range are desirable, and rearward locations of the antennas can also be effective. In some cases, propagation through separated plasmas is detrimental to reentry communications and should be avoided.

6. The reentry communications blackout for large vehicles at superorbital velocity is expected to be extensive and employment of means, such as material addition, to alleviate the signal loss by modification of the plasma may be necessary.

REFERENCES

1. Huber, Paul W.; and Sims, Theo E.: The Entry-Communications Problem. Astronaut. Aeron., vol. 2, no. 10, Oct. 1964, pp. 30-38. (Available also as NASA RP-384.)

2. Brummer, E. A.: X-Band Telemetry Systems for Reentry Research. Paper No. CP 63-663, Inst. Elec. Electron. Engr., Apr. 1963.

3. Cuddihy, William F.; Beckwith, Ivan E.; and Schroeder, Lyle C.: RAM B2 Flight Test of a Method for Reducing Radio Attenuation During Hypersonic Reentry. NASA TM X-902, 1963.

4. Spencer, Dwain F.: An Evaluation of the Communication Blackout Problem for a Blunt Mars-Entry Capsule and a Potential Method for the Elimination of Blackout. Tech. Rept. No. 32-594 (Contract No. NAS 7-100), Jet Propulsion Lab., C.I.T., Apr. 15, 1964.

5. Anon.: Proceedings of the NASA Conference on Communicating Through Plasmas of Atmospheric Entry and Rocket Exhaust. NASA SP-52, 1964.

6. Dunn, M. G.; Daiber, J. W.; and Lordi, J. A.: Nonequilibrium Ionization Phenomena in Apollo Plasma Sheath. (This Symposium.)

7. Lin, Shao-Chi; and Teare, J. Derek: Rate of Ionization Behind Shock Waves in Air. II. Theoretical Interpretations. Phys. Fluids, vol. 6, no. 3, Mar. 1963, pp. 355-375.

8. Eschenroeder, A. Q.; Daiber, J. W.; Golian, T. C.; and Hertzberg, A.: Shock Tunnel Studies of High-Enthalpy Ionized Airflows. Rept. No. AF-1500-A-1 (AFOSR 3025), Cornell Aeron. Lab., Inc., July 1962.

9. Lederman, Samuel; Visich, Marian, Jr.; and Abele, Manlio: Preliminary Results of an Experimental Investigation of the Properties of the Plasma Sheath Around a Hypersonic Reentry Body. PIBAL Rept. No. 856, Polytech. Inst. Brooklyn, Dec. 1964.

10. Gibson, Walter E.: Dissociation Scaling for Nonequilibrium Blunt Nose Flows. ARS J. (Tech. Notes), vol. 32, no. 2, Feb. 1962, pp. 285-287.

11. Pallone, Adrian J.; Moore, Jeffrey A.; and Erdos, John I.: Nonequilibrium, Nonsimilar Solutions of the Laminar Boundary-Layer Equations. AIAA Jour. Vol. 2, No. 10, Oct. 1964.

12. Blottner, F. G.: Nonequilibrium Laminar Boundary-Layer Flow of Ionized Air. AIAA Jour., Vol. 2, No. 11, November 1964.

13. Kane, J. J.: Nonequilibrium Sodium Ionization in Laminar Boundary Layers. AIAA Journal, Vol. 2, No. 9, September 1964.

14. Kane, John J.; and Li, Frank: Ablation Effects on RF Attenuation in the Turbulent Boundary Layer. AIAA Journal, Vol. 3, No. 8, August 1965.

15. Reeves, Barry L.; and Lees, Lester: Theory of the Laminar Near Wake of Blunt Bodies in Hypersonic Flow. Paper No. 65-52, Am. Inst. Aeron. Astronaut., Jan. 1965.

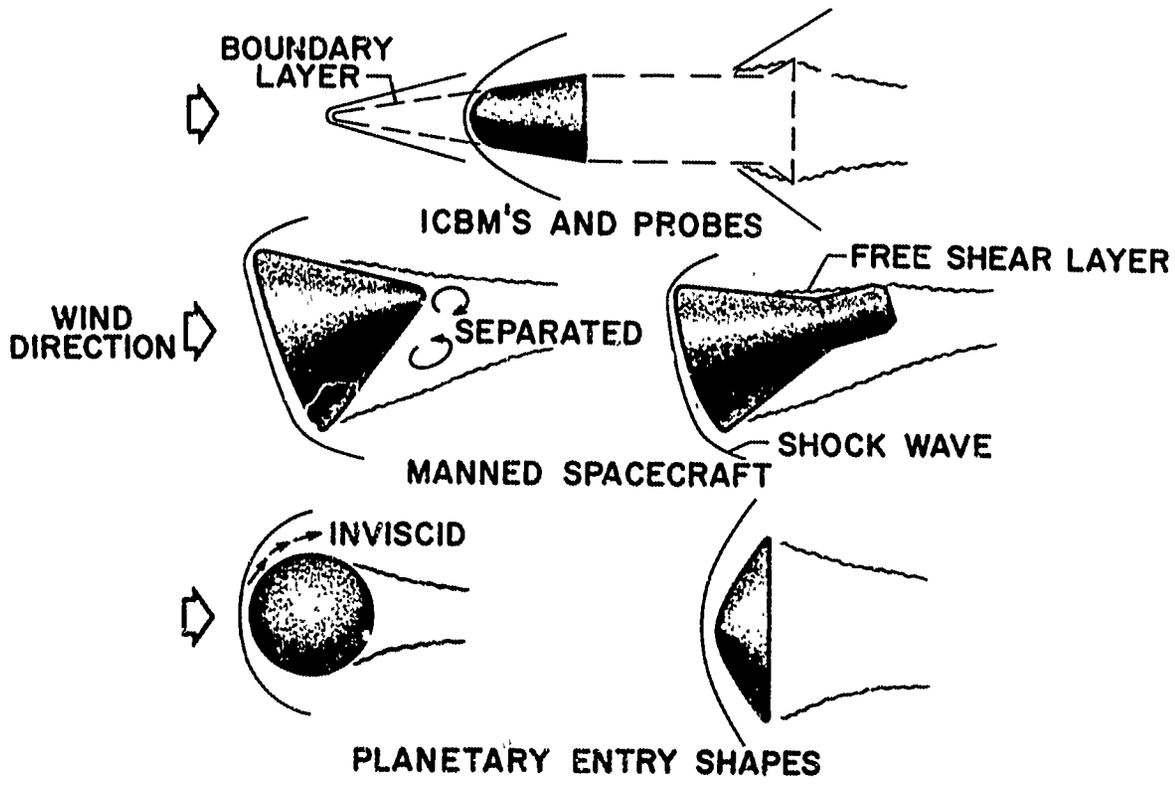
16. Beckwith, Ivan E.; Bushnell, Dennis M.; and Huffman, Jarrett K.: Fluid Mechanics Aspects of the Gemini Reentry Communications Experiment. Paper No. 23. Conference on Langley Research Related to Apollo Mission, NASA SP-101. Confidential, June 22-24, 1965.

17. Swift, C. T.; and Hodara, H.: Effects of the Plasma Sheath on Antenna Performance. Presented at 10th Symposium of the AGARD Ionospheric Research Committee on Propagation Factors in Space Communications. Sept. 21-25, 1965, Rome, Italy.

18. Evans, J. S.: Reduction of Free Electron Concentration in a Reentry Plasma by Injection of Liquids. (This Symposium.)

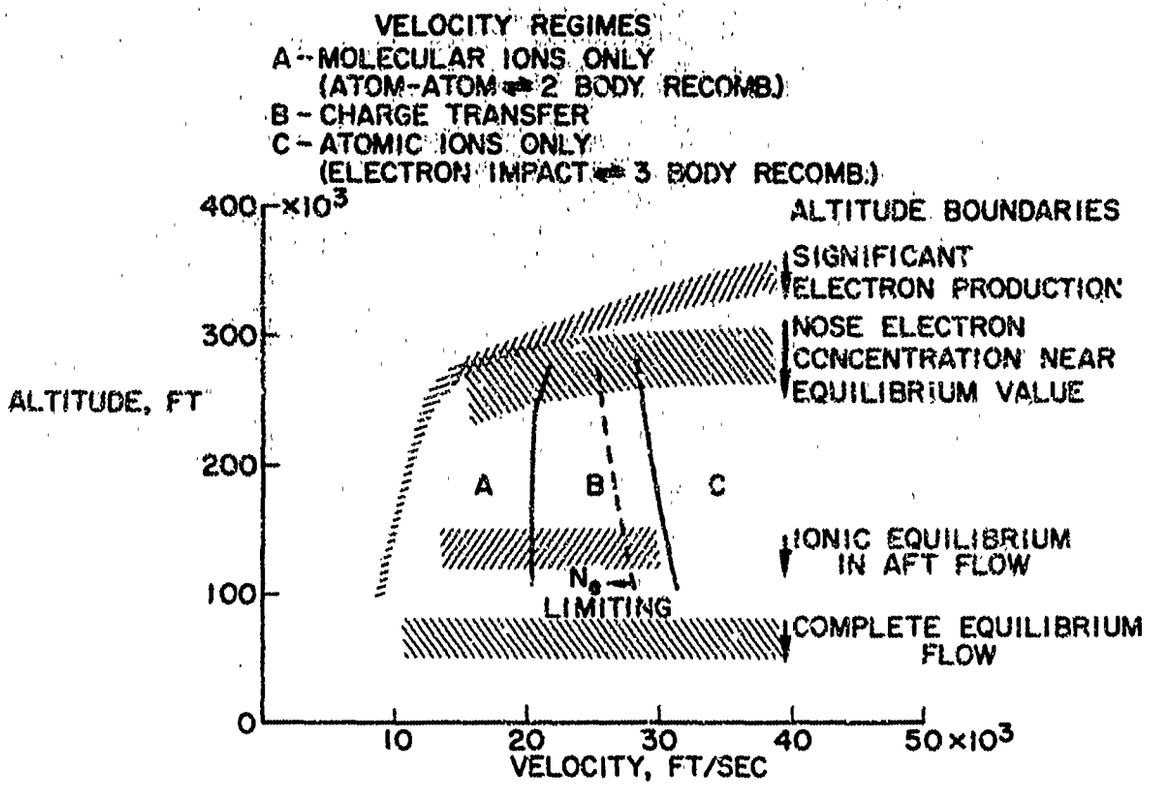
19. Grantham, W. L.: Analysis of Plasma-Sheath Electron Density Measurements at Entry Velocities. (This Symposium - Classified Proceedings.)

20. Schroeder, L. C.: Gemini Reentry Communications Experiment. (This Symposium - Classified Proceedings.)



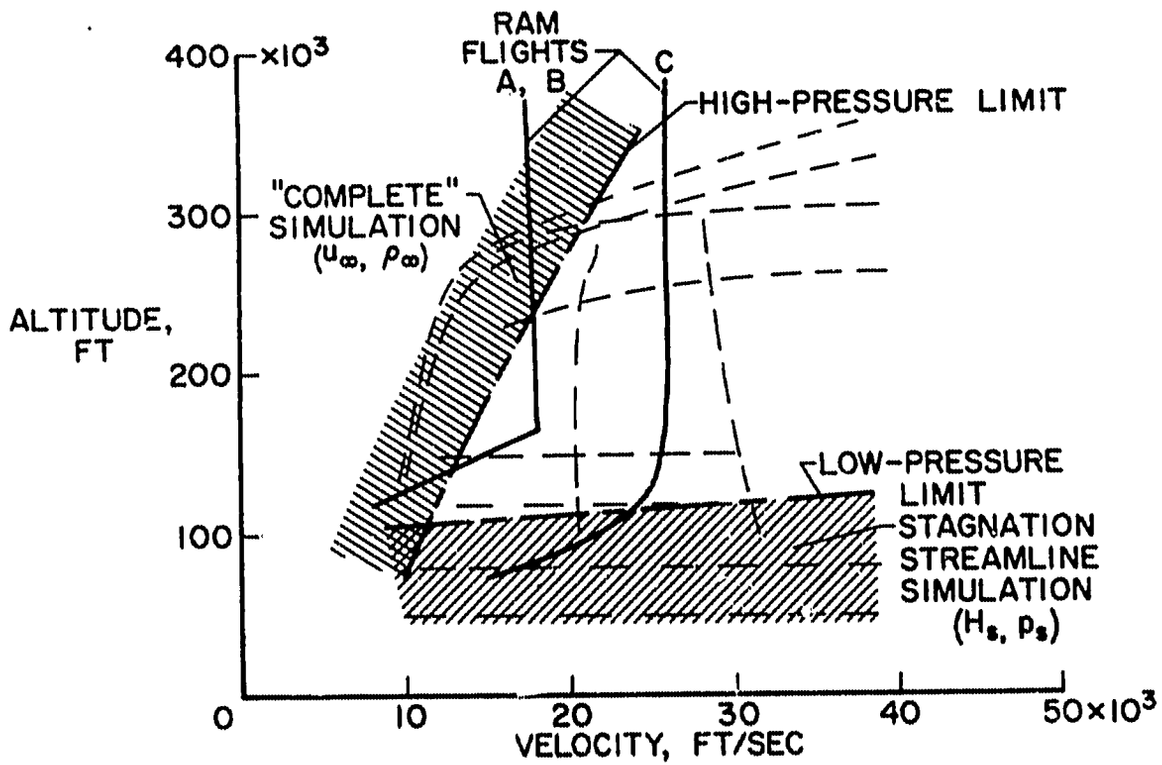
NASA

Figure 1.- Reentry flow-field plasmas.



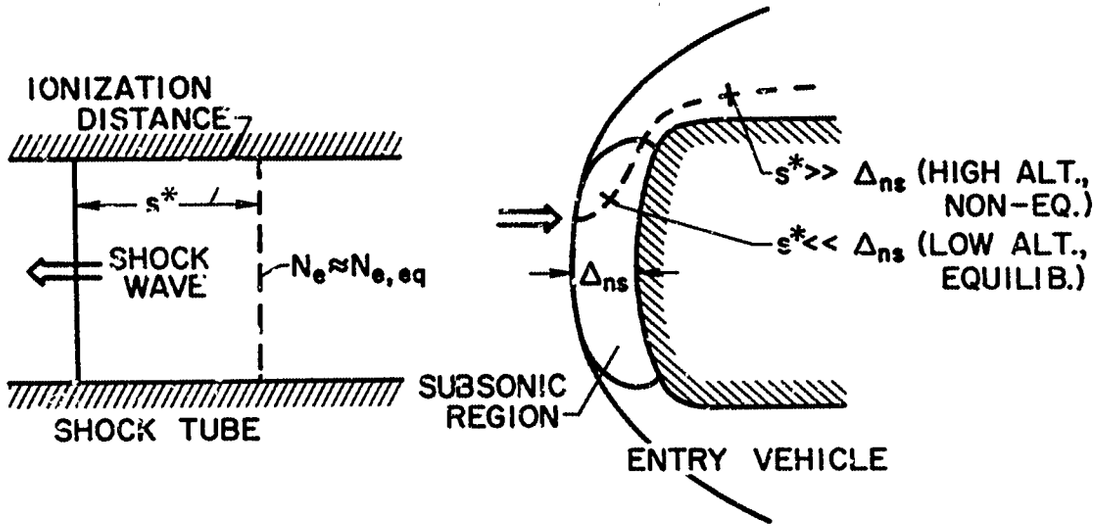
NASA

Figure 2.- Ionic chemical-kinetic regimes for blunt-body reentry.



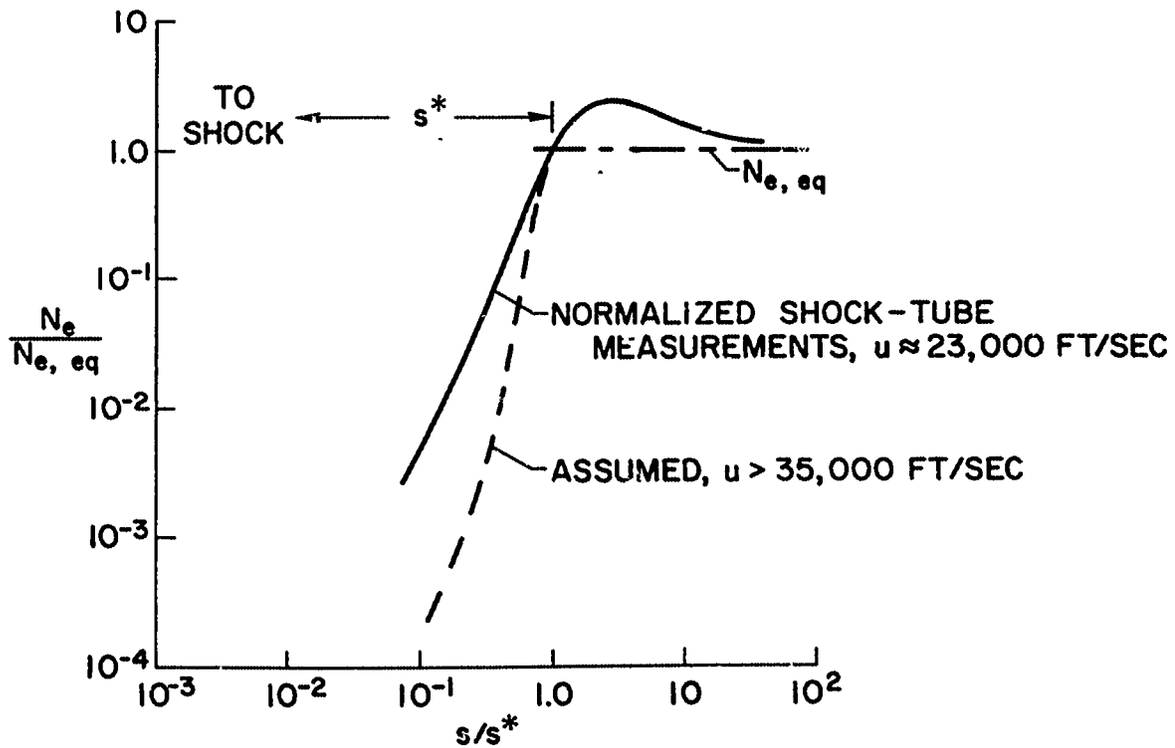
NASA

Figure 3.- Shock-tunnel flow-field simulation.



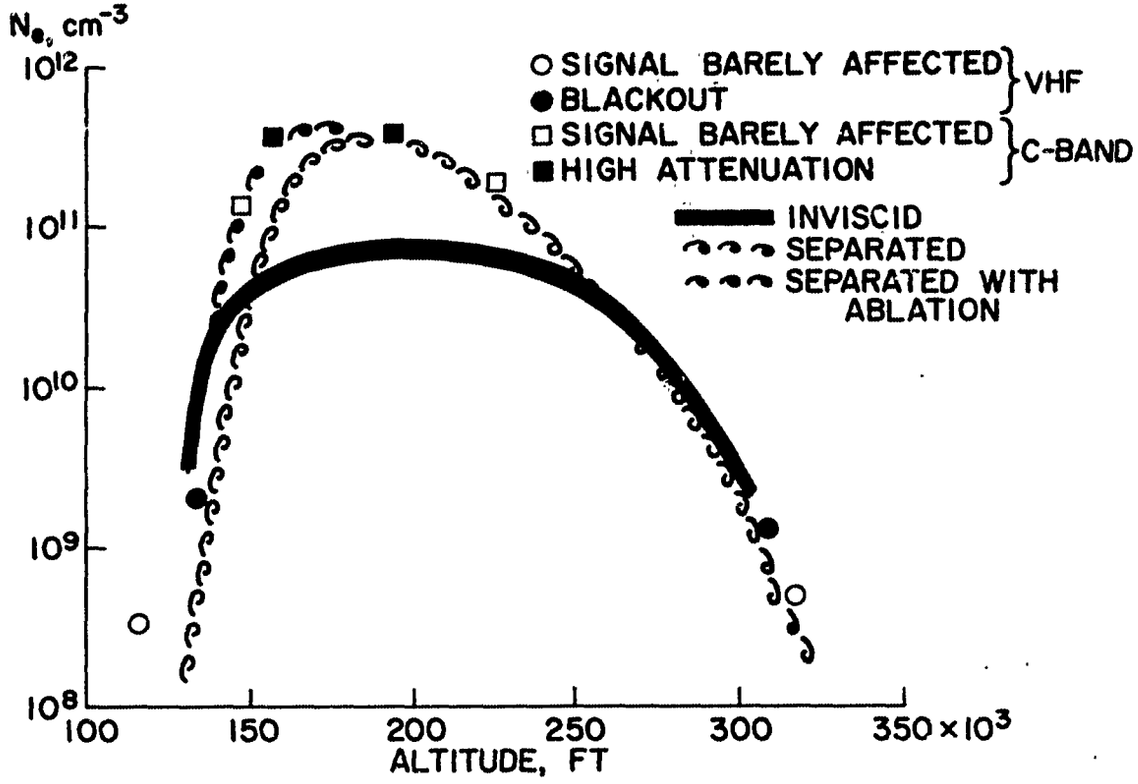
NASA

Figure 4. Nose-flow nonequilibrium ionization.



NASA

Figure 5.- Shock-wave ionization.



NASA

Figure 6.- Flow-field electron densities for Mercury-Atlas flights.

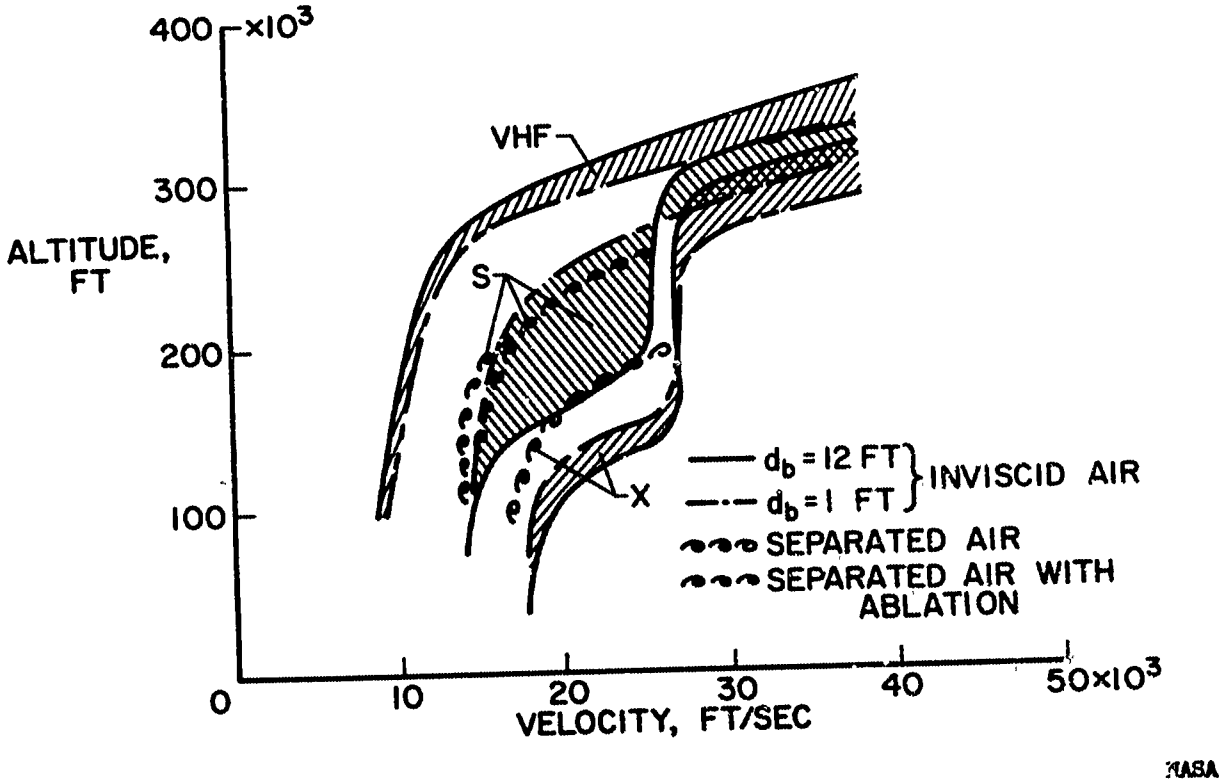


Figure 7.- Estimated signal blackout bounds for blunt bodies.

II. ESTIMATES OF NONEQUILIBRIUM IONIZATION PHENOMENA IN THE INVISCID APOLLO PLASMA SHEATH*

by

M. G. Dunn, J. W. Daiber, J. A. Lordi, and R. E. Mates**

Cornell Aeronautical Laboratory, Inc.
Buffalo, New York 14221

ABSTRACT

Estimates of nonequilibrium ionization phenomena in the asymmetric plasma sheath have been made for an Apollo-type body entering the earth's atmosphere at superorbital velocity. For an entry velocity of 30,000 ft/sec and an attack angle of 20°, results are presented for altitudes of 200,000 ft and 250,000 ft for the pitch plane.

The charged species are taken as N_2^+, O_2^+, NO^+, N^+, O^+ and e^-. The chemical model employed permits three-body recombination reactions, two-body dissociative-recombination reactions, charge-exchange reactions, and ion-atom-exchange reactions. Nonequilibrium species concentrations for both the neutral and the charged particles are presented along several streamlines for both altitudes investigated. The species distributions have a defined pattern which is readily interpreted in terms of the local temperature, velocity, and density fields. With the exception of the body stagnation point and a relatively small region on the body surface, the plasma-sheath fluid is found to be in a nonequilibrium state. The dominant electron-depletion reactions are shown to be $NO^+ + e^- \rightarrow N + O$, $N_2^+ + e^- \rightarrow N + N$, $N^+ + e^- \rightarrow N + e^-$, and $O^+ + e^- + e^- \rightarrow O + e^-$. Other important chemical reactions involving the charged species are discussed for various portions of the plasma sheath.

---

* This report is based on Research Sponsored by Goddard Space Flight Center, Greenbelt, Maryland under Contract No. NAS 5-3976.

** Consultant to Cornell Aeronautical Laboratory, Inc. State University of New York at Buffalo.

Contours of electron density in the forebody and near afterbody region are presented for altitudes of 200,000 ft and 250,000 ft. For the 200,000 ft case, the maximum forebody electron density in the stagnation region is calculated to be approximately 5×10^{15} electrons/cm^3. In the windward corner region the electron density is on the order of 5×10^{13} electrons/cm^3 and in the leeward corner region, is approximately 5×10^{12} electrons/cm^3. Corresponding values of electron density for an altitude of 250,000 ft. are found to be approximately 50 times less.

Electron-neutral and electron-ion collision frequencies are also calculated along each streamline in the plane of symmetry. The solution for an altitude of 200,000 ft indicated a maximum electron-neutral collision frequency in excess of 1×10^{10} rad/sec in the forebody region. In the corner region the electron-neutral collision frequencies are on the order of 5×10^{9} rad/sec. The electron-ion collision frequencies in the forebody region are slightly less than the electron-neutral collision frequencies for the same region. The corner region values are approximately one-fifth the corresponding electron-neutral collision frequencies. Similar calculations are conducted for an aititude of 250,000 ft. For a given streamline the electron-neutral collision frequencies are found to be approximately an order of magnitude less than at 200,000 ft. The electron-ion collision frequencies are found to be approximately 1/100 those for corresponding plasma sheath locations at 200,000 ft.

The electron density distribution and the collision frequency distribution for two selected paths through the plasma sheath are presented. The peak electron densities and collision frequencies for these paths occur at a significant distance from the body. The high electron density and collision frequencies in the inviscid flow-field emphasize the importance of the inviscid flow-field chemical kinetics. Additionally, they suggest that the influence of ablation products and viscous effects on the electromagnetic propagation should be more closely evaluated.

The attenuation for the propagation of one-dimensional plane waves along these two paths is presented. The implication of these results is that for the particular trajectory position and transmission paths selected it would be exceedingly difficult to communicate with the craft at a carrier frequency in the range of 1 to 10 Gc.

LIST OF SYMBOLS

A	Avogadro's number
A_i	constant term in reaction rate constant of i^{th} reaction
$\bar{c}$	mean electron speed
H	total enthalpy
h	static enthalpy
k	Boltzmann's constant
k_{F_i}	forward rate constant of i^{th} reaction
ℓ	characteristic length
M	collision partner
m_e	mass of an electron
n_e	local electron density
n_i	temperature exponent in reaction rate constant of i^{th} reaction
n_j	particle density of j^{th} species
P	streamline static pressure
P_o'	streamline static pressure immediately behind translational shock
P_i	defined by Eq. 10
Q_j	electron-neutral scattering cross-section for j^{th} species
Q_{ion}	electron-ion scattering cross-section (defined by Eq. 6)
R_{f_i}	forward rate of i^{th} reaction
R_{r_i}	reverse rate of i^{th} reaction
T	temperature
u_t	tangential velocity component
u_n	normal velocity component
x	distance along streamline

$\bar{x}$ non-dimensional distance along streamline, x/ℓ

β_{ij} defined by Eq. 9

γ species concentration

γ_j^+ concentration of j^{th} charged species

θ_i activation energy of i^{th} reaction

ν_{ij} stoichiometric coefficient of the j^{th} species on the reactant side of the i^{th} reaction

ν'_{ij} stoichiometric coefficient of the j^{th} species on the product side of the i^{th} reaction

ν electron-neutral collision frequency (defined by Eq. 5)

ν^+ electron-ion collision frequency (defined by Eq. 7)

ρ density

η_i defined by Eq. 11

Subscripts

∞ evaluated at free-stream conditions

2 evaluated downstream of translational shock

1. INTRODUCTION

Previous experience with the Mercury and Gemini earth-orbiting space vehicles which entered the atmosphere at a maximum velocity of approximately 24,000 ft/sec has indicated that communication with the craft at customary radio frequencies is impossible during a significant portion of the entry trajectory due to free electrons in the plasma sheath. Future entry conditions such as the 36,000 ft/sec superorbital velocity typical of the Apollo return from lunar missions imply considerable higher plasma-sheath electron densities than previously experienced. Thus, the blackout period of radio-frequency transmission can be expected to increase. If accurate estimates of the blackout boundaries are to be made, it is necessary that the ionization kinetics occurring within the plasma sheath be understood.

The purpose of this paper is to present detailed estimates of nonequilibrium ionization phenomena which have been obtained as part of an extensive study being conducted at CAL to investigate the asymmetric flow-field associated with an Apollo-type body at angle of attack. The objective of these estimates was to aid in the formulation of meaningful experiments and theoretical models of the plasma-sheath. With regards to the experiments, the important plasma-sheath electron production and depletion reactions are to be determined. For the theoretical models, it is necessary to obtain preliminary estimates of the flow field chemical composition and to determine those chemical reactions that must be included in future more exact calculations. A further goal is to obtain estimates of electron density and collision frequency distributions in the plasma sheath to aid in theoretical and experimental studies of electromagnetic propagation in dense plasmas.

In the present study, nonequilibrium ionization phenomena were calculated along fourteen streamlines in the pitch plane of an Apollo-type, asymmetric plasma sheath. The location of these streamlines in the plasma sheath and their corresponding pressure distributions were determined from an exact solution to the ideal-gas asymmetric flow field. This solution has been obtained using a time dependent direct method developed by Bohachevsky

and Mates[1,2] under support of the theoretical phase of this contract. The particular solution utilized was for a 30,000 ft/sec ideal-gas flow over an Apollo-type body at 20° angle of attack. The effects of the viscous boundary layer and the injection of ablation products were not included. For the given streamline pressure distribution an exact nonequilibrium ionization calculation was carried out using a streamtube computer program previously developed at CAL.[3]

Nonequilibrium species concentrations are presented for several of these streamlines for altitudes of 200,000 ft. and 250,000 ft. Contours of plasma sheath electron density determined from these calculations are presented for both altitudes. Corresponding electron-neutral and electron-ion collision frequencies are presented for selected streamlines. The results are then used to obtain electron density and collision frequency distributions along two paths through the plasma sheath. These distributions are utilized to calculate the attenuation of one-dimensional plane waves along the two paths.

These results are new in that an exact flow field solution for a blunt body at angle of attack was available so that a more realistic calculation of the plasma sheath ionization could be made. In view of this better flow field solution, a relatively complete air chemistry model was employed to perform the nonequilibrium ionization calculations along selected streamlines in the plane of symmetry.

2. METHOD OF CALCULATION

2.1 Flow Field

The time-dependent direct method[1,2] utilized to describe the asymmetric plasma sheath is founded on the principle that the physically correct steady-state solution is obtainable in the limit, for large time, of an appropriate nonsteady or transient solution. The technique starts the body from rest at time zero with constant velocity. The resulting nonsteady field is then computed until the desired steady-state solution is attained (i.e., when the flow field ceases to change). The retention of the time derivatives in the governing conservation equations results in a system of hyperbolic differential equations. Therefore, arbitrary free-stream parameters can be specified everywhere, except at the body, where the normal component of the velocity must vanish. This method describes the inviscid flow field for an arbitrary body shape with an arbitrary orientation.

The time-dependent direct method has been used to calculate the ideal-gas flow field for an Apollo-type vehicle at 20° angle of attack and a free-stream velocity of 30,000 ft/sec at an altitude of 200,000 ft. Bohachevsky and Mates[2] have located streamlines in the plane of symmetry and on the body surface. Figure 1, taken from their work, is presented here to illustrate the sonic line locations and the relative position in the plasma sheath of the fourteen streamlines used in the present study. The corresponding pressure distributions for these streamlines have also been determined and were used to calculate the plasma-sheath, nonequilibrium chemical kinetics by means of a streamtube technique. The details of this calculation are described in the next section.

In order to perform the nonequilibrium ionization calculation at 250,000 ft. it was assumed that the shock shape, shock standoff distance, and location of streamlines within the plasma sheath were identical to those in the 200,000 ft. solution. It was further assumed that the respective streamline pressure ratios P_2/P_o', where P_o' is the pressure immediately behind the shock for a given streamline, remained unchanged. However, the values of P_o' were evaluated for each streamline at both altitudes.

Of course, the present calculations do not include the effects of real gas phenomena on the basic gas dynamic characteristics of the flow field, such as shock shape and streamline geometry. However, it is felt that inclusion of such effects would not significantly alter the basic nature of the results.

2.2 Streamtube Calculations

The gasdynamic properties and flow composition along selected streamlines in the plasma sheath were obtained in the following manner. The previously described pressure distributions were used as input data to the [illegible] computer program which has been developed for numerical solutions of the quasi-one-dimensional, inviscid flow of reacting mixtures.[3,4] This program computes the flow of a general mixture of ideal gases through a streamtube of specified cross section or one having a specified streamwise pressure variation. The vibrational and electronic degrees of freedom are assumed to remain in thermal equilibrium with translation while the chemical reactions proceed at finite rates. Ionized mixtures are treated by considering electrons to be a separate chemical element.

In performing the nonequilibrium ionization calculations it was necessary to assume that the free-electron temperature was equal to the gas translational, vibrational, and electronic temperature. There is reason to believe that this assumption may not be valid on the basis of Daiber's studies[5] of the dissociative recombination of NO^+ in an expanding nozzle flow using microwave techniques. The results of that work indicated that the electron temperature is most likely higher than the gas translational temperature. Hurle and Russo[6] studied the coupling between free-electron temperature and N_2 vibrational temperature in expanding flows using a spectrum-line reversal technique. They concluded that in the presence of trace amounts of N_2 the electron temperature and the nitrogen vibrational temperature were essentially equal but higher than the translational temperature. At this time it is not possible to estimate the influence of this uncertainty on the electron density distributions. Additional research is underway at CAL to determine the effect of such energy coupling on the chemical kinetics.

In the streamtube computer program the enthalpy and chemical potential of each species are specified. In addition to the reaction-rate information, it is necessary to specify data for the thermodynamic properties of the species. Since the gas is assumed to be a mixture of ideal gases, the species properties must be specified functions of temperature only. Two methods are used to describe the species thermodynamic properties: polynomial fits to tabulated data or alternately, a simple harmonic-oscillator model. In the present calculation the polynomial fits to tabulated data were used for temperatures between 6000°K and 24,000°K and the harmonic-oscillator model was used below 6000°K. The polynomial fits employed were those obtained by Marrone[7] from the tabulated data of Gilmore.[8] The species data used in the harmonic-oscillator model are given by Marrone.[9]

In addition to the specification of the streamline pressure distribution and the chemical model, the streamtube computer program requires the specification of initial conditions. For the present study, the initial point of the calculation is just behind the translational, rotational shock. The vibrational and electronic degrees of freedom were assumed to attain equilibrium with the translational and rotational mode prior to any chemical reaction.

The pressure at the initial post-shock position was taken to be the value immediately behind the shock in the ideal-gas solution. Then, using this pressure P_o' and the free-stream conditions, the velocity components u_{t2} and u_{n2} were evaluated from the oblique shock relations.

$$u_{t2} = u_{t\infty} \tag{1}$$

$$u_{n2} = u_{n\infty} - \frac{P_2 - P_\infty}{\rho_\infty u_{n\infty}} \qquad \text{(for this condition } P_2 = P_o'\text{)} \tag{2}$$

The velocity components ahead of the shock are given by $u_{t\infty} = u_\infty \cos\theta$ and $u_{n\infty} = u_\infty \sin\theta$ where θ is the angle the tangent to the shock makes with the free-stream velocity vector. Then the static enthapy behind the shock is obtained from

$$h_2 + \frac{u_2^2}{2} = (H_o)_\infty \tag{3}$$

where $u_2^2 = u_{n2}^2 + u_{t2}^2$ and $(H_o)_\infty$ is the total enthalpy of the freestream.

In order to find the temperature consistent with the condition of vibrational and electronic equilibrium at the initial point, the following procedure was adopted. Using the polynomial fits to the thermodynamic data of N_2, O_2, and Ar the quantity

$$h(T) = (\gamma_{O_2})_\infty h_{O_2}(T) + (\gamma_{N_2})_\infty h_{N_2}(T) + (\gamma_{Ar})_\infty h_{Ar}(T) \tag{4}$$

was plotted as a function of temperature. The variables $(\gamma_{O_2})_\infty$, $(\gamma_{N_2})_\infty$ and $(\gamma_{Ar})_\infty$ represent the free-stream concentrations in moles/gm and h_{O_2}, h_{N_2}, h_{Ar} represent the species enthalpies in cal/mole. Then T_2 was obtained from the calculated value of h_2 using this graph of h versus T. Using P_o', T_2, and assuming the composition to be frozen at the free-stream values, the density at the initial point, ρ_2, was calculated from the state equation.

Typical streamline pressure distributions are illustrated in Figures 2, 3, and 4. The relative location of these streamlines in the plasma sheath is illustrated by the insert. The pressure distribution has been nondimensionalized by dividing the local static pressure, P_2, by P_o'. Polynominal fits to the streamline pressure distributions were obtained and used as input data to the streamtube program. Any discrepancies between the polynomial fits and the ideal-gas solution were comparable to the approximation that the nonequilibrium effect on the pressure distribution was negligible.

2.3 Air Chemistry Model

Table I presents the chemical kinetic data utilized for reactions involving neutral species. The rate constants used in these calculations were taken from Eschenroeder, Boyer, and Hall[3] and by Hall, Eschenroeder and Marrone.[10] The neutral species permitted in this model are N_2, O_2, NO, N, O, and Ar. It will be illustrated later that the species concentrations of the neutral particles N and O are, in general, an order of magnitude or two greater than the electron concentration. Thus, the neutral chemistry has a significant influence on the streamline gas dynamics and hence on the ionization kinetics.

Table II defines the chemical kinetic data utilized for reactions involving charged species. The charged species are taken to be N_2^+, O_2^+, NO^+, O^+ and e^-. The model employed permits three-body recombination reactions, two-body dissociative-recombination reactions, charge-exchange reactions, and ion-atom exchange reactions. The rate constants presented in Table II were taken from the published literature.[11-14]

Rate constants for the dissociation of N_2 and O_2 and the formation of NO are generally considered to be better known than those for chemical reactions involving charged particles. These reactions involving only neutral species have been measured for relatively high gas temperatures. The recombination rates, however, for these species have not been measured for high-temperature expanding flows. It is difficult to determine the rate-constant uncertainty for reactions involving neutral species but it is estimated to be less than an order of magnitude.

The uncertainty in the ionized-species reaction-rate constants is significantly greater than that of the neutral chemistry model. Table III presents a comparison at selected temperatures for six of the charged species chemical reactions which were found to be important in the plasma sheath. Many other reactions were found to be important but not as consistently so as those included in this comparison. The results of this comparison indicate that the rate constant value can differ by several orders of magnitude depending on the source one selects.

The influence of rate-constant uncertainty on the streamtube electron-density distribution for an expanding flow, using the complete chemical model given in Tables I and II, has been investigated as part of the present program at CAL. The rate constants for the charge-exchange reactions and the three-body, electron-ion recombination reactions were independently perturbed by two orders of magnitude. The results of these calculations indicated that such an uncertainty can have an order of magnitude influence on the streamtube electron distribution. Bortner[15] has previously determined that an order of magnitude variation in the O_2 dissociation rate constant can change the electron density by two orders of magnitude. He further illustrates that an order of magnitude decrease in the NO^+ ionization reaction rate (NO^+ is the only ion considered in his model) results in a corresponding order of magnitude decrease in the electron density. It has thus been illustrated that the rate constant uncertainty has a significant influence on the plasma sheath electron density. From a communication viewpoint this uncertainty is quite important. This is the reason for the experimental program currently underway at CAL to measure the important chemical reaction rate constants for Apollo-type plasmas.

The largest rate-constant uncertainty illustrated by Table III is that for the three-body, electron-electron-ion recombination reactions. This particular reaction was found to be important near the body corner in the region of rapid expansion. However, the reverse of this reaction was found to be a dominant source of electrons in the forebody region. Several authors[13, 16] have published predictions of the rate constant for the electron recombination reaction. In addition, Hinnov and Herschberg[17] have studied the three-body recombination rate of He^+ in the quiescent afterglow of the B-1 stellarator discharge. In light of current information on this particular reaction, it makes little difference whether the ion is He^+, H^+, O^+, or N^+. The rate constants proposed by Makin and Keck,[13] Bates, Kingston, and McWhirter,[16] and Hinnov and Herschberg[17] are all in agreement. Bortner[14] also suggests a value for the electron-electron-ion recombination rate constant. However, in view of the results of References 13, 16 and 17 the value suggested by Makin and Keck[13] has been utilized in this study.

3. RESULTS

3.1 Basic Chemical Kinetics

Before discussing in detail the nonequilibrium ionization results, a few remarks concerning general aspects of the streamtube chemistry are in order. In a gross sense, the nonequilibrium streamtube species distributions should be expected to illustrate trends similar to the more familiar normal shock solutions as modified by the gas dynamic environment of the curved shock layer. The gas passing through the more normal portion of the translational shock can be expected to experience significantly more molecular dissociation than the flow passing through the outer extremities as a result of the higher static temperature associated with the stagnation region. As dissociation proceeds in these streamtubes the static temperature decreases and the rate of dissociation also decreases. The higher temperature streamtubes should also have correspondingly higher ionized species concentrations as a result of their greater internal energy.

Streamtubes in the immediate vicinity of the stagnation region and in close proximity to the body surface are the most likely locations for the occurence of a local equilibrium state as a result of the higher temperature and increased residence time of the fluid. Obviously, at the inviscid stagnation point, where the velocity becomes zero, the fluid achieves equilibrium. The peak ionization along the inner streamtubes should occur at shorter streamtube distances from the shock than the corresponding peaks for the extremity streamtubes as a result of the lower fluid velocities and higher temperature. With regard to the influence of ambient density on the chemical kinetics it should be expected that if equilibrium is achieved the respective streamtube temperatures will be decreased. Molecular dissociation can be expected to become more complete and the charged species concentrations should increase. For a given streamtube, a reduction of the initial density effectively reduces the number of particle collisions and can be expected to increase the streamtube distance required to achieve maximum ionization.

3.2 Streamline Species Distributions for 200,000 ft.

This section discusses the calculated neutral and charged species distributions for 200,000 ft. altitude. Typical results for the neutral species are presented in Figs. 5, 6, and 7 for streamlines, 10, 3, and 14 (see Fig. 1 for relative location of streamlines). These results illustrate that for the higher static temperature streamlines (10 and 3) the dissociation of N_2 and O_2 is greater than it is for the lower temperature streamline 14. The maximum neutral species concentrations were found to be approximately an order of magnitude greater than the maximum charged-particle species concentrations. Thus, the neutral chemistry has a strong influence on the thermodynamic properties of the plasma and the ionization kinetics. Near the end of each of the streamlines the atomic species N and O and the N_2 molecule tend to a constant concentration. However, the molecular species NO and O_2 do not illustrate this trend.

Figures 8 and 9 illustrate the charged species distributions along streamlines 5 and 3 in the windward plasma sheath. Because of the relatively high temperature of streamline 5, the maximum electron concentration along this streamline is approximately four times greater than that along streamline 3. The peak concentration is attained in approximately one-fourth the corresponding distance for streamline 3 as a result of the lower streamtube velocity. The difference in the pressure distribution for these two streamlines is unimportant as regards to streamline chemistry.

Figure 8 illustrates that for the first centimeter along the streamline the dominant ion is N_2^+. After 5 centimeters the dominant ion becomes N^+. The initial concentration of O_2^+ is slightly greater than the NO^+ concentration. However, O_2^+ is depleted so rapidly that at a distance of 100 centimeters its concentration is several orders of magnitude less than the other ions.

The species distributions along streamline 3 are indicative of the lower temperature streamlines. The electron concentration at the shock is significantly lower than in the previous case. Again the dominant ion in the first centimeter is N_2^+. Further along the streamline NO^+, N^+, and

O^+ become the dominant ions. The species distribution presented in Figures 8 and 9 do not give indications of a chemically frozen flow. In addition, the fluid along these streamlines is far from equilibrium as determined by evaluating the ratio of the forward to the reverse reaction rate for each reaction at selected points along the streamlines. The forward and reverse rates were in all cases significantly different.

Figures 10, 11, and 12 present species distributions along three streamlines in the leeward portion of the flow field. The distributions are presented in order of decreasing streamtube static temperature. Streamline 8 is the streamline that wets the leeward body surface. The maximum electron concentration for streamline 8 is 3.5 times greater than that for streamline 12 and 200 times greater than that for streamline 14. The peak electron concentration is observed to occur much closer to the shock for the higher temperature streamlines, once again illustrating the influence of temperature and local velocity on the chemical kinetics.

Figure 10 indicates that as the gas expands along the leeward forebody surface the electron concentration remains relatively constant until the corner region is reached. In the vicinity of the corner the gas begins to expand and rapid changes in species concentration are observed. The ratio of the forward to the reverse reaction rate was also investigated for the streamline. At a distance of approximately 100 centimeters from the translational shock a local equilibrium was approached. This is the only location within the entire flowfield, with the exception of the inviscid stagnation point, where local equilibrium was approached. The species distribution for streamline 12, which is shown in Figure 11, does not exhibit a pronounced region of constant electron concentration. However, the influence of the corner expansion on the species concentrations is observed in the rapid decrease of species concentration near the end of the streamline. Figure 12 illustrates that for streamline 14, the minimum static temperature line investigated, approximately 100 centimeters of streamline travel were required for the electron concentration to reach its maximum. The ionized species concentrations are decreasing rapidly at 250 centimeters, the terminal point of the calculation.

From Figures 10, 11, and 12, the dominant ion near the shock was determined to be N_2^+. Further along streamline 8 the dominant ions were found to be the atomic ions N^+ and O^+. At distances greater than 10 centimeters along streamline 12 the ions N^+, O^+, and NO^+ were of approximately the same order of magnitude. Figure 12 indicates that beyond 10 centimeters along streamline 14 the dominant ion is clearly NO^+.

The results presented above can be summarized by noting that several regions exist in which the dominant charged species are different. Immediately behind the translational shock a molecular ionization region was found for all streamlines. For the fluid passing through the more normal portion of the shock this molecular ionization region is followed by an atomic ionization region within a short distance behind the shock. For streamlines crossing the translational shock intermediate to the near-normal and outer portion, this molecular ionization region is followed by a combined molecular and atomic ionization zone in which N_2^+, N^+, NO^+, and O^+ become the dominant ions. In the case of the outer extremity streamlines the molecular ions N_2^+ and O_2^+ are significantly depleted and the dominant ion becomes NO^+ instead of the atomic ions N^+ and O^+. These regions are classified, the dominant ions noted, and the chemical reactions responsible for these trends discussed in detail in Section 3.5 and summarized in Table IV.

Contours of forebody electron density were constructed using the streamline species distributions and are presented in Figure 13 for an altitude of 200,000 ft. at a velocity of 30,000 ft/sec. In the stagnation region the electron density is in excess of 1×10^{15} electrons/cm^3 but less than 5×10^{15} electrons/cm^3. The windward-side electron density in the corner region varies from approximately 1×10^{15} to 5×10^{13} electrons/cm^3. The flow-field solution used for the nonequilibrium calculations has not, at this time, been extended to include more of the afterbody flow. Thus, the windward, contours for lower than 5×10^{13} are not available. Leeward side contours are presented for electron densities from 1×10^{15} to approximately 5×10^{12}.

3.3 Electromagnetic Propagation in Plasma Sheath

In addition to calculating nonequilibrium species concentrations along each streamline, the electron-neutral and electron-ion collision frequencies were also calculated. The electron-neutral scattering cross sections Q_j used in this work were obtained by suitably averaging [18, 19] the monoenergetic values suggested by Shkarofsky, et al[20]. The electron-neutral collision frequency as a function of position on a given streamline was then determined by the relation

$$\nu = \bar{c} \sum_j n_j Q_j \qquad \text{rad/sec} \qquad (5)$$

where the mean electron speed $\bar{c}$ is given by $\frac{4}{3}\sqrt{\frac{8kT_e}{\pi m_e}}$, the neutral particle density n_j is given by $\rho A \gamma_j$, A is Avogadro's number; and T_e is the electron temperature. The electron-ion scattering cross sections were calculated from Eq. (6) using the method suggested by Spitzer[21] and including the additional term suggested by Lin[22] to account for close collisions.

$$Q_{ion} = \frac{2.51}{T_e^2} \times 10^{-6} \ln \left[\frac{8.77 \times 10^3 (T_e)^{1.5}}{(n_j)^{0.5}} \right] + \frac{9.74 \times 10^{-7}}{T_e^2} \qquad (6)$$

The electron-ion collision frequency was then calculated as a function of position along the streamline using Eq. (7).

$$\nu^+ = \bar{c}\, n_e\, Q_{ion} \qquad \text{rad/sec} \qquad (7)$$

where $\bar{c}$ is given above and n_e is the local elect on density in particles/cm^3.

In these calculations, as well as in the calculation of species concentration, the electron temperature T_e is assumed equal to the gas translational temperature.

Figures 14 and 15 present the electron-neutral and the electron-ion collision frequencies in the plane of symmetry for a free-stream velocity of 30,000 ft/sec at an altitude of 200,000 ft and an angle of attack of 20°. The electron-neutral collision frequency was somewhat in excess of 1×10^{10} rad/sec in the forebody region and in the corner region is on the order of 5×10^{9} rad/sec. The electron-ion collision frequency in the forebody region is slightly less than the electron-neutral collision frequency in the same region. However, the corner values are approximately a factor of five less than the electron-neutral collision frequencies.

The electron density distribution and the collision frequency (electron-neutral plus electron-ion) distribution for two selected paths through the plasma sheath have been calculated. Figure 13 illustrates the relative location of path "A" and path "B". Figures 16 and 17 present the electron density distribution and the collision frequency distribution for path "A". The peak electron density for path "A" is approximately 2×10^{14} electrons/cm^3 and occurs at approximately 60 centimeters from the body. As the shock is approached the electron density decreases rapidly. On the other hand, the collision frequency for path "A" is relatively constant through the plasma sheath. The peak value is approximately 1.1×10^{10} rad/sec at 60 centimeters from the body and the minimum value is 5×10^{9} rad/sec just behind the translational shock. Path "B" results are given in Figs. 18 and 19. The plasma is almost twice as thick as in the previous path. The maximum electron density for path "B" is 6×10^{13} and occurs at approximately 20 centimeters from the body. The maximum collision frequency for path "B" is also less than that for path "A". A maximum value of 6.5×10^{9} rad/sec occurs at 70 centimeters from the body.

The fact that the peak electron densities and collision frequencies for these paths occur at a significant distance from the body is important. The values of the peak electron densities and collision frequencies are high emphasizing the importance of the inviscid flow field. For the purposes of communication, the influence of ablation products and viscous effects on the electromagnetic-propagation should be compared to that of the inviscid flow field.

The attenuation for the propagation of one-dimensional plane waves along path "A" and path "B" has been calculated using a technique suggested by Bein[23]. Application of the technique requires that the electron density and collision frequency gradients normal to the direction of electromagnetic propagation be negligible. This condition was not met for the plasma sheath of interest in this work. Although realizing the limitations of its application to the plasma of interest, the technique was used to obtain qualitative estimates of the attenuation of plane electromagnetic waves. Calculations were initiated at a frequency of 9.0×10^{11} cycles/sec. The frequency was decreased until the attenuation exceeded approximately - 115 db. Calculations were also attempted at 3 Mc and 30 Mc. For these low frequencies the reflection coefficients approach unity. These could probably be reduced by properly matching the near field of the antenna to the plasma. However, the calculated absorption losses in the plasma were in excess of -150 db so that electromagnetic propagation at these frequencies still appears difficult.

Figure 20 presents the plasma sheath attenuation of the electromagnetic propagation as a function of carrier frequency for path "A" and path "B". These results indicate that the attenuation exceeds - 70 db for carrier frequencies less than 175 Gc along path "A" and 100 Gc along path "B". The implication of these results is that for this trajectory position and transmission path it would be exceedingly difficult to communicate with the craft at a carrier frequency in the range of 1 to 10 Gc. However, it must be emphasized that the accuracy of the electromagnetic-propagation calculation leading to the attenuation prediction is presently unknown. Before accurate estimates of the transmission and reflection coefficients can be made for plasmas of this type, a significant amount of theoretical and experimental research must be completed in the area of electromagnetic propagation.

3.4 Streamline Species Distributions for 250,000 ft.

Nonequilibrium ionization calculations for an altitude of 250,000 ft. were also performed. The shock shape, the relative position of the streamlines within the plasma sheath, and the nondimensional pressure distribution along the streamlines were assumed to be the same as for the 200,000 ft. case. Of course, the significant reduction of free-stream pressure, temperature, and density were accounted for in the calculations.

Nonequilibrium charged-species distributions along the windward streamlines 5 and 3 are presented in Figures 21 and 22. The electron concentration is increasing for almost the entire length of the streamlines. For a distance of approximately 10 centimeters along the streamlines the molecular ions N_2^+ and O_2^+ are dominant. At distances greater than 10 centimeters the molecular ions NO^+ and N_2^+ and the atomic ions N^+ and O^+ become dominant. The observed trend is similar to the 200,000 ft. results except that peak ionization for the higher altitude is achieved much further along the streamline. This is indicative of the lower density and thus fewer particle collisions. Figures 23 and 24 present the species distributions along the leeward streamlines 8 and 12. At relatively short distances along the streamlines the dominant ions are N_2^+, O_2^+, and NO^+. Near the end of the calculation the dominant ions are in general N^+, NO^+, N_2^+ and O^+. Thus once again the qualitative results are similar to the 200,000 ft. results except for the greater distance required to achieve peak ionization.

If the fluid flow were in equilibrium the streamline charged species concentrations for the 250,000 ft. calculations should have been greater than corresponding values at 200,000 ft. This, in fact, was not the case. Charged species concentrations for the 200,000 ft. case were in all cases greater than those for 250,000 ft. It is thus noted that the flow field at 250,000 ft. is also far from equilibrium. This conclusion was verified by reviewing the ratio of the forward and reverse reaction rates along the streamline.

The plasma-sheath electron density contours for 250,000 ft. altitude are presented in Figure 25. Both the maximum electron concentrations and the electron densities for a given streamline are less for this higher altitude case. The plasma-sheath electron densities for corresponding locations are 10 to 50 times less than for the 200,000 ft. case. Portions of the contours in the leeward region are dotted indicating an uncertainty in their location.

Electron-neutral and electron-ion collision frequencies for this higher altitude are presented in Figures 26 and 27 respectively. For a given streamline the electron-neutral collision frequencies are shown to be approximately 10 times less than at 200,000 ft. The electron-ion collision frequencies are approximately 100 times less than those for corresponding plasma-sheath locations at 200,000 ft. The reduced electron densities and collision frequencies at the higher altitude are indicative of the influence of nonequilibrium chemistry and initial density.

3.5 Determination of Important Chemical Reactions

The important chemical reactions involving charged species have been determined by comparison of the contribution of each reaction to the change in species concentration with distance along each streamline ($d\gamma_j^+/d\bar{x}$) This study was undertaken in an effort to truncate the chemical model currently in use and to determine the important electron-depletion and electron producing reactions. Comparisons were made for many points along each streamline in the plasma sheath. The value of ($d\gamma_j^+/d\bar{x}$) is given by Eq. (8)

$$\frac{d\gamma_j^+}{d\bar{x}} = \sum_{i=1}^{n} \beta_{ij} P_i X_i \qquad (8)$$

where $\bar{x}$ is the nondimensional distance x/ℓ

$$\beta_{ij} = \nu'_{ij} - \nu_{ij} \qquad (9)$$

$$P_i = \frac{\ell R_{fi}}{\rho u} \qquad (10), \qquad X_i = 1 - \frac{R_{ri}}{R_{fi}} \qquad (11)$$

and R_{fi} and R_{ri} are the forward and reverse rates of the ith reaction. The magnitude of ($d\gamma_j/d\bar{x}$) is indicative of the importance of the particular reaction for producing or depleting the species of interest. In this study a reaction was deemed important at a particular point along a streamline if the absolute value of its $P_i X_i$ product was within two orders of magnitude $P_i X_i$ at that point.

By use of the technique described above it was found that a negligible number of reactions could be dropped from the model currently in use. At some point or another within the flow field all but two of the reactions are important. The two reactions that could be eliminated from the model are the reactions:

$$e^- + N + O_2^+ \longrightarrow N + O_2$$

$$e^- + O + O_2^+ \longrightarrow O + O_2$$

This raises the always present question as to whether or not some of the possible reactions not included in the 64-reaction model might be important. This possibility is currently under investigation.

As suggested previously, in analyzing the streamtube results it was found that the species distributions through the flow field could be classified according to the location at which the streamtube crosses the shock. Table IV summarizes the various regions, the dominant ions, and the important reactions for that region. For a relatively short distance behind the translational shock there is in all cases what might be classed as a high-temperature, molecular ionization region. The dominant ions in this region are N_2^+, NO^+ and O_2^+. In the case of streamtubes that crossed the translational shock in the near normal portion, this molecular ionization region is followed by a high-temperature atomic ionization region. The dominant ions in the atomic ionization region are found to be N^+ and O^+. An intermediate-temperature, atomic and molecular ionization region was also found for which the dominant ions are N^+, NO^+ and O^+. This region immediately follows the high-temperature, molecular ionization region and is applicable to streamtubes that cross the translational shock between the near normal portion and the outer extremities. A low-temperature molecular ionization region was also found for which NO^+ is the dominant ion. Its location immediately follows the high-temperature, molecular ionization region for streamtubes crossing the outer extremities of the translational shock. The dominant chemical reactions for these three regions are distinctly different as illustrated by Table IV. The important electron-producing reactions are also shown in Table IV.

The dominant electron-depletion reactions were found to be the two-body dissociative-recombination reactions

$$NO^+ + e^- \longrightarrow N + O$$

$$N_2^+ + e^- \longrightarrow N + N$$

and the three-body electron-ion-recombination reactions

$$N^+ + e^- + e^- \rightarrow N + e^-$$

$$O^+ + e^- + e^- \rightarrow O + e^-$$

The two-body dissociative-recombination reactions are of approximately equal importance throughout the plasma sheath for these particular flight conditions. The three-body electron-ion recombination reactions become important beginning in the corner regions near the body. The reason for these reactions becoming important is the relatively large negative exponent of temperature appearing in the reaction rate constant and the rapid decrease in static temperature with the flow expansion.

The dominant charge-exchange reactions were determined for many locations within the plasma sheath. The particular reactions found to be important again vary with position in the plasma sheath. However, the following charge-exchange reactions are consistently important, although not necessarily the most important, at various plasma sheath locations.

$$O + N^+ \rightarrow N + O^+$$

$$O + N_2^+ \rightarrow N_2 + O^+$$

$$NO + N^+ \rightarrow N + NO^+$$

It is emphasized that specific plasma-sheath locations were found where other charge-exchange reactions given in Table II were equally important.

Similarly, the dominant ion-atom exchange reactions were determined for the entire plasma sheath. The following reactions were found to be the most consistently important.

$$N_2 + O^+ \longrightarrow N + NO^+$$

$$O + N_2^+ \longrightarrow N + NO^+$$

$$O + N_2^+ \longrightarrow NO + N^+$$

However, all of the ion-atom-exchange reactions were found to be important at some point within the plasma sheath.

The charge-exchange and ion-atom exchange reactions are important to the over-all chemical kinetics of the plasma. Both of these classes of reactions aid production of the molecular ion NO^+ which is then involved in the relatively fast dissociative-recombination reaction noted above.

Based on the model presented in Table II the important chemical reactions for various plasma sheath locations have been defined. Uncertainties in the values of the reaction rate constants utilized in these calculations have been discussed in Section 2.3. It is important to note that the selected values of rate constant have a significant influence on the determination of the dominant reactions. It is felt, however, that the best available values have been used, and thus the results are as accurate as can be obtained at this time.

To illustrate the importance of utilizing a relatively complete chemical model for the calculation of the ionized flow field, the electron concentration along streamline 8 was recomputed for a truncated model Fig. 28, in which the charged species N^+, O^+, N_2^+ and O_2^+ and all reactions involving these species were deleted, only NO^+ being retained. As shown in Figure 28, the peak electron concentration for Model I is approximately an order of magnitude greater than that for Model II. Farther along the streamline the difference between the electron concentrations for the two models is reduced to a factor of approximately five. A similar comparison along the extremity streamlines for which N^+ and O^+ are not the dominant ions gives considerably better agreement between the streamline electron concentrations calculated using the different models. Thus, there are regions of the flow field for which the truncated model can be justifiably used to calculate the charged species concentrations.

4. CONCLUDING REMARKS

Nonequilibrium species concentrations along selected streamlines in the asymmetric Apollo plasma sheath have been presented. The species distributions have a defined pattern which is readily interpreted in terms of the local temperature, velocity, and density fields. With the exception of the body stagnation point and a relatively small region on the body surface, the plasma-sheath fluid was found to be in a nonequilibrium state for the trajectory points considered. The results indicate that the dominant ion in the early portion of the streamtube flow is, in general, N_2^+. At further distances along the higher initial temperature streamlines, N^+ and O^+ are dominant, whereas for the lower initial temperature streamlines NO^+ becomes dominant. For streamlines of intermediate static temperature, the ions NO^+, N^+ and O^+ are equally important. The calculations also illustrate the influence of initial density and local fluid velocity on the variation in species concentration with distance along the streamline. The streamlines of lower initial density were shown to require significantly longer flow distances to achieve maximum ionization. The dominant electron producing, electron depleting, charge exchange, and ion-atom exchange reactions are determined for many locations in the plasma sheath.

Contours of electron density in the forebody and near afterbody region have been presented for altitudes of 200,000 ft and 250,000 ft. For the 200,000 ft case, the maximum forebody electron density in the stagnation region was calculated to be approximately 5×10^{15} electrons/cm^3. In the windward corner region the electron density was on the order of 5×10^{13} electrons/cm^3 and in the leeward corner region, was approximately 5×10^{12} electrons/cm^3. Corresponding values of electron density for an altitude of 250,000 ft were found to approximately 50 times less.

Electron-neutral and electron-ion collision frequencies were also calculated along each streamline in the plane of symmetry. The solution for an altitude of 200,000 ft indicated a maximum electron-neutral collision frequency in excess of 1×10^{10} rad/sec in the forebody region. In the corner

region the electron-neutral collision frequencies were on the order of 5×10^9 rad/sec. The electron-ion collision frequencies in the forebody region were slightly less than the electron-neutral collision frequencies for the same region. The corner region values were approximately one-fifth the corresponding electron-neutral collision frequencies. Similar calculations were conducted for an altitude of 250,000 ft. For a given streamline the electron-neutral collision frequencies were found to be approximately an order of magnitude less than at 200,000 ft. The electron-ion collision frequencies were found to be approximately 1/100 those for corresponding plasma sheath locations at 200,000 ft.

The electron density distribution and the collision frequency distribution for two selected paths through the plasma sheath are presented. The peak electron densities and collision frequencies for these paths occur at a significant distance from the body. In addition, the values of the peak electron densities and collision frequencies are high emphasizing the importance of the inviscid flow field. From a communications viewpoint, it is important that the influence of ablation products and visous effects on the electromagnetic-propagation be compared to the influence of the inviscid flow field.

The attenuation for the propagation of one-dimensional plane waves along these two paths is presented. It must be emphasized that the accuracy of this electromagnetic-propagation calculation leading to the attenuation prediction is presently unknown. However, the implication of these results is that for the particular trajectory position and transmission paths selected, it would be exceedingly difficult to communicate with the craft at the currently available carrier frequencies.

REFERENCES

1. Bohachevsky, I. O. and Mates, R. E., A Direct Method for Computation of Nonequilibrium Flows with Detached Shock Waves; Part II. Axisymmetric Blunt-Body at Angle of Attack, AIAA Paper No. 65-24, presented at the AIAA 2nd Aerospace Sciences Meeting (January 1965)

2. Bohachevsky, I. O. and Mates, R. E., Axisymmetric Blunt Body at an Angle of Attack, Submitted for publication in AIAA Journal (August 1965)

3. Eschenroeder, A. Q., Boyer, D. W., and Hall, J. G., Nonequilibrium Expansions of Air with Coupled Chemical Reactions, Phys. Fluids, Vol. 5, p. 615 (1962)

4. Lordi, J. A., Mates, R. E., and Moselle, J. R., Computer Program for the Numerical Solution of Nonequilibrium Expansions of Reacting Gas Mixtures, Cornell Aeronautical Laboratory Report AD-1689-A-6 (June 1965)

5. Daiber, J. W., Studies of Thermal Plasmas Associated with Hypersonic Re-entry Conditions, Cornell Aeronautical Laboratory First Semi-Annual Technical Summary Report, Contract Nonr 3960(00) (1962)

6. Hurle, I. R. and Russo, A., Spectrum-Line Reversal Measurements of Free Electron and Coupled N_2 Vibrational Temperatures in Expansion Flows (to be published in J. Chem. Phys.)

7. Marrone, P. V., Normal Shock Waves in Air: Equilibrium Composition and Flow Parameters for Velocities from 26,000 to 50,000 Ft/Sec Cornell Aeronautical Laboratory Report AG-1729-A-2 (1962)

8. Gilmore, F., Equilibrium Composition and Thermodynamic Properties of Air to 24,000 °K, Rand Corp. Rept. RM-1543 (1955)

9. Marrone, P. V., , Inviscid, Nonequilibrium Flow Behind Bow and Normal Shock Waves, Part I. General Analysis and Numerical Examples, Cornell Aeronautical Laboratory Report QM-1626-A-12 (I) (1963)

10. Hall, J. G., Eschenroeder, A. Q., and Marrone, P. V., Inviscid Hypersonic Air Flows with Coupled Nonequilibrium Processes, J. Aero. Space Sci., Vol. 29, p. 1038 (September 1962)

11. Eschenroeder, A. Q., Daiber, J. W., Golian, T. C., and Hertzberg, A., Shock Tunnel Studies of High Enthalpy Ionized Airflows, Cornell Aeronautical Laboratory Report AF-1500-A-1, AFOSR 3025 (July 1962)

12. Lin, S. C., Neal, R. A., and Fyfe, W. I., Rate of Ionization Behind Shock Waves in Air; I. Experimental Results, Phys. Fluids, Vol. 5, p. 1633 (1962)

13. Makin, B. and Keck, J. C., Variational Theory of Three-Body Electron-Ion Recombination Rates, Phys. Rev. Letters, Vol. 11, p. 281 (1961)

14. Bortner, M. H., Chemical Kinetics in Reentry Flow Field, General Electric Co. Report R63SD63 (August 1963)

15. Bortner, M. H., The Effect of Errors in Rate Constants on Nonequilibrium Shock Layer Electron Density Calculations, Electromagnetic Effects of Re-entry, Edited by Rotman and Meltz, Pergamon Press, p. 74 (1961)

16. Bates, D. R., Kingston, A. E., and McWhirter, R. W. P., Recombination Between Electrons and Atomic Ions; II. Optically Thick Plasmas, Proc. Roy. Soc., A, Vol. 270, p. 155 (1962)

17. Hinnov, E. and Hirschberg, J. G., Electron-Ion Recombination in Dense Plasma, Phys. Rev., Vol. 125, p. 795 (1962)

18. Margenau, H., Conductions and Dispersion of Ionized Gases at High Frequencies, Phys. Rev., Vol. 69, p. 508 (1946)

19. Margenau, H., Conductivity of Plasmas to Microwaves, Phys. Rev., Vol. 109, p. 6 (1958)

20. Shkarofsky, I. P., Bachynski, M. P., and Johnston, T. W., Collision Frequency Associated with High Temperature Air and Scattering Cross-Sections of the Constituents, Electromagnetic Effects of Re-entry, Edited by W. Rotman, Pergamon Press (1961)

21. Spitzer, L. and Harm, R., Transport Phenomena in a Completely Ionized Gas., Phys. Rev., Vol. 89, p. 977 (1953)

22. Lin, S. C., A Rough Estimate of the Attenuation of Telemetering Signals Through the Ionized Gas Envelope Around a Typical Re-entry Missile, AVCO-Everett Res. Rept. 74 (February 1956)

23. Bein, G. P., Plane Wave Propagation at Arbitrary Angles of Incidence in Inhomogeneous, Lossy Plasmas. A High-Speed Computation Technique for Determining Complex Transmission and Reflection Coefficients, Cornell Aeronautical Laboratory, (to be submitted for publication in IEEE)

TABLE I
AIR REACTIONS FOR NEUTRAL SPECIES

$k_{F_i} = A_i T^{n_i} \exp(-\theta_i/T)$, cc/mole sec for T in °K

SPECIES CONSIDERED ARE: N_2, O_2, NO, N, O, Ar

REACTION	COLLISION PARTNER, M	A_i	n_i	θ_i
$N_2 + M \xrightarrow{k_{F_i}} 2N + M$	N_2	3.0×10^{21}	-1.5	113260
$N_2 + M \longrightarrow 2N + M$	N	1.5×10^{22}	-1.5	113260
$N_2 + M \longrightarrow 2N + M$	Ar, O, O_2, NO	9.9×10^{20}	-1.5	113260
$O_2 + M \longrightarrow 2O + M$	O_2	3.6×10^{21}	-1.5	59380
$O_2 + M \longrightarrow 2O + M$	O	2.1×10^{18}	-0.5	59380
$O_2 + M \longrightarrow 2O + M$	Ar, N, N_2, NO	1.2×10^{21}	-1.5	59380
$NO + M \longrightarrow N + O + M$	Ar, N_2, O_2, N, O	5.2×10^{21}	-1.5	75490
$N + O_2 \longrightarrow NO + N$		1.0×10^{12}	0.5	3120
$O + N_2 \longrightarrow NO + N$		5.0×10^{13}	0	38000
$NO + NO \longrightarrow N_2 + O_2$		4.8×10^{23}	-2.5	43000

TABLE II
AIR REACTIONS FOR IONIZED SPECIES

$k_{F_i} = A_i T^{n_i}$ $cm^3/mole\ sec$ (2 body reactions)

$k_{F_i} = A_i T^{n_i}$ $cm^6/mole^2\ sec$ (3 body reactions)

for T in °K

SPECIES CONSIDERED ARE: N_2^+, O_2^+, NO^+, N^+, O^+, and e^-

REACTION	M	A_i	n_i
DISSOCIATIVE RECOMBINATION REACTIONS			
$e^- + NO^+ \longrightarrow N + O$		1.8×10^{21}	-1.5
$e^- + N_2^+ \longrightarrow N + N$		4.0×10^{21}	-1.5
$e^- + O_2^+ \longrightarrow O + O$		1.0×10^{21}	-1.5
THREE-BODY RECOMBINATION REACTIONS			
$e^- + NO + NO^+ \longrightarrow N_2 + O_2$	NO, N, O, O_2, N_2	1.0×10^{24}	-2.5
$e^- + N + N^+ \longrightarrow N + N$		6.0×10^{24}	-2.5
$e^- + O + N^+ \longrightarrow O + N$		6.0×10^{24}	-2.5
$e^- + N_2 + N^+ \longrightarrow N_2 + N$		2.22×10^{26}	-2.5
$e^- + O_2 + N^+ \longrightarrow O_2 + N$		8.8×10^{26}	-2.5
$e^- + NO + N^+ \longrightarrow NO + N$		1.31×10^{28}	-2.5
$e^- + e^- + N^+ \longrightarrow e^- + N$		8.3×10^{39}	-4.5
CHARGE-EXCHANGE REACTIONS			
$O + N^+ \longrightarrow N + O^+$	N, N_2	7.8×10^{11}	0.5
$N + N_2^+ \longrightarrow N_2 + N^+$			
$O_2 + N^+ \longrightarrow N + O_2^+$	O, N, N_2		
$NO + N^+ \longrightarrow N + NO^+$	O, N, O_2, N_2		
ION-ATOM EXCHANGE REACTIONS			
$O + N_2^+ \longrightarrow N + NO^+$		7.8×10^{11}	0.5
$N + O_2^+ \longrightarrow O + NO^+$			
$N_2 + O^+ \longrightarrow N + NO^+$			
$N_2 + O_2^+ \longrightarrow NO + NO^+$			
$O_2 + N^+ \longrightarrow NO + O^+$			
$O_2 + N^+ \longrightarrow O + NO^+$			
$O_2 + N_2^+ \longrightarrow NO + NO^+$			
$NO + O^+ \longrightarrow N + O_2^+$			
$NO + N^+ \longrightarrow O + N_2^+$			
$NO + N^+ \longrightarrow N_2 + O^+$			

TABLE III

ESTIMATED RATE CONSTANT UNCERTAINTY

REACTIONS	RATE CONSTANT	RATE CONSTANT EVALUATED AT			REF.
		290°K	2000°K	4000°K	
(A) ELECTRON DEPLETION					
(1) $NO^+ + e^- \rightarrow N + O$	(1) $k = 1.8 \times 10^{21} T^{-1.5}$ cm^3/mole sec $k = 2.0 \times 10^{19\pm2} T^{-1.0}$ cm^3/mole sec	(1) 3.6×10^{17} $6.9 \times 10^{16\pm2}$	(1) 2.0×10^{16} $1.0 \times 10^{16\pm2}$	(1) 7.1×10^{15} $5.0 \times 10^{16\pm2}$	12 14
(2) $N_2^+ + e^- \rightarrow N + N$	(2) $k = 1.0 \times 10^{21} T^{-1.5}$ cm^3/mole sec $k = 5.0 \times 10^{18\pm1} T^{-0.5}$ cm^3/mole sec	(2) 2.0×10^{17} $2.9 \times 10^{17\pm1}$	(2) 1.1×10^{16} $1.1 \times 10^{17\pm1}$	(2) 3.9×10^{15} $8.0 \times 10^{16\pm1}$	11 14
(3) $O^+ + e^- + e^- \rightarrow O + e^-$	(3) $k = 8.3 \times 10^{39} T^{-4.5}$ cm^6/mole^{2}sec $k = 4.0 \times 10^{21\pm1} T^{-1}$ cm^6/mole^{2}sec	(3) 6.9×10^{26} $1.4 \times 10^{19\pm1}$	(3) 6.4×10^{24} $2.0 \times 10^{18\pm1}$	(3) 2.9×10^{23} $1.0 \times 10^{18\pm1}$	13 14
(B) CHARGE EXCHANGE					
(4) $O + N^+ \rightarrow N + O^+$	(4) $k = 7.8 \times 10^{11} T^{0.5}$ cm^3/mole sec $k = 5.0 \times 10^{13\pm2} T^{-0.5}$ cm^3/mole sec	(4) 1.3×10^{13} $2.9 \times 10^{12\pm2}$	(4) 3.5×10^{13} $1.1 \times 10^{12\pm2}$	(4) 5.0×10^{13} $7.8 \times 10^{11\pm2}$	11 14
(C) ION-ATOM EXCHANGE					
(5) $N_2 + O^+ \rightarrow N + NO^+$	(5) $k = 7.8 \times 10^{11} T^{0.5}$ cm^3/mole sec $k = 1.0 \times 10^{13\pm2} T^{-0.5}$ cm^3/mole sec	(5) 1.3×10^{13} $5.9 \times 10^{11\pm2}$	(5) 3.5×10^{13} $2.2 \times 10^{11\pm2}$	(5) 5.0×10^{13} $1.6 \times 10^{11\pm2}$	11 14
(6) $O + N_2^+ \rightarrow N + NO^+$	(6) $k = 7.8 \times 10^{11} T^{0.5}$ cm^3/mole sec $k = 1.0 \times 10^{14\pm2} T^{-0.5}$ cm^3/mole sec	(6) 1.3×10^{13} $5.9 \times 10^{12\pm2}$	(6) 3.5×10^{13} $2.2 \times 10^{12\pm2}$	(6) 5.0×10^{13} $1.6 \times 10^{12\pm2}$	11 14

TABLE IV

SUMMARY OF NONEQUILIBRIUM IONIZATION CALCULATIONS

CLASSIFICATION OF REGION	LOCATION	DOMINANT IONS	IMPORTANT CHEMICAL REACTIONS
I. HIGH-TEMPERATURE, MOLECULAR IONIZATION REGION	RELATIVELY SHORT DISTANCE BEHIND TRANSLATIONAL SHOCK FOR ALL STREAMLINES CONSIDERED (SEE FIG. 1)	N_2^+, NO^+, O_2^+	(a) $e^- + N_2 \rightarrow e^- + e^- + N_2^+$ (b) $O + N_2^+ \rightarrow N + NO^+$ (c) $N_2 + N^+ \rightarrow N + N_2^+$ (d) $N_2 + O_2^+ \rightarrow NO + NO^+$ (e) $N_2 + NO \rightarrow e^- + NO + N_2^+$
II. HIGH-TEMPERATURE, ATOMIC IONIZATION REGION	REGION IMMEDIATELY FOLLOWING MOLECULAR IONIZATION REGION FOR STREAMTUBES THAT CROSS NEAR NORMAL PORTIONS OF TRANSLATIONAL SHOCK. (FOR EXAMPLE, STREAMLINES 5 AND 8).	N^+, O^+	(a) $e^- + N \rightarrow e^- + e^- + N^+$ (b) $O + N^+ \rightarrow N + O^+$ (c) $e^- + O \rightarrow e^- + e^- + O^+$ (d) $N_2 + O^+ \rightarrow NO + N^+$
III. INTERMEDIATE-TEMPERATURE, ATOMIC AND MOLECULAR IONIZATION REGION	REGION IMMEDIATELY FOLLOWING MOLECULAR IONIZATION REGION FOR STREAMTUBES THAT CROSS TRANSLATIONAL SHOCK BETWEEN NORMAL PORTION AND OUTER EXTREMITIES (FOR EXAMPLE, STREAMLINES 3 AND 12).	N^+, NO^+, N_2^+, O^+	(a) $O + N^+ \rightarrow N + O^+$ (b) $N_2 + O^+ \rightarrow N + NO^+$ (c) $O + N_2^+ \rightarrow NO + N^+$ (d) $e^- + N \rightarrow e^- + e^- + N^+$ (e) $O + N_2^+ \rightarrow N + NO^+$
IV. LOW-TEMPERATURE, MOLECULAR IONIZATION REGION	REGION IMMEDIATELY FOLLOWING MOLECULAR IONIZATION REGION FOR STREAMTUBES THAT CROSS TRANSLATIONAL SHOCK AT OUTER EXTREMITIES (FOR EXAMPLE, STREAMLINE 14).	NO^+	(a) $N_2 + O_2^+ \rightarrow NO + NO^+$ (b) $O + N_2^+ \rightarrow N + NO^+$ (c) $O + N_2^+ \rightarrow NO + NO^+$ (d) $NO + NO \rightarrow NO + NO^+ + e^-$

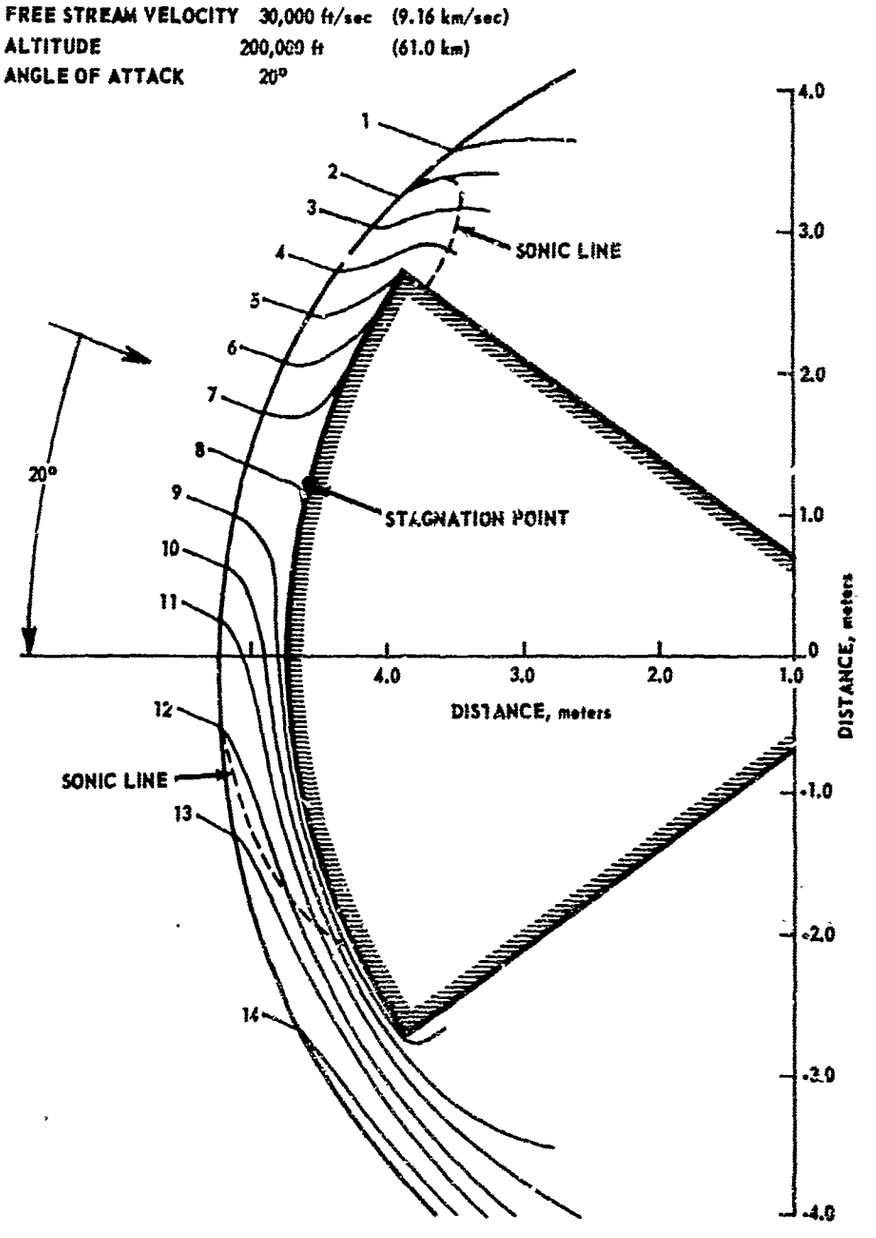


FIGURE 1 STREAMLINE PATTERN IN THE PLANE OF SYMMETRY

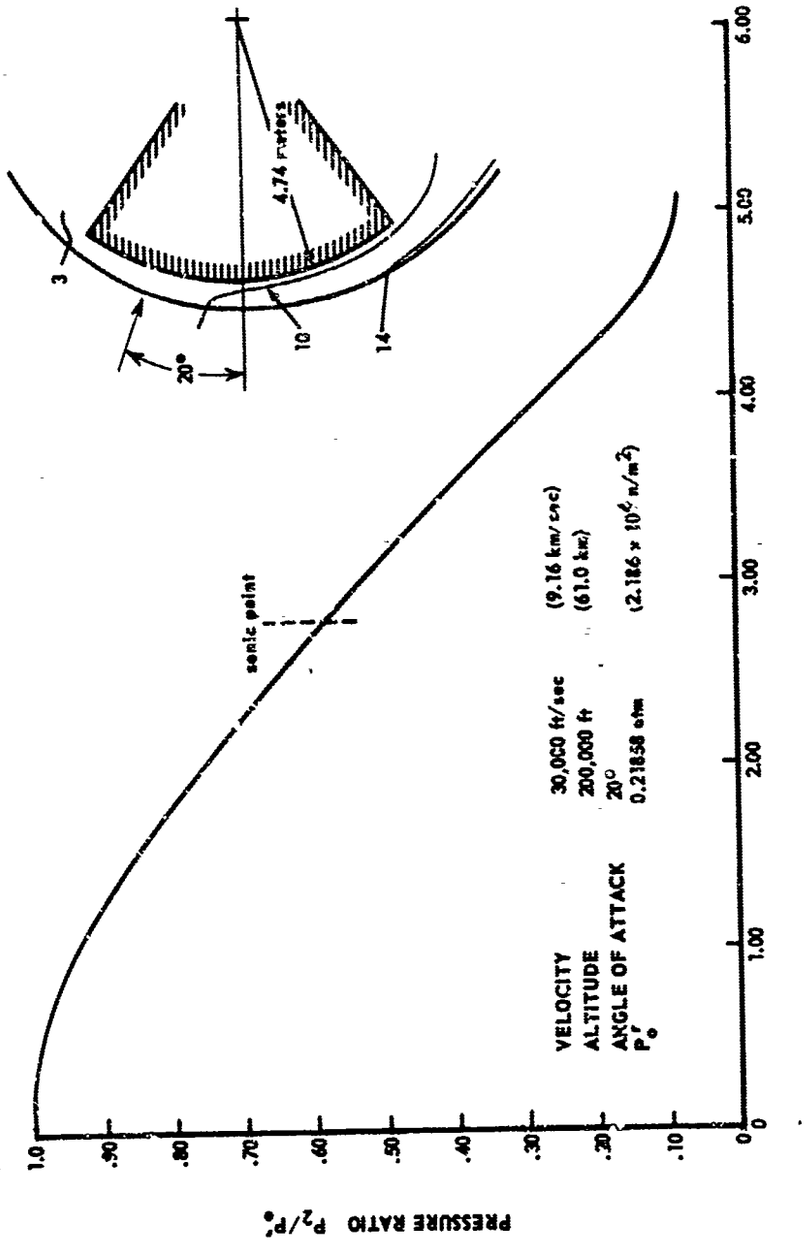


FIGURE 2 PRESSURE DISTRIBUTION IN PLANE OF SYMMETRY FOR STREAMLINE 10

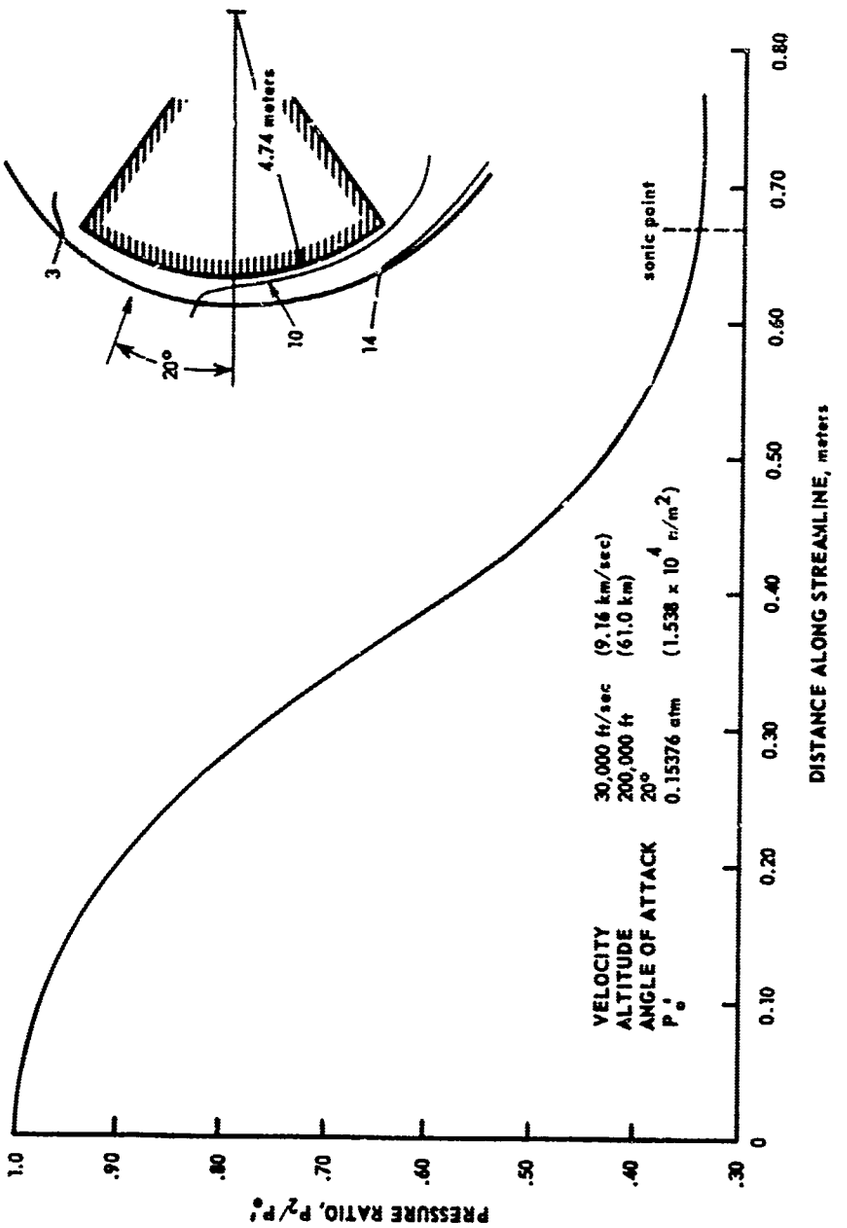


FIGURE 3 PRESSURE DISTRIBUTION IN PLANE OF SYMMETRY FOR STREAMLINE 3

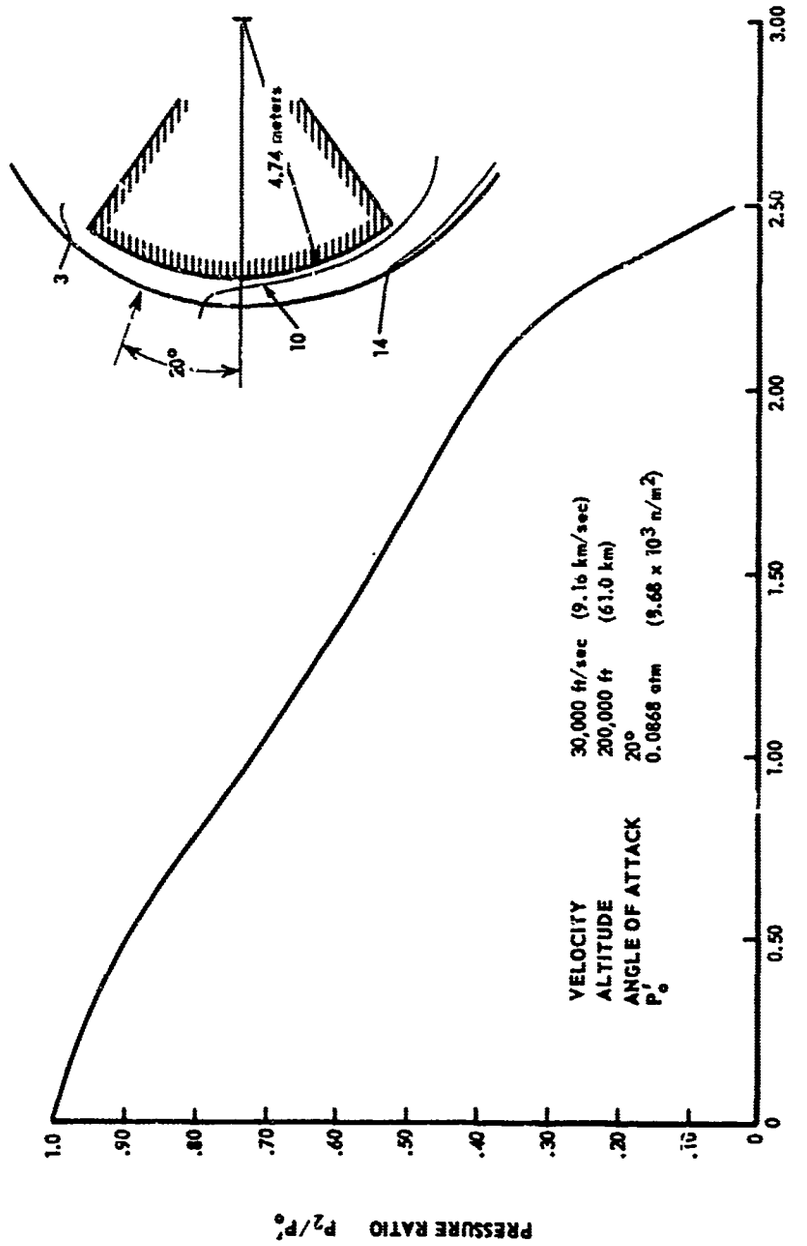


FIGURE 4 PRESSURE DISTRIBUTION IN PLANE OF SYMMETRY FOR STREAMLINE 14

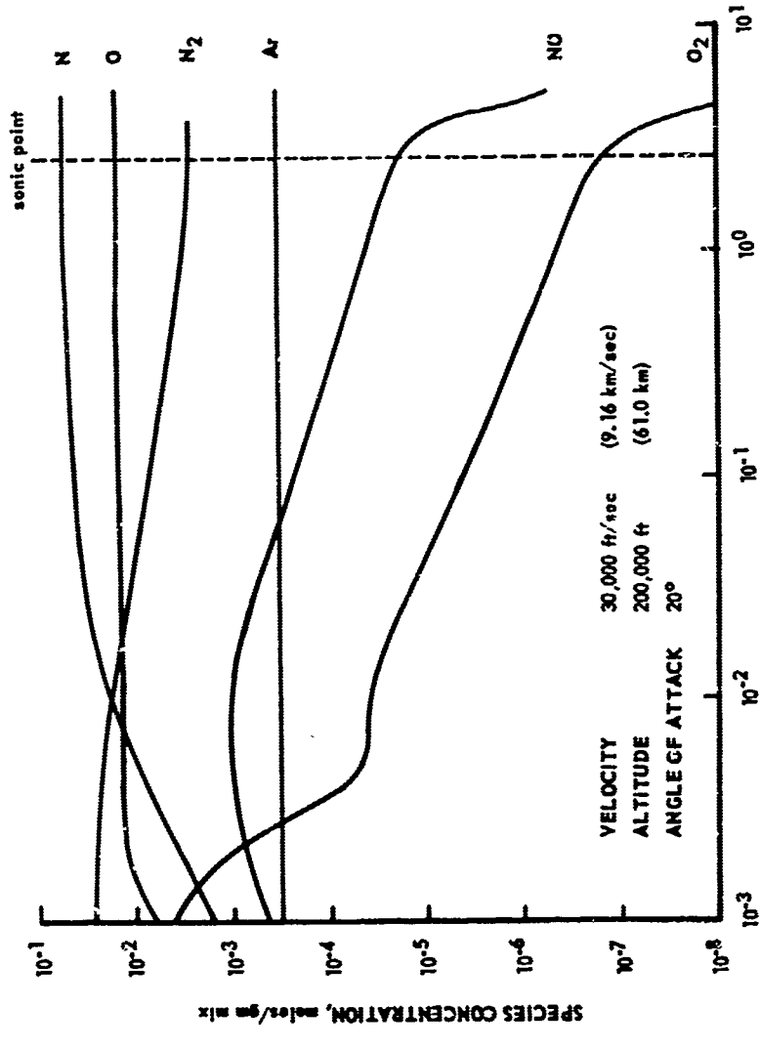


FIGURE 5 NONEQUILIBRIUM SPECIES DISTRIBUTION ALONG STREAMLINE 10 IN PLANE OF SYMMETRY

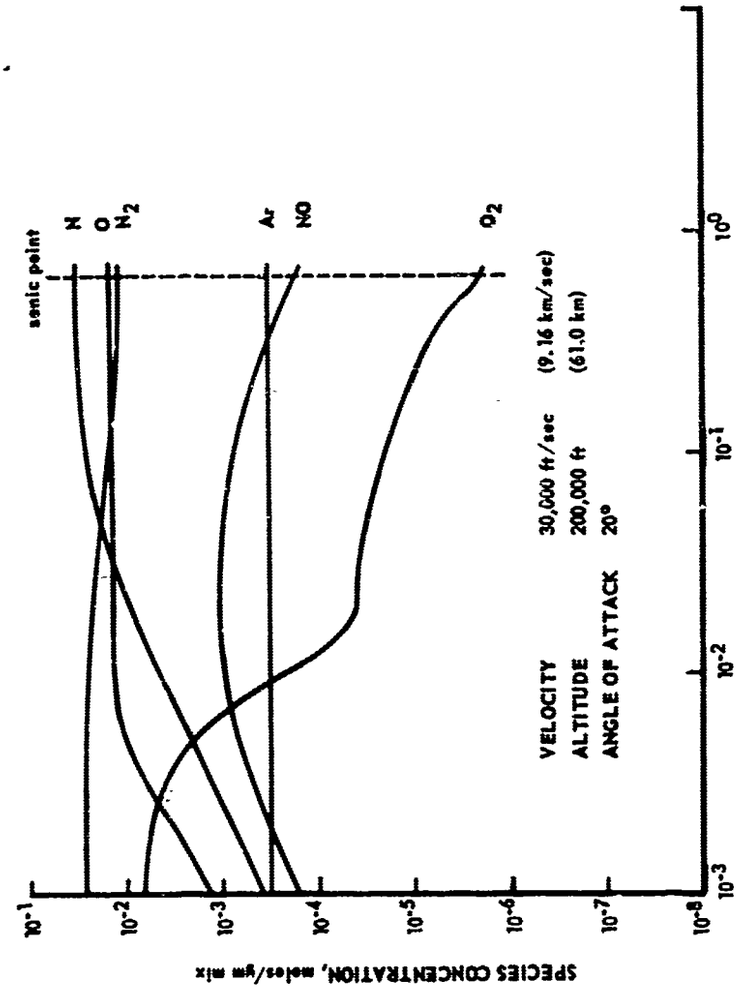


FIGURE 6 NONEQUILIBRIUM SPECIES DISTRIBUTION ALONG STREAMLINE 3 IN PLANE OF SYMMETRY

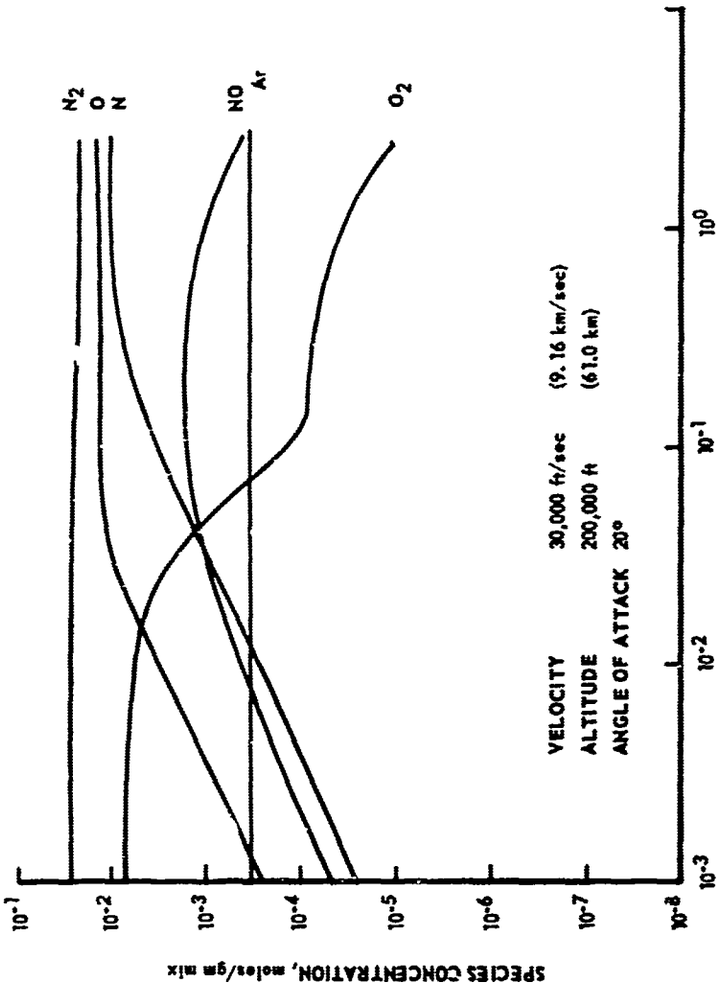


FIGURE 7 NONEQUILIBRIUM SPECIES DISTRIBUTION ALONG STREAMLINE 14 IN PLANE OF SYMMETRY

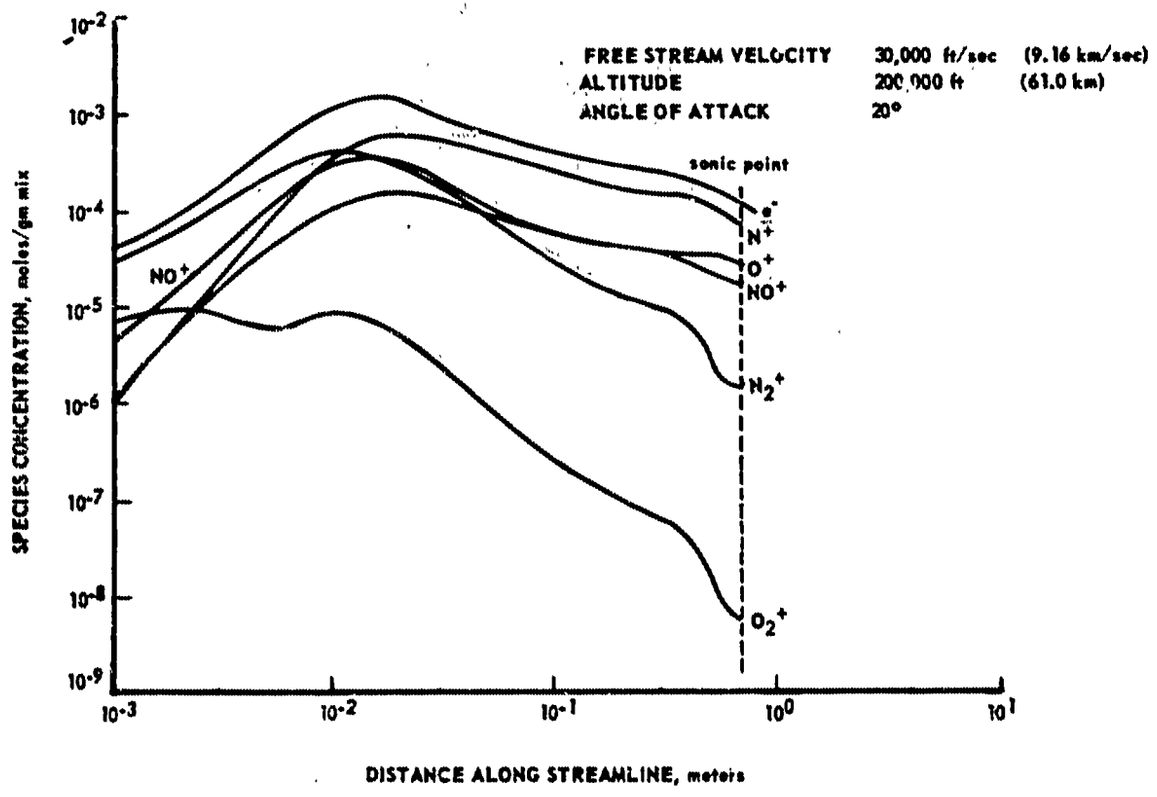


FIGURE 8 NONEQUILIBRIUM SPECIES DISTRIBUTION ALONG STREAMLINE 5 IN PLANE OF SYMMETRY

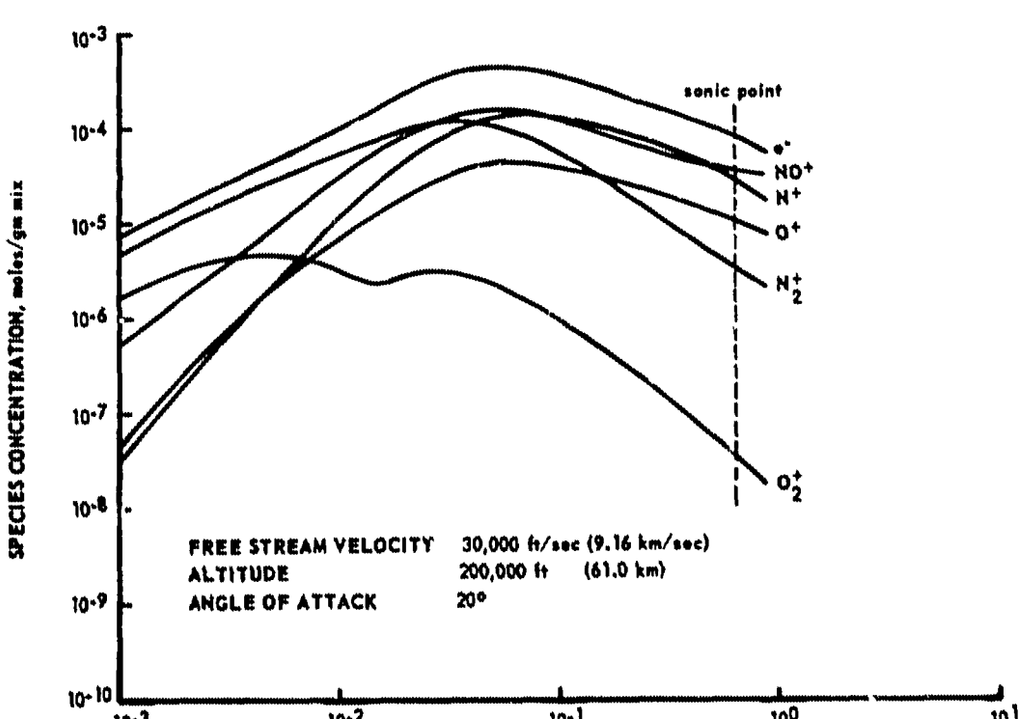


FIGURE 9 NONEQUILIBRIUM SPECIES DISTRIBUTION ALONG STREAMLINE 3 IN PLANE OF SYMMETRY

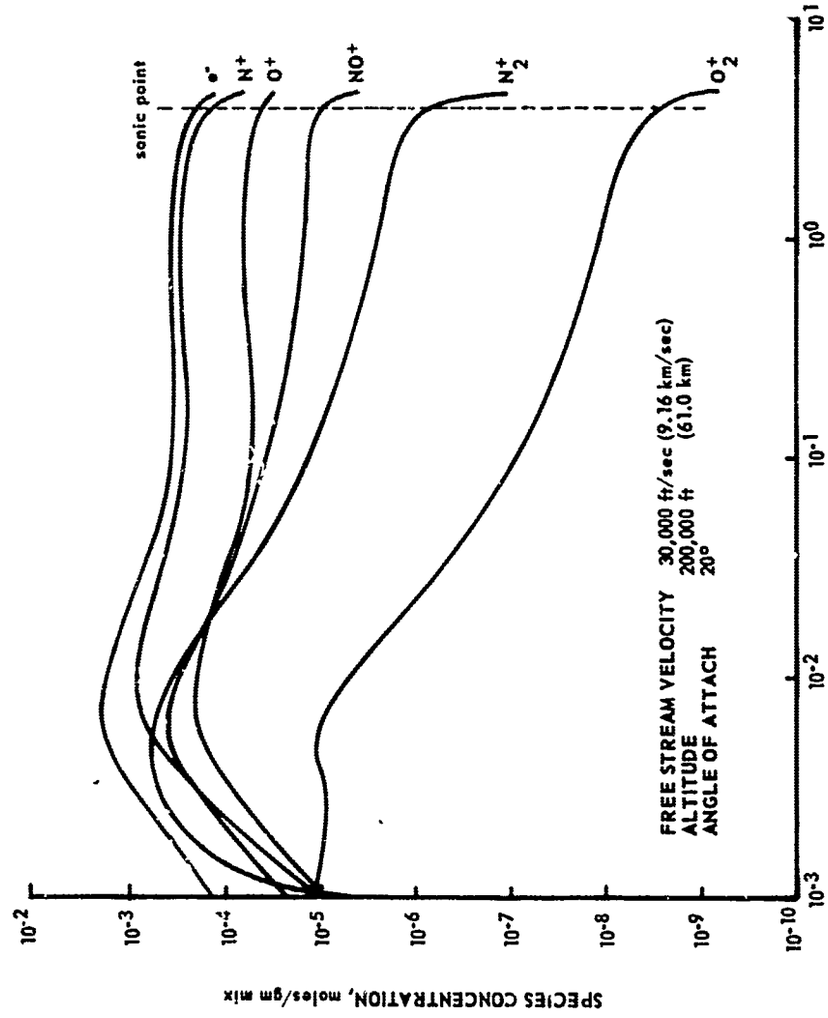


FIGURE 10 NONEQUILIBRIUM SPECIES DISTRIBUTION ALONG STREAMLINE 8 IN PLANE OF SYMMETRY

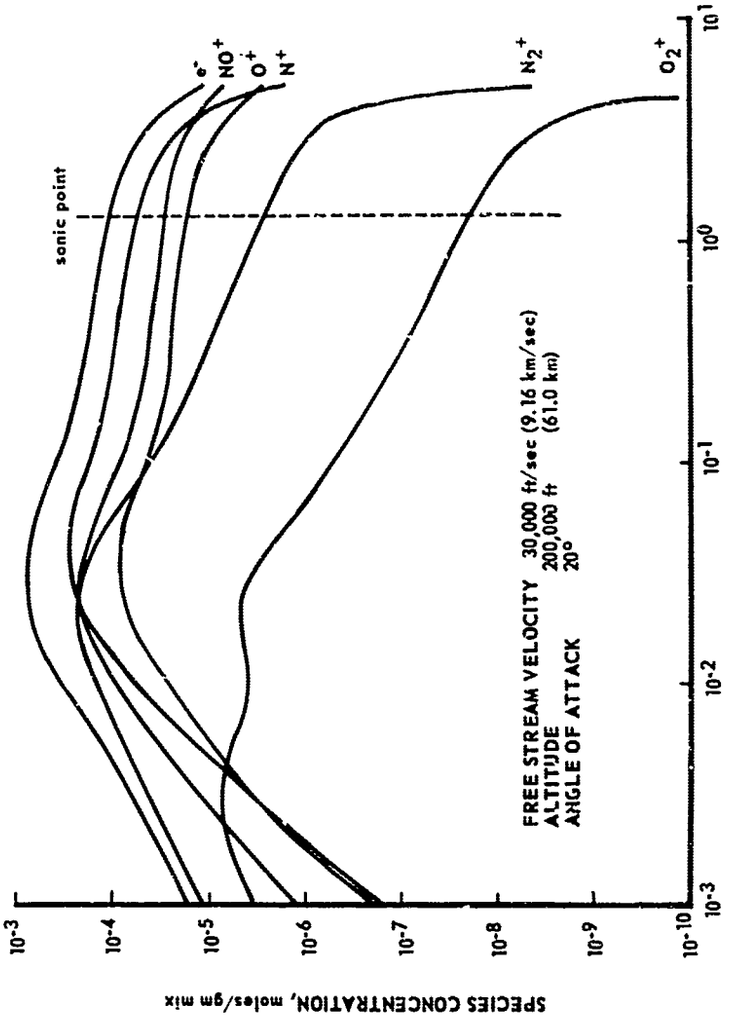


FIGURE 11 NONEQUILIBRIUM SPECIES DISTRIBUTION ALONG STREAMLINE 12 IN PLANE OF SYMMETRY

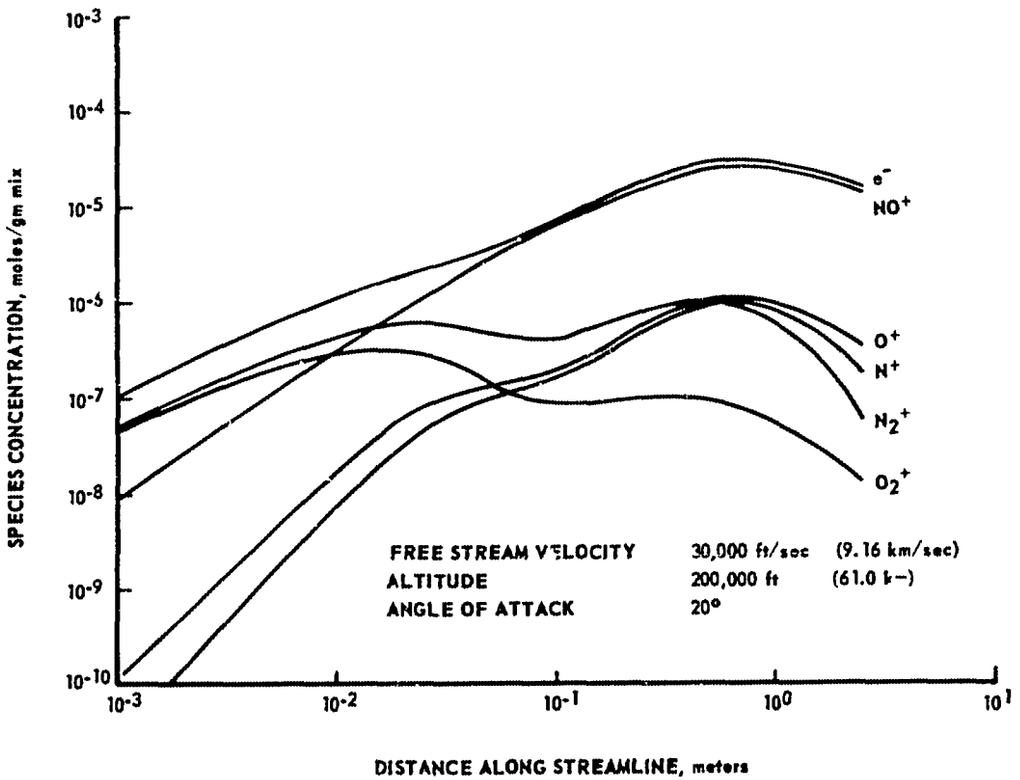


FIGURE 12 NONEQUILIBRIUM SPECIES DISTRIBUTION ALONG STREAMLINE 14 IN PLANE OF SYMMETRY

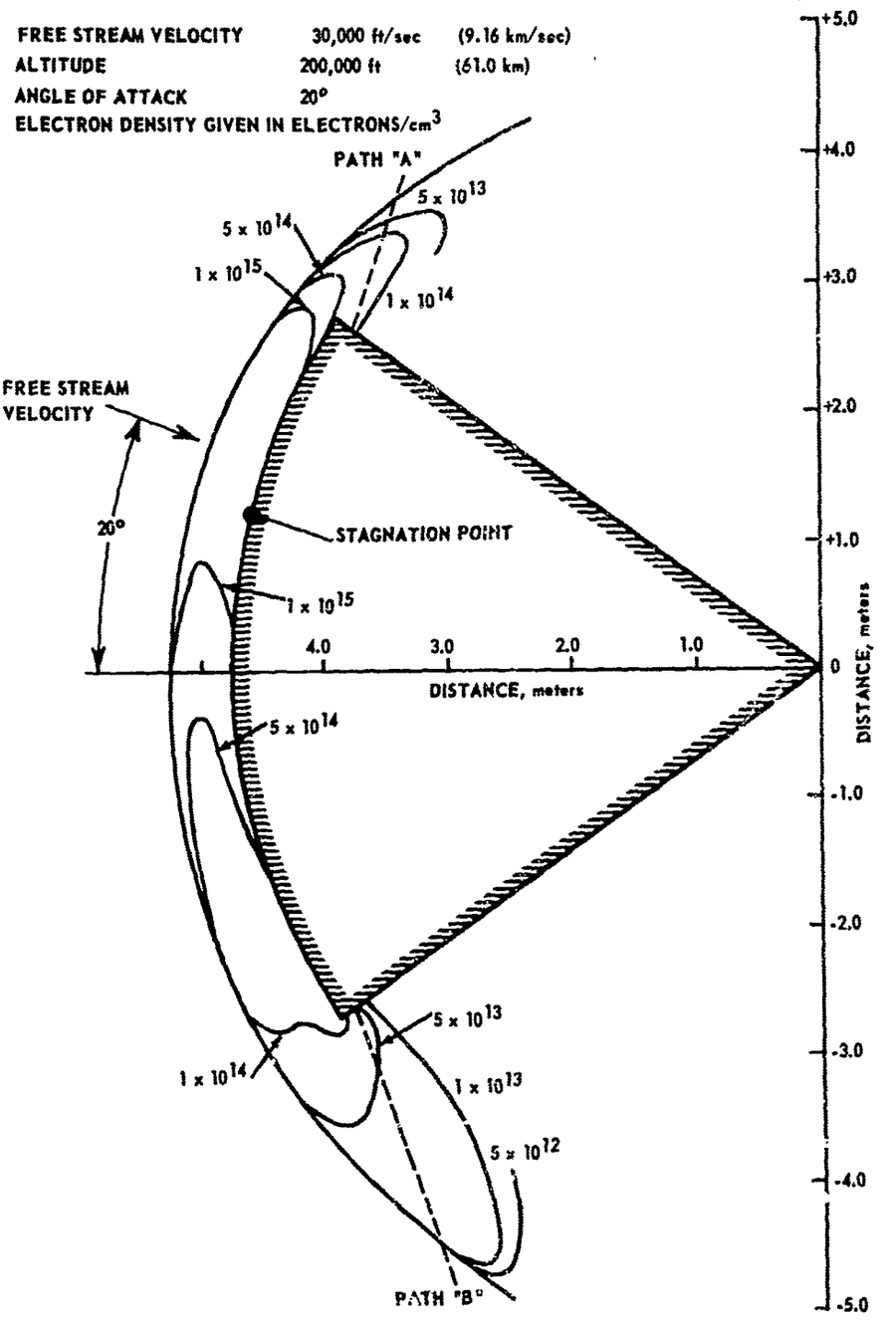


FIGURE 13 ELECTRON DENSITY DISTRIBUTION IN PLANE OF SYMMETRY

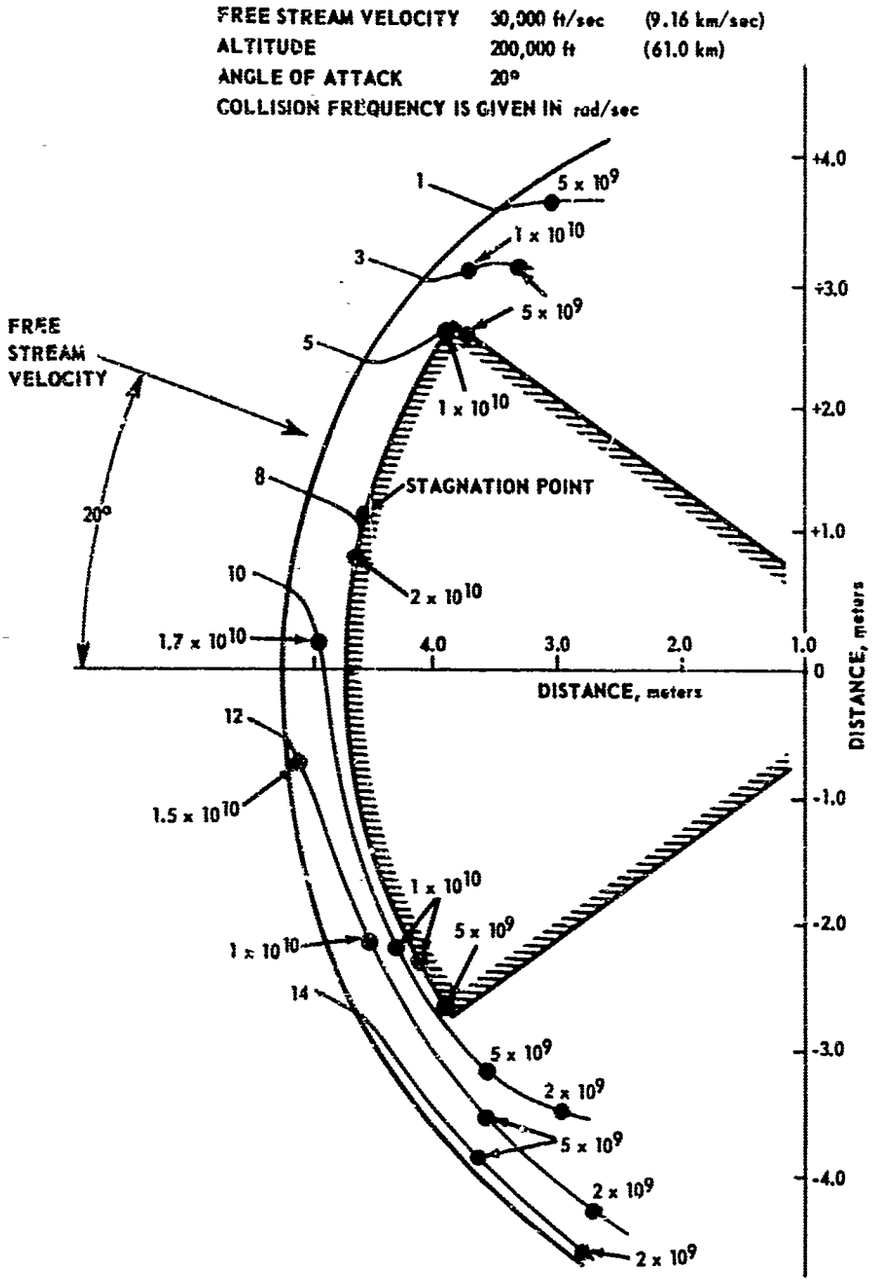


FIGURE 14 ELECTRON-NEUTRAL COLLISION FREQUENCY (ν) IN PLANE OF SYMMETRY

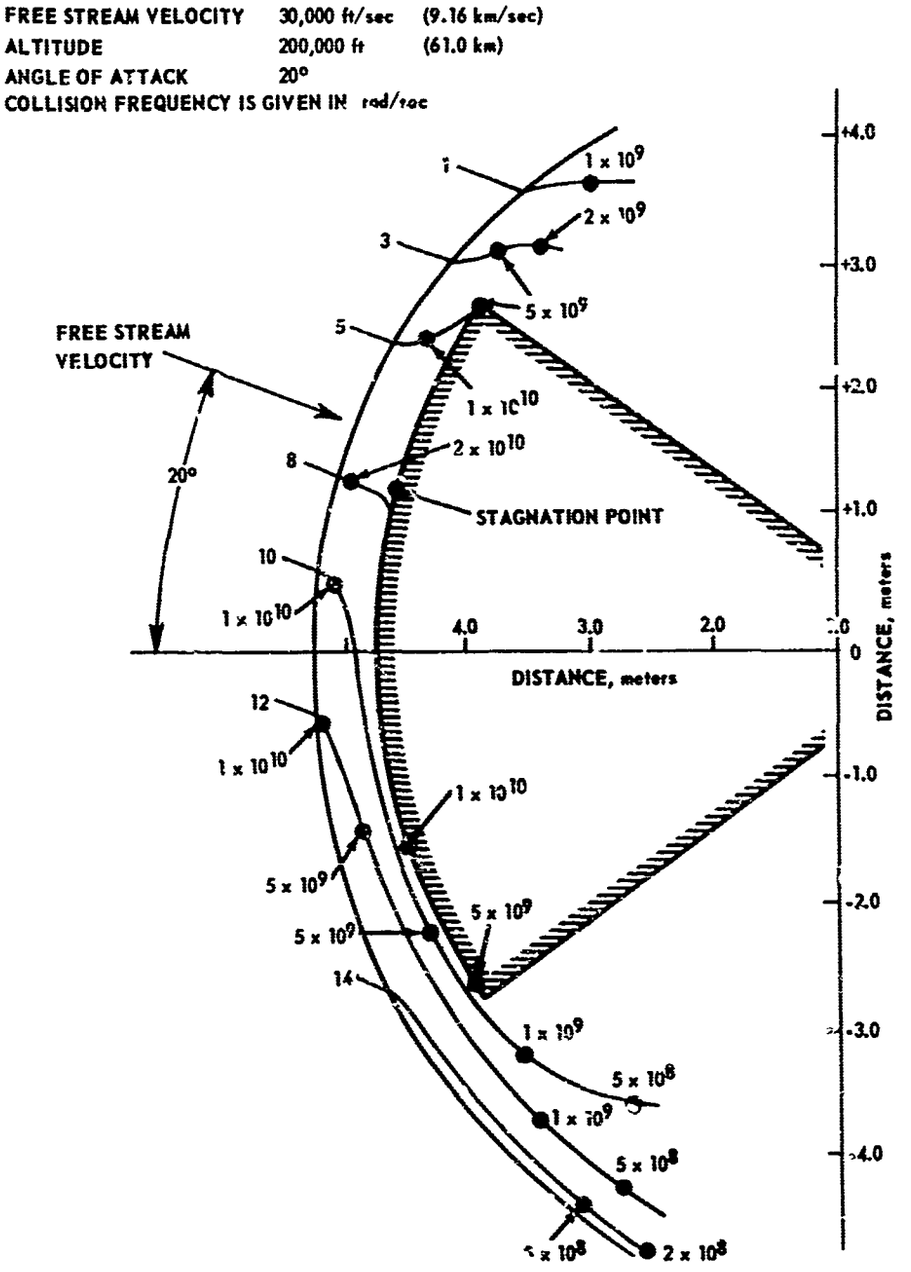


FIGURE 15 ELECTRON-ION COLLISION FREQUENCY (ν^+) IN PLANE OF SYMMETRY

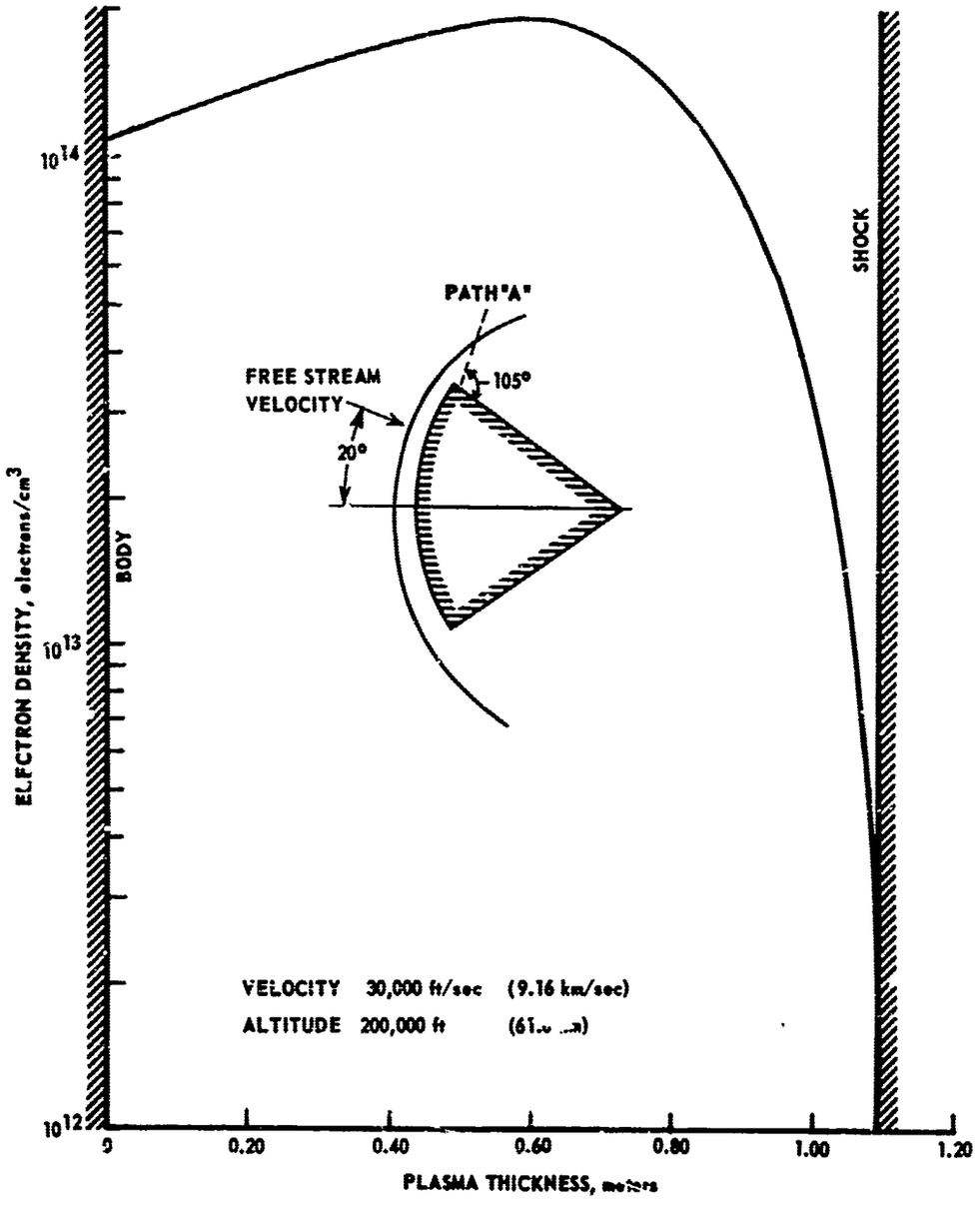


FIGURE 16 ELECTRON DENSITY DISTRIBUTION IN PLANE OF SYMMETRY FOR PATH "A"

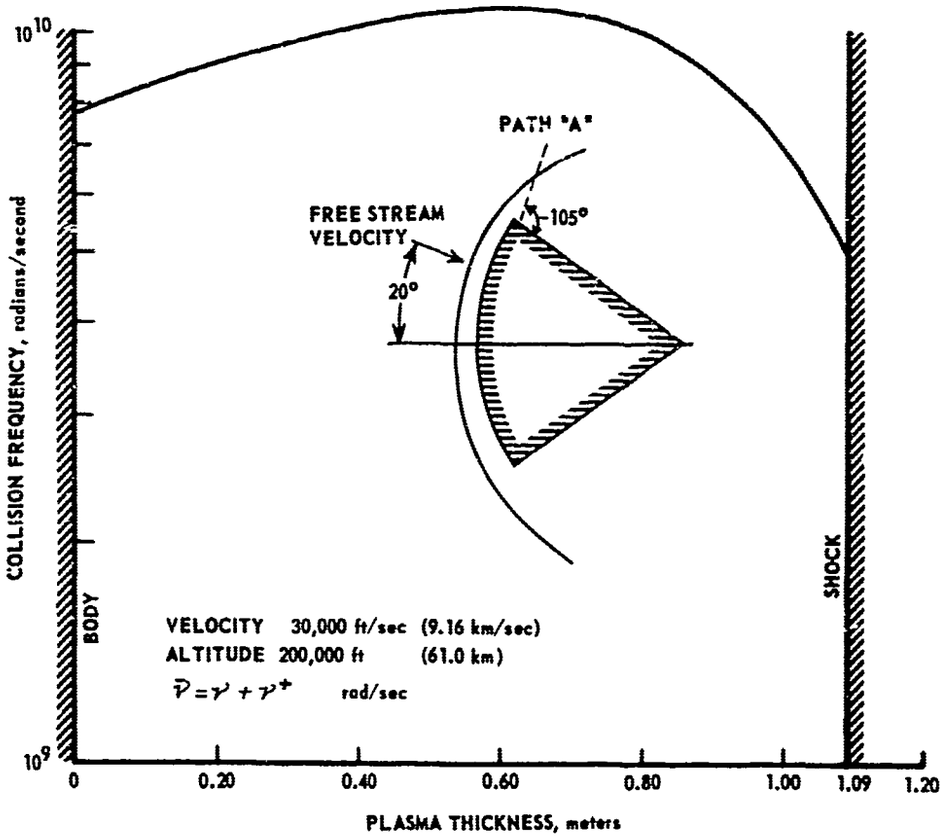


FIGURE . COLLISION FREQUENCY ($\bar{\nu}$) IN PLANE OF SYMMETRY FOR PATH "A"

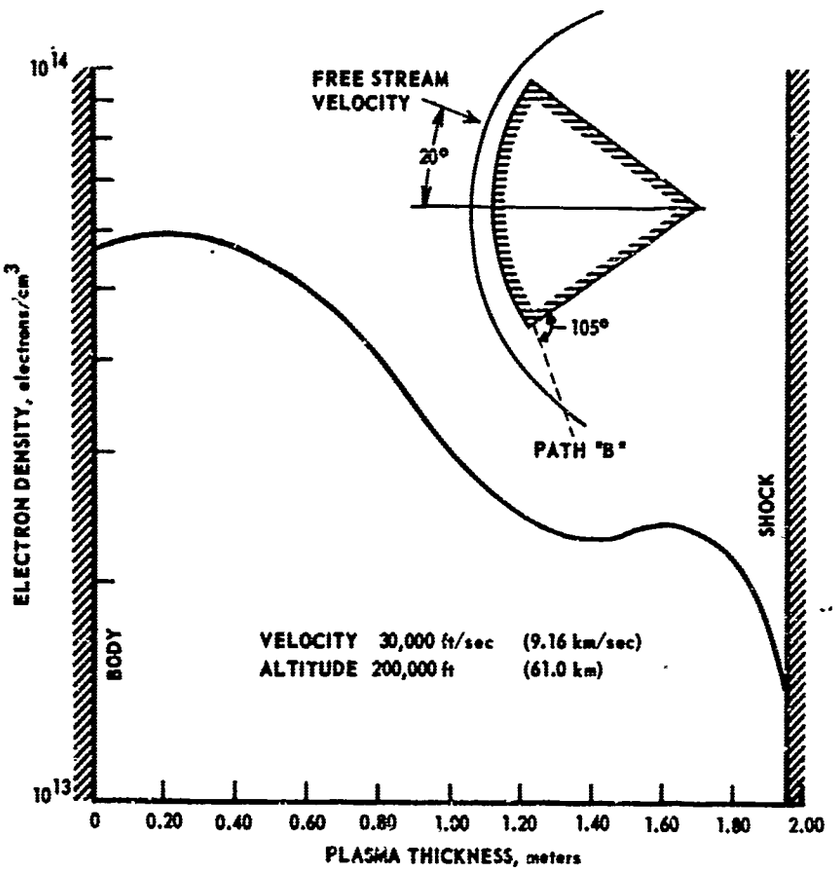


FIGURE 18 ELECTRON DENSITY DISTRIBUTION IN PLANE OF SYMMETRY PATH "B"

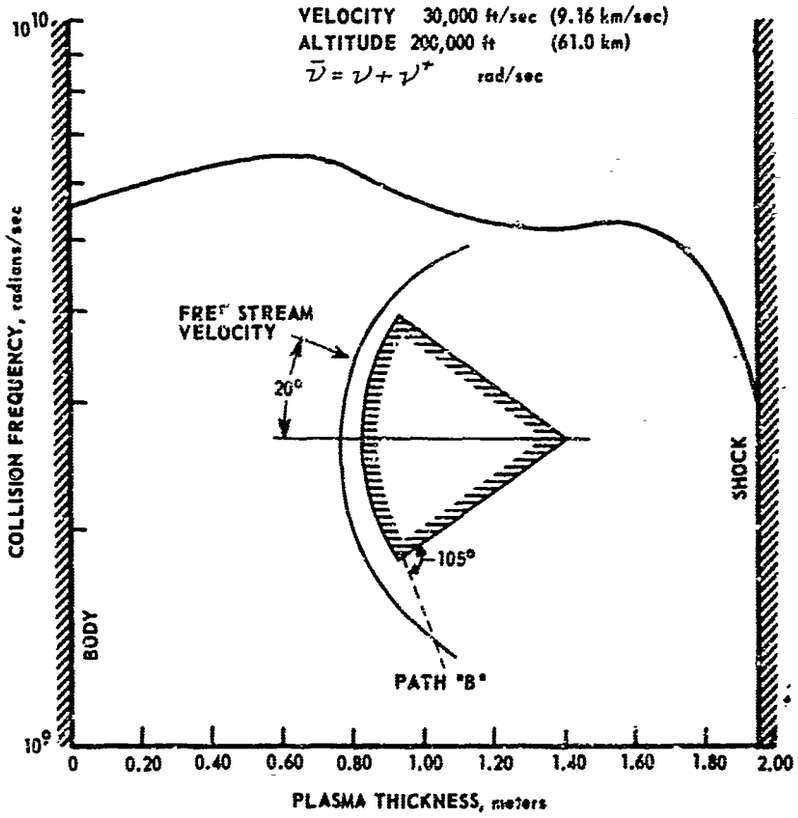


FIGURE 19 COLLISION FREQUENCY ($\bar{\nu}$) DISTRIBUTION IN PLANE OF SYMMETRY FOR PATH "B"

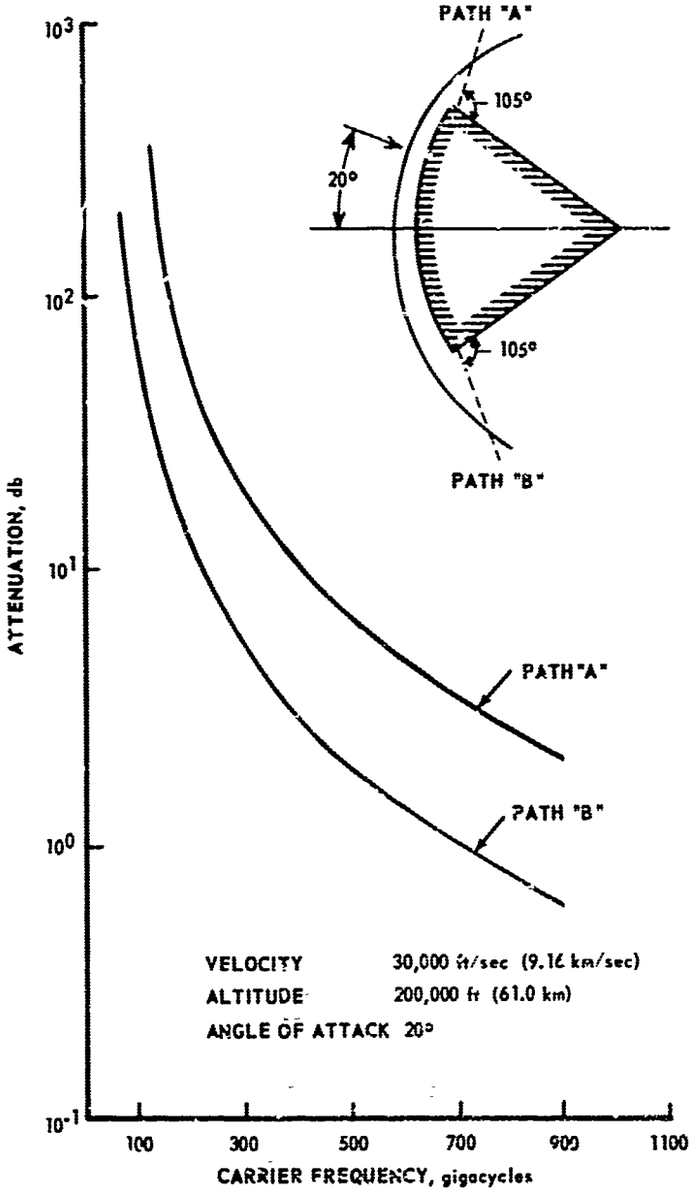


FIGURE 20 CALCULATED ATTENUATION OF ONE-DIMENSIONAL PLANE WAVES

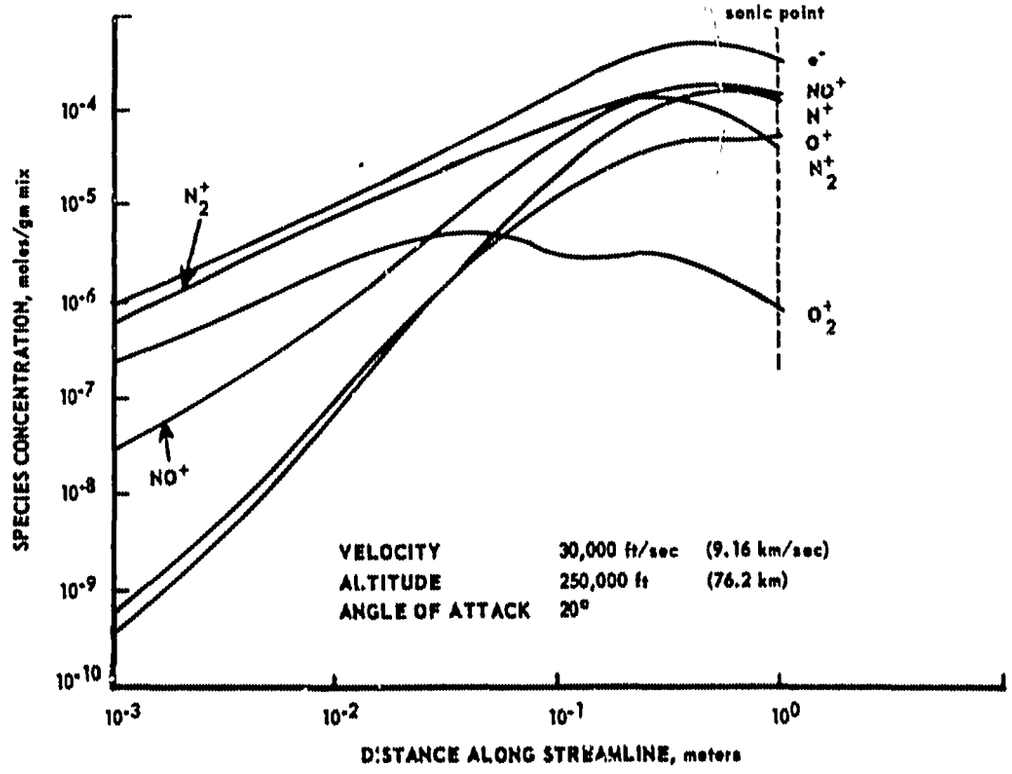


FIGURE 21 NONEQUILIBRIUM SPECIES DISTRIBUTION ALONG STREAMLINE 5 IN PLANE OF SYMMETRY

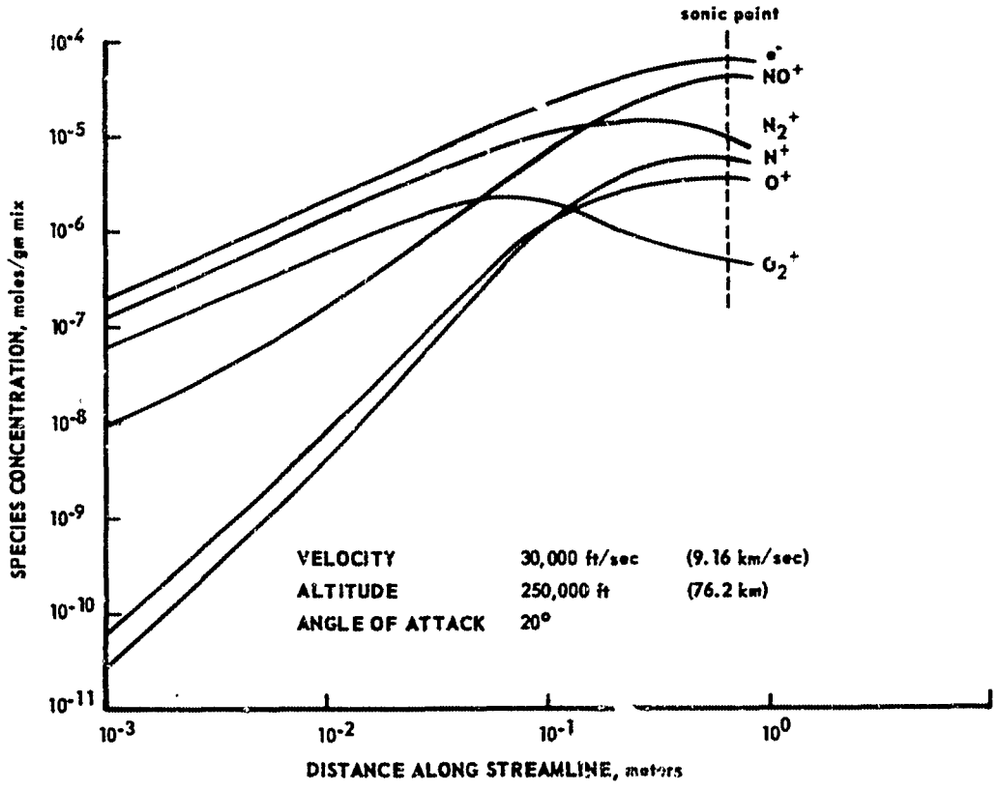


FIGURE 22 NONEQUILIBRIUM SPECIES DISTRIBUTION ALONG STREAMLINE 3 IN PLANE OF SYMMETRY

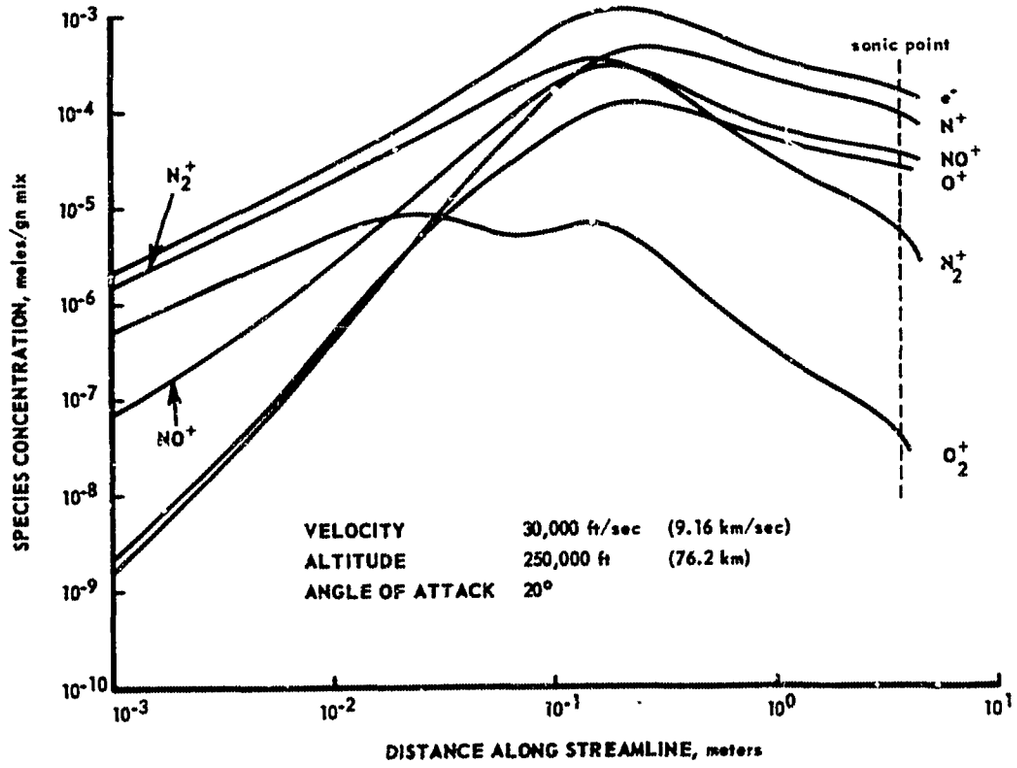


FIGURE 23 NONEQUILIBRIUM SPECIES DISTRIBUTION ALONG STREAMLINE 8 IN PLANE OF SYMMETRY

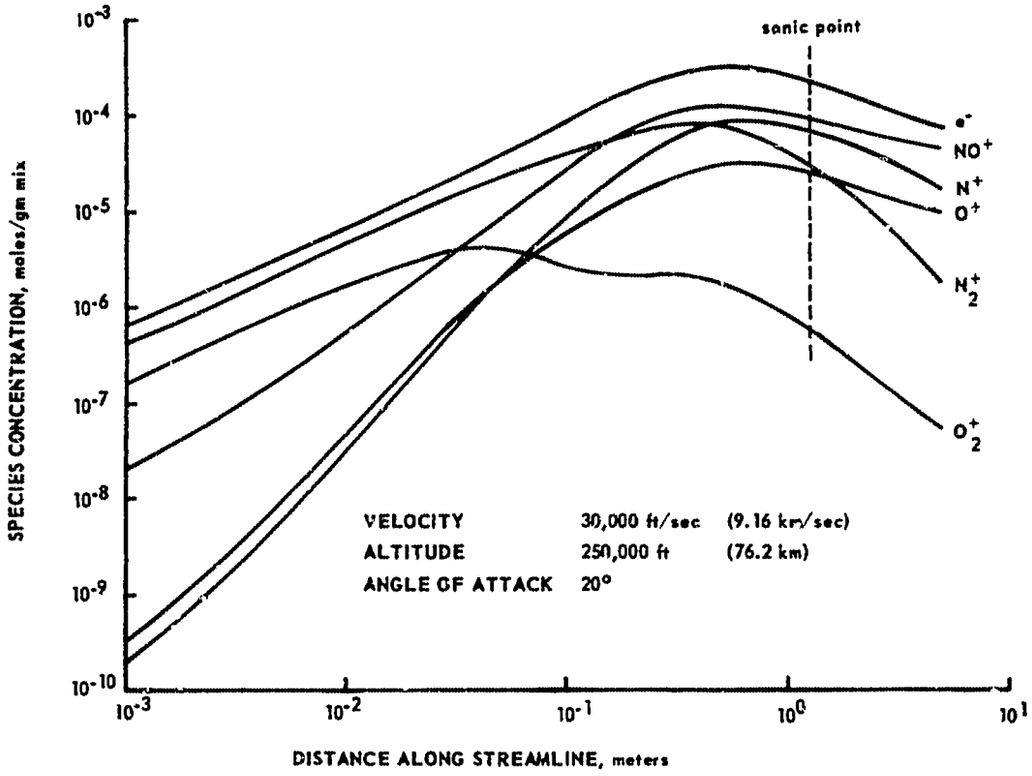


FIGURE 24 NONEQUILIBRIUM SPECIES DISTRIBUTION ALONG STREAMLINE 12 IN PLANE OF SYMMETRY

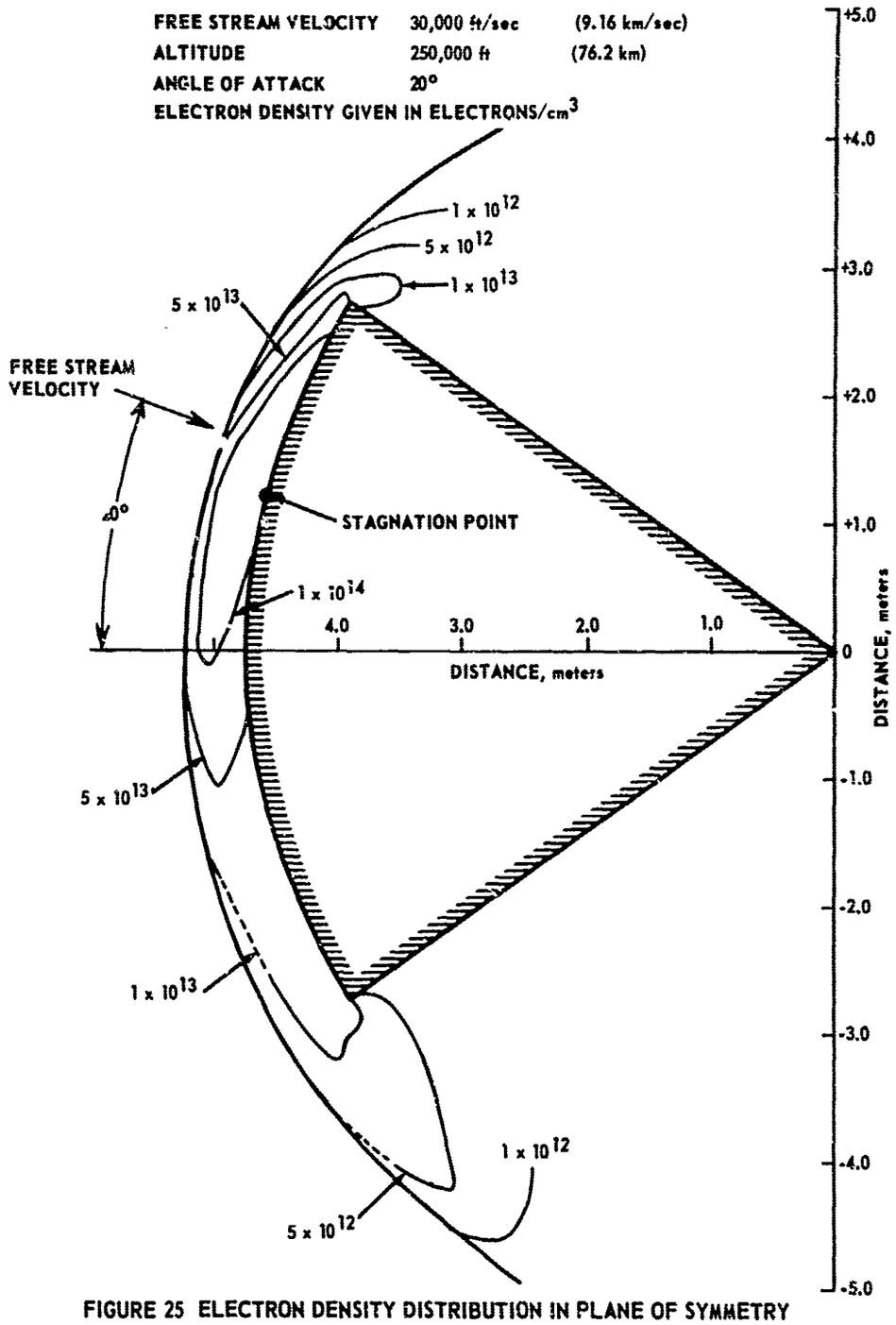


FIGURE 25 ELECTRON DENSITY DISTRIBUTION IN PLANE OF SYMMETRY

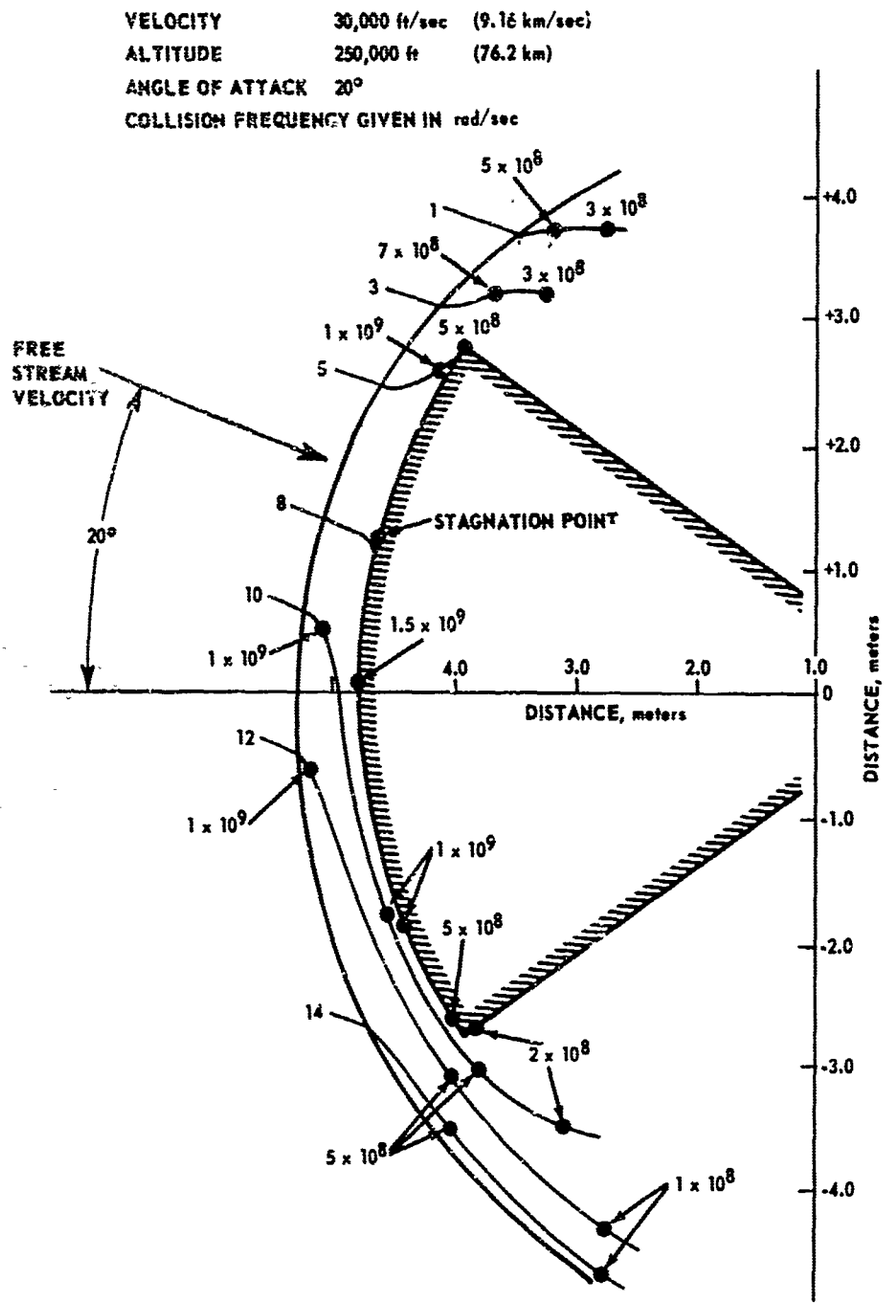


FIGURE 26 ELECTRON-NEUTRAL COLLISION FREQUENCY (ν) IN PLANE OF SYMMETRY

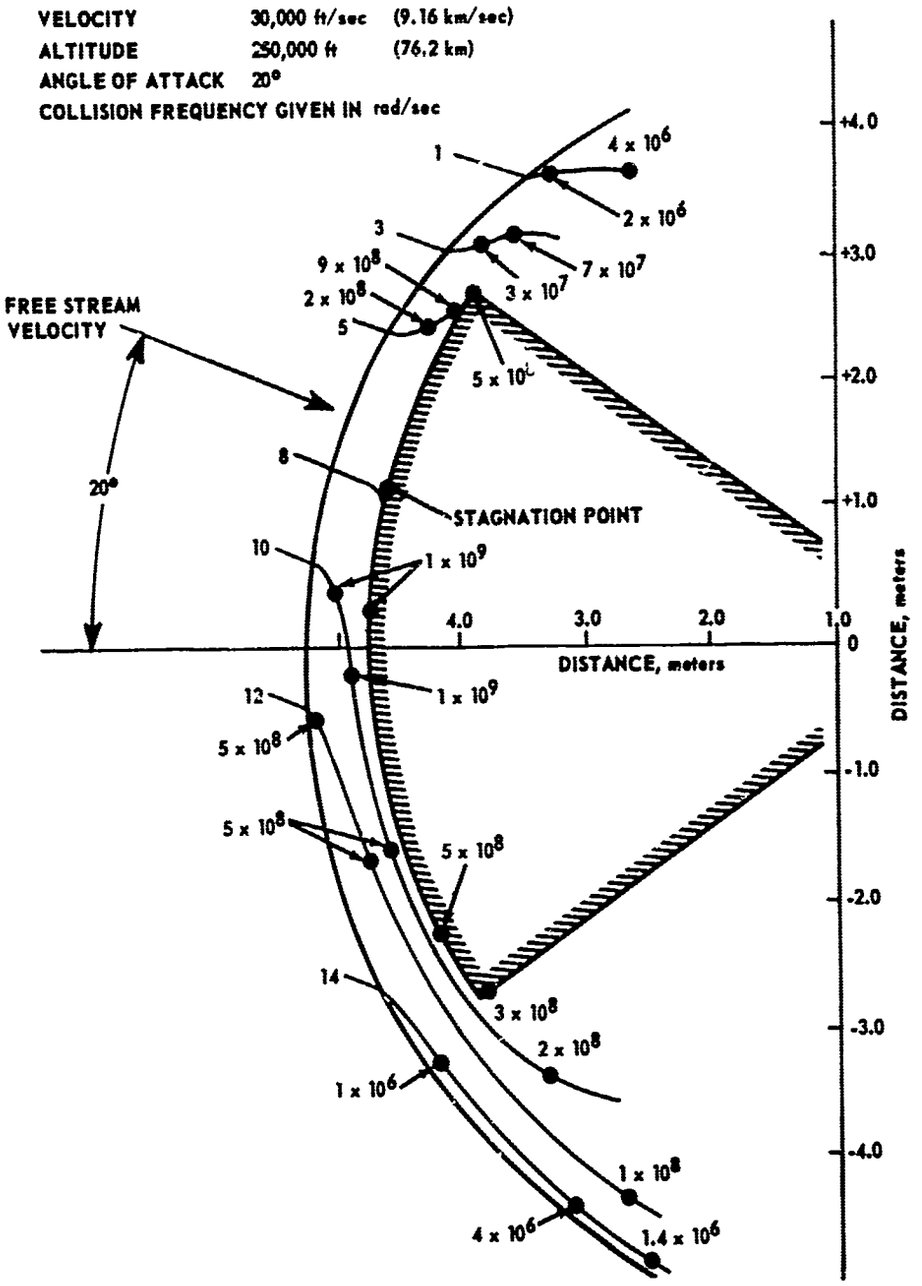


FIGURE 27 ELECTRON-ION COLLISION FREQUENCY (ν^+) IN PLANE OF SYMMETRY

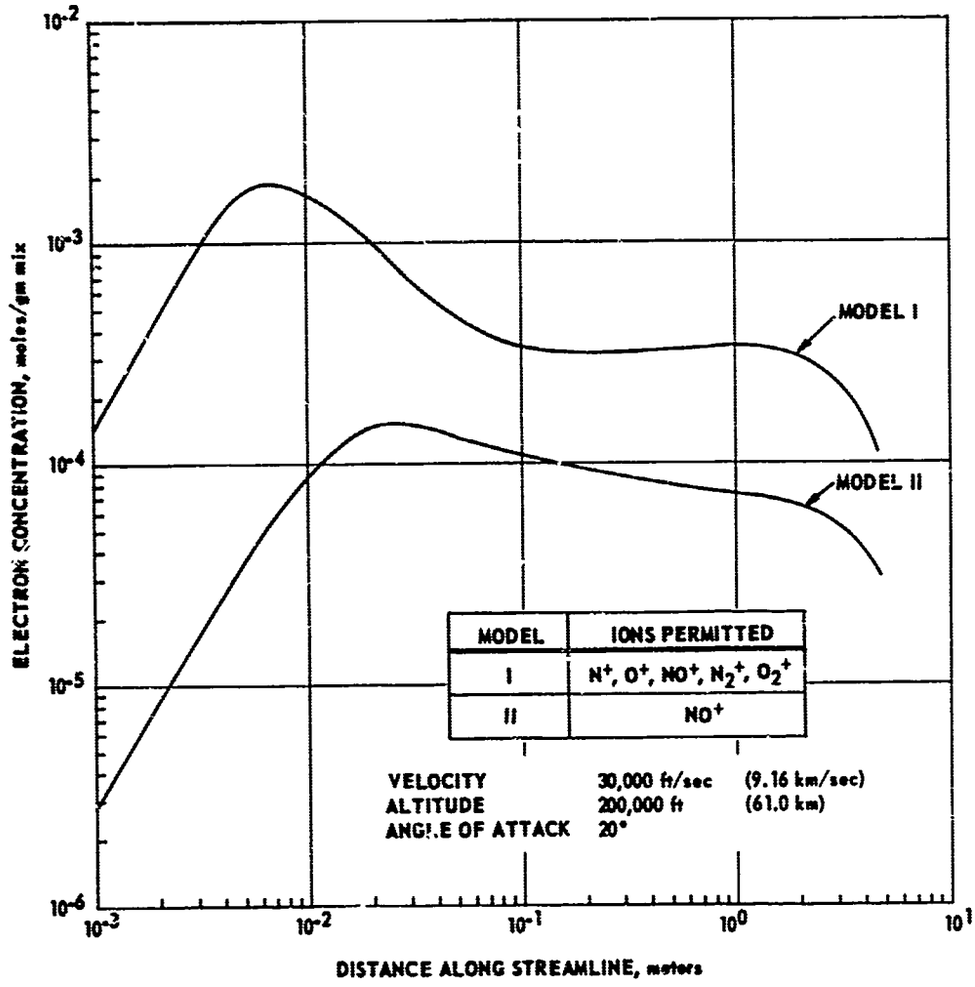


FIGURE 28 INFLUENCE OF CHARGED SPECIES TRUNCATION ON STREAMLINE 5 ELECTRON CONCENTRATION

III. THE EFFECT OF GLIDE RE-ENTRY SHOCK INDUCED IONIZATION ON THE COMMUNICATION SYSTEM OF THE ASSET VEHICLE

Philip M. Krause
Space and Missile Engineering Division
McDonnell Aircraft Corporation
St. Louis, Missouri

ABSTRACT

Ionization effects encountered during sustained lifting re-entry of the unmanned ASSET glide vehicle are presented. A brief description of the vehicle and communications system provide the background necessary for the interpretation of the flight results. Graphs of actual VHF plasma attenuation and the method used in extracting this from the raw data are discussed. Data consistency and agreement are indicated throughout. Flight results cover three important phases: the period of retrograde, the pitch up maneuver, and the steady state glide phase. The effects of firing hydrogen peroxide stabilization jets are also shown and discussed.

INTRODUCTION

The ASSET program has provided the first quantitative measure of the ionization effects on the communication systems for a glide vehicle during sustained lifting re-entry at near orbital velocities. Of the six vehicles flown during the contractual period, three of the flights produced pertinent data. The vehicles used in these flights were equipped with VHF, C-Band, and X-Band transmitters. A study of the received signals at these three frequencies was made in order to determine the specific effects of the plasma surrounding the vehicle. Curves of actual plasma attenuation for the VHF frequency were normalized against

the usual signal variations caused by transmitter power changes, antenna detuning, transmitting antenna pattern variations, and individual receiving station sensitivities, in order to isolate for study the attenuation associated with shock ionization. These curves were plotted as a function of velocity and angle of attack for various station locations. The VHF signal attenuation provided almost all the information about plasma effects except at the time of retrofire and subsequent vehicle-booster separation. At that time the VHF and C-Band signals were completely blacked out for some stations and the X-Band signal strength was slightly reduced.

BACKGROUND

The primary objective of the ASSET (Aero-Thermodynamic/Elastic Structural System Environmental Tests) program was to obtain combined aerodynamic, thermodynamic, structural and flutter data from a hypersonic glide reentry vehicle in environmental conditions which cannot be simulated in existing ground test facilities. Measurement of plasma effects upon communications was not within the scope of this primary test objective, and, therefore, it was limited to that which could be performed on a non-interference basis.

The vehicle shape and antenna locations are shown in Fig. 1 and Fig. 2. The primary telemetry system was a VHF PDM/FM system operating at 237.8 Mc. with a 0.5 Mc. bandwidth. Its antenna was an 8" x 6.75 " x 0.5" cavity backed U-slot filled with a solid block of aluminum oxide. The upper part of the vehicle body on which the antenna was mounted would not have been a load bearing structure if the antenna was mounted flush with the skin; therefore, the VHF antenna was mounted external to it. This resulted in additional antenna heating, and consequently

a high temperature specification of sustained operation at 1300°F was required. Because temperature variations cause dimensional and dielectric changes, the antenna was off-tuned at room temperature and tuned to be properly matched at flight temperature. The C-Band unit was comprised of a conventional radar transponder which operated at 5.755 Gc. and a cavity backed helix filled with quartz. X-Band equipment included a PPM/AM telemetry system operating at 9.32 Gc. and an open ended waveguide with an aluminum oxide window. Complementary receiving equipment was used at each of the ground stations.

EXTRACTION OF PERTINENT DATA

The data analyzed was received in the form of calibrated AGC records made during the flight for the VHF and X-Band telemetry and C-Band radar. In order to determine the attenuation caused by ionization, signal margins assuming no ionization were predicted for each station during the entire time of flight and were then subtracted from the actual margins. Both margins were computed with the aid of the measured noise level at each station[1]. These predictions were in part determined by a six-degree of freedom computer program, SDF-10, used in conjunction with the SF-49 subprogram. SDF-10 was provided with inputs of injection conditions and aerodynamic coefficients; SF-49 was provided with receiving station locations and a figure of merit for each link. The computer solved for the trajectory and resolved the geometry to provide signal margin (figure of merit minus the transmission loss), aspect angles of the vehicle as viewed by each ground station, and azimuth and elevation angles of the ground station antenna. Since the program considered only omnidirectional onboard antennas, the computer results for signal margin were manually corrected to account for the

actual antenna pattern which included polarization loss. Further correction of the VHF margin was required because of the change in antenna characteristics with aerodynamic heating. The VHF vehicle antenna VSWR loss and the resultant transmitter power reduction had been determined experimentally as a function of temperature. Using values of in-flight antenna temperature, these losses were determined and subtracted from the margins to obtain the final values which would be experienced in the absence of any shock ionization. Figure 3 shows how the actual signal margin compared to that predicted for a no-plasma condition. It is seen that in regions where no significant attenuation due to the plasma was expected, there was very good agreement between the two curves.

ASV-1, ASV-3, and ASV-4 FLIGHT DESCRIPTION

This series of the ASSETS were boosted to an approximate altitude of 200,000 feet where separation from the launch vehicle took place. The injection conditions at this point, where the angle of attack was 0^{o}, are listed in Table 1.

Shortly after injection, the angle of attack was programmed over a period of approximately seven seconds to a final value which was maintained for the remainder of the flight. Figure 4 presents this change in angle as a function of time for the various flights. The subsequent equilibrium altitude versus velocity profile is indicated in Fig. 5. During the flights, telemetry and tracking support were provided by facilities at Cape Kennedy, Patrick AFB, Grand Bahama, San Salvador, Grand Turk, and several ships. The ground tracks of these flights relative to the supporting stations are shown in Fig. 6.

This portion of the flight is divided into three significant phases: (a) the period of booster separation when the retro-rockets were fired, (b) the pitch up phase when the ASSET moves from zero angle of attack to its final value, and (c) the steady state period of glide flight.

ASV-1, ASV-3, and ASV-4 FLIGHT RESULTS

SEPARATION (BOOSTER RETROGRADE)

In order for the vehicle to separate from the last stage, three solid propellant retro rockets fixed on the underside of the launch vehicle must fire forward. The flame of the retro rocket in effect washes over the ASSET vehicle flaring out beneath it and filling a good portion of the volume within the bow shock. The firing time was estimated at a little more than two seconds with a decreasing intensity towards the end of this period. The resulting ionization always produced a complete loss of VHF telemetry. The actual C-Band signal margins at various stations are shown in Fig. 7. Station 1 was at a vehicle azimuth angle of 180° to the right looking at the rear of the vehicle and through most of the rocket flame. It was, therefore, expected that the signal would be strongly attenuated for the entire duration of the motor firing since slight movement of the rocket flame away from the vehicle will not substantially alter the look angles with respect to the flame. Figure 7 bears this out. Station 3 was in a more favorable position - 150° to the right of the nose. In this case, the records show that the plasma attenuation lasted approximately one second, indicating that when the vehicle and the flame

were separated sufficiently there was no effect on the signal strength. Station 5, at 40°, emphasizes the azimuth angle sensitivity even more, showing very little drop in signal strength in much less than a second.

In addition to AGC voltage records, photographs of the received pulse were made at Stations 1, 3, and 5 for all ASV's. This data was used to determine whether C-Band or X-Band antenna voltage breakdown occurred during ionization periods. No evidence of breakdown could be found in the pictures of the received pulse.

X-Band data showed a slight change in signal level at Station 1; however, it was not appreciable. This was the only phase in which there occurred any plasma effect on the X-Band and C-Band transmissions.

PITCH-UP PHASE

Immediately following booster separation the vehicle angle of attack was changed to 38°, 38°, and 28° for ASV-1, ASV-3, and ASV-4 respectively. During this short period the velocity and altitude remained constant for each flight so that the data presented in Fig. 8 shows the effect that the changing angle of attack had on the plasma surrounding the antenna as well as the effect of aspect angle.

At zero degrees the ionization created around the nose flowed back past the antenna. The Cape Kennedy station at this point looked through a major portion of the wake in order to see the antenna, and as Fig. 8 shows its received signal was attenuated the most. San Salvador was a considerable distance in front of the vehicle and, therefore, viewed a significant portion of the plasma between the nose and the antenna. This explains why it had the second highest attenuation. Station 3 was located at an azimuth of about 85° and, since it only looked through the thin plasma covering the antenna, it was the lowest on the curve. The pitch angle did not have to change much in order for Cape Kennedy to see

considerably less of the wake. Figure 8 illustrates the resultant sharp drop in attenuation with a small, increasing angle. This attenuation decrease continued until about 10° when significant ionization from the underside of the vehicle changed the wake conditions to again make it unfavorable for reception at the Cape. Stations 3 and 5 did not see this rapid increase in attenuation until after angles of 18 and 24 degrees, respectively.

Figure 9 shows the results of the ASV-3 flight for the pitch up phase at a velocity of 18,000 FPS. This increase in velocity caused more ionization and, therefore, merely shifted the curves for the various stations upward in relation to Fig. 8. Again the drop in attenuation occurred within the same angle of attack ranges as ASV-1 (9° to 10° and 21° for Stations 3 and 7 respectively). The azimuth aspect angle of Grand Bahama in this case was similar to that of the Cape in Fig. 8. Thus, it exhibited the same characteristics.

Attenuation data for the ASV-4 pitch-up phase is shown in Fig. 10 for a velocity of 19,400 FPS. Again, the curve was shifted upward because of the higher velocity. Figure 10 is particularly interesting since it shows a drop both at 9° and 22° indicating the presence of a transition period. Table 2 presents the angles where the data of Figures 8, 9, and 10 show the attenuation to decidedly drop. In conjunction with this, the various related azimuth aspect angles corresponding to a particular flight and station are listed. This table better displays the consistency maintained in the data for all three flights. It also indicates a trend in which the attack angle decreases in the range 24° - 18° as the vehicle azimuth angle increases. At 64° azimuth

angle, both attack angles appear. Increasing from 64°, the larger attack angle no longer shows a drop in attenuation, and only the smaller one of 9° or 10° is evident. All of the VHF AGC signal records have been used for ASV-1, ASV-3, and ASV-4 except those for which the signal level was not measurable.

GLIDE PHASE

During the period of glide flight, ASV-1 and ASV-3 both flew at a 38° angle of attack. The period of measurable VHF attenuation for ASV-1 was from about 12,000 to 14,400 FPS. For higher velocities, attenuation reduced the signal level to that of noise. The change in altitude during the time corresponding to this velocity range did little to affect the characteristics of the plasma. Thus, it was possible to present attenuation data as a function of velocity alone. This is shown in Fig. 11 and Fig. 12. Two salient features exhibited by the data were the high aspect sensitivity and the linearity of attenuation with velocity. The aspect sensitivity can be attributed to the varying portions of the flow field through which the stations viewed the antenna. Figure 6 gives an idea of the azimuth angles existent for the stations and the various flights. During this phase of the flight no measurable attenuation was observed for the X-Band and C-Band transmissions.

HYDROGEN PEROXIDE JET FIRINGS

The ASSET vehicle was equipped with H_2O_2 roll, yaw, and pitch jets which provided stabilization during flight. Figure 13 shows the positioning of these jets. The largest one at the top was a 40# pitch jet while the others were 5# thrusters. When a thruster was fired 700°K

steam and oxygen expanded from the nozzle at high velocity in a wide plume configuration. The hot air in the boundary layer was cooled by this injection thereby reducing the degree of ionization. The rate of firings was highest during the transition or pitch phase. It was only at this time that the 40# jet was used. Since it was the largest, its effect on reducing the attenuation was most noticeable. The 40# firing primarily affected the wake ionization so that the largest reduction in attenuation was observed by the Cape. Station 1 saw the magnitude of this decrease in attenuation only in the ASV-1 flight since the signal was below noise level during the other flights. The change in signal margin for this station is shown in Fig. 14 to be 23db. Station 3's azimuth during ASV-3's transition period was not as large as Station 1's azimuth during ASV-1's transition and, therefore, the signal margin of Station 3 did not show as much change. These signal margins as well as Station 5's are depicted in Fig. 15A and Fig. 15B. The jet firing was not observed by the other station in these two flights since their azimuth aspect angles were all less than 90°.

Telemetry data from ASV-3 indicated that during the transition phase the pitch jet fired for the first 4.5 seconds at a rate of about six times per second. The 5# roll jets were used at about the same rate after the first second of pitch up[2]. The AGC recordings presented in Fig. 16 for the various stations clearly show the different motor firings. Station 1 saw six large increases in the signal per second - alternating with six smaller signal increases. These were caused by the 40# jet and the roll jet respectively. Both the Cape and Grand Bahama showed similar results since their azimuth angles are 180° and 149° respectively. Since

San Salvador and Grand Turk had azimuth angles of 33° and 25° and, therefore, did not view the wake, the roll jet firings were the only ones seen. Figure 16 verifies this.

CALCULATION OF PLASMA ATTENUATION

Accurate prediction of the expected attenuation for the ASSET vehicle is very nearly impossible because of the complex vehicle and flow field geometry. An exception to this might be found given conditions of a zero degree attack angle and a 90° vehicle azimuth. These conditions were closely approximated in the ASV-1 flight at Station 3 just before pitch up. Figure 8 shows the plasma attenuation suffered at this point to be 4 db. In order to arrive at the attenuation theoretically, the gas conditions and flow both from the nose and on the forward section of the body were determined from a blunt cone analysis. The gas was then expanded over the cone-cylinder break and reshocked at the leading edge of the protruding VHF antenna. The plasma conditions were considered constant over the antenna face and were allowed to vary in the direction normal to it. Equilibrium gas conditions were assumed, and any near field effects were neglected. A plane wave analysis was then performed, and the attenuation arrived at was 1.0 db[3]. The agreement between the two numbers was extremely good considering the assumptions.

CONCLUSIONS

The ASSET program has provided a rather unique opportunity to measure the effect that shock ionization has on communication during the re-entry of a glide vehicle. The attenuation data presented has indicated the problems associated with communication during glide



re-entry and has also pointed the way to possible solutions. It would seem that real time data acquisition is possible for a significantly greater part of re-entry with the use of an advantageous aspect angle for the entire trajectory, a corresponding antenna location, proper aerodynamic shaping, as well as judicious H_2O_2 injection.

Since results of the three ASV flights show consistency throughout and agree closely with the one calculation made for this study, it may be concluded that further development of plasma and flow field models may be confidently based on the data presented herein.

REFERENCES

1. J.W. Dean, et. al., "Analysis of ASSET Communications Links", ASD-TR-62-778, August 1962.

2. ASV-3 Flight Test Report, McDonnell B251.

3. C.F. Stolwyk and C.A. Hinrichs, "Effects of Re-Entry Ionization on the ASSET Communication System", IEEE International Space Electronics Conference, Las Vegas, Nevada, October 3, 1964.

ACKNOWLEDGEMENT

The work in this paper was carried out in the Space and Missile Engineering Division of McDonnell Aircraft Corporation and was supported in part by the U.S. Air Force under Contract AF33(616)-8106. The writer wishes to acknowledge the information gleaned from the team of engineers responsible for the ASSET program, in particular J.W. Dean, C.A. Hinrichs, and R.J. VanderVoort.

TABLE 1

Injection Conditions

Flight	Velocity	Altitude
ASV-1	16,800 FPS	200,000 feet
ASV-2	18,000 FPS	212,000 feet
ASV-3	19,400 FPS	205,000 feet

TABLE 2

Angles at Which a Marked Decrease in Attenuation Occurred

Station and Flight	Azimuth Aspect Angle	Angle of Attack
Sta. 5 - ASV-1	22°	24°
Sta. 7 - ASV-3	25°	21°
Sta. 3 - ASV-1	60°	18°
Sta. 5 - ASV-4	64°	22° and 9°
Sta. 3 - ASV-3	149°	9° and 10°
Sta. 1 - ASV-1	180°	9°

FIGURE 1

ASSET VEHICLE

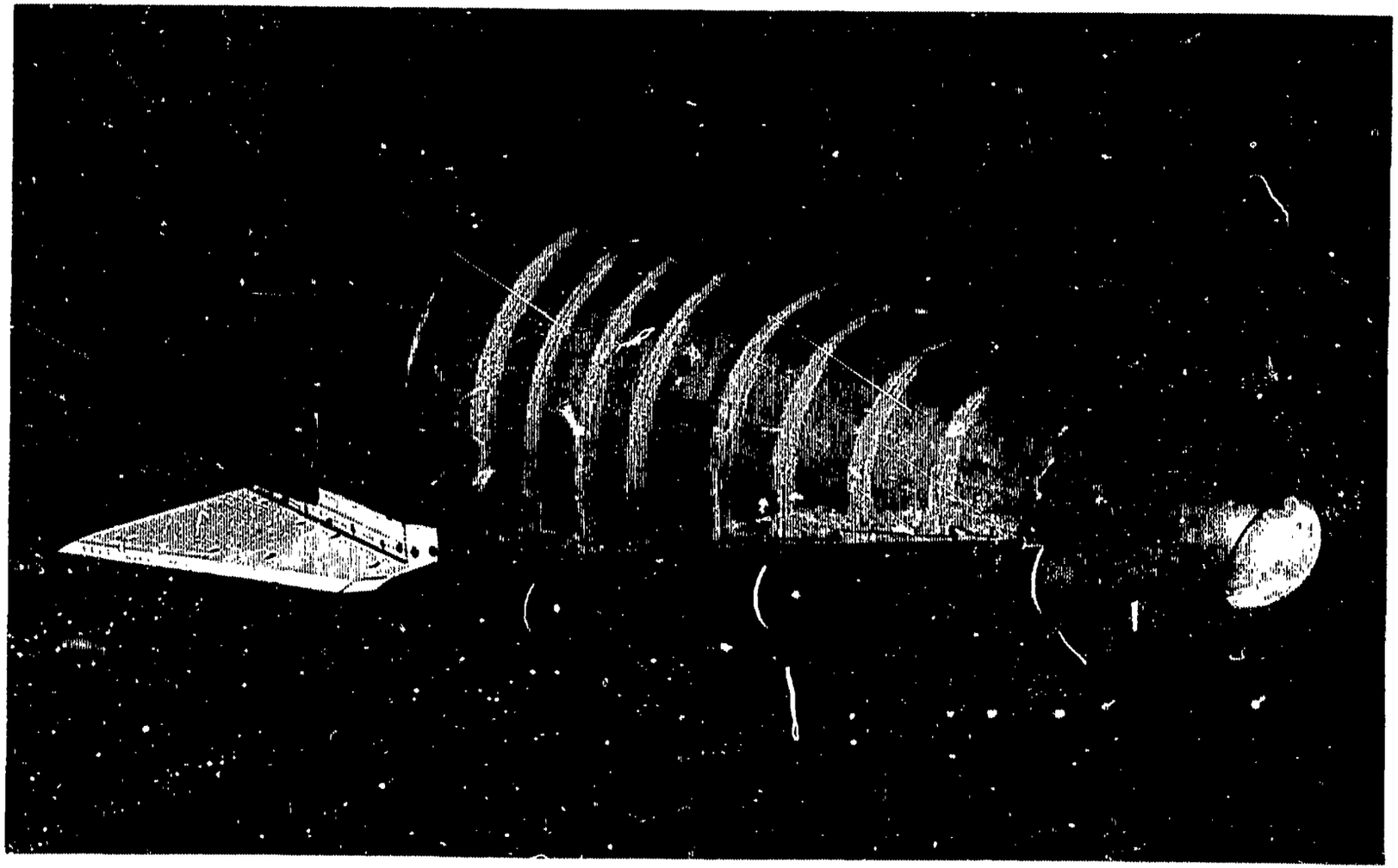


FIGURE 2

ASSET VEHICLE OUTLINE AND ANTENNA LOCATIONS

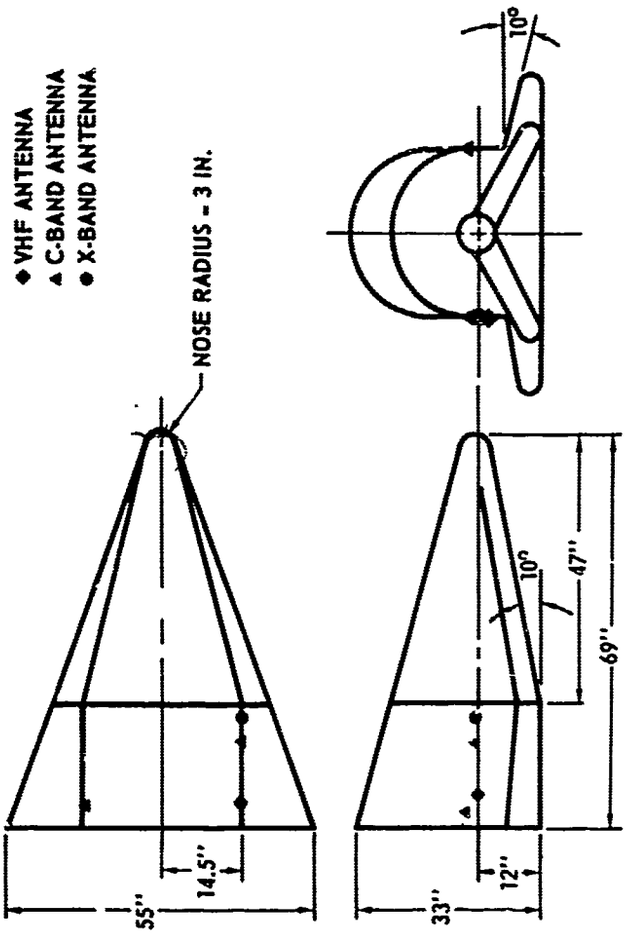


FIGURE 3

ASV-1 (TEST 3680)
STA. 3 VHF SIGNAL STRENGTH

RIGHT HAND (TRI-HELIX)

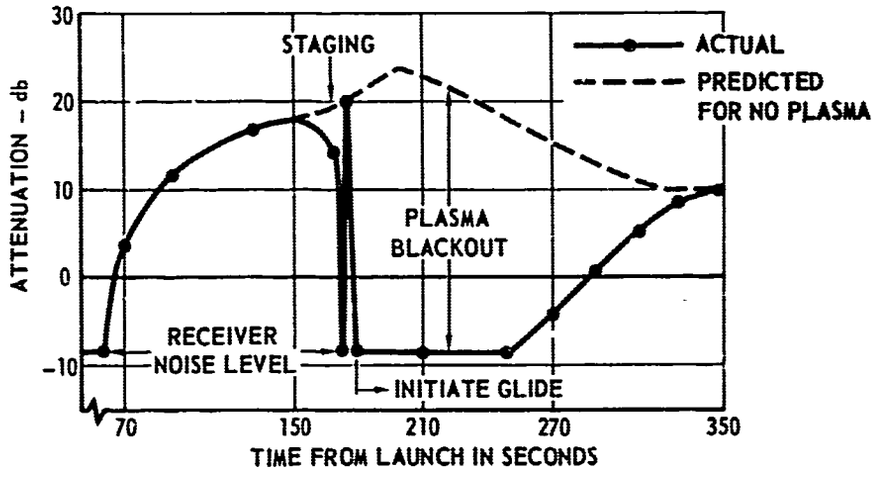


FIGURE 4

ASSET ASV 1-3-4 ANGLE OF ATTACK DURING PITCH-UP PHASE

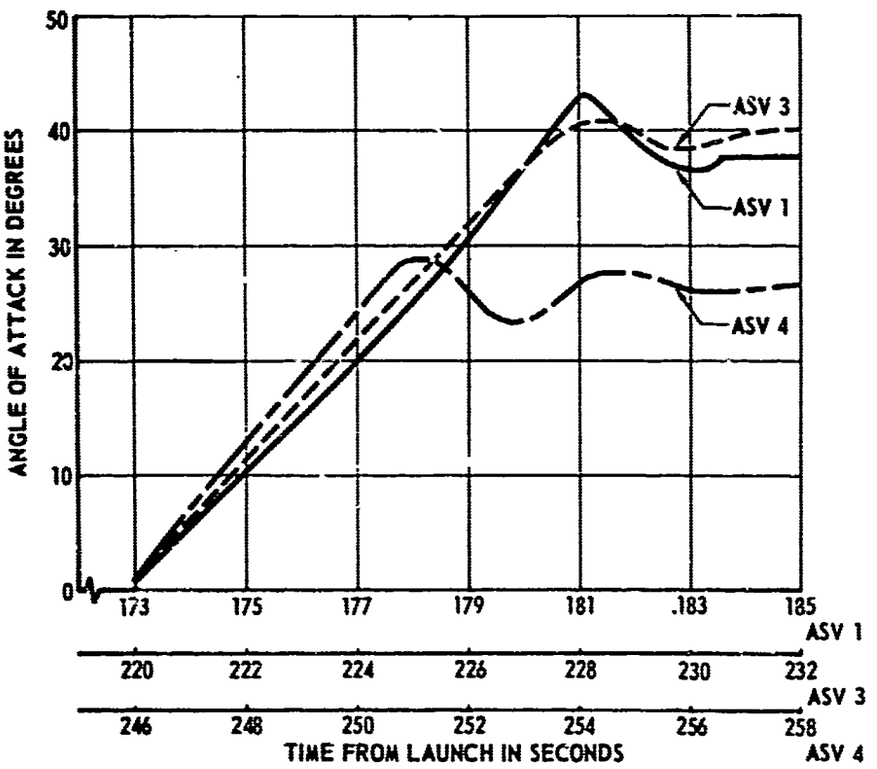


FIGURE 5

ASSET ASV 1-3-4 ALTITUDE VS VELOCITY

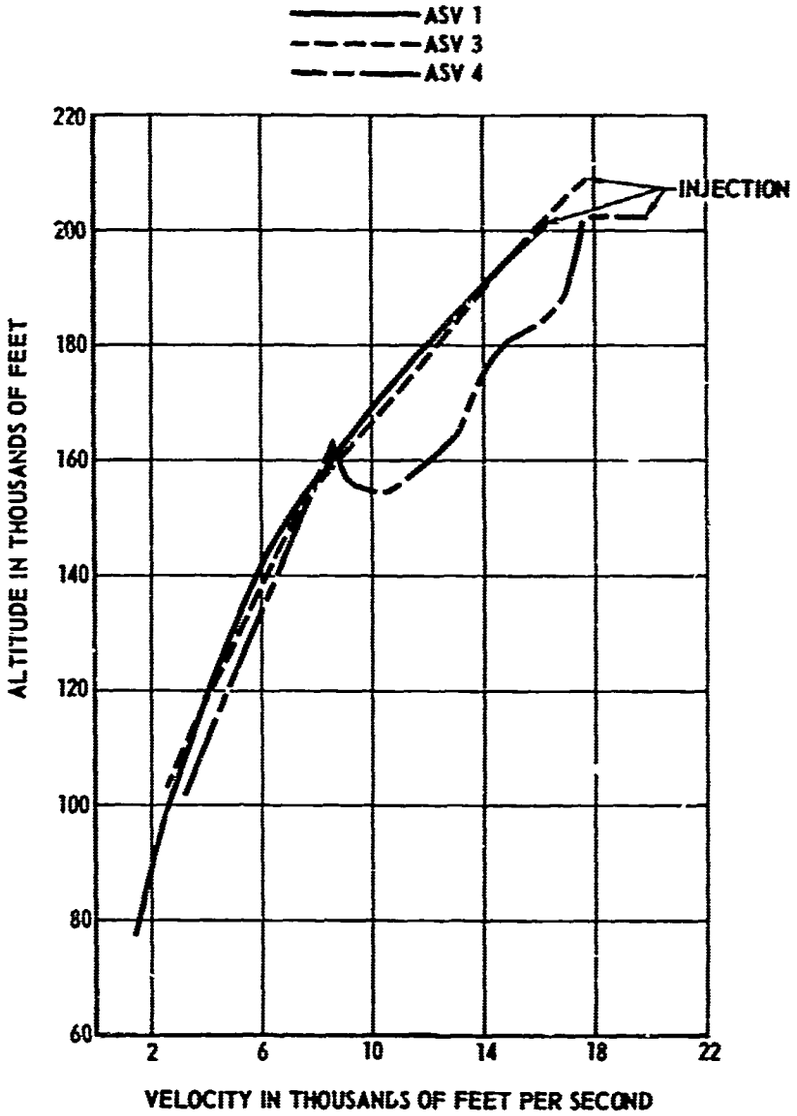


FIGURE 6

ASSET GROUND TRACKS

ASV 1-3 FOLLOW SAME GLIDE PATH AS SHOWN FOR ASV 4

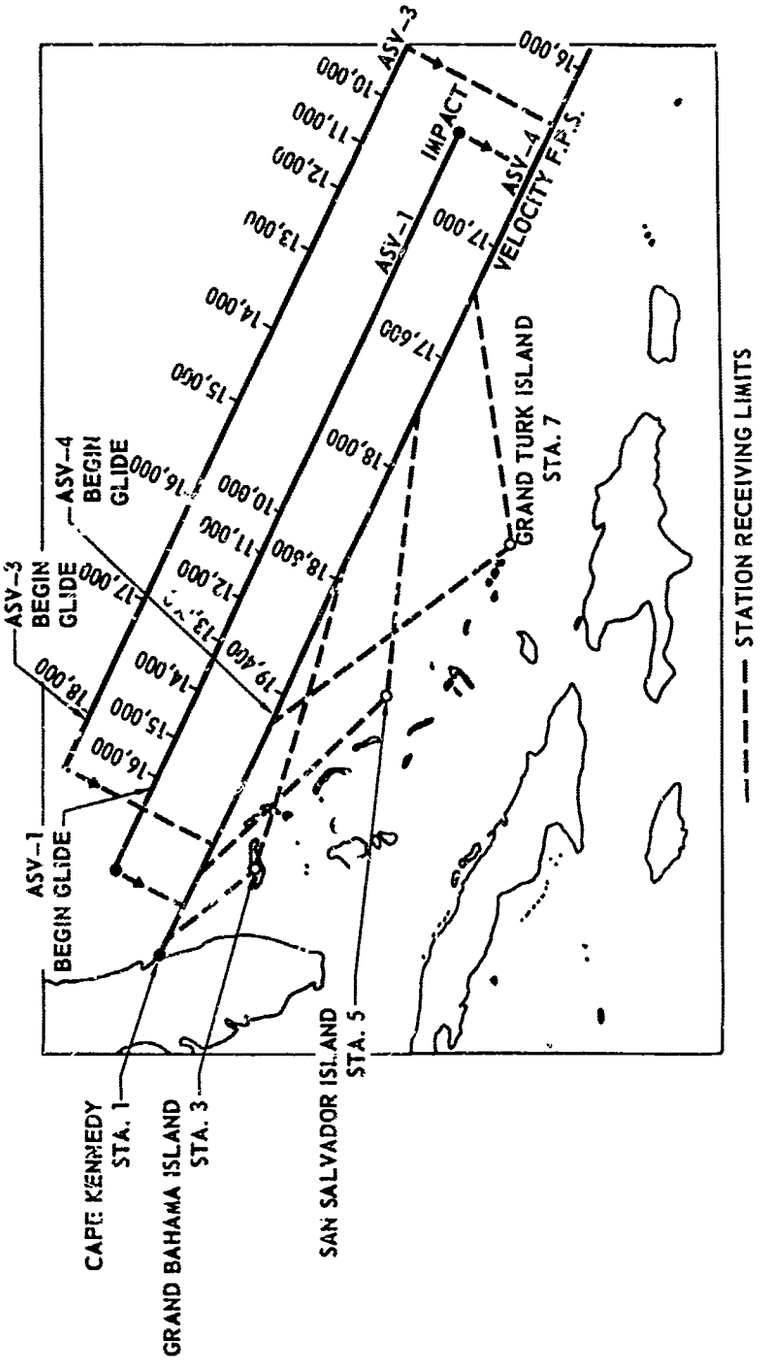


FIGURE 7

ASV-3 C-BAND SIGNAL LEVEL DURING THE RETRO FIRE PERIOD RECORDED AT STATIONS 1, 3 AND 5

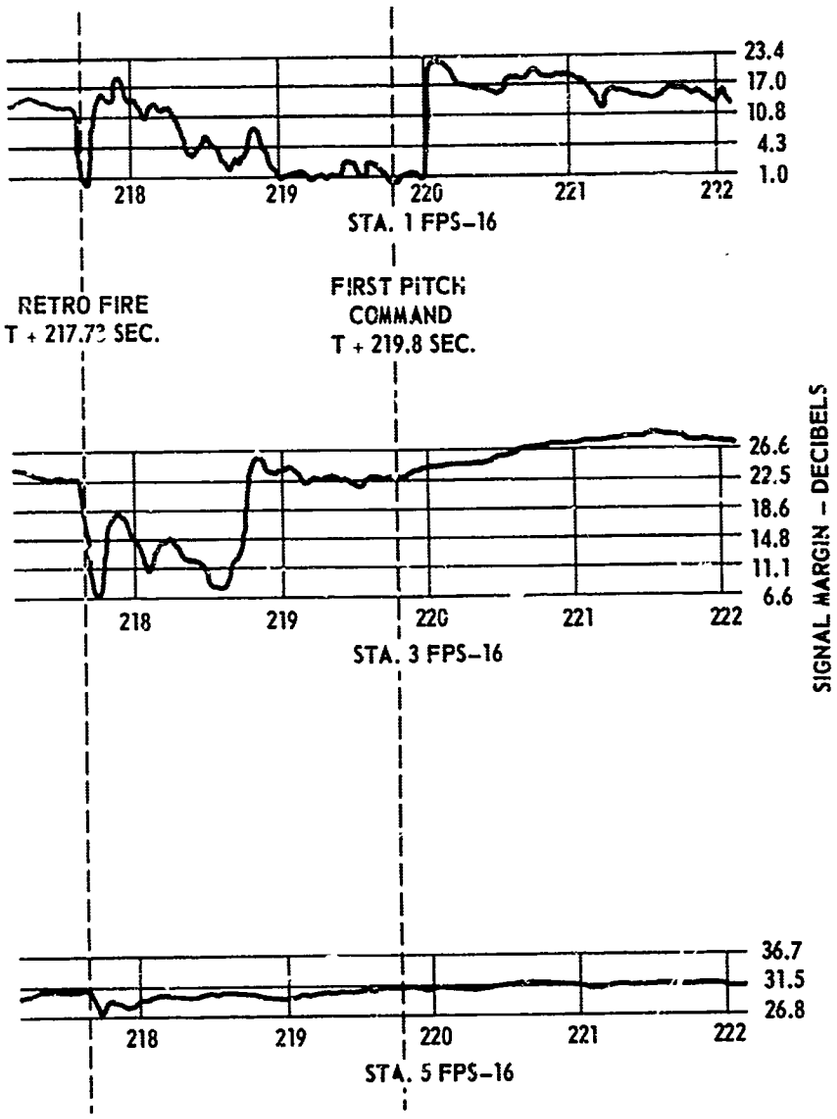


FIGURE 8

ASSET ASV-1 VHF ATTENUATION

16,100 FPS
200,000 FT.
7 SECOND PITCH-UP PERIOD

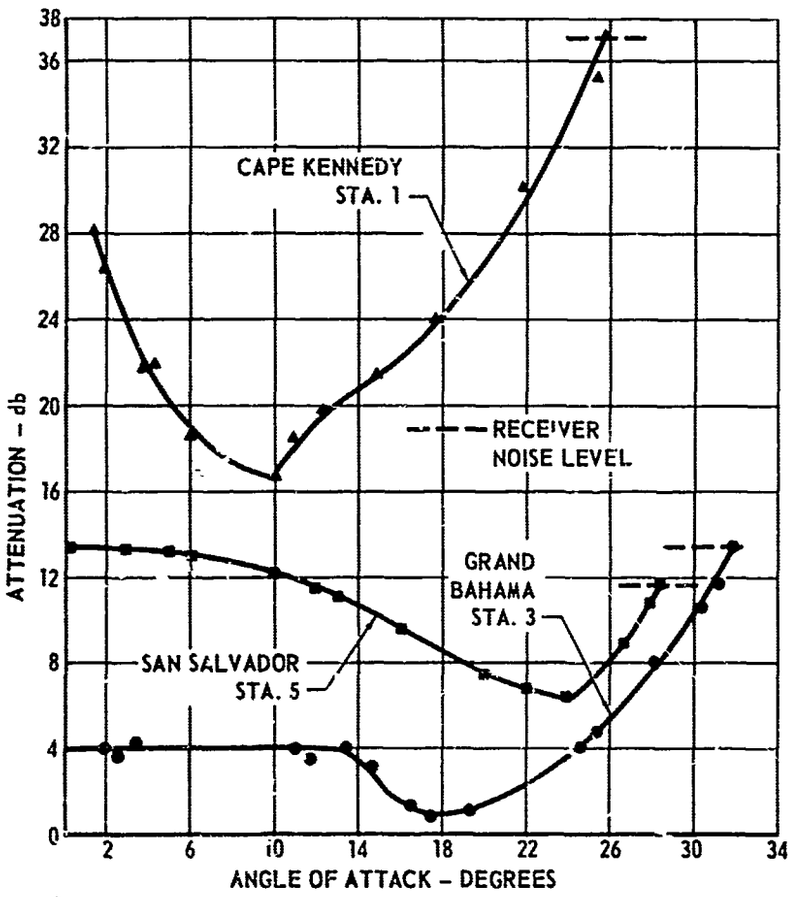


FIGURE 9

ASSET ASV-3 VHF ATTENUATION

18,000 FPS
212,000 FT.
6 SECONDS PITCH-UP PERIOD

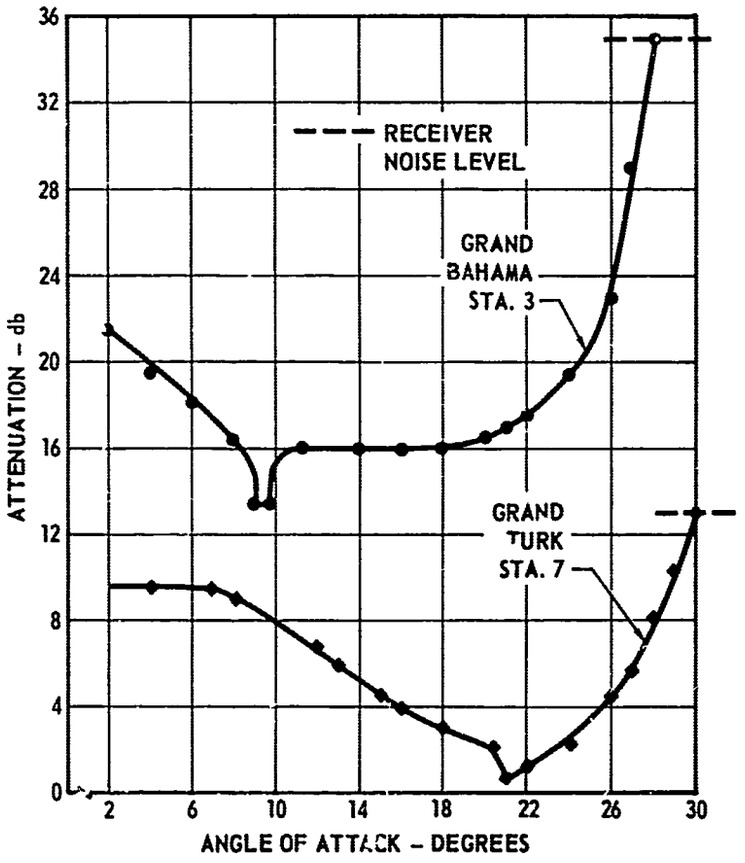


FIGURE 10

ASSET ASV-4 VHF ATTENUATION

19,400 FPS

205,000 FT.

6 SECOND PITCH-UP PERIOD

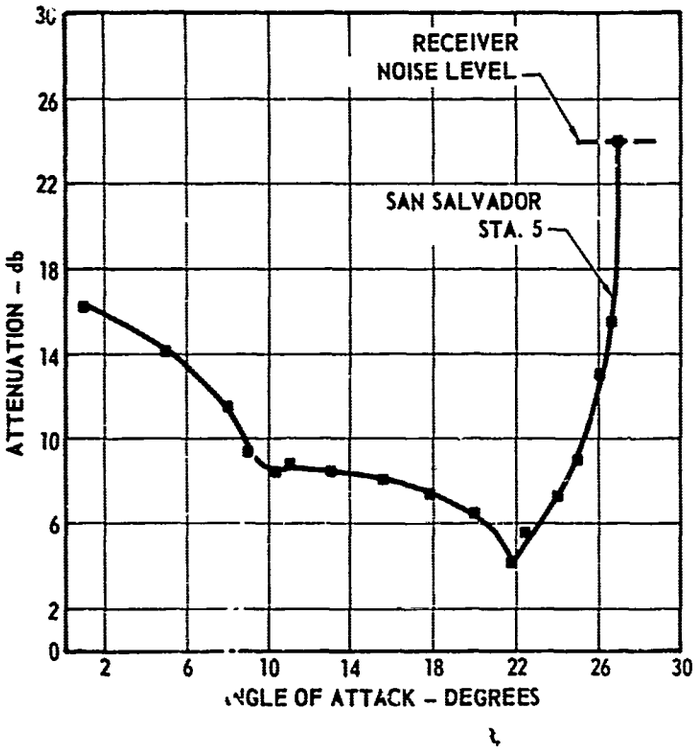


FIGURE 11

ASSET ASV-1
VHF ATTENUATION
GLIDE PHASE
ANGLE OF ATTACK=38°

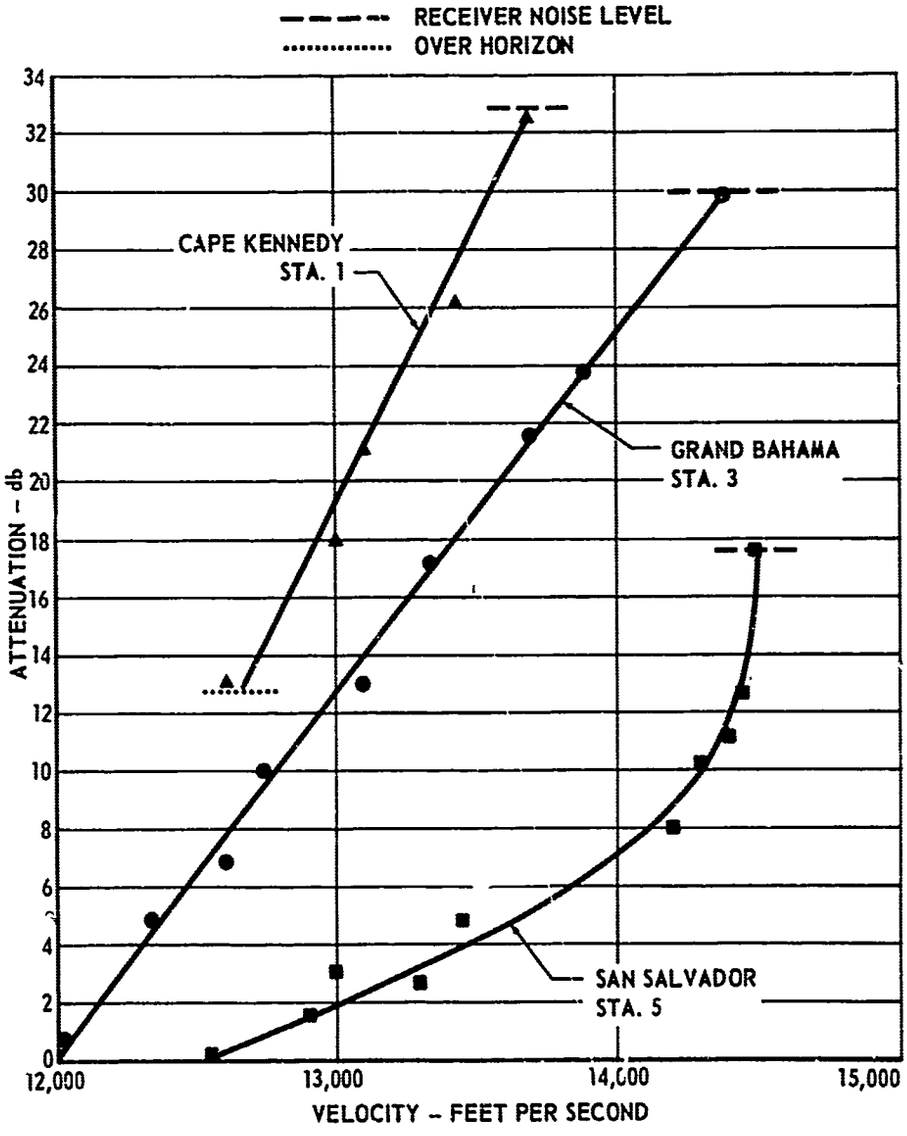


FIGURE 12

ASSET ASV - 3
VHF ATTENUATION
GLIDE PHASE

ANGLE OF ATTACK=38°

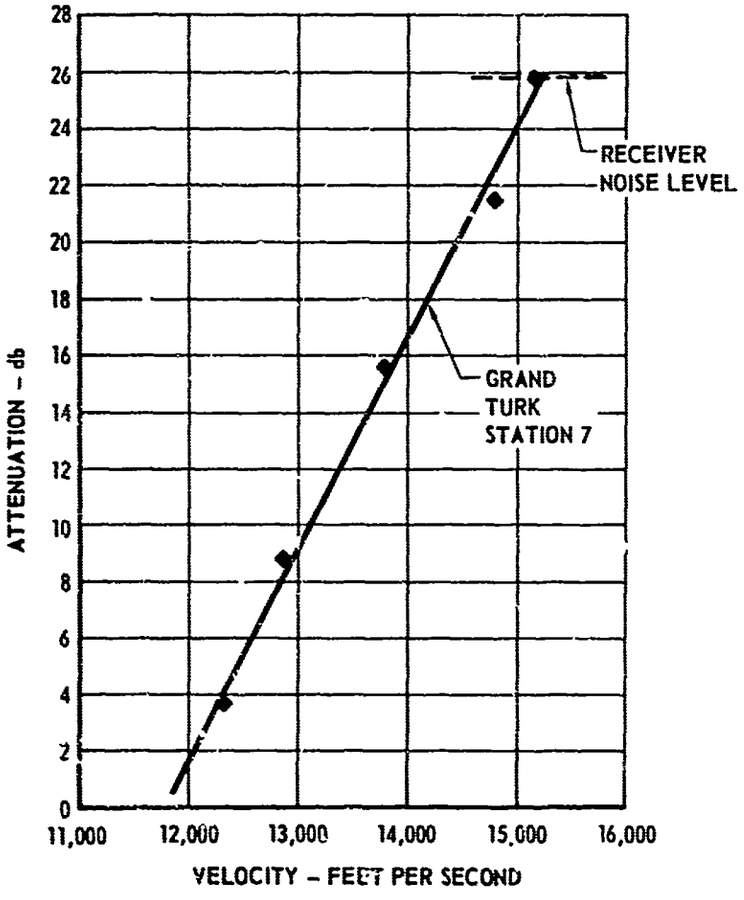


FIGURE 13

ASSET VEHICLE REAR VIEW AND REACTION JET LOCATIONS

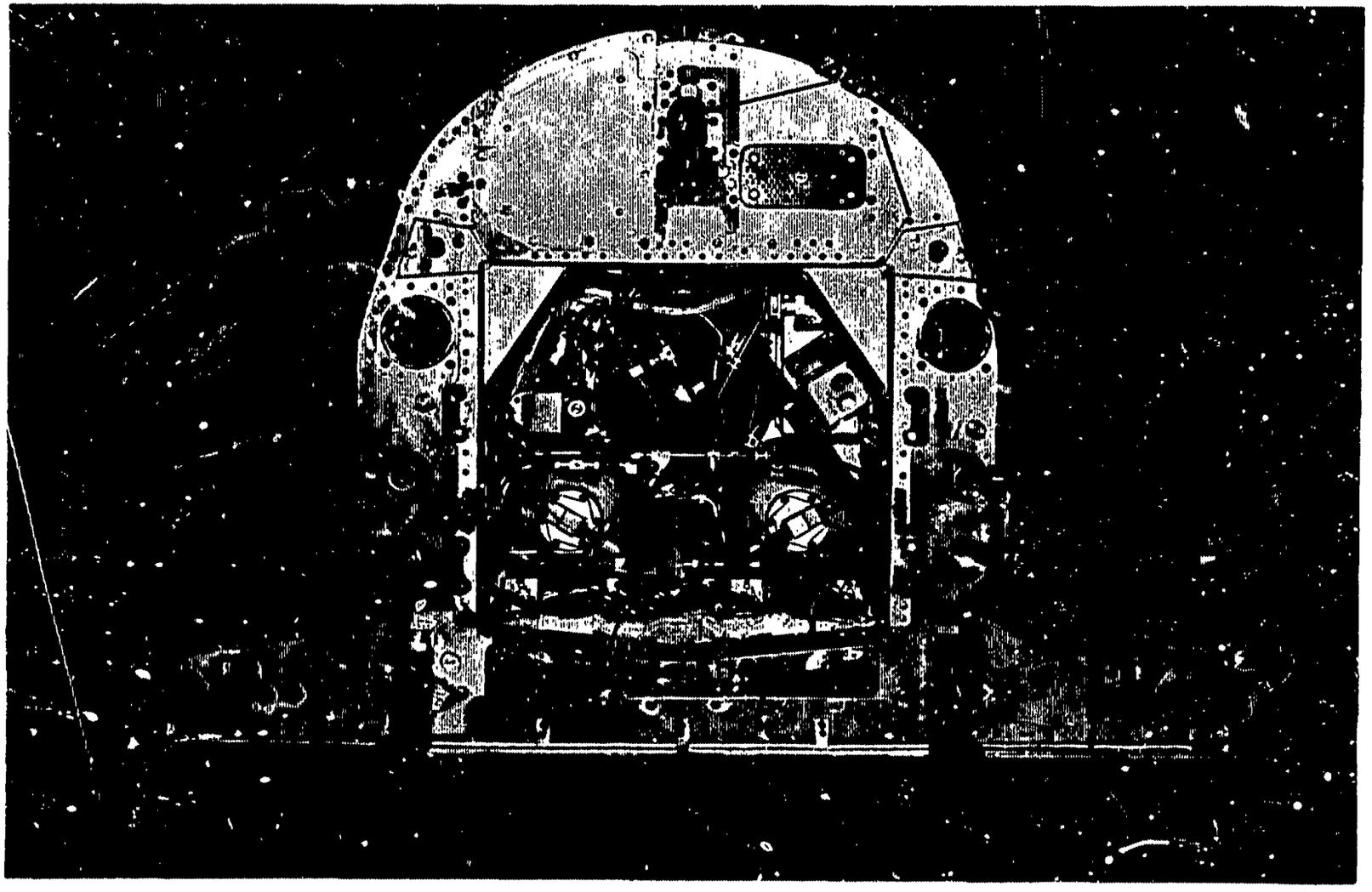


FIGURE 14

ASV-1 STA. 1 VHF SIGNAL MARGIN

H_2O_2 FIRINGS DURING PITCH-UP PERIOD

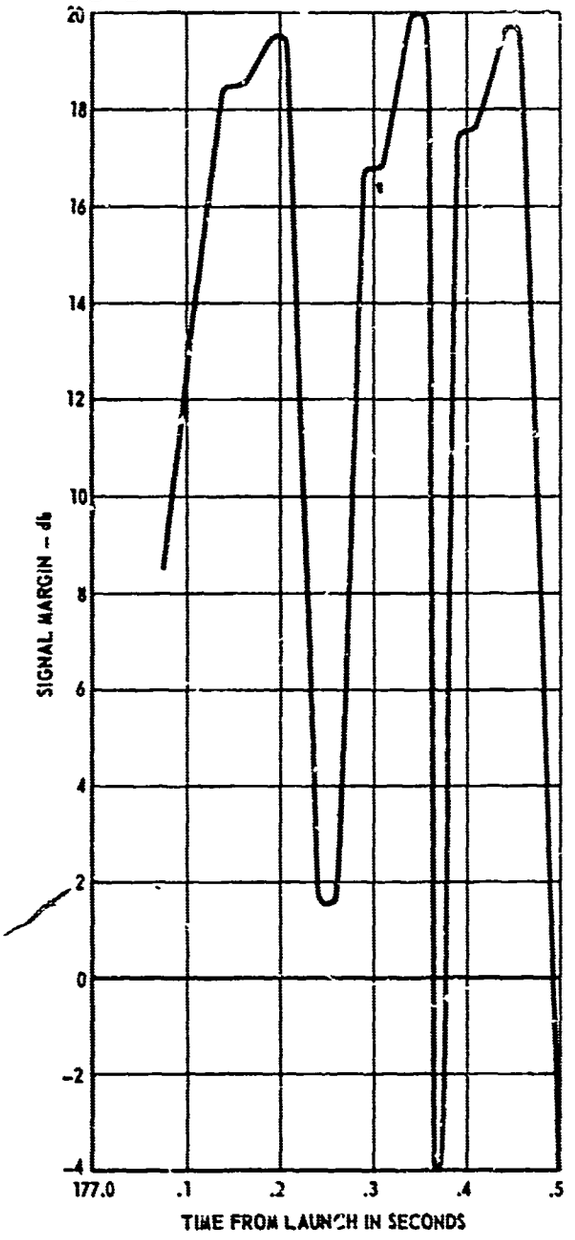


FIGURE 15A

ASV-3 STA. 3 VHF SIGNAL MARGIN

H_2O_2 FIRINGS DURING PITCH-UP PERIOD

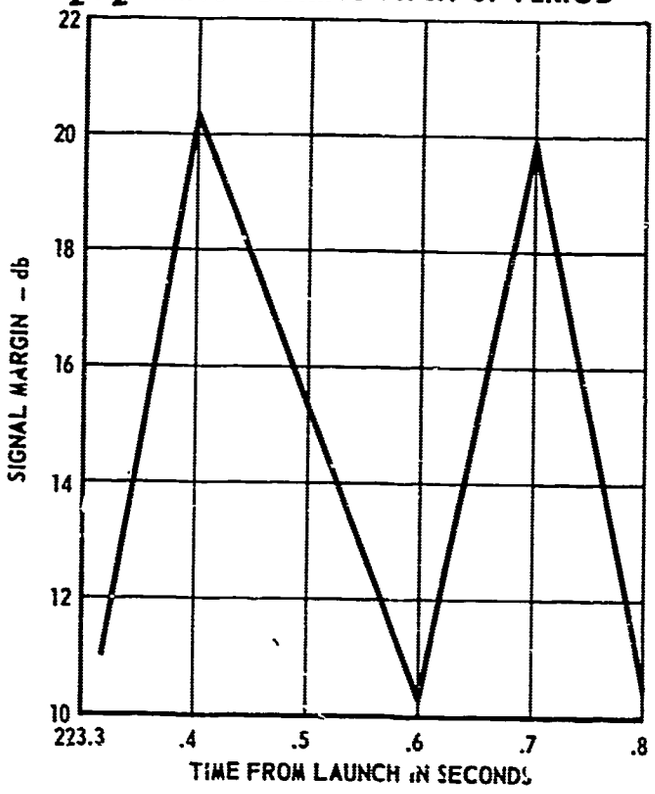


FIGURE 15B

ASV-4 STA. 5 VHF SIGNAL MARGIN

H_2O_2 FIRINGS DURING PITCH-UP PERIOD

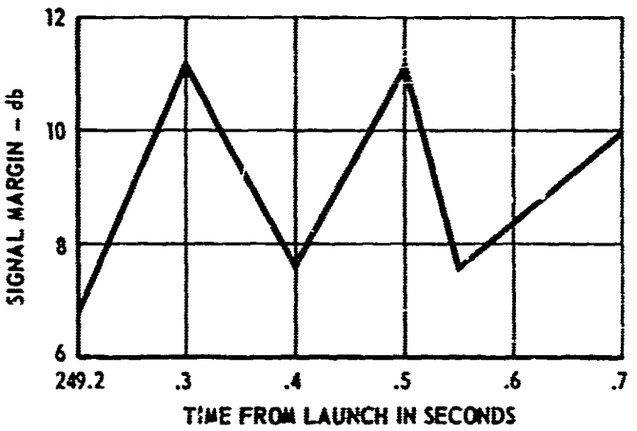
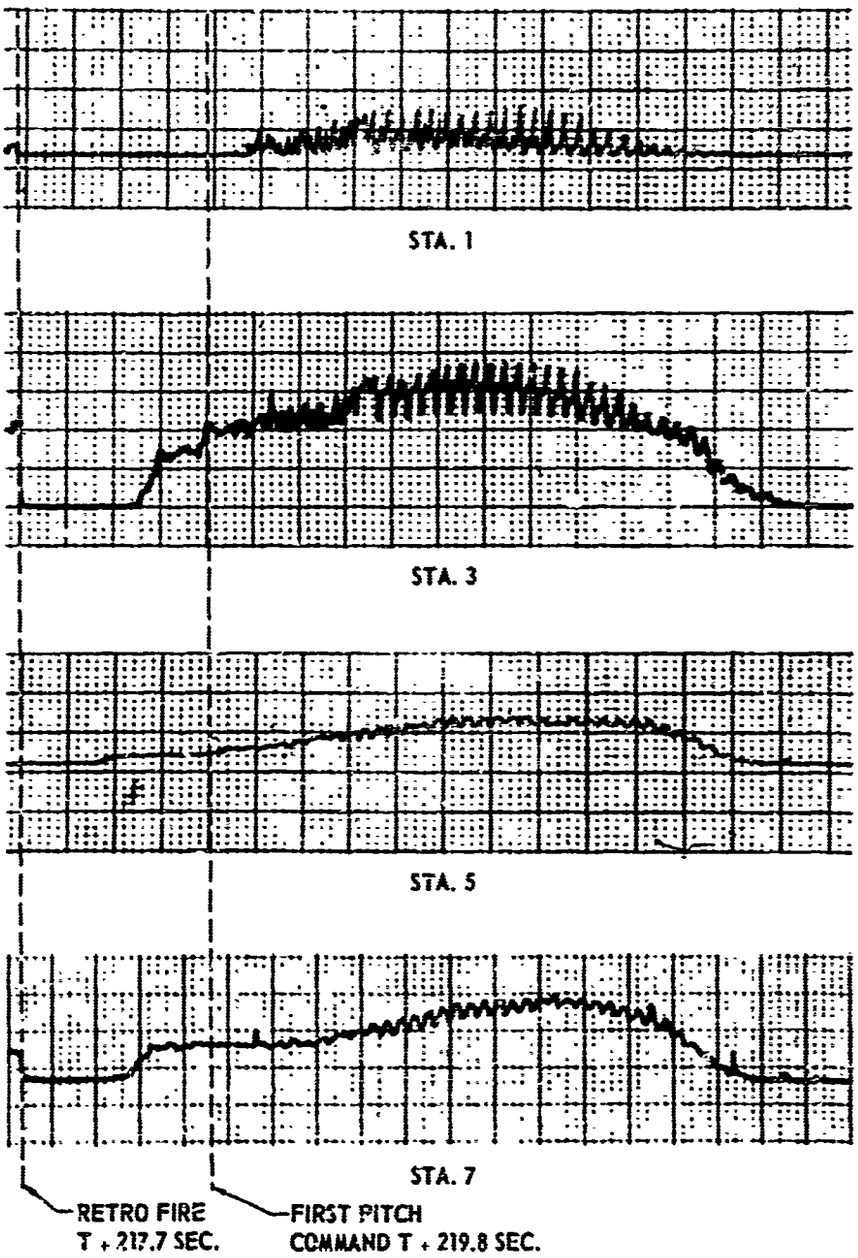


FIGURE 16

ASV-3 VHF SIGNAL STRENGTH



IV. THE USE OF LANGMUIR PROBES IN DIAGNOSING IONIZED FLOW FIELDS

W. E. Scharfman, H. Bredfeldt, ' Guthart, and T. Morita

Stanford Research Institute
Menlo Park, California

The work reported in this paper was supported by NASA-Langley Research Center under Contract NAS1-3942 and by ARPA under Order 281-62, Project Code 7400.

I INTRODUCTION

The determination of the electron density surrounding a reentry vehicle from gas-dynamic calculations is hampered by uncertainties in the rate constants of the ionization processes as well as by the effects of ablation products. However, calculations have been made, and it would be desirable to be able to check them with flight-test data.

One common method of determining electron density is to measure the absorption and phase shift of microwaves that propagate through the plasma sheath. However, these measurements give only limited information; one obtains only an integrated value of absorption and phase shift. In order to interpret the results in terms of electron density and collision frequency, it is necessary to estimate the spatial distribution of these parameters, although the spatial distribution is itself one of the parameters of interest. In addition, the dynamic range of parameters that can be measured by such methods in a realistic flight test is usually quite small. For a given microwave frequency, it is usually possible to determine the electron density only when the plasma frequency is of the order of the microwave frequency.

The limitations in the use of microwaves apply equally well to the technique in which the reflected signal is monitored. This signal is appreciable only when the plasma frequency is greater than the microwave frequency. When the plasma frequency is greater than the microwave frequency the reflected signal approaches a constant value, and no further information about the plasma is obtained. Therefore, the reflected signal technique is useful mainly in determining when the plasma frequency is the same as the microwave frequency and is noted by the rapid rise in reflected signal.

As interest in hypersonic flows of the order of Mach 30 increases, the usefulness of microwaves becomes even smaller. This is true because the electron densities produced at these velocities are so high that it would

be impracticable to fly transmitters of sufficiently high frequency to prevent the plasma frequency from being higher than the microwave frequency, once ionization starts.

An alternative technique for measuring electron density during flight tests is to use electrostatic probes. The convention of calling electrostatic probes that operate under the classical Langmuir conditions "Langmuir" probes will be adopted. All probes that do not satisfy these conditions will be called simply "electrostatic" probes. It is possible to design these probes so that measurements can be made with a spatial resolution of less than 1 mm. Thus, use of a probe that could move radially outward from the reentry vehicle would make it possible to determine the spatial distribution of electrons. Alternatively, one could use several probes mounted at different radial distances from the vehicle surface.

Several flight test programs using probes (RVIP and LGRV) have been carried out, while several others (RAM and TRAILBLAZER) will be flown shortly. This paper presents studies which are aimed at interpreting the results of such flight tests.

Langmuir probes are inherently capable of measuring a wide range of electron densities. They appear to be worthy of consideration for flight tests. Probe theory, however, is predicated upon a number of conditions that will not hold true over an entire trajectory. It is necessary to determine the errors involved in the inferred plasma parameters and to develop a theory that will enable one to interpret the data over the complete trajectory.

The theory of Langmuir probes is well established for the free-molecular case, i.e., when the mean free path is much greater than the probe radius and the sheath thickness.[1*] Furthermore, the classical Langmuir theory does

*References are listed at the end of the text.

not consider the case of a flowing plasma moving with supersonic velocity. For probes to be useful as diagnostic tools aboard reentry vehicles it is necessary to have a theory that will include flow effects. The usefulness of such probes will be further enhanced if measured probe current under short mean free path conditions can be interpreted to yield values for the electron density.

This paper presents the results of a study of both the effects of flow velocity and short mean free path. The experiments were conducted in an arc-driven shock tube. The shock-heated test gas slug provided equilibrium, supersonic samples of partially ionized air. The properties of the gas, including mean free path, are thus presumed known. The operational characteristics of cylindrical and flush mounted probes have been investigated. Theories of cylindrical probe operation have been recently developed for the case of free-molecular supersonic flow, and data presented here show that these theories can be used to measure electron density for probe diameters up to several mean free paths. A quantity of data was also gathered for the case that is more difficult to handle theoretically--supersonic flow with the mean free path much smaller than the probe diameter. It is to be expected that under these conditions the probe will have a shock surrounding it, and thus interpretation of the probe current in terms of the incident plasma properties would have to take into account the change in properties due to the shock. The problem is further complicated by the fact that the flow times around the probe are so short that for a large range of conditions the flow around the probe will not be in equilibrium. It would thus be necessary to introduce the appropriate rate constants and solve the flow problem with finite time chemistry. This is a very difficult problem theoretically, and it is clear that solutions would not be any more accurate than the rather poorly known rate constants.

The initial approach has been to gather data on probe operation under these conditions and then look for applicable scaling relations which enable

one to generalize the results. Such scaling relations could also be used by the theoretician as a guide in identifying the dominant processes and hence simplifying his analysis. Through analysis of the data gathered to date, it appears that a scaling relation does exist when the probes are in continuum flow regime.

Flush mounted probes are of interest since they do not disturb the flow field. Flush probe measurements have been made of the electron density in the non-uniform plasma formed by the boundary layer of a shocked gas flowing over a flat plate. A probe theory is proposed and experimental confirmation of the probe theory has been obtained by measurements in the boundary layer.

II SUMMARY OF ELECTROSTATIC PROBE THEORY

A. Ion Collection With No Flow Velocity--Free Molecular Case

The theory of electrostatic probe operation in a non-flowing, free molecular plasma has been widely discussed in the literature.[2-4] Often these analyses are for special cases--sheath area limited or orbital motion limited operation. However, Hok[5] has calculated the dependence of ion current on ion density and temperature for a cylindrical probe for the whole range of $\tilde{\eta}$ (eV/kT) and a/r_p (sheath to probe radius) with no flow velocity. His results are presented in Fig. 1. I is the measured current, A the probe area and J the random in current density. In the section on ion collection with flow velocity a discussion on how this figure may be modified to include the effects of flow will be presented. The coordinates in brackets refer to the flow case and will be discussed in Sec. II-B.

Although this plot is extremely useful for a general understanding of the different regimes under which a probe may operate, a/r_p must be known in order to use it for determining the electron density from a measurement of current. The space-charge-limited diode equation may be manipulated so that values of a/r_p can be found in terms of the measured

current and other measurable parameters--probe length, diameter, and potential. The results are shown in Fig. 2. The probe-to-plasma potential, V is not the same as the applied potential, but can be taken as the applied potential plus 5 kT/e (the difference between the plasma and floating potential) for the purposes of estimating a/r_p. In order to estimate η, it is necessary to have some idea of the electron temperature, but for large values of η, this term, which only varies as the square root, does not contribute significantly.

B. Ion Collection With Flow Velocity--Free Molecular Case

Several theoretical treatments[6-8] of the problem of ion collection in a flowing plasma have been made for the case where there are no collisions in the sheath and where the probe is smaller than the mean free path. It is also usually assumed that the form of the sheath is not distrubed by the flow.

The theoretical relation between probe current and flow velocity is shown in Fig. 3 for the case where the sheath thickness is small compared to probe radius. The abscissa is the ratio of the current collected with flow velocity to the current which would be collected with only thermal velocity. Under these conditions, a useful parameter that indicates whether the flow has a significant effect on ion current collection is the ratio of flow velocity, v_f, to thermal velocity, $v_+ [v_+ = (2kT_+/m_+)^{\frac{1}{2}}]$. This ratio is approximately 0.8 times the Mach number for air before dissociation. When the Mach number is much less than unity, the effect of flow is negligible. When the Mach number is greater than about three, the current is essentially made up of the flow of ions into the projected area of the probe. Thus, for $a/r_p \approx 1$,

$$I_+ = n_+ e v_f 2 r_p L \qquad \text{(for cylindrical probes with flow perpendicular to axis)}$$

and

$$I_+ = n_+ e v_f \pi r_p^2 \qquad \text{(for spherical probes)}$$

When the sheath thickness is larger than the probe radius, the problem is more complicated. In addition to the Mach number, one must consider the relation between the potential field around the probe, which pulls the ions toward the probe, and the inertia of the ions, which can carry them through the potential field without their being collected. This problem was treated by Smetana;[8] his results are shown in Fig. 4. The actual current collected is obtained by multiplying the random current collected through the physical area of the probe by the factor F, given in Fig. 4.

When S (which is v_f/v_+) is equal to zero the current increases with $(\bar{\eta} + 1)^{\frac{1}{2}}$. As S becomes greater than zero, the current at low values of $\bar{\eta}$ increases; at high values of $\bar{\eta}$, the current is unchanged.

This behavior can be explained as follows. At low $\bar{\eta}$ and large a/r_p, the potential field is so weak that most of the ions that enter the sheath orbit past the probe and leave the sheath without being collected. Under these conditions, the current collected is equal to the random current density times the physical area of the probe. Thus, at low $\bar{\eta}$, when the current is only proportional to the physical area of the probe with $S = 0$, the addition of flow increases the current collected, just as it would in the case of $a/r_p \approx 1$. When values of S are large, $F \approx S$ and $I_+ \approx nev_f A_p$, where A_p is the projected area.

At higher values of $\bar{\eta}$, with $S = 0$, a larger percentage of the ions that enter the sheath are collected by the probe. From simple orbital calculations one finds that for a given potential V and particles entering with initial energy V_o, the radius at which particles will just be collected if $r_a = r_p(1 + V/V_o)^{\frac{1}{2}}$. Therefore, the current that is collected is proportional to the flux entering the sheath out to a radius r_a times the area at that radius:

$$i_+ = [ne(2V_o e/M)^{\frac{1}{2}}] \quad r_p\,[1 + V/V_o]^{\frac{1}{2}}\ L \quad .$$

For S equal to zero, $V_o = (kT_-/e)$ and I_+ is given by the usual electrostatic probe analysis for $a/r_p \gg 1$. In the limit when $\eta \gg 1$ and $a/r_p > \eta^{\frac{1}{2}}$, the current increases with $\eta^{\frac{1}{2}}$. When $S \gg o$, the flux is proportional to $SV_o^{\frac{1}{2}}$ and $r_a = r_p\,(1 + V/S^2V_o)^{\frac{1}{2}}$. Thus the absorption radius is decreased, while the flux entering the sheath increases so that

$$I_+ = [neS(2V_o e/M)^{\frac{1}{2}}]\, r_p \left(1 + \frac{V}{S^2V_o}\right)^{\frac{1}{2}} L.$$

When $\eta \gg S^2$, this reduces to the same value as when $S = 0$.

With this understanding of current collection under flow conditions, Hok's results may be amended to include flow. Using the asymptotic solutions for $S = 0$ and $S \gg 1$, a transformation of the coordinates which will be useful for analyzing probes in flowing as well as non-flowing plasmas may be formulated. Hok's results are shown in Fig. 1 with his coordinates and transformed coordinates.

The abscissa, η, is the ratio of the potential energy of the electric field to the kinetic energy of the electrons. For a flowing plasma, the kinetic energy of the electron, at large values of S, is S^2 times as great as their kinetic energy of random motion. Thus, if η is replaced by η/S^2, the abscissa will measure the same ratio of energies, including that of the flowing plasma. A more correct formulation would be $\eta/(1 + S^2)$, since when $S = 0$, the transformation should reduce to η.

Similarly, the ordinate, I/AJ, is a measure of the ratio of the current collected by the probe to the random flux which enters the physical area at a velocity proportional to the square root of the kinetic energy. But with flow, the flux is increased by a factor S, and therefore the ordinate may be written as $I/(AJ)S$, or, to cover the case of $S = 0$, $I/(1 + S^2)^{\frac{1}{2}}(AJ)$.

If the ordinate and abscissa in Fig. 1 are transformed in this way, a chart for probe operation both with and without flow and for both

large and small sheaths may be obtained. The values obtained in this way agree with Smetana's results quite well. In the experimental section of this paper verification for the case of small sheaths will be presented.

C. Cylindrical Probes in Continuum Flow

When the probe dimension becomes much larger than the mean free path, it is to be expected that a shock will be formed around the probe.[9] No theoretical treatment exists for cylindrical probe operation under such conditions; in this section some of the processes that might be operative will be mentioned.

When a shock forms around a cylindrical probe in a flowing plasma, the probe will be "isolated" from the incident plasma in the sense that it will be sampling conditions behind the secondary shock rather than conditions in the incident plasma. The probe will still measure the flux across the sheath, but the problem will be in relating this flux to the incident quantities.

The gas which goes through the shock will be compressed, so that even if no additional ionization occurs, the electron density will increase from that of the incident flow. The gas velocity will be slowed down and its direction changed. Since the gas temperature will increase, the Mach number behind the shock will be reduced.

The shock detachment distance is essentially a function of probe radius and Mach number, being roughly of the order of a few tenths of the probe radius. If this distance is too short for chemical relaxation to occur, the gas will be in a condition of nonequilibrium. The gas molecules may flow around the probe before their high translational energy can be converted into ionization and dissociation.

Even if the gas does equilibrate, a boundary layer will always form and will almost certainly not be in ionization equilibrium. (The electron density will not equal the value for equilibrium conditions at a given temperature and gas density.) Except for very weak shocks, the

sheath will generally be embedded in the boundary layer, so that it is important to be able to relate the boundary-layer parameters to the incident flow parameters. Recombination in the boundary layer may be important at the very high electron densities formed by the secondary shock.

Adequate handling of this case theoretically would be a formidable undertaking. Our approach has been first to gather data on probe operation under these conditions, and then to see whether there are any applicable scaling relations which enable one to generalize the results. Such scaling relations could also be used by the theoretician as a guide in identifying the dominant processes and simplifying his analysis. The results of such an experimental program will be presented in Sec. III.

D. Narrow Wedge Probes

Use of a wedge structure is of interest because the wedge offers the possibility of providing minimal disturbance of the flow field near the probe while maintaining adequate mechanical strength. To avoid disturbing the flow, cylindrical probes must have radii that are small compared to the mean free path, and thus they are mechanically poor. With a wedge, it may be possible to maintain the flow undisturbed simply by the geometry of the structure, and since the base of such a wedge would be much larger than a free-molecular cylinder, the wedge would be much stronger.

Recent theoretical investigations of the flow field about slender cones under reentry conditions have indicated that these bodies produce electrons only in the boundary layer surrounding the body.[10,11] Furthermore, the values of the electron densities in the boundary layer are quite low compared to the electron densities produced by blunt-nosed bodies at the same altitude and velocity as the cones. On slender cones the boundary-layer electrons are produced only after the gas has moved many feet down the body.

Applying these ideas to probes, a two-dimensional wedge was constructed in order to determine whether the shock structure produced by such a body would minimize the change of the incident flow parameters. There are two ways in which such a wedge could be used to advantage. First, if the leading edge of the wedge were made sufficiently sharp so that it was free-molecular, this edge could be electrically isolated from the rest of the wedge and used as a free-molecular electrode. The changes in electron density due to the shock formed around the wedge would not affect the plasma at the electrode, because in supersonic flow, changes produced downstream from a point cannot propagate upstream and alter the gas properties at the upstream point. Thus, changes produced by the shock structure downstream of a leading edge of the wedge could not reach the leading edge. An example of such a probe is a small wire used as the leading edge of a wedge made of dielectric. The wire serves as the electrode, and the rest of the wedge is a mechanical support.

Alternatively, the entire wedge could be used as an electrode. In this case, the shock structure produced by the wedge would be sufficiently weak and the flow times sufficiently short that the incident plasma would not be appreciably changed in the vicinity of the probe.

In order to interpret the current collected by a narrow wedge, a free-molecular theory derived for a flat plate inclined at an angle to the flow has been used. The results are shown in Fig. 5.[7] This figure shows a velocity factor which must be used to multiply the thermal flux in order to give the net current

$$I = \left(\frac{n_+ e v_+}{4}\right) \times (\text{velocity factor}) \times (\text{area})$$

Note in Fig. 5 that the velocity factor tends to 1 as the angle between the flow velocity and the normal to the plate increases. Under these conditions, the flow velocity becomes less important, because the area projected into the flow tends toward zero as θ goes to 90 degrees. When this occurs, the current collected is attributable only to the thermal motion of the electrons.

A narrow wedge at zero-degree angle of attack can be considered as two flat plates inclined at opposite angles to the flow. Thus, the current to the wedge can be interpreted using Hoegy's and Brace's theory. Of course, their theory is for free-molecular conditions, whereas the interest here is in continuum flow conditions. However, if the wedge does not disturb the flow, the free-molecular theory may be applicable even under continuum conditions. The results of measurements with a narrow wedge of about 40 mean free paths at the base is presented in Sec. III-B, "Experimental Results".

E. Ion Collection by Flush Probes in Nonuniform Plasmas

In order to avoid perturbations of the flowing plasma surrounding a reentry vehicle, it may be necessary to place probes on the surface of the vehicle rather than in the flow field. Since the electron density varies as a function of distance from the vehicle surface, the question arises as to what current the probe will measure.

Ordinarily, a probe samples the plasma at the edge of the sheath. For the classical case, where the mean free path is much larger than the sheath radius, the density without the probe present cannot change significantly in a sheath thickness. However, in the immediate vicinity of the vehicle surface, the electron density may be so low that the sheath extends out many mean free paths to a point where the electron density has increased significantly. Under these conditions, there will be many collisions in the sheath. The following is a first attempt at a one-dimensional theory to handle this case.

A planar geometry is assumed, with the probe sufficiently large that the physical and sheath areas are approximately equal; most of the current drifts into the sheath from a place d_s centimeters from the surface. Assuming that there is neither recombination nor ionization in the sheath, an equation for the current may be written as:

$$I = An_{+s}ev_{+}/4 \qquad (1)$$

where

n_{+s} = ion density at the sheath edge

v_+ = thermal velocity at the sheath edge.

If these assumptions are correct, a measurement of the ion current coupled with a knowledge (either theoretical or from another measurement) of the thermal velocity at the sheath edge is sufficient to determine the ion density at the sheath edge. In order to establish the location of the sheath edge, it is assumed that the charge density redistributes itself within the sheath in such a manner that the current flowing across the sheath to the electrode is governed by the same relationships as for a space-charge-limited diode at high pressures.[12] This relationship is given by

$$I = (9/8)\varepsilon_o \mu_+ \left(V^2/d_s^3\right) A \qquad (2)$$

where

μ_+ = ion mobility

V = potential across the sheath

d_s = distance from the wall to the sheath edge

A = area of the electrode

Equation (2) may be solved for d_s in terms of the experimental parameters, I, V, and μ_+. Equation (2) is for a constant mobility through the diode. For a sheath formed near the vehicle surface, the mobility will vary through the sheath, decreasing toward the surface by a factor that is generally less than three. The diode equations have been solved with a mobility decreasing exponentially from the cathode. It is found that for a decrease in mobility of a factor of three, the solution has the same form as Eq. (1) with μ_+ equal to the mobility at the sheath edge, but with the constant reduced to about three quarters of value shown above. Considering the order of the other approximations, Eq. (1) will be used as it stands, with μ_+ equal to the mobility at the sheath edge.

If these assumptions are valid, the measurement of current to an electrode flush with the vehicle surface will enable one to determine the ion flux at a distance d_s from the surface. It is interesting to note from Eq. (2) that the sheath edge may be moved by varying the probe potential, so that there is the possibility of measuring the electron density profile near the wall. The distance d_s will be a function of the plasma parameters as well as the potential. For reasonable potentials, d_s will be of the order of 0.025 mm (1 mil) for electron densities around 10^{13} electron/cc, and will increase to about a centimeter for densities around 10^7 electron/cc. Thus, the degree to which the boundary layer near the vehicle can be sampled by a flush probe will depend strongly upon the density levels involved.

Preliminary results using this theory to interpret data taken in a shock tube are discussed in Sec. III.

III ELECTROSTATIC PROBE MEASUREMENTS

A. Introduction

In order to check the theory of probe operation in supersonic ionized flows under free-molecular conditions and to gather data for construction of a theory under continuum flow conditions, measurements were made in a pressure-driven shock tube. The characteristics of the shock tube are described in the Reference 13.

A set of three cylindrical probes was used for the measurements. The probe dimensions were 0.01 inch (diameter) x 1/4 inch (length); 1/16 x 5/8 inch; and 1/4 x 2-1/2 inch. Each probe was at least twenty times longer than its radius so that end effects would be negligible.

Measurements were made at two initial shock-tube pressures, $p_1 = 1$ mmHg and $p_1 = 0.1$ mmHg. Shock velocities ranged from about 3 to 5 mm/μsec at the high pressure, and from 4 to 7 mm/μsec at the

lower pressure. The ratio of shock velocity to v_+, behind the shock, varied from about 2.3 to 3.7 over this range of pressures and shock velocities. The electron density varied from 10^{10} to 10^{14} elec/cc and the gas temperature from 2500 to 6000° K.

The probe sizes, in units of neutral-neutral mean free paths behind the incident shock, are shown in Table 1. For strict free-molecular flow the probe radius should be smaller than the incident mean free path. This was not the case for any of the above conditions, but, as will be discussed later, the 0.01- x 1/4-inch probe at p_1 = 0.1 mmHg operated as though it were in the free molecular regime. There is no sharply defined value of r_p/λ above which the flow can be considered a continuum, but from the work of Probstein a ratio of about r_p/λ = 30

Table I

EXPERIMENTAL PROBE SIZES

p_1 = 0.1 mmHg

v (mm/μsec)	Mean Free Path λ_2 (mils)	r_p/λ_2		
		r_p = 5 mils	r_p = 31 mils	r_p = 125 mils
4	2.0	2.5	15	62
5	1.95	2.7	17	68
6	1.57	3.2	20	80
7	1.38	3.6	22	91

p_1 = 1 mmHg

v (mm/μsec)	Mean Free Path λ_2(mils)	r_p/λ_2		
		r_p = 5 mils	r_p = 31 mils	r_p = 125 mils
4	0.213	23	146	590
5	0.198	25	157	630
6	0.165	30	190	760
7	0.135	37	230	925

seems sufficient for transition well into the continuum regime. If this is true, then only the 1/4-inch diameter probe at 0.1 mmHg and the 1/16- and 1/4-inch probes at 1 mmHg were in continuum flow. Certain scaling relations that were discovered upon analyzing the data reinforce the idea that these probes were operating in a similar flow regime.

Tests were made with a 33 Gc microwave interferometer to determine whether the electron density in the slug behind the shock front was the equilibrium value. The results showed that equilibrium electron densities were obtained at 1 mmHg even after the tube was fired 40 times without cleaning. Since the electron density is such a sensitive function of gas temperature and impurity level, it was concluded that if the electron density was the equilibrium value, it was likely that the other gas properties were also in equilibrium. At 0.1 mmHg the electron density was below equilibrium by as much as an order of magnitude at electron densities below about 10^{12} elec/cc if the tube was not properly cleaned. However, it took several shots before the deviation from equilibrium became significant, therefore cleaning after every shot was not required.

Measurements were made with a fixed bias voltage of -15 volts, applied to the cylindrical probe with respect to the shock tube wall. This value was judged sufficiently negative to ensure operation in the ion saturation portion of the current-voltage characteristic. This region of operation has been found to be the most reliable for measurements of electron density in a variety of laboratory plasmas (electromagnetic shock tubes, flames, and dc and RF discharges). The electron saturation current has often been found to give erroneously low readings, depending on the type of plasma.

The tests were made with many probes at a single station. In order to be certain that there was no coupling or interference between the probes, all of which had a common ground in the shock-tube wall, tests were run both with a single probe and with many probes at the same station. There was no discernible difference between the two conditions.

B. Experimental Results

1. Cylindrical Probes

A typical probe response is shown in the upper trace of Fig. 6. When the shock arrives there is an abrupt rise in current to a level that stays approximately constant until the contact surface arrives, at which time the current rises sharply and becomes rather erratic. No attempt was made to study the rise in electron density with time across the shock front, although at the lower shock speeds the ionization rise time could be measured. Probes would be an excellent tool for such a study, and would enable information on rate constants to be determined.

The results from the measurements have been reduced to a value of electron density by assuming that the measured current is attributable to collection of the incident flux by the projected area of the probe. This is the case when $a/r_p \approx 1$ and the flow is free-molecular. The relation between electron density and current that was used is:

$$n_+ = \frac{I_+}{e\, v_f\, d\, L}$$

where I_+ is the measured current and v_f is the shock velocity.

The flow behind the incident shock is less than the shock velocity by a factor of less than 10 percent and varies slowly with shock strength. For ease of data reduction the shock speed rather than the actual flow speed behind the shock has been used.

Over most of the range of electron density the sheath was no larger than the probe radius, but for $p_1 = 1$ mmHg the flow was not free-molecular. We therefore did not expect the current to reach the probe with velocity v_f, but with a somewhat slower velocity, corresponding to the temperature of the electrons behind the shock formed around the probe. However, we have calculated a value of n_+ from the above equation and reduced all of the data in this way simply to have a uniform basis for comparison and some idea of the electron densities measured at the sheath edge. If,

in fact, the proper velocity is some fraction of v_f, this should only change the results by a scale factor. If the current is attributable to thermal energy, and so drifts into the probe around the entire circumference rather than only the portion facing the flow, there is a correction of only $\pi/4$.

a. Results at 1 mmHg

The 1-mmHg results are plotted in Fig. 7 in the form of the ratio of the inferred value of n_+ to n_{eq} (the equilibrium value) as a function of n_{eq}. The equilibrium value is determined from the measured value of the shock velocity. Although there is some scatter of points, especially for the 0.01 x 1/4-inch probe at the lower electron densities, a clear pattern is discernible in the data.

None of the probes yield a horizontal line, which would indicate a linear relation between n_+ and n_{eq}. All of them are approximately straight lines on log-log paper, with a value which decreases with increasing values of n_{eq}. This relation may be expressed approximately by $n_+/n_{eq}^{-2/3}$, which means that the value of n_+ increases only with $n_{eq}^{1/3}$. In other words, the probe is much less sensitive to the incident electron density than when it is free-molecular.

The value of the ratio is both greater and smaller than unity, although too much significance should not be attached to this fact. If the particles are being collected at a much slower velocity than v_f, then the inferred values of n_+, and hence the ratio n_+/n_{eq}, would be higher.

It is clear from these results that the cylindrical probes for high r_p/λ_2 are disturbing the flow and not simply sampling the incident flow. The error in assuming that the probe operated as if it were free-molecular is as large as plus and minus one order of magnitude over the range of the measurements.

b. Results at 0.1 mmHg

Measurements were made at a pressure of 0.1 mmHg with the

same set of cylindrical probes used for the measurements at 1 mmHg. Measurements at 0.1 mmHg pressure with a 0.01- x 1/4-inch probe checked within about 20% with the results from a 33-Gc microwave interferometer over the electron density range of 4×10^{11} to 4×10^{12} elec/cc. Since cleaning the tube required so much time, it was decided to use the 0.01- x 1/4-inch probe, which had been checked against microwave measurements, as an indicator of the actual electron density level and as a standard for comparison with the other probes. The tube would then be fired even when it was so dirty that the electron density was other than the equilibrium value. The results of this series of measurements are shown in Fig. 8.

In this figure the ratio of n_+ has been plotted as inferred above, to $n_{0.01}$, the electron density indicated on the 10-mil probe, as a function of the value of $n_{0.01}$. At the lowest value of electron density a sheath correction was necessary for the 0.01 probe, a correction which amounted to a factor of less than three. For the 10-mil probe, which was free-molecular, the curves of Fig. 2 were used with the modifications to account for flow velocity discussed in Sec. II-B.

Both similarities and differences between the 1-mmHg and the 0.1-mmHg data may be noted. At both pressures, the 1/16- and 1/4-inch diameter probes disturbed the incident plasma, as evidenced by the fact that the ratio of n_+/n_{eq} is not constant with n_{eq}. The ratio at both pressures decreases with increasing values of free-stream electron density, however, at 0.1 mmHg, the 1/16- and 1/4-inch data were not parallel, as was the case at 1 mmHg, and furthermore, the slope for the 1/16-inch probe is less than at 1 mmHg. These similarities and differences will be discussed more fully in Sec. IV.

2. Narrow Wedge Probe

Measurements were made at a pressure of 0.1 mmHg with a 10-degree half-angle wedge mounted at zero-degree angle of attack. The wedge dimensions

are shown in Fig. 9. The data for the wedge were interpreted using the theory indicated in Sec. II-D. At the lowest electron densities, the sheath was large enough for a modest correction to account for the increased area of current collection.

The data indicate that the plasma flowing over the leading 1/8 inch edge is not significantly different from the incident flow. These data agree with the 0.01 inch probe data within a factor of two over the entire range of electron densities. This indicates that such a probe may be a feasible solution to the problem of constructing a probe that is mechanically strong but that does not disturb the flow. The next logical step is to make measurements with this probe at higher pressures and for other than zero-degree angle of attack.

3. Flush Probes

In order to check the theory of flush probe operation in non-uniform plasmas measurements were made by inserting a flat plate with a flush electrode into the center of a shock tube. The configuration is shown in Fig. 10. The electrode consists of a platinum plate 6.3 x 3.2 mm inserted into a dielectric insulator which is flush with the plate surface. At the same time measurements were made with a series of 1 mil diameter wire probes that were mounted at various distances from the plate. For the conditions of this experiment these probes operate as free molecular probes. The wire probes thus enabled us to determine the variation of electron density through the boundary layer. The theory given in Section II-E was used to determine the electron density and location of the sheath edge for the flush probes. In this way the wire probe data could be used to check the flush probe theory.

The results for several runs at an electron density of about 10^{10} elec/cc and about 10^{12} elec/cc are shown in Fig. 11. The agreement between the wire probes and the flush probes interpreted according to Section II-E is better than 30%. Note that at the lower electron density

the flush probe is reading about 63% of free stream. Even at the higher electron density the flush probe was sampling the plasma at a level which was within an order of magnitude of free stream. This result has been obtained for electron densities as high as 10^{14} elec/cc. This is in large part due to the fact that the sheath grows out a considerable distance through the boundary layer and thus is sensitive to electron densities many mean free paths away from the probe surface. Experiments are currently in progress to study the effect of varying the probe potential in moving the sheath location and hence to vary the region which the probe samples.

Measurements of the current density measured by the flush probe as a function of free stream ion density are shown in Fig. 12 for a range of ion densities from about 10^{9} to 10^{14} elec/cc. At the lower densities the current density increases linearly with free stream density. Under these conditions the sheath extends out to a region where the ion density is approximately free stream density so that the measured current densities are equal to the free stream current densities. At densities above about 10^{12} elec/cc the current density increases more slowly than linearly with free stream ion density. This may be due to recombination effects beginning to take effect as the electrons diffuse through the boundary layer. Some plausibility is given to this hypothesis by the other curve on the figure. It gives the calculated current density based upon a zeroth order theory for the distribution of electrons through the boundary layer assuming frozen flow. It agrees quite well with the measured results at low electron densities where the frozen flow assumption would be correct. At the higher electron densities recombination is more likely to occur, and the measured results deviate from the theoretical solution assuming frozen flow. The effects of recombination on the boundary layer profile is currently being studied.

IV SCALING RELATIONS

The measured data presented in the previous section display some striking characteristics. The data at 1 mmHg show that each probe collected current at a rate proportional to $n_{eq}^{1/3}$. Furthermore, the ratio of the proportionality constants for the 1/16- and 1/4-inch probes (the two probes that are clearly in continuum flow at this pressure) is in inverse proportion to the probe radii. That is, at a given shock velocity and initial pressure, the 1/16-inch probe collected four times more current than the 1/4-inch probe. This suggests some sort of scaling that depends upon the product $n_+ r_p$, since this product is constant for the probes considered so far.

In order to investigate the effect of pressure on this scaling relation, we calculated the product $n_+ r_p$ obtained from the measured data at 0.1 mmHg for the 1/4-inch probe (the only probe clearly in the continuum flow regime). In Fig. 13 the results for the data at the two pressures are plotted. In order to get sufficient overlap in the curves a straight-line extrapolation the 1-mmHg data of Fig. 10 to higher shock velocities was made. This is a reasonable assumption, since the data exhibited straight-line characteristics over three orders of magnitude in electron density.

From the available data it appears that $n_+ r_p$ is approximately constant, not only with probe radius but also with pressure. If this assumption proved to be true over the whole continuum flow regime, it would be a valuable aid in interpreting probe data obtained under this flow condition. The data at present are suggestive, but they are too scanty to permit a high degree of confidence in predictions at other pressures and probe radii. It is therefore very desirable to study continuum probe operation to clarify the scaling relations.

This sort of scaling relation can be accounted for by considering the flow through the stagnation region formed around the probe. Dissociative recombination of the electrons and ions diffusing through the

boundary layer close to the probe is the dominant mechanism in determining the electron density at the sheath edge. A more complete analysis is given in Reference 14.

V CONCLUSIONS

Some conclusions which can be drawn from the work presented in the previous sections are given below. Extensions of the work along several lines are also indicated.

1. The theory of cylindrical electrostatic probes in flowing plasmas outlined in Sec. II-B has been verified for the case in which the sheath thickness is small compared to the probe radius ($a/r_p \approx 1$). Extension of this work to the case in which $a/r_p > 1$, which would correspond to lower electron densities, would be a valuable addition to our understanding of this type of probe operation. The assumption that the sheath shape is not changed by flow will be more critical for $a/r_p > 1$. Also, the effect of collisions in the sheath will be more dominant.

2. The experimental results show that the free-molecular theory for flowing plasmas gives accurate results for probe radii as large as three times the neutral-neutral mean free path of the flowing gas. Significant deviations from free-molecular operation were noted when the ratio of probe radius to mean free path was greater than 20. The transition between $r_p/\lambda_2 = 3$ and $r_p/\lambda_2 = 20$ was not measured. It would be desirable to make measurements which would cover the transition from free-molecular to continuum flow. It is also of interest to know the maximum value of r_p/λ_2 for which free-molecular theory will give results accurate to a specified level.

Such information could be obtained from measurements in the transition region.

3. Cylindrical probes operating in the continuum region (say, $r_p/\lambda_2 > 30$) do not collect current at a rate proportional to the electron density of the incident plasma. The electron density indicated by such probes varied as only the 1/3 power of the incident electron density; that is, $n_{+\ probe} \sim (n_{incident})^{1/3}$. Cylindrical probes are thus much less sensitive instruments for measuring electron densities in a flowing continuum plasma than free molecular probes.

4. For probes operating in continuum flow over the range of pressures and shock velocities that were measured, it appears that the product $n_{+s} r_p$ is a constant with respect to initial pressure and probe radius and is only a function of shock velocity. The value of n_{+s} is that inferred from the relation $I_+ = n_{+s}\ e\ v_f\ 2r_p\ L$. Measurements should be made over a wider range of probe sizes and initial pressures to investigate the apparent constancy of $n_{+s} r_p$ with these parameters. The constancy of $n_{+s} r_p$ may be accounted for by recombination in the boundary layer.

5. A narrow wedge-shaped structure at zero-degree angle of attack, with base dimensions of 30 mean free paths, collected current as a free-molecular probe. Such probes will be useful for measurements on reentry vehicles, since they incorporate mechanical strength with good probe performance. The angle of attack will not, in general, be zero degrees, so that it is necessary that these structures be tested

at other angles of attack. It is to be expected that their performance as probes will deteriorate at large angles of attack, but it is desirable to have a measure of the range of angles of attack over which such probes can work with a specified degree of accuracy. The present measurements were limited to an initial pressure of 0.1 mmHg. Measurements should be performed at higher pressures to verify the capability of such probes to sample the incident plasma accurately.

6. Flush probe measurements indicated that these probes sample the electron density at the sheath edge. Due to nonequilibrium effects in the boundary layer, the electron density at the sheath edge may be much closer to the free-stream values than an equilibrium theory would predict. There is a possibility that the electron density profile near the probe may be measured by varying the probe potential. The distance out from the surface to which this can be effectively done is a function of the free-stream electron density, the distance decreasing as the electron density increases.

7. All the measurements presented in this report were made at a fixed bias of -15 volts. Measurements should be made of the entire current-voltage characteristic to determine the ability of such probes to yield measurements of temperature, as well as to see if the ion current characteristic is behaving as predicted by theory.

8. It has been noted that under certain conditions

probe surfaces may become contaminated and give erroneous measurements unless properly cleaned. It is not clear whether the effect is due to oxidation on the surface or the deposit of some material that was in the plasma. Since probes may be used on reentry vehicles which ablate material into the flow field, it is important to know how such materials would affect probe operation. This area requires a systematic investigation.

REFERENCES

1. I. Langmuir and H. Mott-Smith, "Studies of Electric Discharges at Low Pressures," General Electric Review 27, Nos. 7, 8, 9, pp. 449-455, 538-548, 616-623 (July, August, September 1924).

2. D. Bohm, E.H.S. Burhop, and H.S.W. Massey, "The Use of Probes for Plasma Exploration in Strong Magnetic Fields," in Characteristics of Electrical Discharges in Magnetic Fields, pp. 13-76, Ed. Guthrie and Wakerling (McGraw-Hill Book Company, New York, New York, 1949).

3. G. Schultz and S.C. Brown, "Microwave Study of Positive Ion Collection by Probes," Phys. Rev. 98, No. 6, pp. 1642-1649 (15 June 1955).

4. J.F. Allen, R.L.F. Boyd, and P. Reynolds, "The Collection of Positive Ions by a Probe Immersed in a Plasma," Proc. Phys. Soc. (London) Sec. B 5, p. 70 (1957).

5. G. Hok, et al., "Dynamic Probe Measurements in the Ionosphere," Scientific Report PS-3, University of Michigan Research Institute, Reprinted under Contract AF 19(604)-1843 (November 1958).

6. W. K. Scharfman, "The Use of Langmuir Probes to Determine the Electron Density Surrounding Reentry Vehicles," Final Report, Contract NAS 1-2967, SRI Project 4456, Stanford Research Institute, Menlo Park, California (January 1964).

7. W. R. Hogey and L.H. Brace, "The Dumbbell Electrostatic Ionosphere Probe: Theoretical Aspects," Scientific Report JS-1, ORA Projects 2816-1, 03484, and 03599, Space Physics Research Laboratory, University of Michigan, Ann Arbor, Michigan (September 1961).

8. F.O. Smetana, "On the Current Collected by a Charged Circular Cylinder Immersed in a Two-Dimensional Rarified Plasma Stream," Proc. Third Symposium on Rarified Gas Dynamics, Vol. II, pp. 65-91 (Academic Press, New York, New York, 1963).

9. R. E. Probstein, "Shock Wave and Flow Field Development in Hypersonic Reentry," ARS J., pp. 185-194 (February 1961).

10. A.J. Pallone, J.A. Moore, and J.I. Erdos, "Nonequilibrium, Nonsimilar Solutions of the Laminar Boundary-Layer Equations," AIAA J. 2, No. 10, pp. 1706-1713 (October 1964).

11. F.G. Blottner, "Nonequilibrium Laminar Boundary-Layer Flow of Ionized Air," AIAA J. 2, No. 11, pp. 1921-1927 (November 1964).

12. J. D. Cobine, Gaseous Conductors, pp. 128-129 (Dover Publications, New York, New York, 1958).

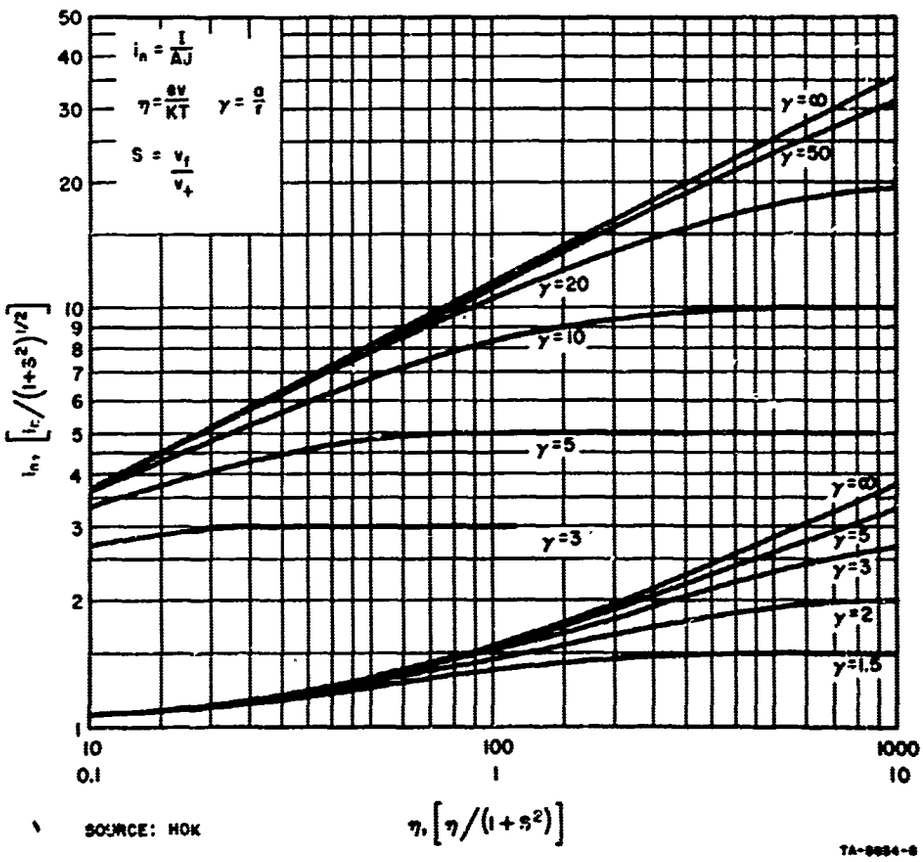
13. H. R. Bredfeldt, et al, "The use of Ion Probes in Reentry Physics," Tech. Report 26, Contract SD-103 under ARPA Order 281-62, Project Code 7400, SRI Project 3857-5, Stanford Research Institute, Menlo Park, California (May 1965).

14. W. E. Scharfman, "The Use of Langmuir Probes to Determine the Electron Density Surrounding Reentry Vehicles," Final Report, Contract NAS1-3942, SRI Project 5034, Stanford Research Institute, Menlo Park, California (June 1965).

ACKNOWLEDGMENT

The measurements were capably performed by J. Granville.

FIG. 1
NORMALIZED PROBE CURRENT AS A FUNCTION OF η, WITH a/r_p AS A PARAMETER



SOURCE: HOK

TA-8654-6

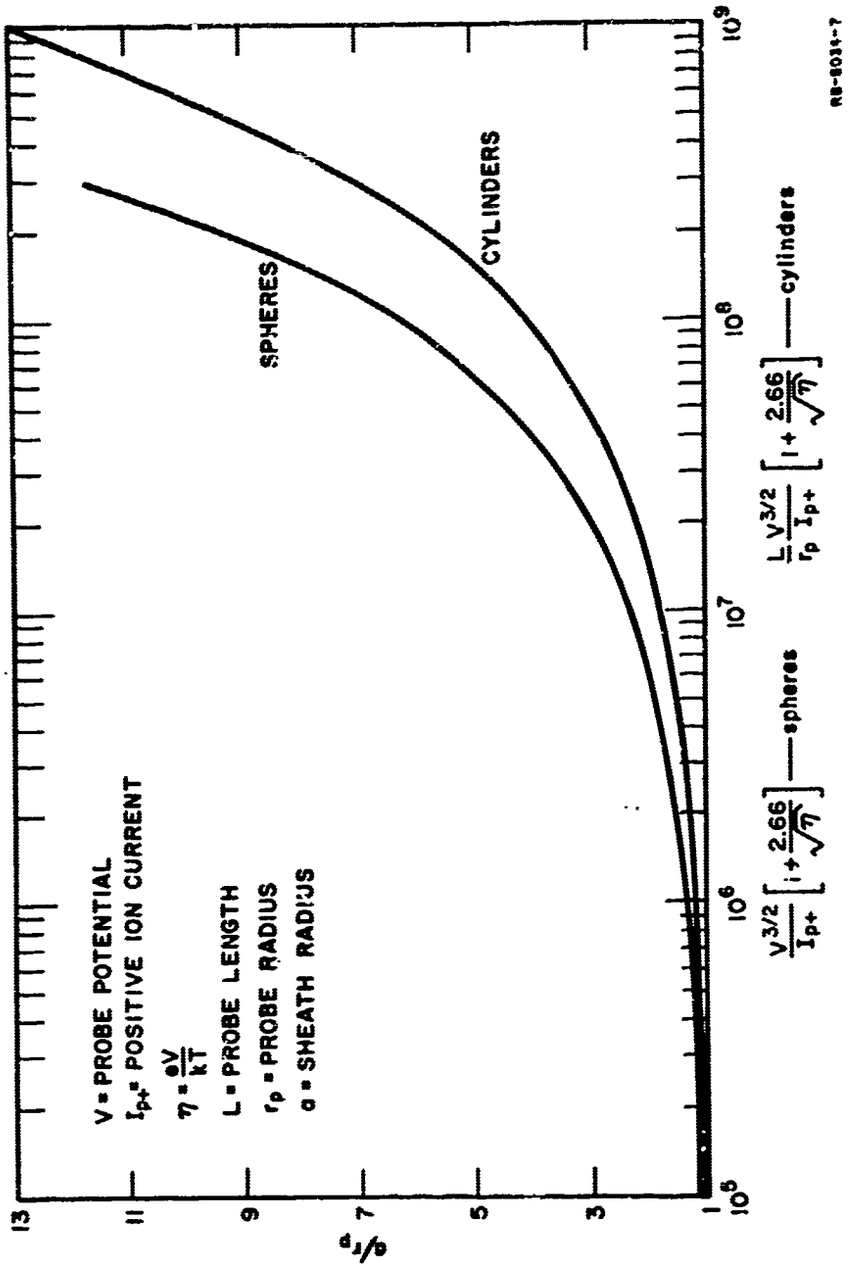


FIG. 2

a/r_p AS A FUNCTION OF THE MEASURED PARAMETERS

FIG. 3
RATIO OF DIRECTED TO RANDOM VELOCITY AS A FUNCTION OF THE NORMALIZED CURRENT COLLECTED BY A PROBE PERPENDICULAR TO THE DIRECTED VELOCITY

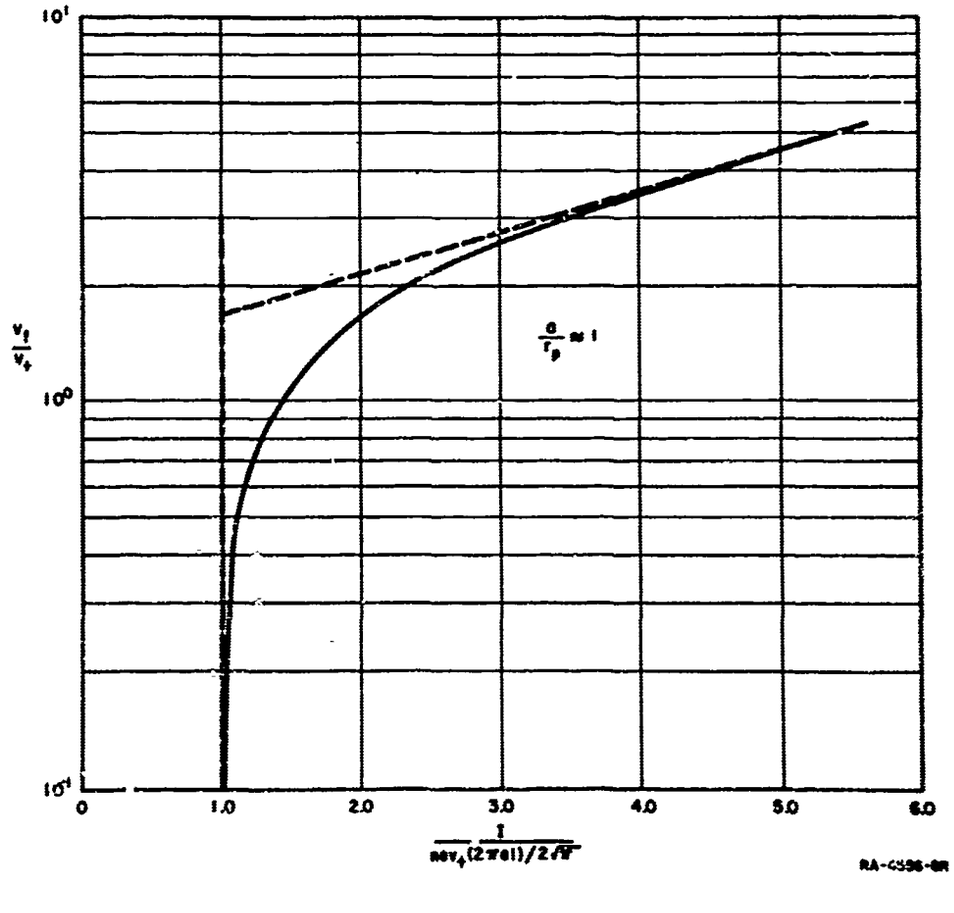


FIG. 4

NONDIMENSIONAL FLUX DENSITY OF ATTRACTED PARTICLES AS A FUNCTION OF DIMENSIONLESS PROBE POTENTIAL FOR VARIOUS SPEED RATIOS, S, AT $a/r_p = 100$

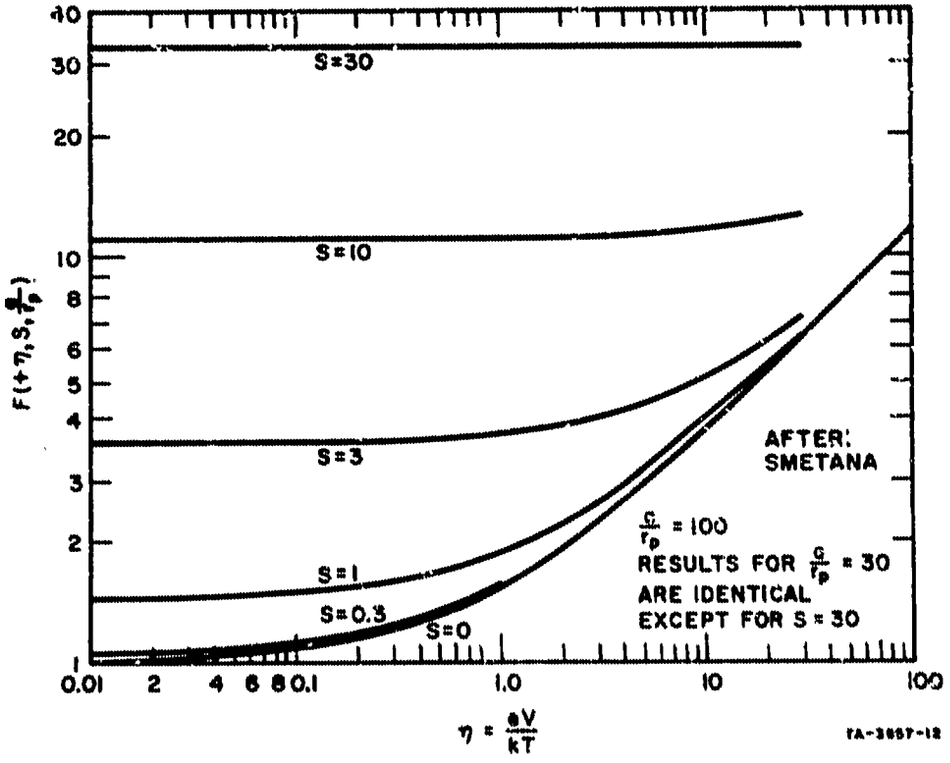
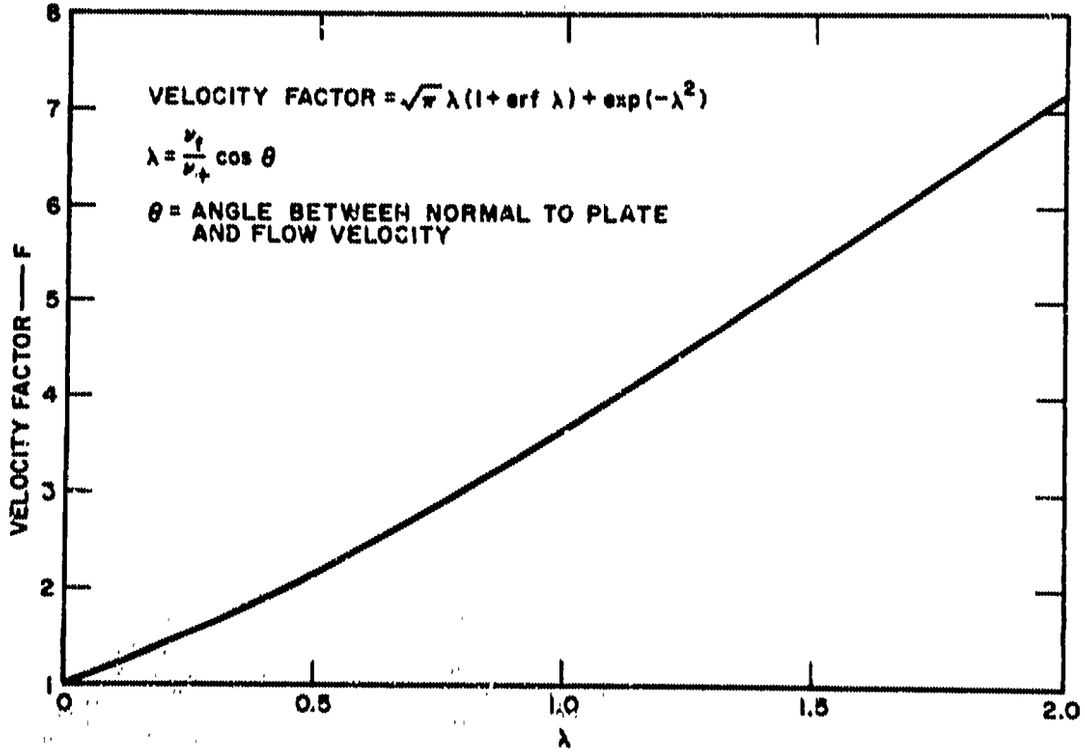


FIG. 5
VELOCITY FACTOR AS A FUNCTION OF VELOCITY PARAMETER FOR FLAT PLATES



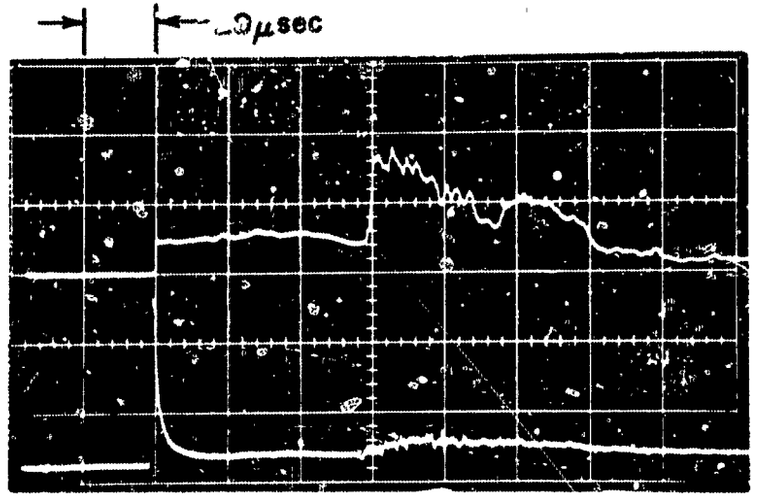
SOURCE: HOSGY & BRACE, U. of Michigan, Scientific Report JS-1, September 1961

TA-8034-2

FIG. 6
TYPICAL FREE-STREAM ION PROBE RESPONSE

UPPER TRACE: FREE-STREAM PROBE
LOWER TRACE: FLUSH PROBE

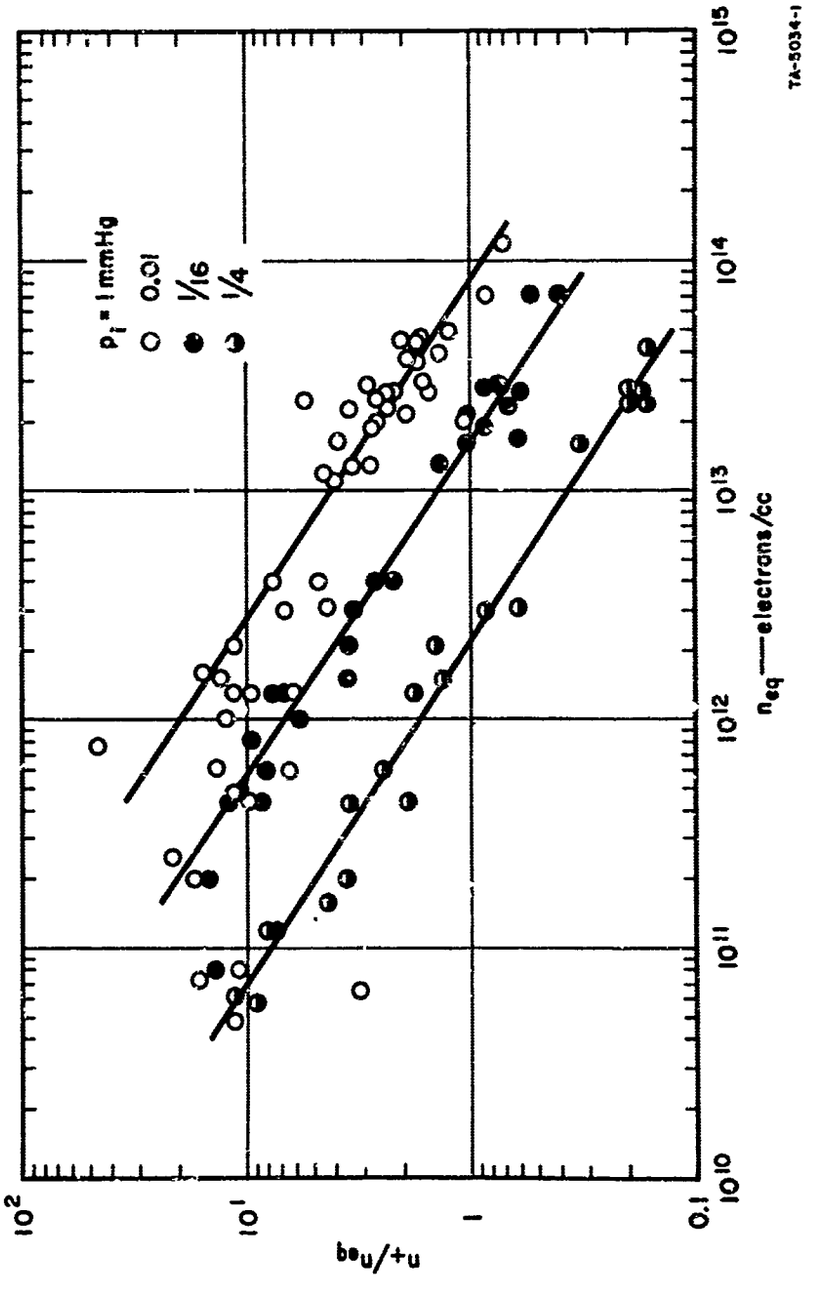
STATION 579
P_1 = 1 mmHg
U_s = 4.25 mm/μsec
$(n_+)_\infty$ = 5 x 10^{12} ions/cc



TA-3857-62

FIG. 7

n_+/n_{eq} AS A FUNCTION OF n_{eq}/p_1 mmHg



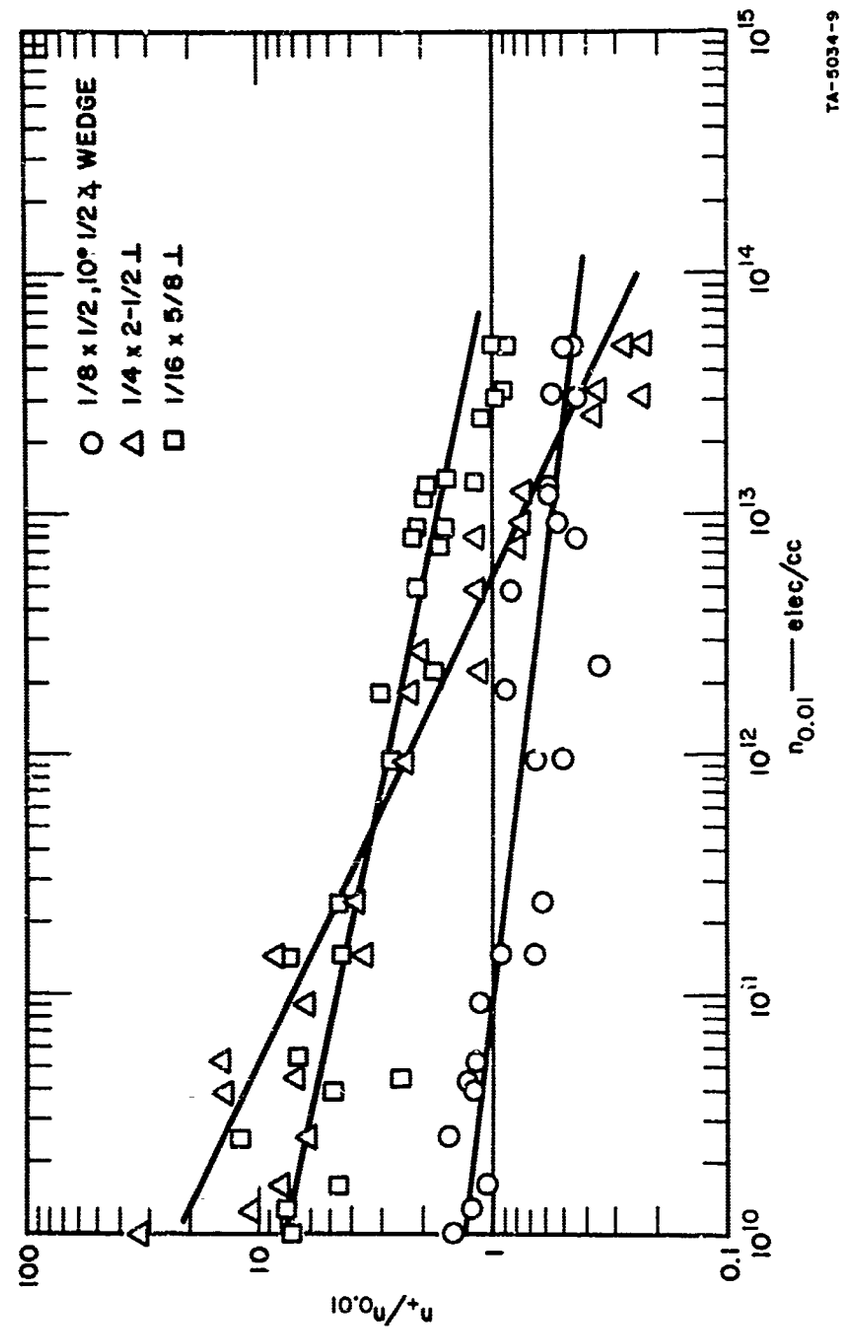
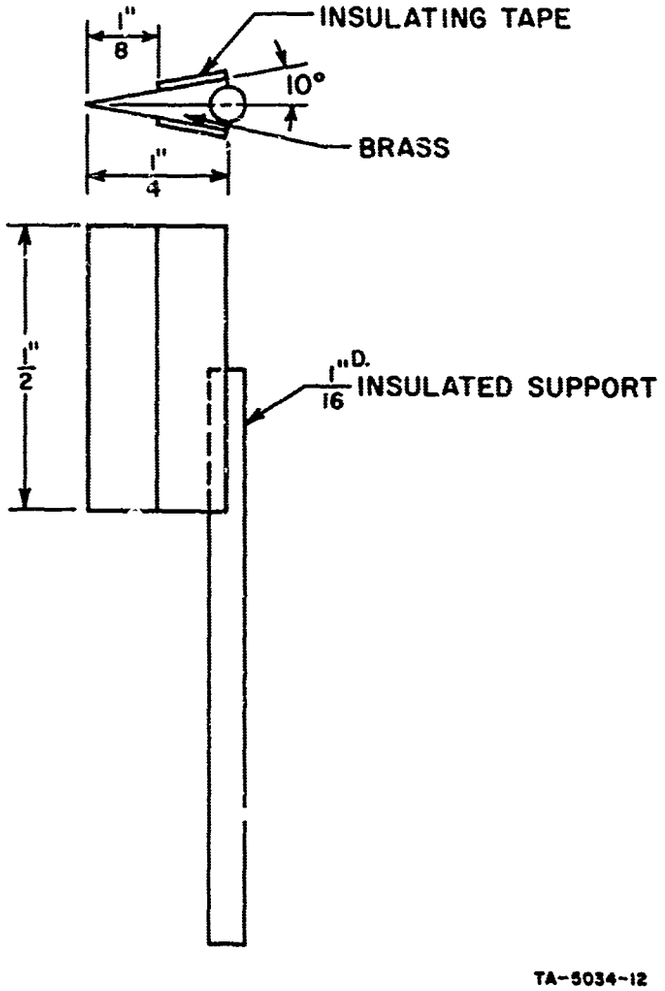


FIG. 8
$n_+/n_{0.01}$ AS A FUNCTION OF $n_{0.01}$, p_I = 0.1 mmHg

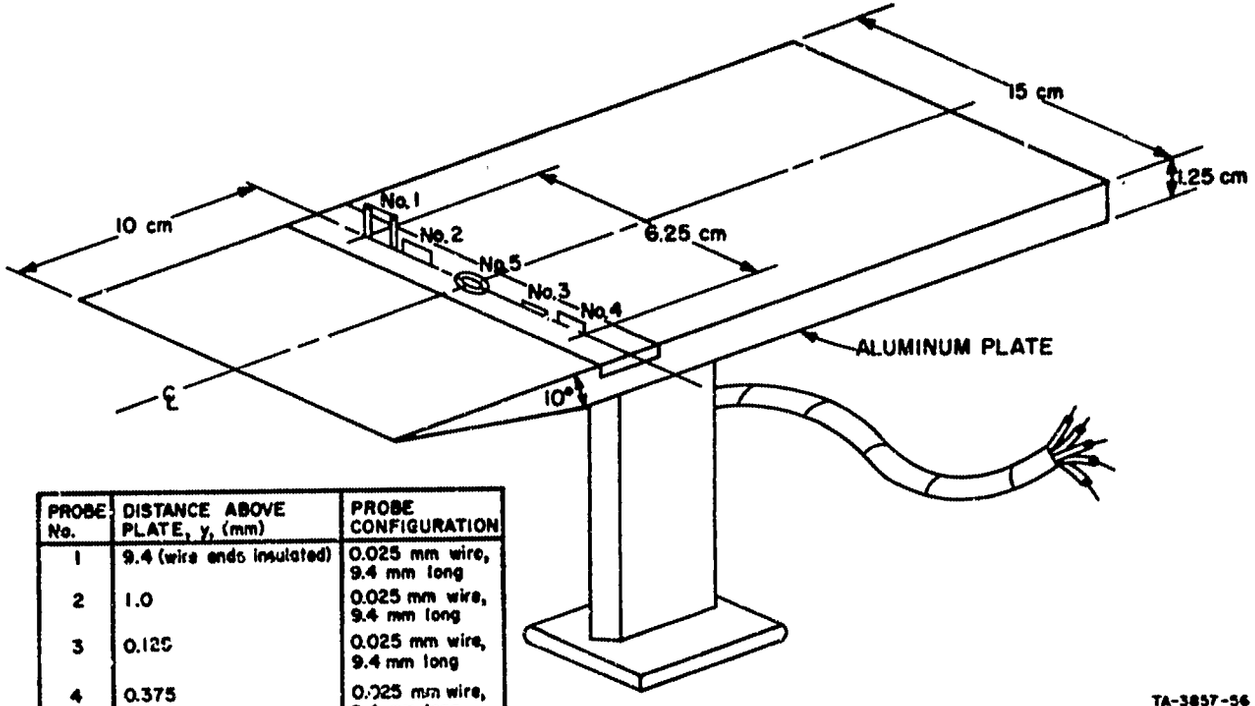
FIG. 9
WEDGE-SHAPED PROBE CONFIGURATION



TA-5034-12

FIG. 10

EXPERIMENTAL ARRANGEMENT OF CYLINDRICAL ION PROBES AND FLUSH PROBES ON A FLAT PLATE TO MEASURE ION DENSITY PROFILE THROUGH THE BOUNDARY LAYER



PROBE No.	DISTANCE ABOVE PLATE, y, (mm)	PROBE CONFIGURATION
1	9.4 (wire ends insulated)	0.025 mm wire, 9.4 mm long
2	1.0	0.025 mm wire, 9.4 mm long
3	0.125	0.025 mm wire, 9.4 mm long
4	0.375	0.025 mm wire, 9.4 mm long
5	FLUSH	6.3 x 3.2 mm

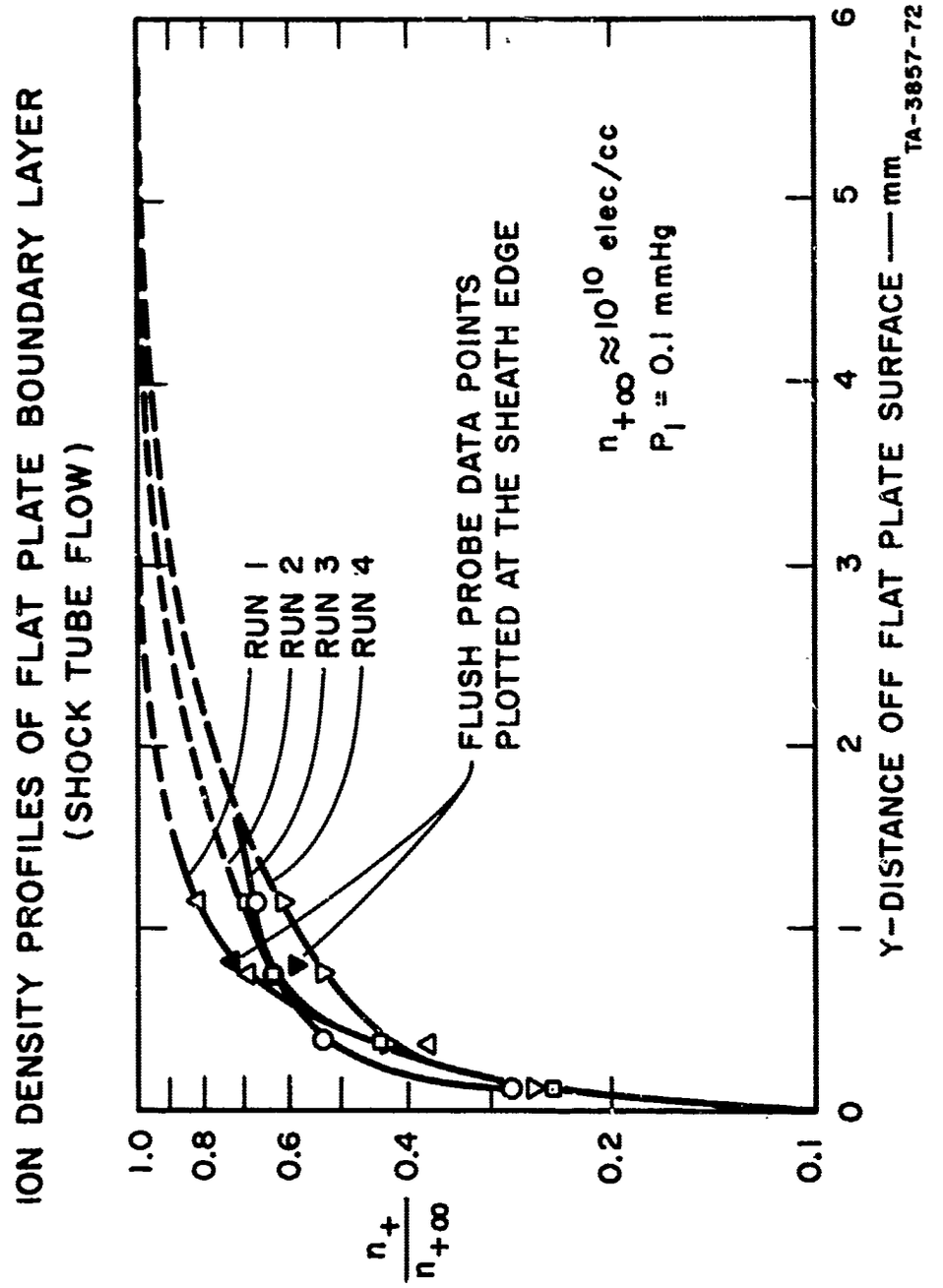


FIG. 11(a)
ION DENSITY PROFILES OF FLAT PLATE BOUNDARY LAYER
(SHOCK TUBE FLOW)

FIG. 11(b)
ION DENSITY PROFILES OF FLAT PLATE BOUNDARY LAYER
(SHOCK TUBE FLOW—FIXED WIRE ARRANGEMENT)

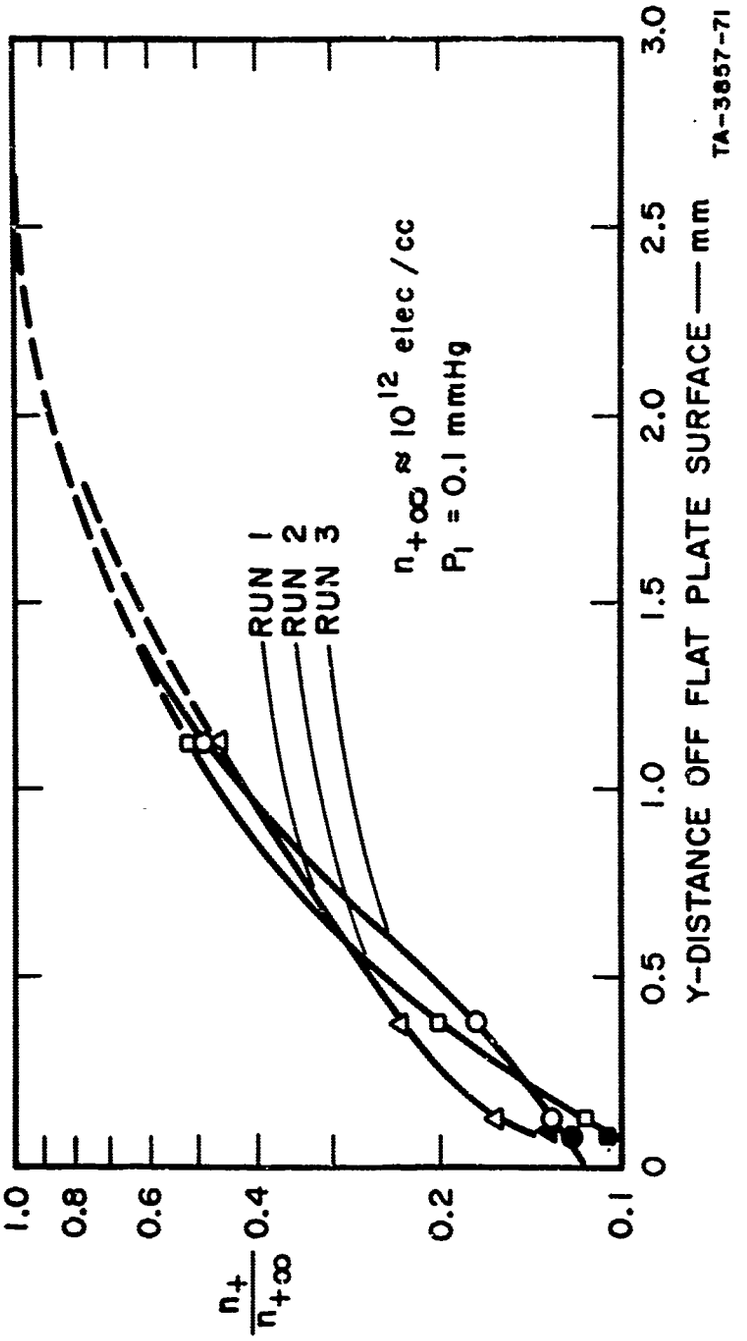


FIG. 12
CURRENT DENSITIES OBTAINED FROM FLUSH PROBE DATA
FREE STREAM MEASURED ION DENSITIES

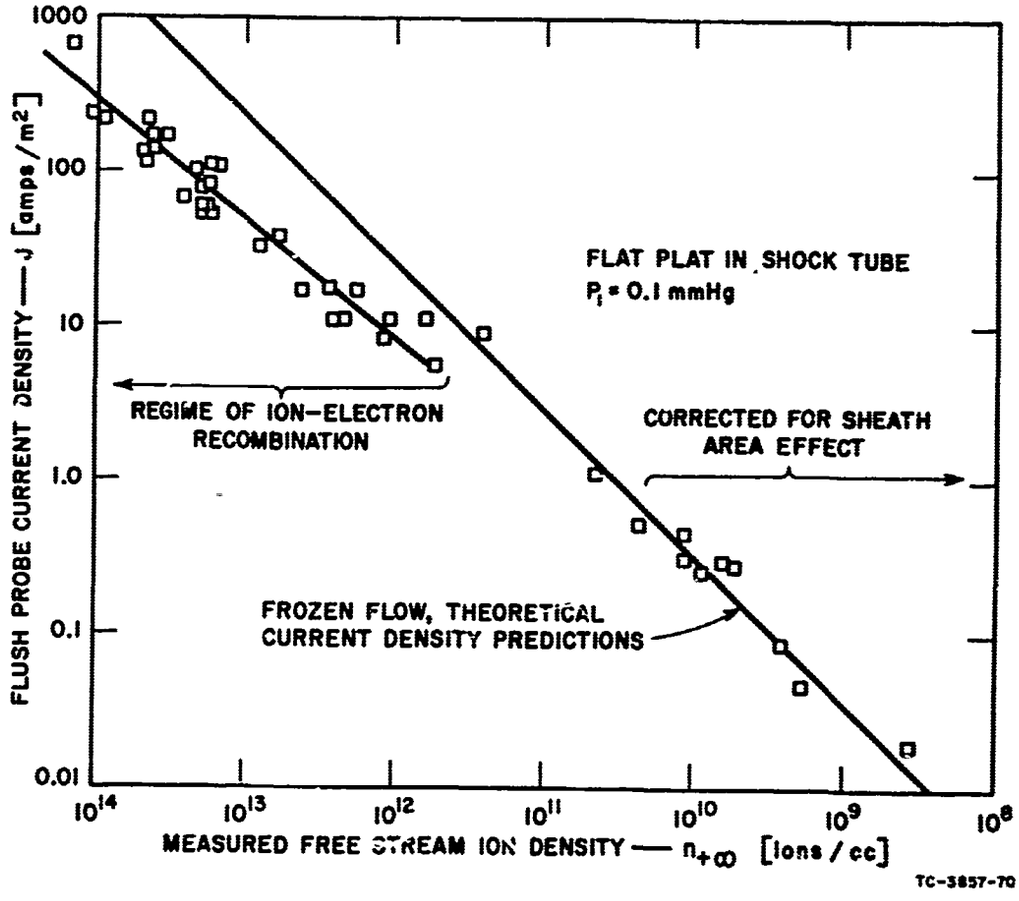


FIG. 13

$n_t r_p$ AS A FUNCTION OF SHOCK VELOCITY FOR CONTINUUM FLOW

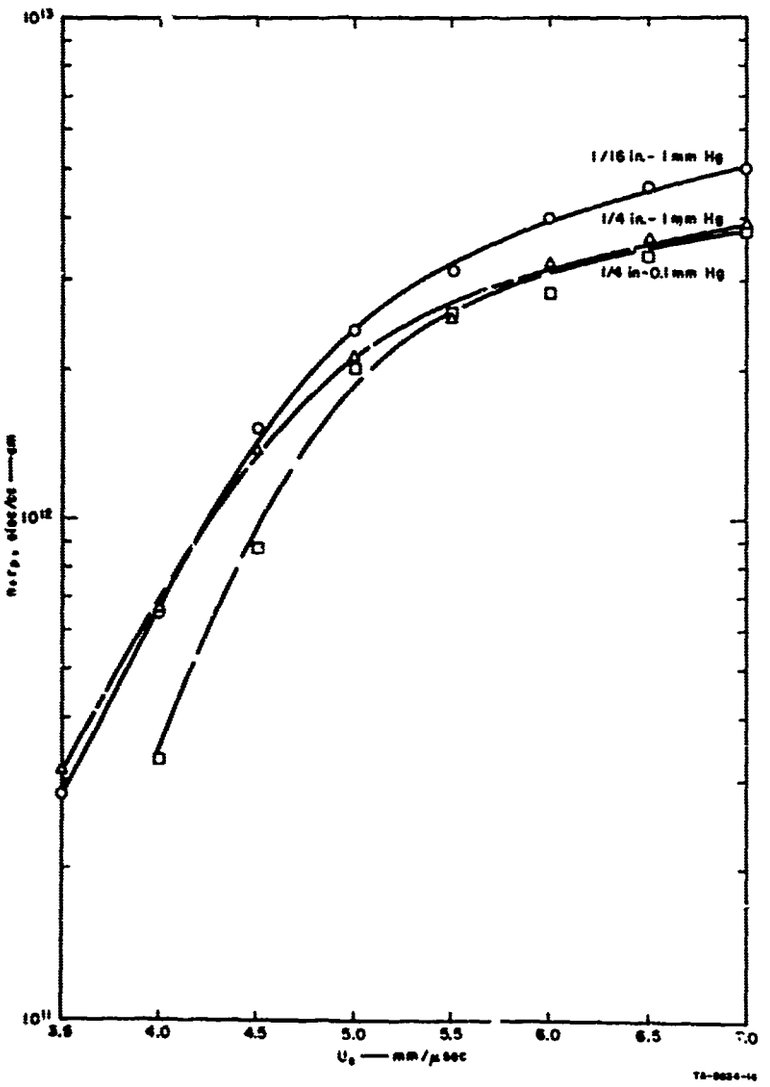
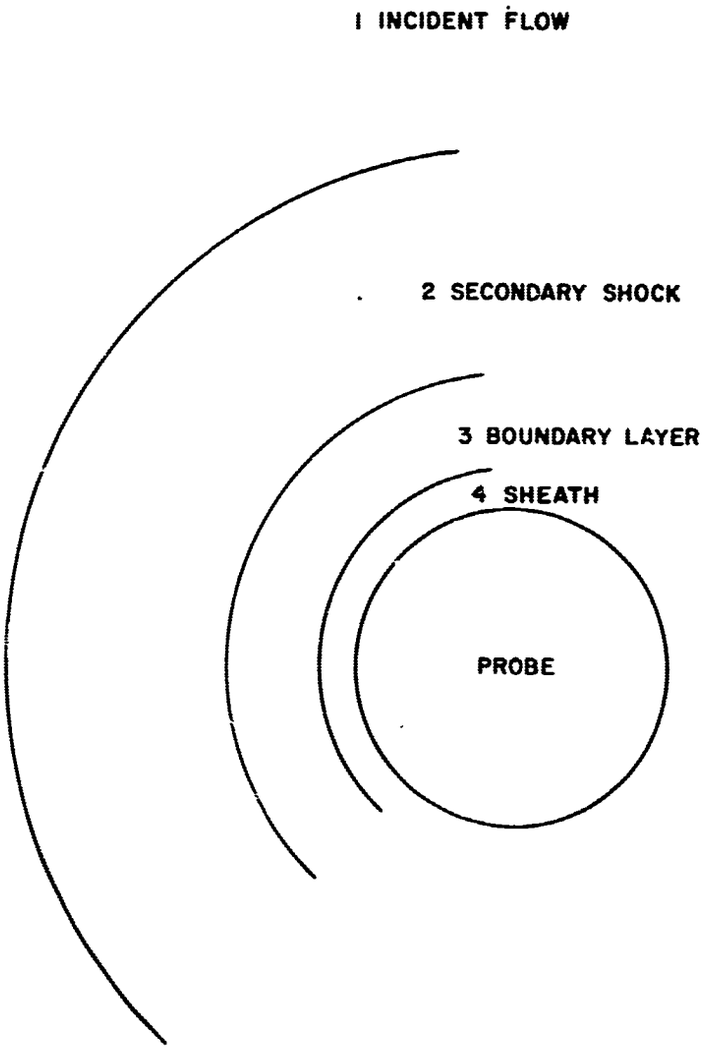


FIG. 14

FLOW FIELD ABOUT A CYLINDRICAL PROBE IN SUPERSONIC CONTINUUM FLOW



V. ANTENNA BREAKDOWN IN A HYPERSONIC RE-ENTRY ENVIRONMENT*

Melvin Epstein
Aerospace Corporation, El Segundo, California

ABSTRACT

An evaluation is presented of the current state of the art for predicting antenna breakdown in a hypersonic re-entry cone boundary layer. It is shown that several significant differences exist between the problems of classical breakdown of cold air and breakdown in a hypersonic re-entry environment. An important consequence of these differences is the reduction of the influence of diffusion and the increased importance of the effects of convection in the high altitude regime. It is also shown that the effects of the re-entry environment on the composition of air require a re-evaluation of the rate coefficients required to predict breakdown. By coupling Maxwell's equations with the breakdown equation, time histories of the growth of electron density in the discharge have been calculated. As a result, it is shown that the definition of breakdown in a re-entry environment requires modification. Such a calculation also allows a prediction of the power transmitted during and after the breakdown process. The results, which indicate that there is a maximum amount of power that can be transmitted regardless of the amount of incident power, are in qualitative agreement with experimental observations.

---

*This work was supported by the U. S. Air Force under Contract No. AF 04(695)-469.

INTRODUCTION

In recent years, a number of applications have arisen for the propagation of strong electromagnetic waves through the plasma sheath surrounding a re-entry vehicle. These applications range from moderate power levels for the purpose of overcoming the blackout and range problems, to very large power levels associated with electronic countermeasure (ECM) systems. In the latter application, one tries to transmit a signal from a re-entering vehicle which is sufficiently intense to mask the radar returns from other re-entering vehicles. In any of these applications, one must anticipate the possibility that the signal may be strong enough to cause electrical breakdown of the air surrounding the re-entry vehicle. In such case, one would like to have answers to the following questions:

1. For a given set of re-entry conditions, what power level (i.e., signal strength) will cause breakdown?
2. How much power is transmitted when the incident power exceeds that required to produce breakdown?

It is the purpose of this paper to review the state of the art of predicting antenna breakdown insofar as it bears on the answers to these questions. An approximate model will be developed which will allow one to discuss, at least in a qualitative way, the manner in which the various properties of the re-entry environment affect the breakdown process.

With respect to the first question, one must make the following observations: Methods for the calculation of electrical breakdown of room temperature

air are fairly well developed. However, under hypersonic re-entry conditions the temperature may become quite high, i.e., on the order of about 1000°K in the shock layer of a slender cone, up to about 5000°K in the boundary layer of a slender cone, and up to about 10,000°K in the shock layer of a blunt re-entry vehicle. As we shall see, the high temperature together with various aerodynamic properties of the flow field can cause substantial changes in the power required for breakdown. Only for the restricted case of the shock layer of the slender cone, wherein the chemical composition is substantially the same as room temperature air, can one expect to use appropriate modifications of the standard breakdown prediction methods with a fair degree of confidence. Such an approach has been followed by Reilly[1] in which he has appropriately modified the classical breakdown calculation to account for convective effects and nonuniform field distributions due to realistic radiation patterns. In this paper, attention will be restricted to consideration of the factors which affect breakdown in the boundary layer of a slender re-entry vehicle. In order to appreciate the effects of such an environment on the breakdown process, a brief description of the classical approach to the prediction of antenna breakdown is given in the next section.

CLASSICAL DESCRIPTION OF BREAKDOWN

It will be sufficient for the present purposes to consider a one-dimensional, parallel plate geometry. The distance between the plates is denoted by δ. In the classical problem, it is assumed that the gas between the plates is stationary and essentially at room temperature. It will be assumed that the electric field is parallel to the walls and oscillates with the signal frequency f. The gas between the walls is essentially un-ionized, but there are always a few free electrons present, primarily because of the passage of occasional cosmic rays. The presence of these few electrons is critical, however, since they are the particles responsible for the initiation of breakdown.

The breakdown process may be described in the following way: The impressed electromagnetic field exerts a force on the free electrons and ions. The electrons, because of their very low mass, are easily accelerated to high speeds. The ions have negligible motion because of their large mass. It can be shown that if electrons never experienced any collisions, their motions would be 90 deg out of phase with the field, and the field does no net work on the electrons. However, if the electrons do collide with other particles (primarily the neutral particles because of their preponderance), this phas relationship is disturbed and, hence, the field does a certain amount of work on the electrons. Thus, if the field is strong enough, it is possible for the average energy of the electrons to greatly exceed the value it would have in the absence of the field. The collisions also randomize the motions of the electrons to a certain extent so that there are always a few electrons in the

high energy tail of the electron energy distribution function. These high energy electrons may, upon collision with a neutral particle, tear loose a bound electron from a neutral particle. The new electron is then free to be acted upon by the field and contributes to the population of electrons in the high energy tail of the distribution function. This increases the probability of further ionizing collisions between electrons and neutral particles. If the field strength is sufficiently high, the rate of production of electrons may become very high.

There are, however, other mechanisms at work which tend to reduce the population of free electrons. The less energetic electrons have a relatively high probability of attaching themselves to neutral particles or recombining with positive ions. In either case they become bound to heavy particles and are not free to respond perceptibly to the field. In addition, electrons may diffuse to the walls where their likelihood of combining with neutral particles is almost ensured. At low electron temperatures, these loss mechanisms predominate over the ionization process and the gas remains essentially un-ionized.

These processes can be described mathematically by writing the continuity equations for the electrons:

$$\frac{dn}{dt} = \nu_i n - \nu_a n + \nabla(D_- \nabla n) \qquad (1)$$

where n is the electron density, t is time, ν_i is the ionization frequency, ν_a is the attachment frequency, and D_- is the electron free diffusion coefficient. For air near room temperature, the attachment loss rate predominates over

the recombination loss rate; hence the latter has been neglected. For the low electron densities that exist in the prebreakdown regime, the appropriate diffusion coefficient is the free diffusion coefficient.

The quantities ν_i, ν_a, and D_- are all functions of the electron energy and therefore of the field strength. The question is then posed: for what field strength does the rate of change of electron density become positive? It can be shown that the spatial variation of electron density corresponds closely to the fundamental diffusion mode, i.e., $n \sim \sin(\pi y/\delta)$. Using this in Eq. (1) and setting $\partial n/\partial t \approx 0$, one finds that the condition for breakdown becomes

$$\nu_i - \nu_a - \frac{D_- \pi^2}{\delta^2} = 0 \qquad (2)$$

If ν_i, ν_a, and D_- are known as functions of field strength, the field strength required to produce breakdown can be determined. It can be shown that these coefficients may be written in the form

$$\nu_i = \alpha \mu_- E_e \quad , \quad \nu_a = \beta \mu_- E_e \quad , \quad D_- = \frac{2}{3} \mu_- \bar{u} \qquad (3)$$

where α and β are ionization and attachment coefficients, respectively, μ_- is the electron mobility, $\bar{u}$ is the average energy of the electrons, and E_e is an effective field strength defined by

$$E_e^2 = \frac{\nu^2 E^2}{\nu^2 + 4\pi^2 f^2} \qquad (4)$$

where ν is the elastic collision frequency for momentum transfer and E is the actual field strength. Substituting these results into Eq. (2) and rearranging, one finds

$$\frac{\alpha}{p} = \frac{\beta}{p} + \frac{2}{3}\pi^2 \frac{\bar{u}}{(E_e/p)(p\delta)^2} \tag{5}$$

where p is the gas pressure.

The problem thus reduces to determining α, β, and $\bar{u}$ as functions of E_e. The theoretical determination of these quantities is an extremely complicated problem and has only been performed successfully for very simple gases such as hydrogen and helium. The results indicate that α/p, β/p, and $\bar{u}$ depend only on the quantity E_e/p and, of course, on the type of gas under consideration. For more complicated gases, these quantities have been determined experimentally. One again finds that α/p, β/p, and $\bar{u}$ are functions of E_e/p.

It turns out that β/p is a relatively weak function of E_e/p. Hence at high pressures, the last term in Eq. (5) is negligible and the field strength required for breakdown is determined by the attachment rate which increases with increasing pressure. Similarly, at low pressures the diffusion losses, characterized by the last term of Eq. (5), dominate. This gives rise to the so-called Paschen curve (Fig. 1) which gives the effective field strength required to initiate breakdown as a function of $p\delta$.

From this discussion, one may conclude that E_e/p is a function of $p\delta$ for a given type of gas. Since ν is directly proportional to the gas pressure,

one sees from Eq. (4) that E/p is a function of E_e/p and f/p. Further, since the power density S is proportional to E^2, one may conclude that the scaling law for classical breakdown is given by

$$\frac{S}{p^2} = f\left(p\delta, \frac{f}{p}\right) \tag{6}$$

It is worth noting here that the classical description of breakdown considers only the field strength required to initiate the breakdown process. It gives no information about the ultimate value of the electron density or the strength of the transmitted signal after the discharge has been established.

With this description of classical breakdown as a background, we are now in a position to discuss the effects of a re-entry environment on the breakdown process.

EFFECT OF RE-ENTRY ENVIRONMENT ON BREAKDOWN

It will now be shown that there are several factors associated with the re-entry environment which significantly affect the breakdown process. The most obvious change is the composition of the gas. Because the composition of the gas changes with both temperature and pressure, the ionization and attachment coefficients are no longer functions of just E_e/p but also of the thermodynamic state of the gas. For example, at room temperature the principal ionization process is due to collisions of energetic electrons with N_2 and O_2 molecules. In a hypersonic cone boundary layer, much of the O_2 is dissociated. There are, in addition, appreciable concentrations of NO which has a significantly lower ionization potential than the other species present. It is possible to estimate the relative importance of NO in the breakdown process by comparing the ionization rate of NO as a function of electron temperature, to the ionization rate of just the N_2 and O_2. Such a comparison is presented in Fig. 2 for a gas temperature of 4000°K. One sees that the contribution of NO to the ionization rate can be very large, depending on how hot the electrons become.

For air at standard conditions, the principal electron loss mechanism is the dissociative attachment to O_2; i.e.,

$$e + O_2 \rightarrow O + O^- \qquad (7)$$

The rate for this process at room temperature is reasonably well established. However, recent theoretical work[2] indicates that at the temperatures occurring

in a re-entry boundary layer, the cross section for this process may be significantly changed because the oxygen is vibrationally excited to an appreciable extent. The result is a substantial increase in the attachment rate with increasing gas temperature (Fig. 3).

The rate of detachment of electrons from the O^- ions is negligible at low temperature. However, for temperatures below 1000°K, there is experimental evidence which indicates that the detachment rate increases markedly with gas temperature. In order to estimate the importance of detachment at re-entry conditions, the detachment cross-section measurements of Muschlitz[3] have been used, together with an assumed Maxwellian distribution for the O^- ions, to calculate the detachment rate. The results indicate that detachment is still negligible at gas temperatures of from 3000° to 5000°K. However, it is known that the O^- ion created in the dissociative attachment process is formed with energy greatly in excess of the average thermal energy of the gas. Hence, the use of a Maxwellian distribution at the gas temperature gives only a lower bound on the detachment rate. Further work is required before a definite conclusion can be made regarding the importance of the detachment process.

A second major effect of the re-entry environment is associated with the presence of a significant degree of ionization generated thermally in the boundary layer. There are two facets to this aspect of the problem: First, if the ambient electron density is such that the corresponding plasma frequency is an appreciable fraction of the signal frequency, then the field strength in the

plasma will be smaller than would exist in free space (the value assumed to exist in the classical breakdown analysis). The appropriate value of field strength to be used can be estimated however by use of the theory that has been developed for the propagation of weak signals through a plasma. On the other hand, we shall see shortly that if one wants to determine the power transmitted during or after breakdown, further modifications are required. The second facet is related to the fact that the presence of appreciable positive ion densities causes the diffusion process to become ambipolar rather than free. One can account for this effect by using the ambipolar diffusion coefficient in place of the free diffusion coefficient. Since ambipolar diffusion is slower than free diffusion by a factor of about forty, the loss of free electrons will be reduced, resulting in a significant reduction in the power required for breakdown at low pressures.

A third major effect of the re-entry environment is associated with the fact that the fluid in the irradiated region is moving at high speed. The classical theory assumes that if the signal is continuous wave, the gas is subjected to the high power long enough for the final electron density to be attained. However, a noninfinitesimal period of time is required for the electrons to be heated and the subsequent ionization to take place. If the sum of the heating and ionization times is long compared to the transit time of the electrons across the aperture, the breakdown process will not be completed. Equation (2) therefore gives a lower bound on the power required for breakdown. Breakdown will occur only if the ionization rate exceeds the loss rate by an amount such that the ionization process is completed by the time the gas

flows across the aperture. This implies that the effect of flow is to increase the power required for breakdown.

The above discussion indicates that the classical approach to the prediction of breakdown must be modified to account for the effects of a re-entry environment. In the next section, a method for evaluating some of these effects are presented. The purpose of this development is not to present a complete theory of breakdown, but merely to indicate the sort of information that is required for the formulation of such a theory and to lend some insight into the parameters that must be scaled in order that free flight conditions can be simulated in the laboratory.

ANALYSIS

We begin with the continuity equation for the electrons. However, the continuity equation of the classical breakdown approach must be modified in the following ways. First, we may consider a steady-state condition in a frame of reference attached to the vehicle surface. Because the gas is flowing, the electrons experience varying conditions as they sweep through the irradiated region. The term d/dt therefore becomes $u(\partial/\partial x)$, where u is the gas velocity parallel to the surface.

Second, because of the high gas temperature and altered composition, additional terms are required to account for the electron production and loss processes. Finally, because of the thinness of the boundary layer, only diffusion perpendicular to the surface need be considered. Thus the continuity equation for the electrons becomes

$$u \frac{\partial n}{\partial x} = \nu_i n - \nu_a n + \frac{\partial}{\partial y}\left(D \frac{\partial n}{\partial y}\right) + \dot{n}_0 + \dot{n}_d - \dot{n}_r \qquad (8)$$

where $\dot{n}_0$ is the ionization rate in the absence of electromagnetic fields, $\dot{n}_d$ is the rate of appearance of electrons due to detachment, and $\dot{n}_r$ is the rate of loss of electrons due to recombination.

It has been pointed out that the magnitudes of the various rate constants depend not only on the pressure and field strength but also on the composition of the gas. Since in the present problem the composition will vary widely, the direct measurement of these rates would require an enormous experimental

program. A more efficient approach to the evaluation of these rates would appear to be as follows.

The dependence of the various rates on field strength is in reality an indirect one. The rates are more directly dependent on the gas density and temperature and on the electron energy. If the cross sections for the various processes were known as functions of the electron energy and the electron energy distribution function were known, the rates could be determined in terms of the state of the unperturbed gas and the electron temperature. This would be a relatively straightforward process if the electron energy distribution function could be assumed to be Maxwellian at the electron temperature T_e. During the initial stage of the breakdown process, this is known not to be an accurate approximation. During the final stage of the breakdown process, the electron density becomes sufficiently high that the electron-electron collisions cause the distribution function to be Maxwellianized at the electron temperature. Although the determination of the electron energy distribution function under these conditions is an extremely difficult problem, it is certainly feasible. Such a calculation has already been done by Carleton and Megill[4] for the slightly simpler case of room temperature air. In the present study, however, it is assumed that the distribution function is always Maxwellian, because then the relative effects of the various properties of the re-entry environment can be assessed. In this way, the various rates can be determined in terms of the properties of the unperturbed gas and the electron temperature. The electron temperature may be determined as a function of the power level by writing an energy balance equation for the electrons.

In order to facilitate this discussion, we make the following further approximations: (a) The electromagnetic energy is uniformly distributed across the aperture. (b) The electromagnetic fields propagate as plane waves in the direction normal to the surface.

The energy balance equation may be written in the form

$$u\frac{\partial}{\partial x}\left(\frac{5}{2}\,nkT_e + \frac{1}{2}\,mnu^2\right) = \frac{\pi f S X Z \mathcal{E}^2}{2c(1+Z^2)} - \sum_j n\nu_{\mathrm{inel}_j} I_{\mathrm{inel}_j} - \sum_j 3\frac{m}{M_j}\,\nu_j k(T_e - T) + \frac{\partial}{\partial y}\left(\lambda\frac{\partial T_e}{\partial y}\right) + \dot{q}_0 \qquad (9)$$

where k is the Boltzmann constant, m is the electron mass, S is the incident power density, X is the square of the ratio of the plasma frequency to the signal frequency, Z is the ratio of collision frequency to signal frequency, $\mathcal{E}$ is the magnitude of the ratio of the local electric field strength to the incident field strength, c is the speed of light, ν_{inel_j} and I_{inel_j} are the collision frequency for inelastic collisions of type j and the energy transferred in each such collision, respectively, M_j is the mass of a neutral particle of species j, λ is the coefficient of electronic thermal conductivity, and $\dot{q}_0$ is the sum of energy transfer terms in the absence of an electromagnetic field (i.e., when $T_e = T$). The left-hand side of this equation represents the rate of change of total enthalpy of the electrons. The terms on the right-hand side represent, respectively, the energy absorbed by the electrons from the field, the energy lost by the electrons due to inelastic impact, the energy lost due to elastic

collisions, the energy transferred by heat conduction, and the rate of change of total enthalpy in the absence of the applied fields.

If the various collision frequencies and transport coefficients can be presumed to be known in terms of the state of the unperturbed gas and the electron temperature, Eqs. (8) and (9) represent two equations in three unknowns: n, T_e, and δ. The system can be made determinate by adding to these equations Maxwell's equations. The resulting system of equations can be solved numerically in the following way: Starting with the unperturbed gas at the upstream edge of the aperture, one may solve Maxwell's equations for the distribution of the electric field in the y direction. Substituting this into the continuity and energy equations, one can determine the distribution of n and T_e a small distance Δx downstream of the upstream edge of the aperture (these steps may be iterated upon to improve accuracy). A new distribution of the electric field is then determined from the resulting n and T_e distributions. This is used to determine new n and T_e distributions a short distance further downstream, etc.

Although these equations appear to be very formidable, they may be considerably simplified for many ranges of interest by estimating the characteristic times for the various processes. Just as in the classical breakdown case where a reasonable approximation to the Paschen curve can be estimated by considering separately the diffusion-controlled and attachment-controlled cases, similar simplifications can be achieved in the present formulation. In the present case, one can consider attachment-controlled, diffusion-controlled, convection-controlled, and recombination-controlled regimes. Further, from

a consideration of the aerodynamics of the re-entry boundary layer, one can conclude that in fact for most situations a diffusion-controlled regime does not exist. This can be shown by comparing the characteristic times for diffusion and convection. If L and δ are the aperture width and boundary layer thickness, respectively, the characteristic times for convection and diffusion are

$$\tau_{conv} = \frac{L}{u} \quad , \quad \tau_{dif} = \frac{\delta^2}{D} \tag{10}$$

In the hypersonic re-entry boundary layer, the electron density is large enough that the diffusion is ambipolar. Simple kinetic theory considerations show that if the gas and electron temperatures are T and T_e, respectively, then the ambipolar diffusion coefficient is $D = D_0(T_e/T)$, where D_0 is the ambipolar diffusion coefficient when $T_e = T$. Further, since the Reynolds number Re based on viscosity is approximately equal to the Reynolds number for diffusion, and the thickness of the boundary layer is given approximately $\delta/x = 5/\sqrt{Re}$, where x is the distance from the nose of the body, one finds

$$\frac{\tau_{conv}}{\tau_{dif}} = \frac{L/u}{\delta^2/D} = \frac{1}{25}\left(\frac{L}{x}\right)\left(\frac{T_e}{T}\right) \tag{11}$$

Since, at breakdown, T_e/T is approximately equal to 10, it would appear that the convection time is much smaller than the diffusion time unless the size of the aperture is comparable to the distance of the aperture from the nose. This means that the gas is convected past the aperture long before the electrons

have had a chance to diffuse across the boundary layer. Thus at high altitudes, the breakdown process will be convection controlled rather than diffusion controlled.

Similar considerations can be given to the other processes appearing in the continuity and energy equations. Sufficient information is not yet available for the dependence of the effective cross sections on the gas temperature for many of these processes to allow any quantitative conclusions to be drawn. On the other hand, it has already been shown that the gas temperature and composition have an appreciable effect on the attachment and ionization processes. Similarly, the energy exchange processes depend significantly on the state of the gas. For example, air in equilibrium at temperatures such as occur in a re-entry boundary layer contains N_2 molecules which are vibrationally excited to an appreciable extent. Using the results of Chen[5] for the partial cross sections for vibrational excitation of N_2 from the first five levels to the first 10 levels, we have computed the net vibrational energy exchange rate. The results are presented in Fig. 4 in the form of the ratio of the actual energy transfer rate to that which one would calculate assuming that all of the N_2 molecules were in the ground state. One sees that there is a very large discrepancy during the initial stages of breakdown. Even in the final stage of breakdown, the vibrational energy exchange rate in a re-entry boundary layer is about 30% less than would exist if the gas were at room temperature.

The most important conclusion to be drawn from this discussion is that the mechanisms upon which the breakdown process depends may be sensitive

to the state of the neutral gas. Hence the simple scaling rules which one deduces from the classical breakdown theory are not adequate to treat the re-entry situation. If one is to conduct a laboratory experiment to determine the power required for breakdown in a flight situation, it is not sufficient to simulate only $p\delta$ and f/p; one must also simulate the thermodynamic state of the gas.

Before this section can be concluded, there is one additional point that requires discussion: that is the way in which breakdown is defined under re-entry conditions. In the classical breakdown calculation, one defines the power required for breakdown as that incident power level which produces a field strength in the gas such that the rate of ionization exceeds the electron loss rate. The classical breakdown method provides no information regarding the way the electron density approaches its final value and hence cannot be used to determine the amount of power transmitted during or at the end of breakdown. Since the boundary layer is very thin, it may be that even though a large electron density is produced, the degradation in the transmitted signal may still be acceptable. In addition, the important question--what happens if the incident power level greatly exceeds the breakdown power level--remains unanswered. This question would be answered by the formulation of the breakdown problem described in the preceding paragraphs. That is, by coupling Maxwell's equations with the equations governing the electron production process, one can compute the field strength, ionization rate, electron density, and transmission coefficient locally at each point over the aperture.

Although adequate information is not available at this time to accurately evaluate all of the rate processes, an indication of how the gas would respond to strong fields can be obtained by applying the same procedure to the classical breakdown equation. That is, instead of using the free space field strength in the classical calculation, one can use Maxwell's equations to determine the local field strength using the local value of electron density obtained by integrating the breakdown equation simultaneously.

To illustrate this procedure, the following relatively simple problem was treated: A uniform slab of plasma is assumed to be flowing across the aperture. In view of the above discussion, diffusion is neglected. The equation governing the electron density is then

$$u\frac{\partial n}{\partial x} = \nu_i n - \nu_a n \tag{12}$$

The quantities ν_i and ν_a are assumed to depend directly on the effective field strength as in the classical breakdown calculation. Using the well-known solution of Maxwell's equation for a homogeneous plasma slab, one determines the field strength distribution for the unperturbed plasma. Since the slab is thin, the field strength varies only slightly in the y direction. The root means square value (averaged over the slab thickness) of the field is used to approximate the field in the plasma. This is used to start the calculation at $x = 0$. Equation (12) can then be used to determine the electron density a short distance downstream of the leading edge of the aperture. Using this new level of electron density, one again solves Maxwell's equations to determine the

effective field at the new location. Using this in Eq. (12), one then determines the electron density at the next increment in x downstream, etc.

Typical results from such a calculation are shown in Figs. 5-7. These calculations were performed using averaged properties which would exist in the boundary layer of a 10-deg cone moving at a speed of 22,200 ft/sec. Figure 5 shows the x distribution of electron density over the aperture. The classical breakdown prediction for these conditions is $S = 2.08\ W/cm^2$. The present calculation shows that at power densities just slightly in excess of this value, the ionization rate is positive but small. As a result, the electron density increases only slightly by the time the gas is convected to the downstream edge of the aperture. At higher incident power levels, the rate of ionization increases and the electron density reaches its steady-state value closer to the upstream edge of the aperture. The maximum electron density attained at the downstream edge of the aperture is shown in Fig. 6 as a function of the incident power level. This maximum electron density increases rapidly at power levels slightly in excess of that predicted from the classical theory. As the incident power level is increased, a greater fraction is reflected back, and the rate of increase of maximum electron density decreases. The average power level transmitted through the second interface of the slab is shown in Fig. 7 as a function of incident power level. Since, at power levels slightly above those required for classical breakdown, the increase in electron density over the aperture is small (Fig. 5), the transmitted power increases beyond that corresponding to the transmitted power at classical breakdown. However, as the incident power level is further increased, the

average electron density over the aperture increases markedly, resulting in a reduction in the transmitted power. This result is typical of the results obtained for other flight conditions. An important conclusion to be drawn from these results is that there is a maximum amount of power that can be transmitted regardless of the magnitude of the incident power.

It can be seen from these results and the preceding discussion that there is some ambiguity regarding the definition of breakdown. Classically, the power required for breakdown is defined as that incident power level which causes the net ionization rate to become positive. Obviously, if convection is present, the classical definition of breakdown would indicate no change in electron density over the aperture; thus, propagation would be unaffected. Reilly[1] recognized this difficulty and hence, in his calculations, he defined the power required for breakdown as the incident power level which produces an initial ionization rate such that the plasma frequency is equal to the signal frequency at the downstream edge of the aperture. This seems to be a reasonable choice since one expects the degradation of the transmitted signal to become significant when $\omega_p \approx \omega$. However, aside from the fact that this is only approximately true, Reilly's analysis does not account for the fact that the rate of growth of electron density is highly nonlinear. In addition, Reilly's work, as well as all other previous analyses, does not predict the power that is actually transmitted when this criterion is satisfied.

It is suggested here that a more useful definition of the power required for breakdown is that incident power level which causes the transmitted power to be a maximum. A comparison between this definition and Reilly's definition

is shown in Fig. 8. One may note that there is qualitative agreement between the two definitions except at high gas densities (low altitudes) where the thermal ionization causes the plasma to be overdense even in the absence of electromagnetic fields. Quantitatively, the two definitions disagree by as much as a factor of two in the high and low density limits. There is also a small difference in the altitudes at which the curves have their minima. Also plotted in Fig. 8 is the variation of maximum transmitted power vs density. It is seen that for these conditions, the transmitted power at breakdown may be as much as 30% less than the incident power.

CONCLUSIONS

According to the classical theory of breakdown, the power required for breakdown is a function of the gas pressure p and the parameters $p\delta$ and f/p, where δ is the characteristic dimension of the geometry and f is the signal frequency. The functional relationship among these parameters is known to depend on the particular gas in question. This functional relationship has been established to within engineering accuracy for air at room temperature. It has been demonstrated in this paper that for the conditions that exist in the boundary layer of a re-entry cone, the composition of air is significantly different from that which exists at standard conditions. These conditions have been shown to significantly affect the various rate coefficients which are important in the breakdown process. It would appear therefore that a re-evaluation of these rate coefficients is necessary for accurate prediction of the power required for breakdown of air in the boundary layer of a re-entering cone. As a result of this conclusion it would appear that in order to extrapolate laboratory experiments to flight conditions, it is necessary that the state of the gas in the laboratory experiments be the same as would occur in the flight condition of interest.

It has also been shown that if the length of the aperture in the direction of flow is small compared to the distance between the apex of the cone and the aperture, the effects of diffusion will be negligible. At high altitudes therefore, the power required for breakdown will be convection controlled rather than diffusion controlled. That is, the smaller the transit time of the gas

over the aperture, the greater will be the power required to achieve a given electron density level. This conclusion suggests that the power required for breakdown may be increased by making the aperture dimension in the flow direction as small as possible.

If the transit time of the gas across the aperture is sufficiently small, the increase in electron density due to the presence of strong fields may not be large enough to seriously affect transmission. In order to determine the level of electron density produced by a strong electromagnetic field, one must solve the equations governing the rate of production of electrons simultaneously with Maxwell's equations. A method for performing such a calculation, including the effects of variable gas composition, has been formulated. Since all of the cross-section data for the various processes of importance in a re-entry environment are not yet available, a qualitative evaluation of the electron density distribution resulting from a strong applied field has been obtained by solving Maxwell's equations simultaneously with the classical breakdown equation. The results indicate that power levels appreciably in excess of those predicted by the classical approach are required to substantially affect the propagation characteristics of the gas. It is further concluded that for a given re-entry environment, there is a maximum amount of power that can be transmitted, regardless of the level of the incident power.

REFERENCES

1. James P. Reilly, "Microwave Breakdown of the Air Around a Conical Re-entry Vehicle," Research Report No. 214, Avco-Everett Research Laboratory (April 1965).

2. D. Rapp, et al., "On the Theoretical Interpretation of Resonance Dissociative Attachment Cross Sections," Report No. LMSC 6-74-64-45, Lockheed Missile Systems (1964).

3. E. E. Muschlitz, Jr., "Elastic and Inelastic Collisions of Low-Energy Negative Ions in Gases," Proceedings of the Fourth International Conference on Ionization Phenomena in Gases, Upsala (1959).

4 N. P. Carleton and L. R. Megill, "Electron Energy Distribution in Slightly Ionized Air Under the Influence of Electric and Magnetic Fields," The Physical Review, vol. 126, no. 6, p. 2089 (1962).

5. J. C. Y. Chen, "Theory of Subexcitation Electron Scattering by Molecules, Part I and II, "The Journal of Chemical Physics, vol. 40, p. 3507 (1964); erratum, Ibid., vol. 41, p. 3263 (1964).

ACKNOWLEDGMENT

The author is grateful to C. Lenander, who supplied much of the information regarding the cross sections for the various collision processes.

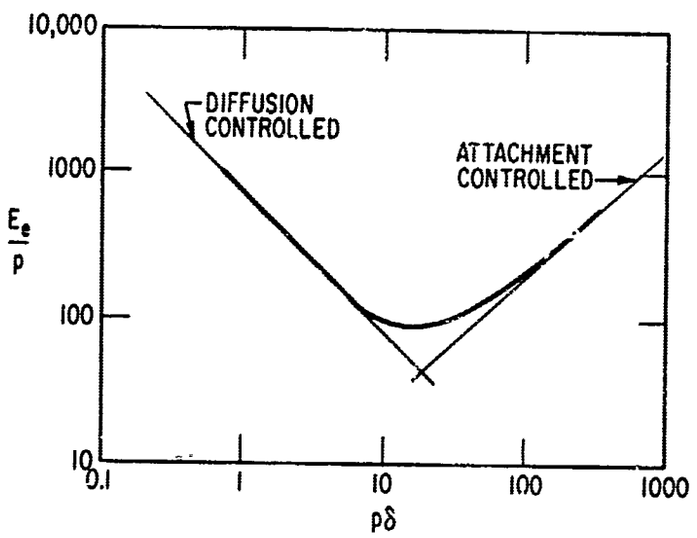


Fig. 1. Paschen curve.

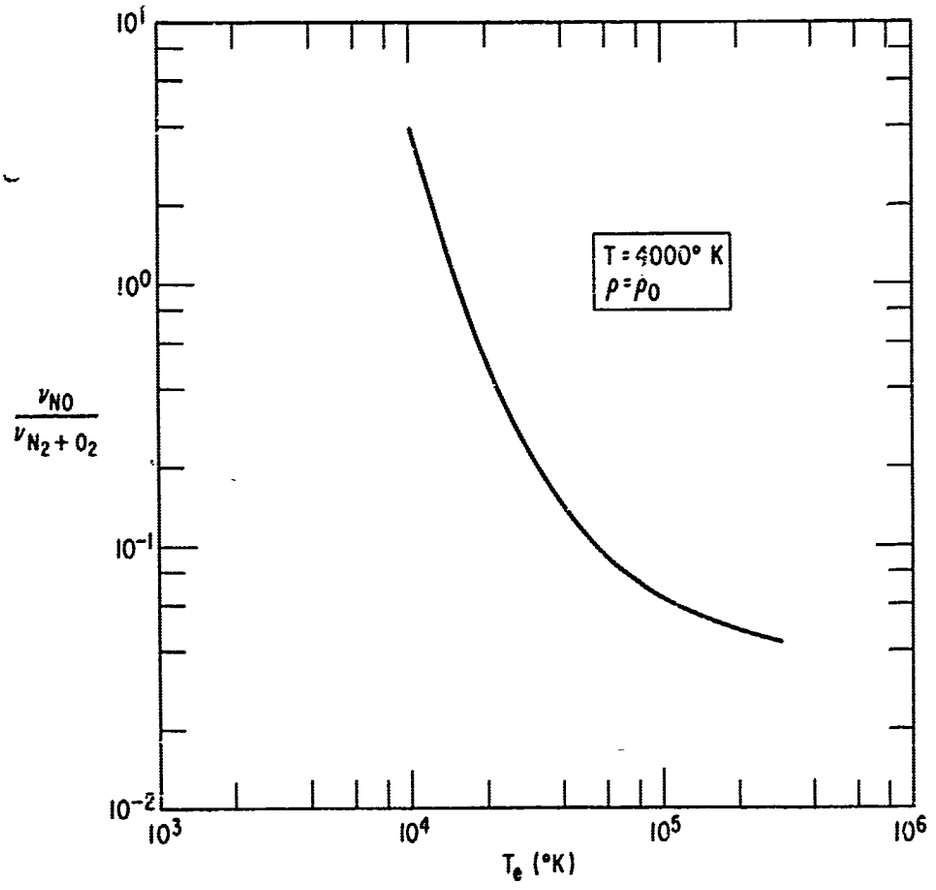


Fig. 2. Relative importance of NO ionization as a function of electron temperature.

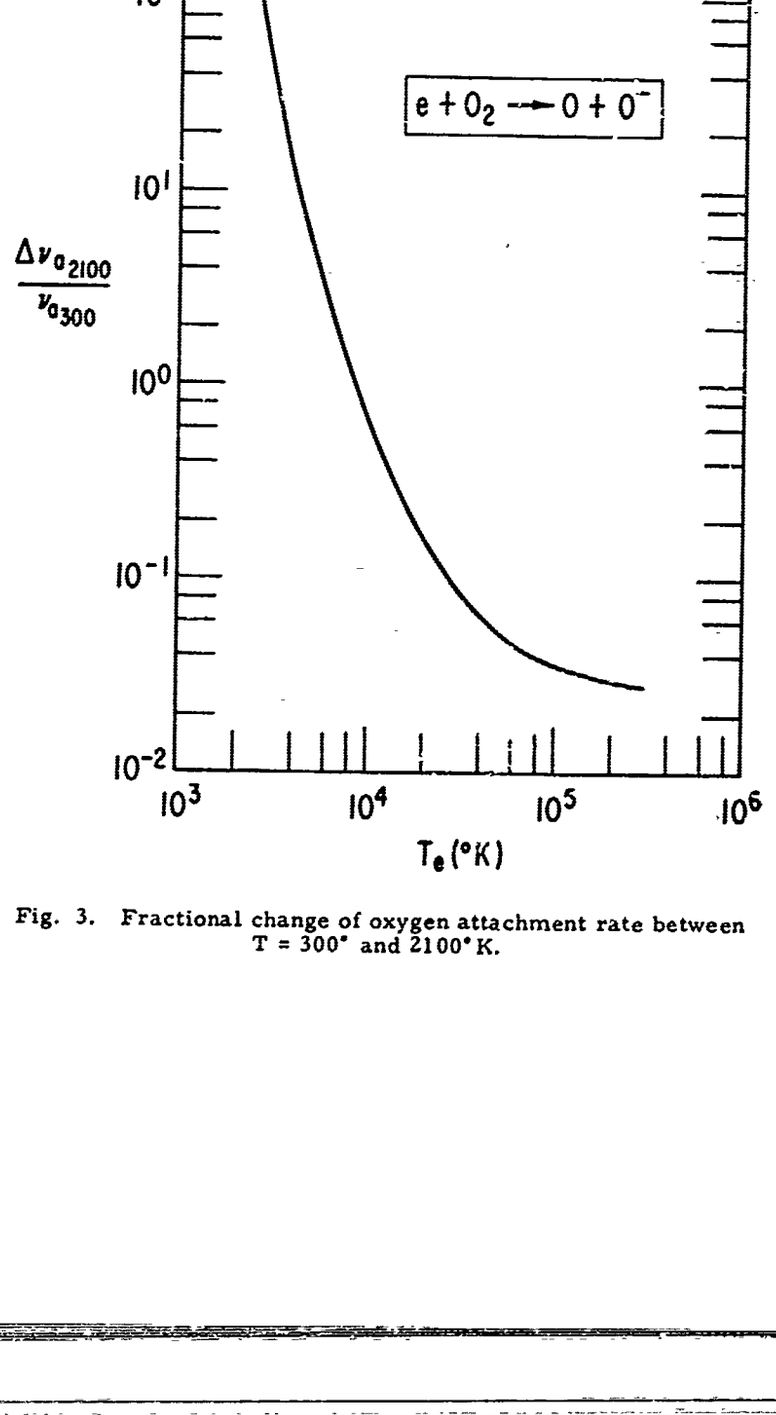


Fig. 3. Fractional change of oxygen attachment rate between T = 300° and 2100° K.

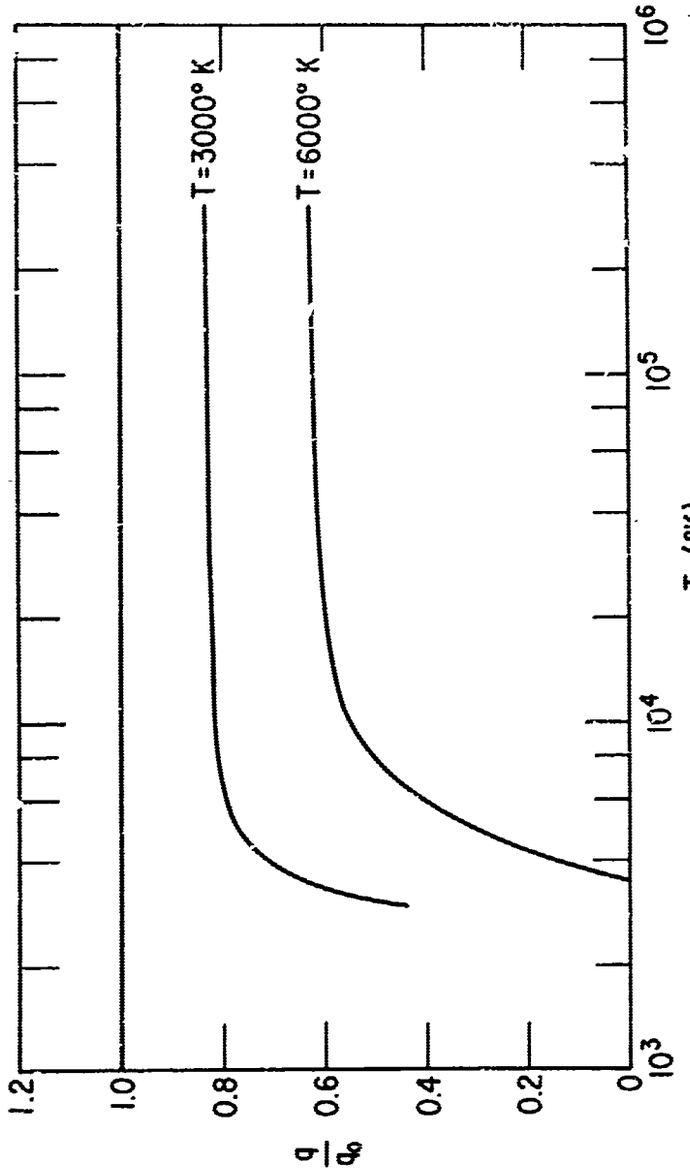


Fig. 4. N_2 vibrational excitation energy transfer.

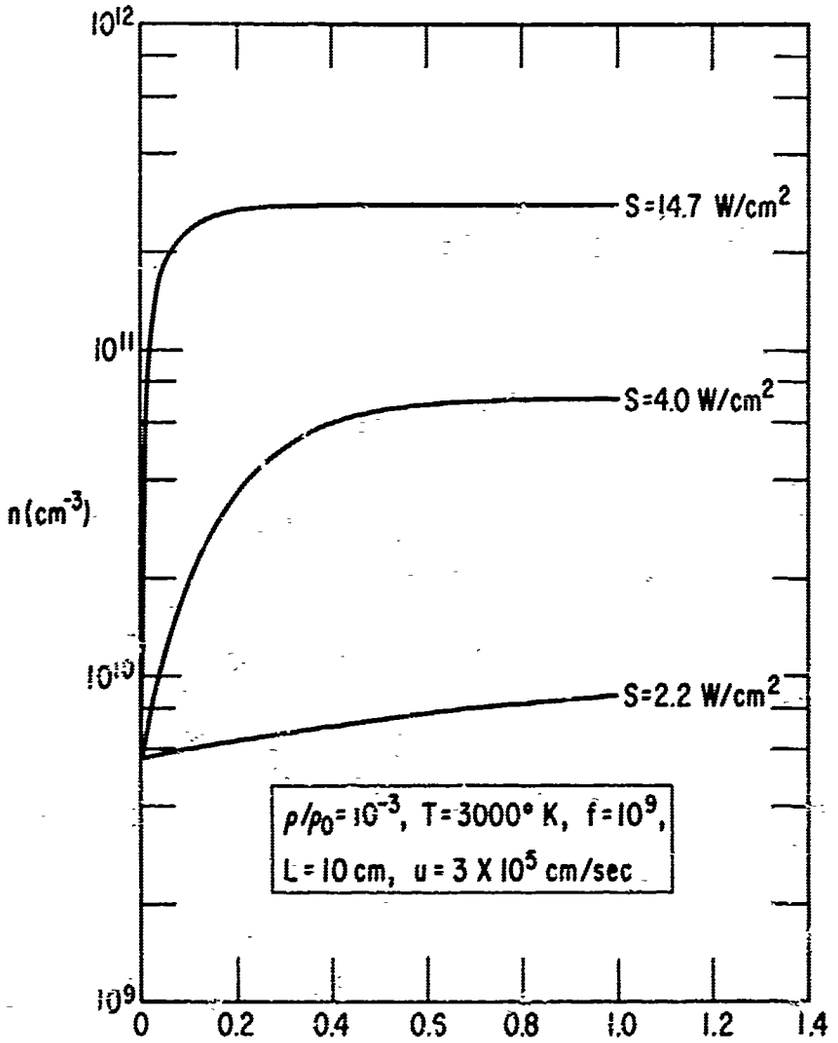


Fig. 5. Distribution of electron density over the aperture.

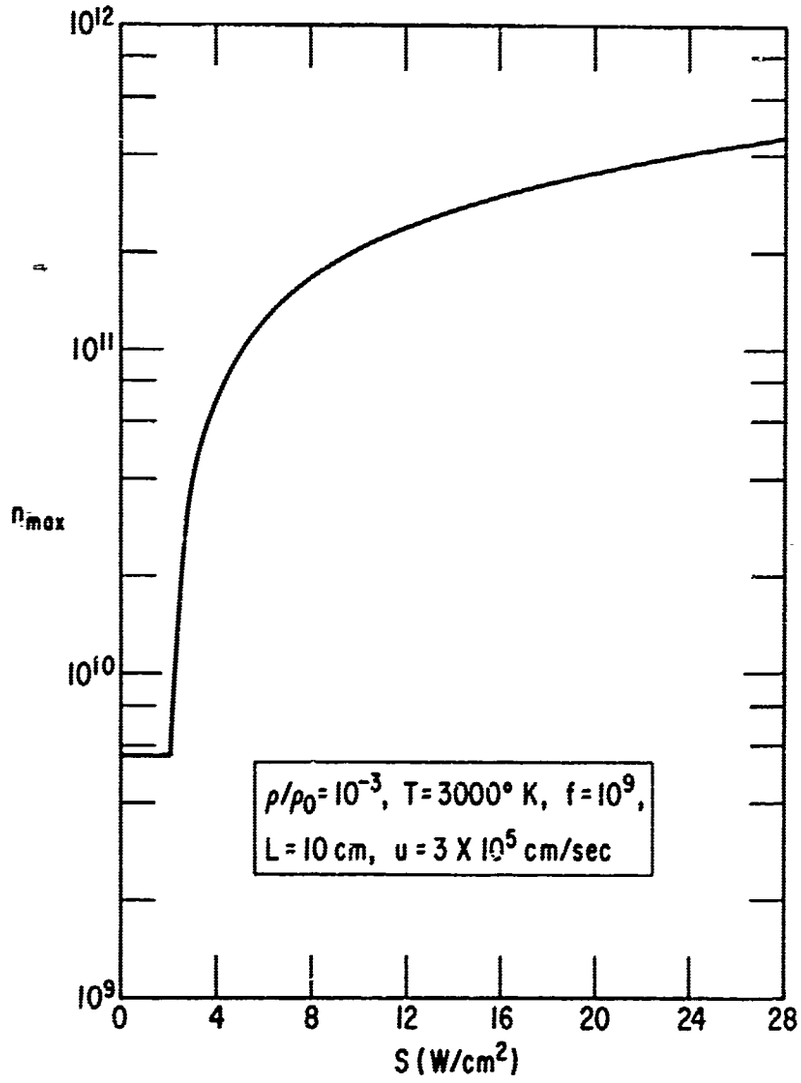


Fig. 6. Maximum electron density.

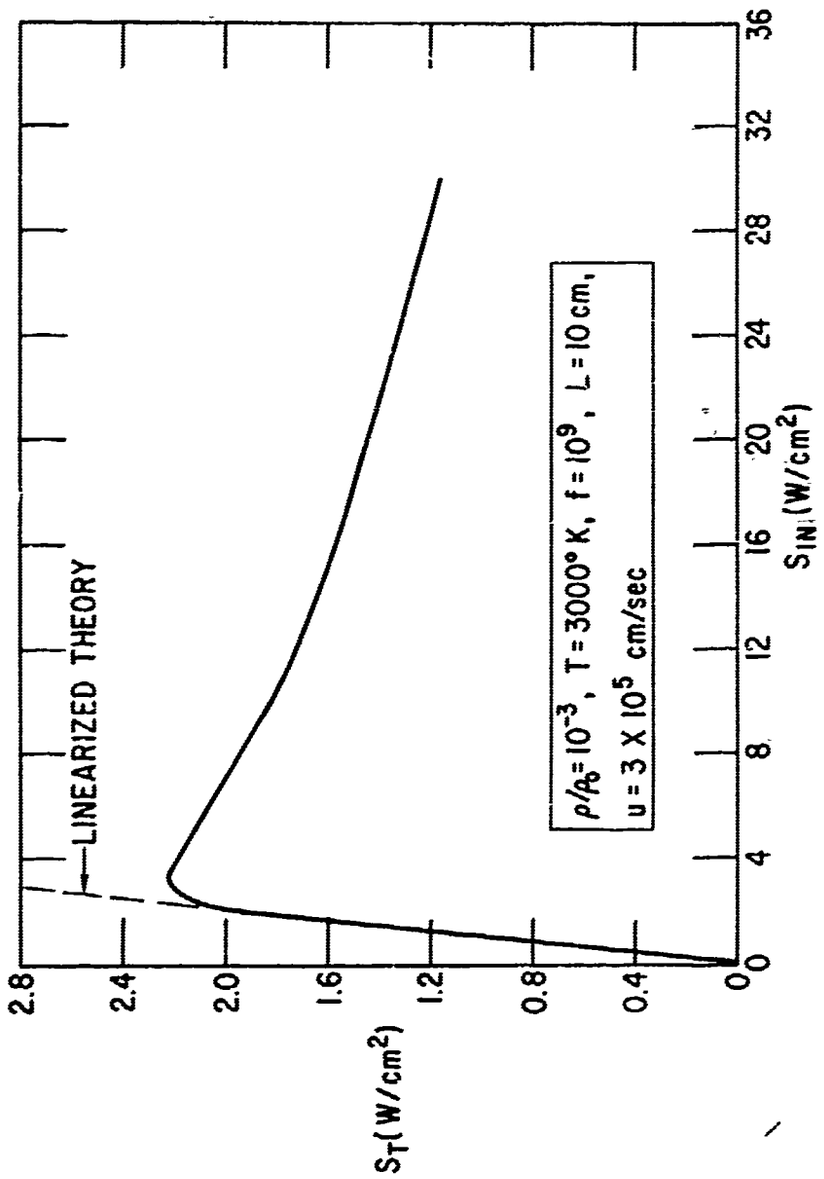


Fig. 7. Transmitted power vs incident power.

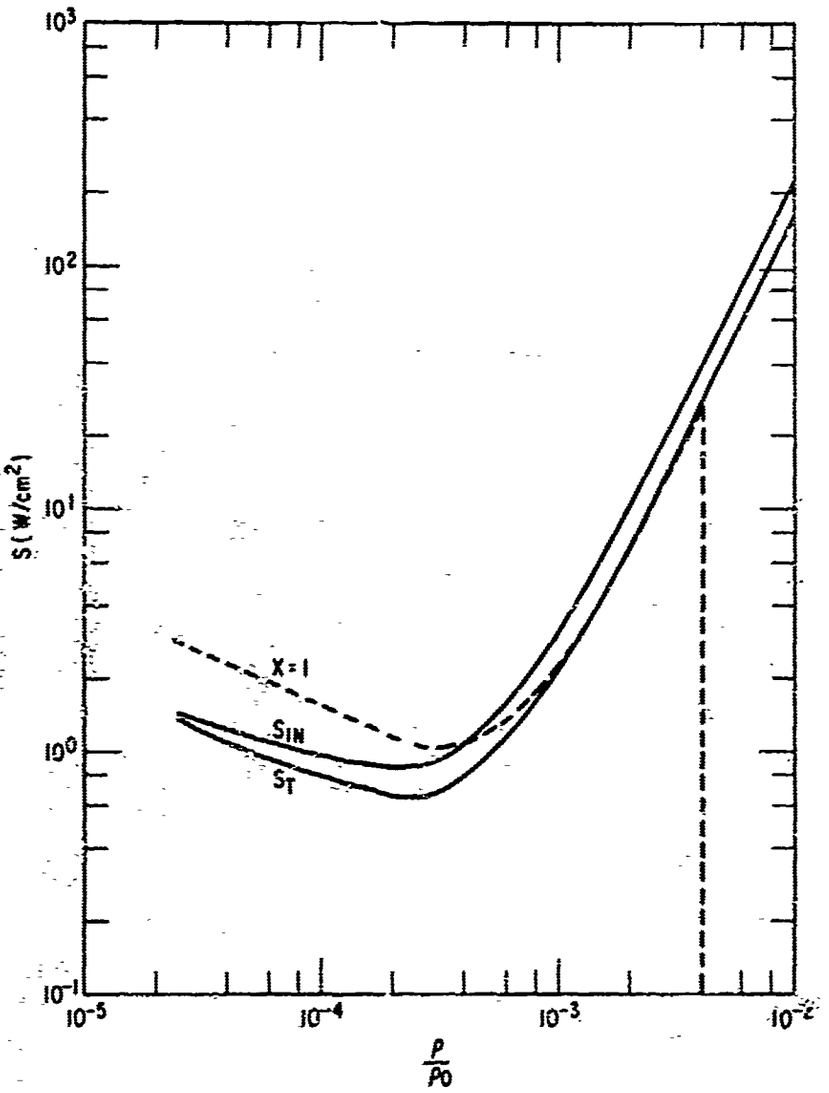


Fig. 8. Power required for breakdown.

VI. ELECTROMAGNETIC WAVE PROPERTIES IN A NONLINEAR, ANISOTROPIC, TIME-DEPENDENT PLASMA MEDIUM

Robert J. Papa

Air Force Cambridge Research Laboratories
Bedford, Massachusetts

INTRODUCTION

The propagation of radio frequency waves in a nonlinear, isotropic, time-dependent plasma has been considered by King[1] and Papa.[2] The description of the nonlinear interaction involves a consideration of the pattern of electromagnetic energy deposition into the plasma, which is, in general, inhomogeneous. The fraction of electromagnetic energy absorbed by the lossy plasma produces changes in the equation of state of the medium. These changes in the equation of state of the partially ionized gas result in alterations of the propagation characteristics of the wave.

King[1] has investigated the perturbations induced in the boundaries defining a plasma medium subjected to strong rf fields when the electron density gradients are slowly varying compared to a wavelength. King[1] has considered a one-dimensional plasma model, in which a monochromatic, transverse plane wave of frequency ω_o is normally incident from $z = -\infty$ and propagates in the positive z direction (Fig. 1). The time-independent WKB approximation has been used to represent the EM field distribution

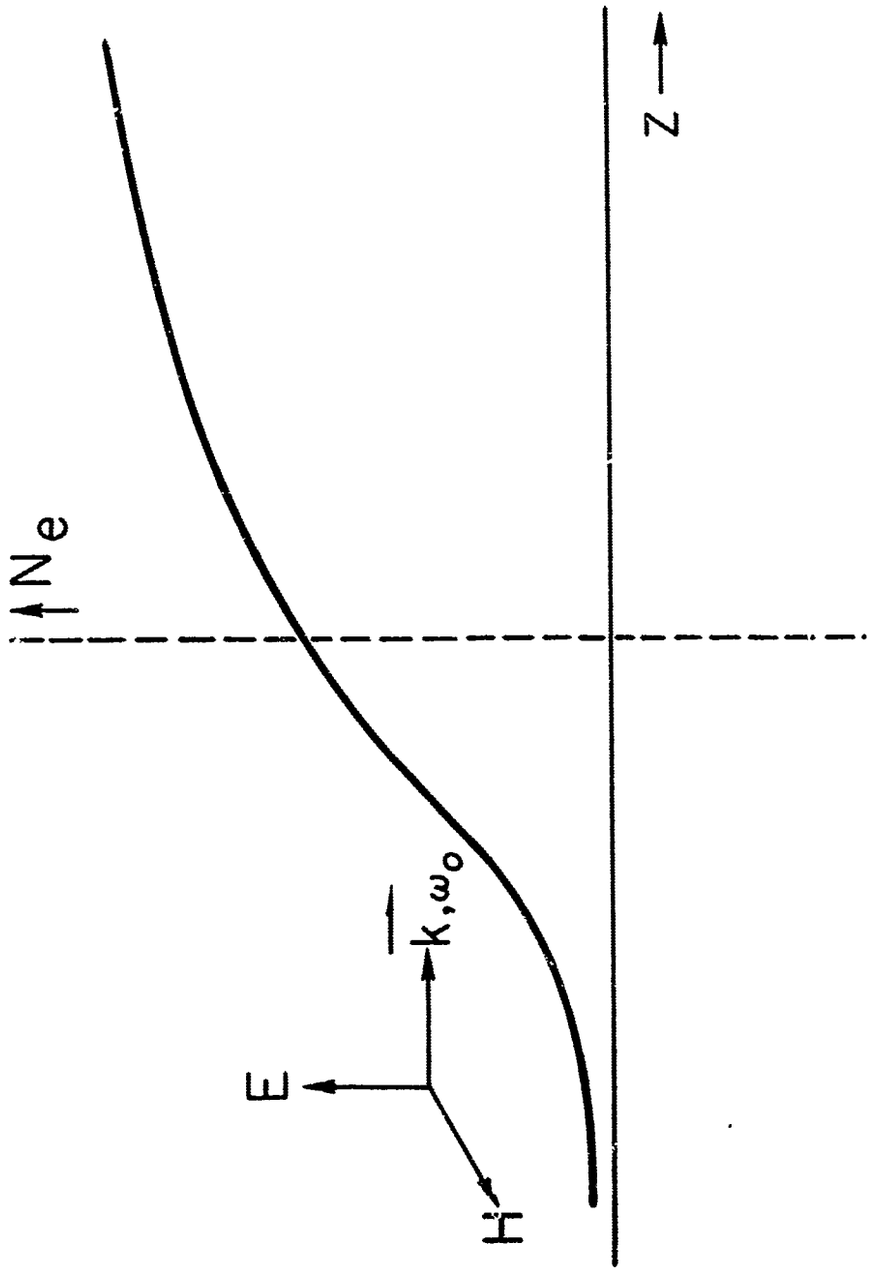


Fig. 1 Transverse monochromatic plane wave incident upon inhomogeneous electron density profile.

in the inhomogeneous, time-varying medium. For exponential-like initial electron density profiles, solutions have been obtained to the continuity equation governing the spatial and temporal behavior of the electron density. The results of the analysis demonstrate that the fraction of EM energy deposited in the lossy plasma is responsible for the creation of additional ionization in such a fashion that the initial electron density profile will be altered in shape and appear to move toward the perturbing rf source with a velocity that depends upon the incident EM flux. There is no mass motion of the plasma; the electrons and ions are created in such a fashion that there is an apparent motion of the electron density profile.

Papa[2] has formulated the time-dependent, nonlinear rf plasma interaction in terms of the Boltzmann equation, in contrast to King[1], who has used only the continuity equation and the Langevin equation to describe the nonlinear interaction. In the Boltzmann equation approach, a spherical harmonic expansion of the electron distribution function is made, and only the first two terms are retained. The results of the analysis by Papa[2] for the isotropic plasma show that when the electron-neutral energy relaxation time (τ_{EN}) is much longer than the period of the EM field ($\tau_{EN} >> T_{em} = 2\pi/\omega_o$), the electron temperature does not follow the rapid variations in field amplitude. Rather, the electromagnetic wave selectively heats the electron gas with a characteristic time constant which is a function of the instantaneous local electron temperature. For certain ranges of the

parameters, such as incident flux, wave frequency, collision frequency and ionization potential, the characteristic time constant for electron density changes τ is much longer than the characteristic time constant for electron temperature changes (τ_{EN}). In this case, the electron temperature builds up at a nonuniform rate to reach a steady state value at each point on the profile, where the final electron temperature attained is a function of position on the profile. On an expanded time scale, the electron density increases with a characteristic time constant (τ) which is a function of position and time. The parameter τ is shortest where the electron temperature (T_e) is highest, corresponding to the upstream portion of the profile closest to the rf source. Hence, the most rapid buildup of electron density occurs at the upstream portion of the profile. For portions of the profile further downstream, the electromagnetic flux is less because the wave attenuates as it propagates into the medium, so that the electron density buildup proceeds at a slower rate.

In this paper, the analysis presented by Papa[2] is extended to include the effect of a dc magnetic field which is parallel to the electron density gradients. A nonlinear constitutive relation may be derived between the macroscopic current density (J) and the transverse electric field (E):

$$J_i = \sigma_{ij} E_j \tag{1}$$

where σ_{ij} = conductivity tensor. The principal coordinate system is that coordinate system in which the conductivity tensor becomes diagonal. When the wave equation is referred to the principal coordinate system, it can be demonstrated that an elliptically polarized, transverse plane wave normally incident upon an electron density profile will split into only two distinct modes provided the dc magnetic field is parallel to the electron density gradients (Fig. 2). These two distinct modes, a right-hand and left-hand circularly polarized wave, are coupled through the second moment of the Boltzman equation which determines the local energy density in the electron gas. The isotropic part of the electron distribution function (f^o) is assumed to be Maxwellian because of the predominance of electron-electron encounters.

It is shown that when three conditions are satisfied between the self-collision time for electron-electron encounters ($1/\nu_{ee}$), the momentum relaxation time ($1/\nu$) and the Larmor period ($2\pi/\omega_b$), then the effect of electron-electron encounters may be neglected in the equation for the first spherical harmonic component of the electron distribution function. The expressions for the components of the conductivity tensor are derived in terms of Dingle integrals when the electron-neutral cross section for momentum transfer is a constant and electron-ion collisions are neglected. A time-dependent WKB approximation is used to obtain solutions to the wave equation expressed in the principal coordinate system when: (1) the electron

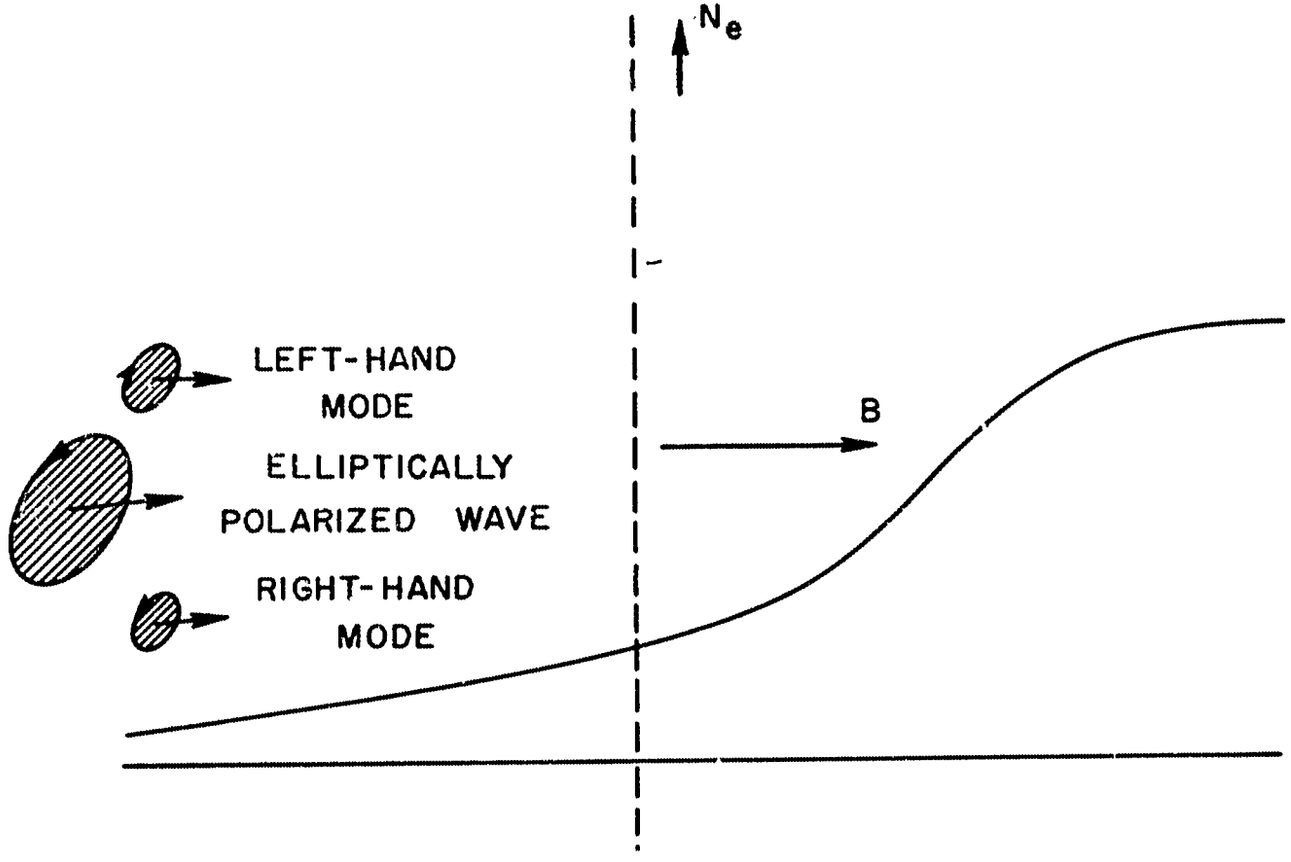


Fig. 2 Elliptically polarized plane wave incident upon inhomogeneous electron density profile.

density gradients are slowly varying compared to a wavelength, (2) the time scale for electron density changes (τ) is long compared to the period of the electromagnetic wave, (3) the effective dielectric constant for either the right- or left-hand mode is not near a cutoff (where the wavelength in the medium becomes large), and (4) the real part of the effective dielectric constant for the right- or left-hand wave is positive so that the mode can propagate. Solutions to the wave equation are investigated for several regions of the Clemmow-Mullay-Allis diagram (the CMA diagram is discussed in Stix[3]). Using first-order finite difference techniques, numerical solutions to the energy balance equation and continuity equation are obtained. The time-dependent response of the electron-temperature and electron density for each point on the profile are presented in the form of stroboscopic pictures. When the time-dependent response of the plasma is computed, it is assumed that the wave fields for the right- and left-hand modes remain monochromatic in the medium. The shift in frequency due to the time-varying electron density and temperature may be computed as a second-order effect. The frequency shift of the left mode is different from the frequency shift of the right mode because the effective dielectric constant of the left mode differs from the effective dielectric constant of the right mode.

THE TIME-DEPENDENT WKB APPROXIMATION FOR A MAGNETOPLASMA

The finite temperature of the electrons can influence EM wave

propagation in plasmas in three distinct ways: (1) through the effect of elastic collisions, which cause wave attenuation, (2) through the effect of inelastic collisions, which govern the electron density, and (3) through the effect of pressure perturbations induced by the EM wave. In the present analysis, the EM wave propagation characteristics are nonlinear to the extent that induced changes in electron temperature affect only the elastic and inelastic collisional processes. The pressure variations in the electron gas induced by the EM wave have a most pronounced effect only upon longitudinal wave propagation, which is not considered in this paper. Transverse waves are relatively unaffected by induced pressure variations in the electron gas, except near cyclotron resonance.

Ailis, Buchsbaum and Bers[4] define a temperate plasma as a plasma for which the following condition is satisfied

$$u >> v_T >> v_D \qquad (2)$$

where $u = c/\sqrt{K_r}$ = wave phase velocity

K_r = real part of dielectric constant

$K_i << K_r$

$v_T = \left[3kT_e/m\right]^{1/2}$ = electron thermal velocity

T_e = electron temperature

v_D = drift velocity of electrons.

When $u >> v_T$, the thermal electrons do not move an appreciable distance during one wave period. If $v_T >> v_D$, the spherical harmonic expansion of the electron distribution function converges rapidly, and the retention of only the first two terms is sufficiently accurate. Near electron cyclotron resonance, $u \approx v_T$, and in this case pressure variations and heat flow will affect the propagation characteristics of the transverse, right-hand wave. Also, near cyclotron resonance, collisionless damping such as electron cyclotron damping (Stix[3]) can become important. In this paper, condition (2) will be assumed to hold, so that the analysis is not accurate very near cyclotron resonance.

For a temperate magnetoplasma, the conductivity tensor assumes the form:

$$\overline{\overline{\sigma}} = \begin{pmatrix} \sigma_{11} & i\sigma_{12} & 0 \\ -i\sigma_{12} & \sigma_{11} & 0 \\ 0 & 0 & \sigma_{33} \end{pmatrix} \qquad (3)$$

where the electric and magnetic fields are assumed to vary in time as $(\exp + i\omega_o t)$.

The eigenvectors of the temperate plasma conductivity tensor are (Allis et al[4], Holt and Haskell[5])

$$|e^{(1)}\rangle = \frac{1}{\sqrt{2}} \begin{pmatrix} 1 \\ -i \\ 0 \end{pmatrix} \qquad (4.1)$$

$$|e^{(2)}\rangle = \frac{1}{\sqrt{2}} \begin{pmatrix} 1 \\ i \\ 0 \end{pmatrix} \tag{4.2}$$

$$|e^{(3)}\rangle = \begin{pmatrix} 0 \\ 0 \\ 1 \end{pmatrix} \tag{4.3}$$

where $|\rangle$ represents the Dirac ket vector. The unitary matrix which refers a vector to the principal coordinate system is given by

$$U = \frac{1}{\sqrt{2}} \begin{pmatrix} 1 & i & 0 \\ 1 & -i & 0 \\ 0 & 0 & \sqrt{2} \end{pmatrix} . \tag{5}$$

The ket vector $|\rangle$ represents a complex column vector. The diagonalization of the conductivity tensor for a temperate plasma and the use of Dirac bra and ket vectors to represent elliptically polarized plane waves is discussed in Holt and Haskell[5]. An arbitrary, elliptically polarized wave may be represented by a column vector $|E\rangle$ whose elements are complex numbers. An elliptically polarized wave can be represented as the sum of a right-hand wave, a left-hand wave and a longitudinal wave:

$$|E\rangle = |e^{(1)}\rangle \langle e^{(1)}|E\rangle + |e^{(2)}\rangle \langle e^{(2)}|E\rangle + |e^{(3)}\rangle \langle e^{(3)}|E\rangle$$

where $\langle e^{(1)}|E\rangle = \tilde{E}_1 = \frac{1}{\sqrt{2}}(E_x + iE_y)$

$\langle e^{(2)}|E\rangle = \tilde{E}_2 = \frac{1}{\sqrt{2}}(E_x - iE_y)$

$\langle e^{(3)}|E\rangle = \tilde{E}_3 = E_z$.

The expressions for the vector and scalar operators curl, grad, and div, when referred to the principal coordinate system are given by Westfold[6].

For a plane wave that is propagating in the positive z-direction and is elliptically polarized in a plane perpendicular to the z-axis, there is no z-component of electric or magnetic field (Fig. 2). Then, the components of Maxwell's equations when referred to the principal coordinate system are (Papa[7, 8]):

$$\frac{\partial \tilde{E}_1}{\partial \xi_3} = \omega_o \mu_o \tilde{H}_1 \qquad (6.1)$$

$$\frac{\partial \tilde{E}_2}{\partial \xi_3} = \omega_o \mu_o \tilde{H}_2 \qquad (6.2)$$

$$\frac{\partial \tilde{E}_1}{\partial \xi_1} = + \frac{\partial \tilde{E}_2}{\partial \xi_2} \qquad (6.3)$$

$$i\frac{\partial \tilde{H}_1}{\partial \xi_3} = \tilde{\sigma}_1 \tilde{E}_1 + i\omega_o \epsilon_o \tilde{E}_1 \tag{6.4}$$

$$-i\frac{\partial \tilde{H}_2}{\partial \xi_3} = \tilde{\sigma}_2 \tilde{E}_2 + i\omega_o \epsilon_o \tilde{E}_2 \tag{6.5}$$

$$\frac{\partial \tilde{H}_1}{\partial \xi_1} = \frac{\partial \tilde{H}_2}{\partial \xi_2} \tag{6.6}$$

where $\tilde{E}_i = U_{ij} E_j$

$\tilde{H}_i = U_{ij} H_j$

$\tilde{\sigma}_{ij} = U_{i\ell} \sigma_{\ell m} U^{-1}_{mj}$

$U^{-1}_{mj} = U^{*}_{jm}$ (Since U is a unitary matrix)

$\xi_i = U_{ij} r_j$.

Here, an asterisk denotes a complex conjugate and the field variables have an $\exp(i\omega_o t)$ time dependence.

A wave equation expressed in the principal coordinate system may be derived by taking the curl of the first Maxwell equation and then substituting this into the second Maxwell equation:

$$\widetilde{\text{grad}}\ \widetilde{\text{div}}\ \underset{\sim}{\widetilde{E}} - \widetilde{\nabla}^2\ \underset{\sim}{\widetilde{E}} = -\left(\frac{1}{c^2}\right)\left[\frac{\dot{\overline{\overline{\sigma}}}}{\epsilon_o}\ \underset{\sim}{\widetilde{E}} + \frac{\overline{\overline{\sigma}}}{\epsilon_o}\ \dot{\underset{\sim}{\widetilde{E}}} + \ddot{\underset{\sim}{\widetilde{E}}}\right] . \qquad (7)$$

Because $\text{div}\ \underset{\sim}{D} = \text{div}\ \overline{\overline{K}}\ \underset{\sim}{E} = 0$ is a scalar equation, which remains invariant under a unitary transformation, then

$$\widetilde{\text{div}}\ \overline{\overline{\widetilde{K}}}\ \underset{\sim}{\widetilde{E}} = 0 \qquad (8)$$

where $\overline{\overline{\widetilde{K}}}$ is the dielectric tensor in the principal coordinate system

$$\overline{\overline{\widetilde{K}}} = \left[I + \frac{\overline{\overline{\sigma}}}{i\omega_o \epsilon_o}\right]$$

and I is the unit matrix. Since ξ_1 and ξ_2 involve only the x and y coordinates, and because the electron density gradients lie only in the z-direction:

$$\frac{\partial \widetilde{K}_1}{\partial \xi_1} = 0 \qquad (9.1)$$

$$\frac{\partial \widetilde{K}_2}{\partial \xi_2} = 0. \qquad (9.2)$$

Using Eqs. (8) and (9) and Maxwell's Eqs. 6, it can be shown that:

$$\widetilde{\operatorname{div}}\,\widetilde{\mathbf{E}} = 0 \tag{10.1}$$

$$\frac{\partial \widetilde{E}_1}{\partial \xi_1} = 0 \tag{10.2}$$

$$\frac{\partial \widetilde{E}_2}{\partial \xi_2} = 0. \tag{10.3}$$

By using Eqs. 10, the wave equation (7) for the right-hand wave and left-hand wave becomes:

$$\frac{\partial^2 \widetilde{E}_1}{\partial z^2} = \frac{1}{c^2}\left[\frac{\widetilde{\sigma}_1}{\epsilon_o}\dot{\widetilde{E}}_1 + \frac{\dot{\widetilde{\sigma}}_1}{\epsilon_o}\widetilde{E}_1 + \ddot{\widetilde{E}}_1\right] \tag{11.1}$$

$$\frac{\partial^2 \widetilde{E}_2}{\partial z^2} = \frac{1}{c^2}\left[\frac{\widetilde{\sigma}_2}{\epsilon_o}\dot{\widetilde{E}}_2 + \frac{\dot{\widetilde{\sigma}}_2}{\epsilon_o}\widetilde{E}_2 + \ddot{\widetilde{E}}_2\right] \tag{11.2}$$

where Eq. 11.1 describes the propagation of the right-hand wave and Eq. 11.2 describes the propagation of the left-hand wave and

$$\tilde{\sigma}_1 = \sigma_{11} + \sigma_{12}$$

$$\tilde{\sigma}_2 = \sigma_{11} - \sigma_{12} \ .$$

The time-dependent WKB approximation consists in assuming solutions to the wave equation in the form:

$$\tilde{E}_1 = \tilde{E}_1^o \exp\left[i \left(\frac{\omega_o}{c}\right) S^R(z, t) \right] \tag{12.1}$$

$$\tilde{E}_2 = \tilde{E}_2^o \exp\left[i \left(\frac{\omega_o}{c}\right) S^L(z, t) \right] \tag{12.2}$$

where $\tilde{E}_1^o$ and $\tilde{E}_2^o$ are slowly varying amplitudes and $S^R(z, t)$ and $S^L(z, t)$ are slowly varying phase factors of space and time. Substituting Eqs. 12.1 and 12.2 into the wave equations 11 and equating terms of equal order of magnitude in (ω_o/c) yields, in each case, three equations determining the amplitudes and phase factors of the right- and left-hand waves (Papa[2, 8]):

$$(\omega_o/c)S^R = \pm \int k_z^R \, dz \mp \int \omega^R dt \tag{13.1}$$

$$(\omega_o/c)S^L = \pm \int k_z^L dz \mp \int \omega^L dt \tag{13.2}$$

$$\tilde{E}_1^o = A_1 \Big/ \sqrt[4]{\tilde{K}_1} \tag{13.3}$$

$$\tilde{E}_2^o = A_2 \Big/ \sqrt[4]{\tilde{K}_2} \tag{13.4}$$

when $(1/L) >> (1/c\tau)$.

Here, $L = \left[\dfrac{\partial \ell n\, N_e}{\partial z}\right]^{-1}$

= characteristic length for electron density gradients

N_e = electron density

$\tau = \left[\dfrac{\partial \ell n\, N_e}{\partial t}\right]^{-1}$

= characteristic time for electron density changes

$\omega^R = \omega_o + \omega_1^R$

$\omega^L = \omega_o + \omega_1^L$

ω_1^R = shift in frequency of right-hand wave

ω_1^L = shift in frequency of left-hand wave

$\tilde{K}_1 = 1 + \tilde{\sigma}_1 \Big/ (i\omega^R \epsilon_o)$

$\tilde{K}_2 = 1 + \tilde{\sigma}_2 \Big/ (i\omega^L \epsilon_o)$

$k_z^R = \pm (\omega^R/c)\ \sqrt{\tilde{K}_1}$

$k_z^L = \pm (\omega^L/c)\ \sqrt{\tilde{K}_2}$.

The parameters A_1 and A_2 are constants independent of space and time.

whereas ω^R and ω^L represent the shift in frequency of the right- and left-hand waves due to the time varying conductivity and are functions of space and time.

Poeverlein[9] has demonstrated that the irrotationality of the four propagation vectors:

$$k_\mu = (k_x,\ k_y,\ k_z,\ i\omega/c)$$

implies the conditions:

$$\nabla\omega^R + \frac{\partial k^R}{\partial t} = 0 \qquad (14.1)$$

$$\nabla\omega^L + \frac{\partial k^L}{\partial t} = 0 \ . \qquad (14.2)$$

Equations (14) insure that the eikonals S^R and S^L will be single-valued scalar functions of space and time. These conditions imply that the wave fields $\tilde{E}_1$ and $\tilde{E}_2$ are single-valued functions of space and time. When the electron density and temperature have been determined as functions of space and time by assuming that the EM field remains monochromatic in the medium, then Eqs. (14.1) and (14.2) may be integrated, using finite differences, to determine, to second order, the shift in frequency of the right- and left-hand waves.

THE CONTINUITY AND ENERGY-DENSITY EQUATIONS

The Boltzmann equation for the electron distribution function is

solved by the standard technique of making a spherical harmonic expansion of the distribution function (f) and retaining only the first two terms. If three terms are retained in the expansion, then first order thermal variations may be taken into account (Johnston[10]). For transverse EM waves, these induced thermal variations are negligible, except very close to cyclotron resonance. In this paper, these first order thermal variations will be neglected:

$$f = f^o + \frac{f_i' v_i}{w} \tag{15}$$

where f^o is the isotropic part of the electron distribution function,

f_i' is one vector component of the first spherical harmonic component of the distribution function,

w is the electron speed,

v_i = one component of electron velocity,

$f_i' = f_i^{10} + f_i^{11} \exp(\mp i\omega_o t)$.

f_i^{10} = dc component of first spherical harmonic component of distribution function, and

f_i^{11} = ac component of first spherical harmonic component of distribution function.

By substituting Eq. (15) into the Boltzmann equation and then projecting out first the isotropic part and then the first spherical harmonic component

in velocity space of the resulting equation, three coupled equations may be obtained for f^o, f_i^{10} and f_i^{11} (Papa[8]). The solutions to the equations for f_i^{10} and f_i^{11} may be expressed in terms of $\frac{\partial f^o}{\partial w}$, $S = \frac{-eB}{m\nu}$, $Y = -\left(\frac{eB}{m\omega_o}\right)$, E_i, ∇N_e and ∇T_e. Here, B = magnetic field (along z-axis), $\nu = \nu_{EN} + \nu_{ei}$, $\nu_{eN} = N_m \sigma(w) w$, N_m = neutral number density, $\sigma(w)$ = velocity dependent cross section for momentum transfer for electron-neutral collisions and ν_{ei} = velocity dependent electron-ion collision frequency.

An equation may be obtained solely for f^o by substituting the expressions for f_i^{10} and f_i^{11} into the isotropic part of the Boltzmann equation and performing a time average over a period long compared to ($T_{em} = 2\pi/\omega_o$) but short compared to τ and τ_{EN}, where it has been assumed that

$$\tau \gg T_{em}$$

and

$$\tau_{EN} \gg T_{em} \quad .$$

Here,

$$\tau_{EN} = \left[\frac{\partial \ell n T_e}{\partial t}\right]^{-1}$$

$$\tau = \left[\frac{\partial \ell n N_e}{\partial t}\right]^{-1} .$$

Using the equation for f^o, it can be shown by the method of successive approximations that f^o is Maxwellian when (Papa[11]):

$$\nu_{ee} >> 1/\tau \tag{16.1}$$

$$\nu_{ee} >> G\nu_{eN} + G_{ION}\nu_{ei} \tag{16.2}$$

$$\nu_{ee} >> \frac{v_T^2}{\nu}\left[(\nabla\, nN_e)^2 + (\nabla^2\, nN_e)\right] \tag{16.3}$$

where G = relative fractional energy loss per electron-neutral collision

G_{ION} = relative fractional energy loss per electron-ion collision.

Here, ν_{ee} is the interelectron collision frequency:

$$\nu_{ee} = (3.73)N_e(\ell n\,\Lambda)T_e^{-3/2} \quad (\sec^{-1})$$

$$\Lambda = \left(\frac{3}{2e^3}\right)\left(\frac{k^3T_e^3}{\pi N_e}\right)^{1/2} \quad (\text{cgs})$$

$$\nu_{ee}(T_e) = \nu_{ei}(T_e)\ .$$

The conditions listed in Eqs. 16 will be assumed to hold in the inhomogeneous plasma subjected to an rf plane wave.

The equation for f_i[10] leads to a dc current density which arises from temperature and density gradients in the electron gas. The current flow is essentially dc because the temperature and density gradients are very slowly varying compared to a wave period. Depending upon the boundary conditions at $z = -\infty$ and $+\infty$, the dc current will either continue to flow or a charge distribution will be set up. If provisions are made to remove the charge, the dc current will continue to flow due to the temperature and density gradients, whereas if the charge density is allowed to build up, then a dc electric field will be set up, in accordance with Poisson's equation. This dc electric field will inhibit further current flow. It can be shown that this secondary dc electric field will have a negligible effect in determining the electron temperature when (Papa[8]):

$$\sigma_r E^2 >> \sigma_o (E^o)^2 \qquad (17)$$

where $\underline{E}^o \approx \frac{D}{\sigma^o} \nabla \underline{N}_e$

D = diffusion coefficient for current flow due to density gradients

σ^o = dc electrical conductivity

σ_r = real part of ac electrical conductivity.

For a given ac electric field amplitude, Eq. 17 sets an upper bound on the steepness of the electron density gradients in order that the electron temperature remain unaffected by the dc electric field set up in the inhomogeneous plasma.

The equation for f_i^{11} yields information on the ac current flow. It can be shown (Papa[8]) that the effect of electron-electron encounters may be neglected in the equation for f_i^{11} when the following three conditions are satisfied:

$$\omega_o >> \nu_{ee} \tag{18.1}$$

$$\omega_b = \left|\frac{-eB}{m}\right| >> \nu_{ee} \tag{18.2}$$

$$\nu >> \nu_{ee} \tag{18.3}$$

where $\nu = \nu_{eN} + \nu_{ei}$.

Although the effect of electron-electron encounters in the equation for f_i^{11} can be included in the present analysis by using numerical methods, it will be assumed that conditions 18.1, 18.2, and 18.3 are satisfied. Then, the expressions for the ac conductivity are greatly simplified. It can be demonstrated (Papa[8]) that the equation for f_i^{11} can be integrated in time if the following six conditions are satisfied:

$$\omega_o >> 1/\tau \tag{19.1}$$

$$\omega_o >> G\nu \tag{19.2}$$

$$\nu >> 1/\tau \tag{19.3}$$

$$\nu >> G\nu \tag{19.4}$$

$$\omega_b >> 1/\tau \tag{19.5}$$

$$\omega_b >> G\nu \tag{19.6}$$

The first two conditions require that the electron density and temperature relaxation times be much greater than the period of the EM wave. The next two conditions require that the electron density and temperature relaxation times be much greater than the momentum relaxation time. The last two conditions require that the electron density and temperature relaxation times be much greater than the Larmor period.

Assuming conditions 19 hold, the integration of the equation for f_i^{11} yields:

$$\underset{\sim}{f}^{11} = \left(\underset{\approx}{Y}^{-1}\right) \left(\frac{ie\underset{\sim}{E}}{m\omega_o}\right) \frac{\partial f^o}{\partial w} \tag{20}$$

where $\left(\bar{\bar{Y}}^{-1}\right) = \left(\frac{1}{D_Y}\right) \begin{pmatrix} U^2 & iYU \\ -iYU & U^2 \end{pmatrix}$

$$U = 1 - i(\nu/\omega_o)$$

$$Y = \omega_b/\omega_o = -\left(\frac{eB}{m\omega_o}\right)$$

$$f^o = N_e \left(\frac{m}{2\pi kT_e}\right)^{3/2} \exp\left(\frac{-mw^2}{2kT_e}\right)$$

$$D_Y = U\left(U^2 - Y^2\right).$$

The dc magnetic field has been taken to be along the z-axis and the ac electric field lies in the x-y plane.

The ac current density is given by the expression

$$J_i = \left(\frac{4\pi}{3}\right) e \int_0^\infty w^3 f_i^{11}\, dw \qquad (21)$$

$$= \sigma_{ij} E_j$$

where, from Eq. 20, the ac conductivity tensor is:

$$\bar{\bar{\sigma}} = \left(\frac{ie^2}{m\omega_o}\right)\left(\frac{4\pi}{3}\right) \int_0^\infty w^3 \left(\bar{\bar{Y}}^{-1}\right) \frac{\partial f^o}{\partial w}\, dw . \qquad (22)$$

In the special case where electron-ion collisions are neglected and the electron-neutral mean free path is taken to be independent of w, the conductivity tensor as expressed by Eq. 22, may be integrated to give:

$$\bar{\bar{\sigma}} = \left(\frac{N_e e^2}{m\omega_c}\right)\left(\frac{m}{2\pi kT_e}\right)^{3/2} \bar{\bar{I}} \qquad (23)$$

where $\bar{\bar{I}}$ is a two-by-two matrix with two independent elements:

$$I^{11} = \left(\frac{4\pi}{3}\right)\left(\frac{kT_e}{m}\right)\left(\frac{2}{\bar{\nu}_o}\right)\left[U_2\ (1/\beta_-) + U_2\ (1/\beta_+)\right]$$
$$-i\left(\frac{\pi}{2}\right)\left(\frac{2\pi kT_e}{m}\right)^{1/2}\left(\frac{1}{\bar{\nu}_o^2}\right) \cdot \qquad (24.1)$$
$$\cdot\left[U_{3/2}\ (1/\beta_-)\ (1 - Y) + U_{3/2}\ (1/\beta_+)\ (1 + Y)\right]$$

$$I^{12} = (i)\left(\frac{4\pi}{3}\right)\left(\frac{kT_e}{m}\right)\left(\frac{2}{\bar{\nu}_o}\right)\left[U_2\ (1/\beta_-) - U_2\ (1/\beta_+)\right]$$
$$+\left(\frac{\pi}{2}\right)\left(\frac{2\pi kT_e}{m}\right)^{1/2}\left(\frac{1}{\bar{\nu}_o^2}\right)\left[U_{3/2}\ (1/\beta_-)\ (1 - Y)\right. \qquad (24.2)$$
$$\left.-U_{3/2}\ (1/\beta_+)\ (1 + Y)\right] \cdot$$

Here, $I^{11} = I^{22}$, $I^{12} = -I^{21}$

$$\bar{\nu}_o = (N_m \sigma_o/\omega_o)$$
$$\beta_- = (2kT_e/m)\ (\bar{\nu}_o)^2\ (1 - Y)^{-2}$$
$$\beta_+ = (2kT_e/m)\ \bar{\nu}_o)^2\ (1 + Y)^{-2}$$
$$Y = -\left(\frac{eB}{m\omega_o}\right)$$

N_m = neutral density (m^{-3}),

σ_o = cross-section for momentum transfer (independent of w) (m^2)

$U_n(a)$ is the Dingle integral defined as:

$$U_n(a) = \frac{1}{n!} \int_0^\infty \frac{x^n e^{-x} dx}{(x + a)} \quad . \tag{25}$$

The zero velocity moment of the isotropic part of the Boltzmann equation yields the continuity equation determining the time-dependent behavior of the electron density. In this paper, the effects of particle diffusion are neglected, but diffusion can be taken into account by an iterative, numerical relaxation procedure. The solution to the continuity equation may be written in dimensionless form (Papa[12]):

$$\bar{N}(z, \mu) = \frac{N_e(z, \mu)}{N_o(z)} = \left[\frac{\exp \int_0^\mu \bar{\nu}_p \, d\mu}{1 + \int_0^\mu \bar{\alpha} \left(\exp \int_0^\mu \bar{\nu}_p \, d\mu \right) d\mu} \right] \tag{26}$$

where N_o = initial electron density at point z

$\mu = \omega_o t$

$\bar{\nu}_p = (\nu_i - \nu_a)/\omega_o$

$\bar{\alpha} = \alpha N_o/\omega_o$

α = recombination coefficient

ν_i = ionizing frequency

ν_a = attachment frequency.

Here, $\nu_i = N_m \left(\frac{8k T_e}{\pi m} \right)^{1/2} (\pi a_o^2) \cdot \exp -(w_i / kT_e)$

a_o = Bohr radius

w_i = ionization potential of neutral constituent.

If the ions and neutral particles have no average velocity (the ions and neutrals may have random thermal motion), the mean mass velocity is almost zero even if the electrons are mobile. In this case, the second velocity moment of the isotropic part of the Boltzmann equation simplifies to the form (Papa[12]):

$$\frac{3}{2} k \frac{\partial (N_e T_e)}{\partial t} = \left[\mathrm{Re}\, \underline{J} \cdot \mathrm{Re}\, \underline{E} \right]_{AV} - \underline{\nabla} \cdot \underline{q} + 2m \int_0^\infty B w^4 \, dw \qquad (27)$$

where q = thermal flux,

B = sum of collision integrals for elastic and inelastic electron-ion and electron-neutral collisions.

A time average has been performed in Eq. 27 over a period long compared to T_{em} but short compared to τ and τ_{EN}. The relationship between the energy flow vector q, the energy flow matrix due to the electric fields, the energy diffusion matrix and the energy conductivity matrix are discussed by Shkarofsky[13] for a partially ionized magneto-plasma. The second velocity moment of the sum of the elastic and inelastic collision integrals may be

written (Papa[12]):

$$2m\int_0^\infty Bw^4 dw = \frac{3}{2} kT_e \frac{\partial N_e}{\partial t} + kT_e^2 \frac{\partial^2 N_e}{\partial T_e \partial t} - \frac{3}{2} kN_e G_{EFF} \nu_{EFF} (T_e - T) \tag{28}$$

where

$$\nu_{EFF} = \frac{\sqrt{2}}{3\sqrt{\pi}} \left(\frac{m}{kT_e}\right)^{5/2} N_m \cdot \int_0^\infty \sigma(w) w^5 \exp\left(\frac{-mw^2}{2kT_e}\right) dw .$$

Eq. 28 has been derived by neglecting diffusion and assuming $\nu_{EN} >> \nu_{ei}$.

For a temperate plasma, it can be shown that (Papa[8]):

$$\left[\mathrm{Re}\,\underset{\sim}{E} \cdot \mathrm{Re}\,\underset{\sim}{J}\right]_{AV} = \frac{1}{2} \mathrm{Re}\,(\tilde{\sigma}_1 \tilde{E}_1 \tilde{E}_1^*) + \frac{1}{2} \mathrm{Re}\,(\tilde{\sigma}_2 \tilde{E}_2 \tilde{E}_2^*) \tag{29}$$

where $\tilde{E}_1 = \frac{1}{\sqrt{2}} (E_x + iE_y)$

$\tilde{E}_2 = \frac{1}{\sqrt{2}} (E_x - iE_y)$.

$$\tilde{E}_1^* = \frac{1}{\sqrt{2}} (E_x^* - iE_y^*)$$

$$\tilde{E}_2^* = \frac{1}{\sqrt{2}} (E_x^* + iE_y^*)$$

$$\mathrm{Re}\,\tilde{\sigma}_1 = \left(\frac{N_e e^2}{m\omega_o}\right)\left[\frac{8}{3\sqrt{\pi}} \frac{1}{\bar{\nu}} \left\{U_2 (1/\beta_-)\right\}\right]$$

$$\mathrm{Re}\,\tilde{\sigma}_2 = \left(\frac{N_e e^2}{m\omega_o}\right)\left[\frac{8}{3\sqrt{\pi}} \frac{1}{\bar{\nu}} \left\{U_2 (1/\beta_+)\right\}\right]$$

$$\bar{\nu} = \frac{(2kT_e/m)^{1/2} N_m \sigma_o}{\omega_o} .$$

Using Eqs. 12 and 13, it can be shown that (Papa[8]):

$$(\tilde{E}_1^* \tilde{E}_1) = \frac{|\tilde{E}_1^o|^2}{\sqrt{\tilde{K}_1}} \exp - \int_{-\eta_o}^{\eta} H^R(\eta)\, d\eta \qquad (30.1)$$

$$(\tilde{E}_2^* \tilde{E}_2) = \frac{|\tilde{E}_2^o|^2}{\sqrt{\tilde{K}_2}} \exp - \int_{-\eta_o}^{\eta} H^L(\eta)\, d\eta \qquad (30.2)$$

where $|\tilde{E}_1^o|$ is the amplitude of the right-hand wave at $z = -z_o$

$|\tilde{E}_2^o|$ is the amplitude of the left-hand wave at $z = -z_o$

$\eta = z/\lambda_o = \omega_o z/2\pi c$

$$H^R(\eta) = 2\sqrt{2}\,\pi \left[-x_1 + \left[x_1^2 + y_1^2 \right]^{1/2} \right]^{1/2}$$

$$H^L(\eta) = 2\sqrt{2}\,\pi \left[-x_2 + \left[x_2^2 + y_2^2 \right]^{1/2} \right]^{1/2}$$

$$x_1 = 1 + \alpha_4 + \alpha_2$$

$$y_1 = \alpha_3 + \alpha_1$$

$$x_2 = 1 - \alpha_4 + \alpha_2$$

$$y_2 = \alpha_3 - \alpha_1$$

$$\alpha_1 = \frac{-N_e e^2}{m\epsilon_o \omega_o^2} \left(\frac{4}{3\sqrt{\pi}} \right) \frac{1}{\bar{\nu}} \left[U_2(1/\beta_-) - U_2(1/\beta_+) \right]$$

$$\alpha_2 = \frac{-N_e e^2}{m\epsilon_o \omega_o^2} \left(\frac{1}{2\bar{\nu}^2} \right) \left[U_{3/2}(1/\beta_-)(1 - Y) - U_{3/2}(1/\beta_+)(1 + Y) \right]$$

$$\alpha_3 = \frac{-N_e e^2}{m\epsilon_o \omega_o^2} \left(\frac{4}{3\sqrt{\pi}} \right) \left(\frac{1}{\bar{\nu}} \right) \left[U_2(1/\beta_-) + U_2(1/\beta_+) \right]$$

$$a_4 = \frac{-N_e e^2}{m\epsilon_o \omega_o^2} \left(\frac{1}{2\bar{\nu}^2}\right)\left[U_{3/2}(1/\beta_-)(1-Y) - U_{3/2}(1/\beta_+)(1+Y)\right] .$$

The solution to the energy density equation (27) may be derived by an iterative, numerical relaxation procedure when the thermal flux $\underline{q}$ is included. In this paper, heat flow will be neglected. The substitution of Eqs. 28, 29, and 30 into Eq. 27 yields the following dimensionless difference equation for determining the electron temperature:

$$\begin{aligned}\bar{T}(\mu + h_\mu) = \bar{T}(\mu) &+ \frac{F_1}{u\left(\sqrt{K_1}\right)}\left(\frac{\omega_{P_o}^2}{\omega_o^2}\right)\left(\frac{1}{\bar{\nu}}\right) h_\mu \cdot \\ &\cdot\left[\left(\frac{8}{3\sqrt{\pi}}\right)\left(U_2(1/\beta_-)\right)\right]\cdot\exp\left[-\int H^R(\eta)\,d\eta\right] \\ &+ \frac{F_2}{u\left(\sqrt{\tilde{K}_2}\right)}\left(\frac{\omega_{P_o}^2}{\omega_o^2}\right)\left(\frac{1}{\bar{\nu}}\right) h_\mu\left[\left(\frac{8}{3\sqrt{\pi}}\right) U_2(1/\beta_+)\right] \cdot \\ &\cdot \exp\left[-\int H^L(\eta)\,d\eta\right] - h_\mu\left[G\,\bar{\nu}\,(\bar{T}-1)\right]\end{aligned} \tag{31}$$

where T = neutral gas temperature

$\bar{T} = T_e/T$

h_μ = the increment in step size in μ

$\omega_{P_o}^2 = N_o e^2/m\epsilon_o$

N_o = value of N_e at $t = 0$

$u = (3/2)kTN_o$

$F_1 = (1/2)\epsilon_o |\tilde{E}_1^o|^2$ = energy density in right-hand wave at $\eta = -\eta_o$

$F_2 = (1/2)\epsilon_o |\tilde{E}_2^o|^2$ = energy density in left-hand wave at $\eta = -\eta_o$.

The trapezoidal rule has been used to evaluate the integrals which appear in the exponential functions of Eq. 31:

$$\int_{-\eta_o}^{\eta} H^R(\eta)d\eta = h_\eta \left[\frac{1}{2}\left(H_o^R + H_n^R \right) + H_1^R + \ldots H_{n-1}^R \right] \quad (32.1)$$

$$\int_{-\eta_o}^{\eta} H^L(\eta)d\eta = h_\eta \left[\frac{1}{2}\left(H_o^L + H_n^L \right) + H_1^L + \ldots H_{n-1}^L \right]. \quad (32.2)$$

Here, h_η = increment step size in η. The time-dependent response of the inhomogeneous plasma may be found by simultaneously solving Eqs. 26 and 31 once the initial conditions $T_e(z, o)$ and $N_e(z, o)$ are specified. These equations are not valid at cyclotron resonance ($Y = 1$).

CONCLUSIONS

The time-dependent response of an electron density profile subjected to a monochromatic, elliptically polarized plane wave has been obtained by numerically integrating Eqs. 26 and 31. The following values have been

selected for the appropriate plasma parameters:

$$G = 5.38 \times 10^{-5} \tag{33}$$

$$\omega_o = 2 \times 10^{11} \text{ rad/sec}$$

$$T = 300^{\circ}K$$

$$\nu_i = 3.51 \times 10^{7}\, \bar{T}^{1\,2} \exp - \left(\frac{833}{\bar{T}}\right)$$

$$\bar{\nu}_p = \left(\frac{\nu_i}{\omega_o}\right) = 1.76 \times 10^{-4} \left(\bar{T}\right)^{1/2}\ 10^{-\frac{362}{\bar{T}}}$$

$$\bar{\nu} = \frac{\left(\frac{2kT_e}{m}\right)^{1/2} N_m\, \sigma_o}{\omega_o} = 7.55 \times 10^{-3}\, \bar{T}^{1/2}$$

$$\bar{F} = \bar{F}_1 + \bar{F}_2$$

$$\bar{F}_1 = \left(\frac{F_1}{uG}\right) \left(\frac{\omega_{p_o}}{\omega_o}\right)^2$$

$$= \frac{\frac{1}{2} \epsilon_o \left|\tilde{E}_1^o\right|^2}{\left(\frac{3}{2} kTN_o\right) G} \left(\frac{\omega_{p_o}}{\omega_o}\right)^2$$

$$= 0 \text{ to } 60$$

$$\bar{F}_2 = \left(\frac{F_2}{uG}\right) \left(\frac{\omega_{p_o}}{\omega_o}\right)^2$$

$$= \frac{\frac{1}{2} \epsilon_o \left|\tilde{E}_2^o\right|^2}{\left(\frac{3}{2} kTN_o\right) G} \left(\frac{\omega_{p_o}}{\omega_o}\right)^2$$

$$\bar{F}_2 = 0 \text{ to } 60$$

$$Y = -(eB/m\omega_o) = 0.1,\ 0.5,\ 0.8,\ 2,\ 5,\ 10.$$

These values of the parameters have been chosen to correspond approximately, to neon gas initially at room temperature and 30 Torr pressure subjected to K-band microwave radiation.

The calculations have been performed for the case where heat conduction in the electron gas and recombination are neglected. When recombination is neglected, Eq. 26 for the electron density becomes:

$$\bar{N} = \exp \int_0^{\mu} \bar{\nu}_p\ (\eta,\ \mu)d\mu\ . \tag{34}$$

The trapezoidal rule has been used to evaluate the integral which appears in the exponent in Eq. 34:

$$\int_0^{\mu} \bar{\nu}_p\, d\mu = h_\mu \left[\frac{1}{2}\left\{ \bar{\nu}_p\ (\eta,\ \mu_o) + \bar{\nu}_p(\eta,\ \mu_n)\right\} + \bar{\nu}_p\ (\eta,\ \mu_1) + \ldots . \bar{\nu}_p(\eta,\ \mu_{n-1})\right]\ . \tag{35}$$

Figs. 3 through 24 depict the electron temperature and electron density time-dependent response of a magnetoplasma for various values of normalized cyclotron frequency (Y) and incident flux of right-hand and left-hand waves.

The perturbing microwave source is located at $\eta = -\eta_o = -\left(\frac{z_o}{\lambda_o}\right) = -1,000.$

The initial conditions are:

$$\bar{T}(\eta, \mu = 0) = 1 \qquad (36.1)$$

$$\log_{10} N_o(\eta) = \begin{cases} 11 \rightarrow \text{for } \eta < -1000 \\ -1.75 \times 10^{-9}\ \eta^3 + 5.25 \times 10^{-3}\ \eta \\ \qquad + 14.5 \\ \qquad \text{for } -1000 < \eta < 1000 \\ 18 \quad \text{for } \eta > 1000 \end{cases} \qquad (36.2)$$

The initial electron density profile $N_o(\eta)$ has the general shape illustrated in Fig. 1 and satisfies the WKB criterion for shallowness of gradient:

$$\frac{d\, \ell n\, N_e(\eta, 0)}{d\eta} << \sqrt{\tilde{K}_1}$$

$$\frac{d\, \ell n\, N_e(\eta, 0)}{d\eta} << \sqrt{\tilde{K}_2} \quad .$$

There are essentially two distinct cases which are considered:

(1) When the initial conditions, incident flux $\bar{F}$ and normalized cyclotron frequency Y are such that $kT_e << W_i$ for all μ,

then the characteristic time scale for density changes (τ) is always much greater than the characteristic time scale for temperature changes (τ_{EN}) for all η:

$$\tau >> \tau_{EN} .$$

(2) When the initial conditions, incident flux $\bar{F}$ and normalized cyclotron frequency Y are such that $kT_e \approx W_i$, then the characteristic time scale for density changes (τ) may become of the same order as the time scale for temperature changes (τ_{EN}), at least for some portion of the profile:

$$\tau \approx \tau_{EN} .$$

For case (1), $\tau >> \tau_{EN}$, when the perturbing microwave field is switched on at t = 0, the electron temperature will rise from its initial value at each point on the profile with a characteristic time τ_{EN}. Since τ_{EN} is a function of $\bar{T}$, and because the wave is attenuated as it propagates into the lossy plasma, $\bar{T}$ and therefore τ_{EN} are functions of position (η). During the initial period, the electron density remains constant - the pattern of EM heating is governed solely by Eq. 31 where $\bar{N}$ remains equal to 1 for all η. A quasi-steady state electron temperature will be reached at each point on the profile during the time interval

$\left(1/G\bar{\nu}\right) << \mu << \left(1/\bar{\nu}_p\right)$. For the initial period when only the electron temperature is changing, the calculations may be most readily accomplished by rewriting Eq. 31 in the form:

$$\bar{T}(\eta, \mu + h_\mu) = \bar{T}(\eta, \mu) - h_\mu \left[4.062 \times 10^{-7} \bar{T}^{1/2}(\eta,\mu)\right] \cdot \left\{\left[\bar{T}(\eta, \mu) - 1\right]\right. \tag{37}$$

$$- \bar{F}_1 D_1 \left[\exp\left(-\int_{-\eta_o}^{\eta} H^R d\eta\right)\right]\left[\frac{0.75255}{\bar{\nu}^2} U_2\left(1/\beta_-\right)\right]$$

$$\left. - \bar{F}_2 D_2 \left[\exp\left(-\int_{-\eta_o}^{\eta} H^L d\eta\right)\right]\left[\frac{0.75225}{\bar{\nu}^2} U_2\left(1/\beta_+\right)\right]\right\}$$

where $D_1 = \left[x_1^2 + y_1^2\right]^{-1/4}$

$D_2 = \left[x_2^2 + y_2^2\right]^{-1/4}$

and $\bar{N}(\eta) = 1.$

Figures 3 through 6 and Figures 11 through 14 are stroboscopic pictures of the electron temperature along the profile, corresponding to case (1), for different values of: (a) incident flux, (b) ellipticity of incident

wave, and (c) normalized cyclotron frequency. The initial conditions are given by Eqs. 36.1 and 36.2. In each of these figures, the numerical integration of Eq. 37 was achieved by choosing the temporal increment step size h_μ equal to $\left(\frac{1}{100}\right)\left[1/G\bar{\nu}\right]_{MIN}$. Here, $\left[1/G\bar{\nu}\right]_{MIN}$ corresponds to the value of $G\bar{\nu}$ at $\eta = -\eta_o$, where the electromagnetic flux, and electron temperature are a maximum. For a fixed value of $\bar{F}_1$, $\bar{F}_2$, and Y, the time scale for temperature changes (τ_{EN}) is in general a function of η and μ. Since τ_{EN} decreases as $\bar{T}$ increases (for early times), and because, at a given instant, $\bar{T}$ decreases as η increases due to EM wave attenuation, the shortest time scale for temperature changes $\left[1/G\bar{\nu}\right]_{MIN}$ for the entire system is at $\eta = -\eta_o$ and the maximum (final) steady state temperature. It should be brought out that the time scale for electron temperature changes τ_{EN} is exactly equal to $\left[1/G\nu\right]$ only when the incident electromagnetic flux is zero ($\bar{F}_1 = \bar{F}_2 = 0$) and T_e is close to T. In general the time scale for temperature changes is a complicated function of $\bar{F}_1$, $\bar{F}_2$, $\bar{\nu}$, Y and $\bar{T}$. Figs. 3 and 4 illustrate the time-dependent response of $\bar{T}$ as a function of η for two different values of $\bar{F}$ when Y = 0.1, corresponding to region 1 of the Clemmow-Mullaly-Allis diagram (Stix[3]). For this situation where Y = 0.1, the influence of the magnetic field is small so that the response of the plasma is similar to the isotropic case considered previously by Papa[2]. Examination of Figs. 3 and 4 reveals a general characteristic of the temperature response: at a given position η, the successive changes

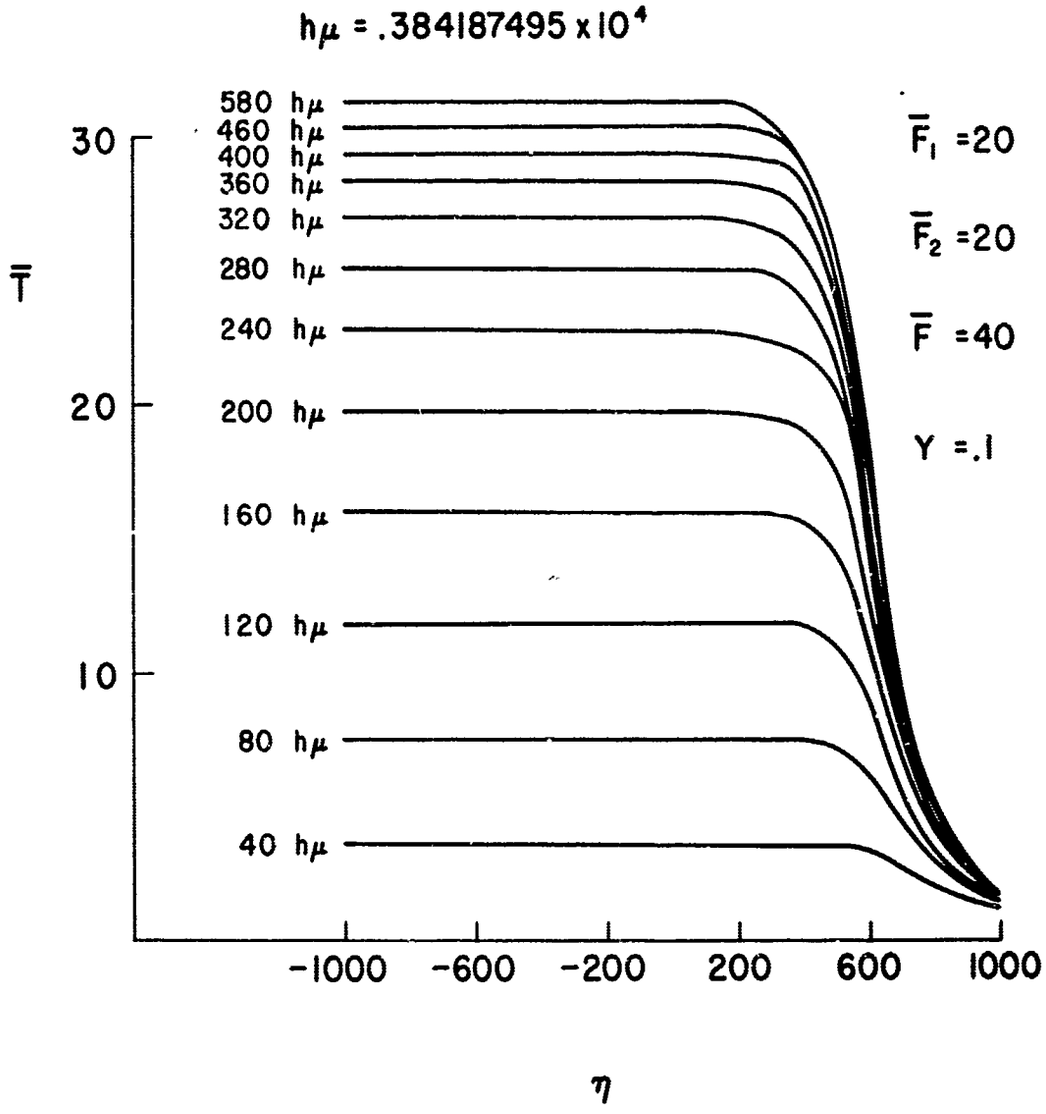


Fig. 3 $\bar{T}$ vs η

$\bar{F} = 40$, $\bar{F}_1 = 20$, $\bar{F}_2 = 20$, $Y = 0.1$

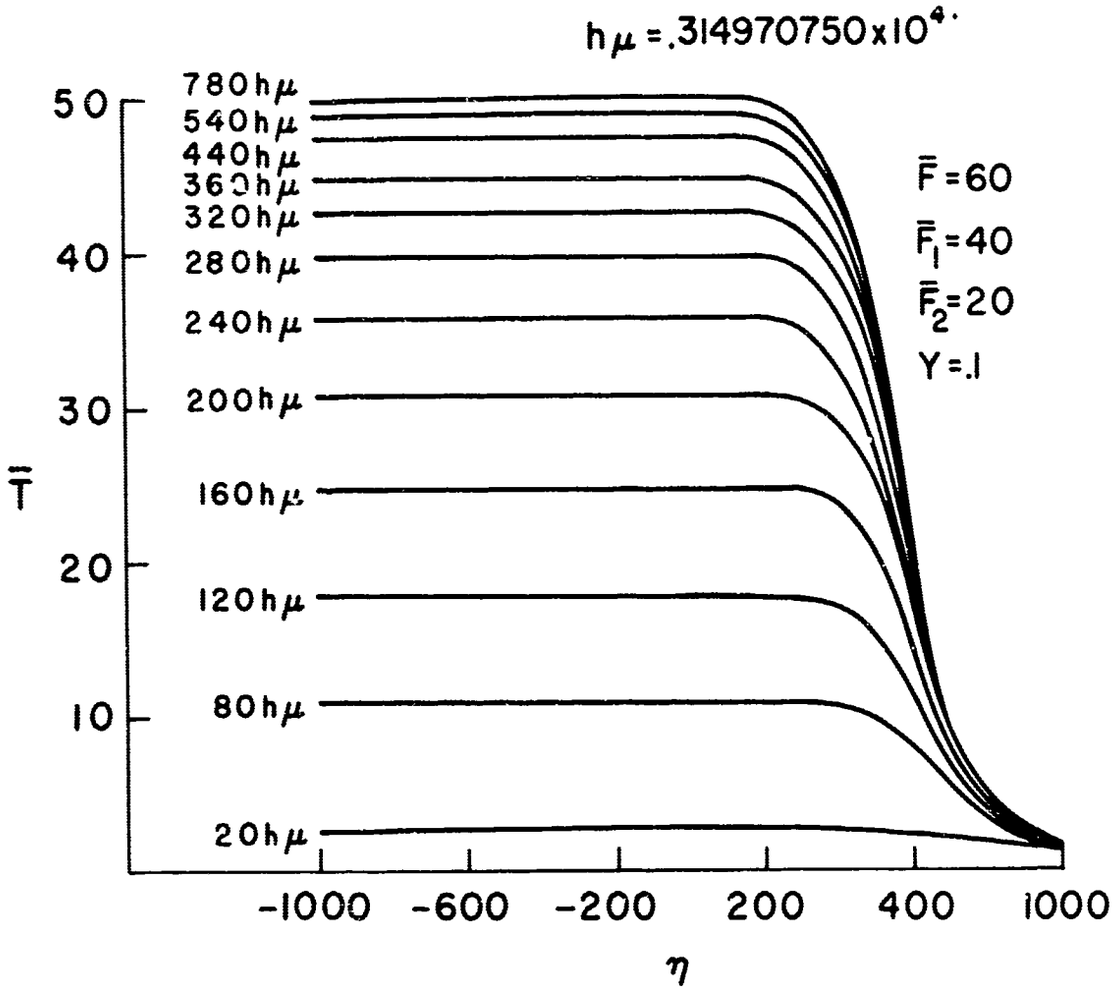


Fig. 4 $\bar{T}$ vs η

$\bar{F} = 60$, $\bar{F}_1 = 40$, $\bar{F}_2 = 20$, $Y = 0.1$

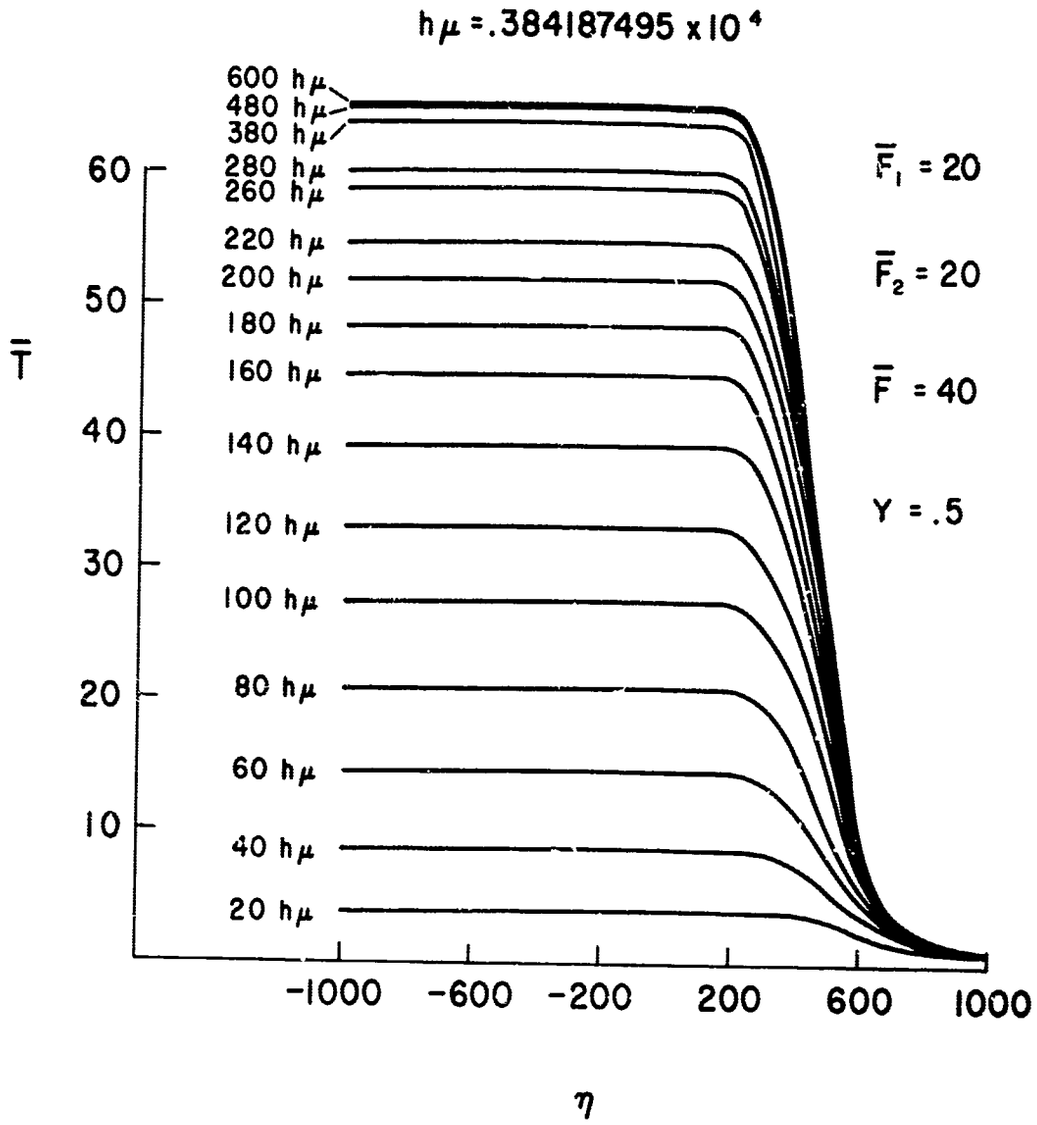


Fig. 5 $\bar{T}$ vs. η

$\bar{F} = 40$, $\bar{F}_1 = 20$, $\bar{F}_2 = 20$, $Y = 0.5$

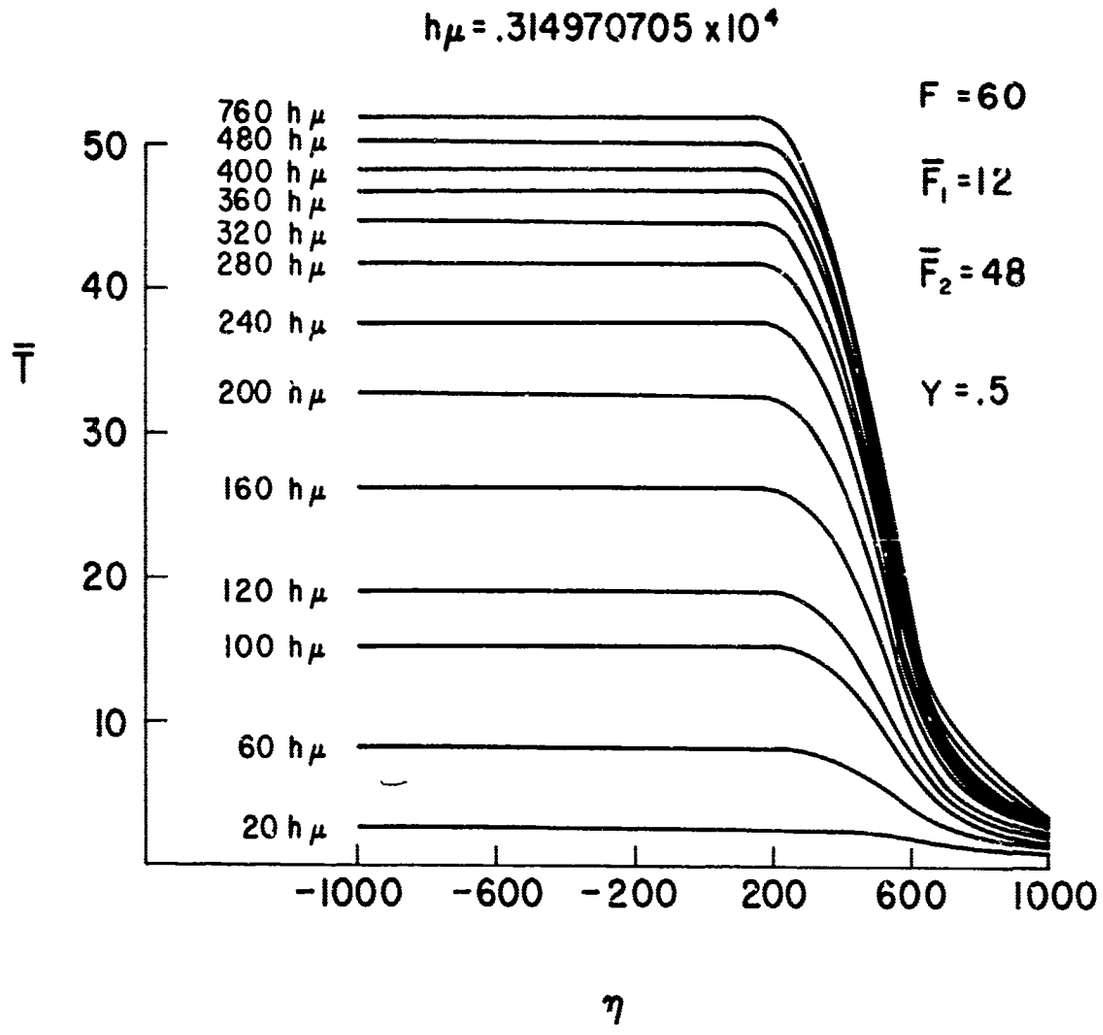


Fig. 6 $\bar{T}$ vs. η

$\bar{F} = 60$, $\bar{F}_1 = 12$, $\bar{F}_2 = 48$, $Y = 0.5$

in $\bar{T}$ for equal time increments at first (for early times) increases. This is due to the contraction of τ_{EN} as $\bar{T}$ increases with time. For late times, as $\bar{T}$ approaches its steady-state value, τ_{EN} dilates as $\bar{T}$ increases, so that the successive temperature changes for equal time increments decreases. Figs. 3 and 4 illustrate that the heating of the electron gas is fairly uniform for $-1000 < \eta < +400$, but that the final steady state temperature rapidly decreases as η increases beyond 400 because of the onset of appreciable EM wave attenuation. Another general feature of the electron temperature response is exhibited in Figs. 3 and 4: for any particular time increment μ to $\mu + h_\mu$, the change in $\bar{T}$ decreases as η increases. This is a result of the dilation of τ_{EN} as $\bar{T}$ decreases. The final steady-state temperature shown in Fig. 4 is much higher than that depicted in Fig. 3 because the EM flux in the right-hand wave ($\bar{F}_1$) has been doubled.

The ellipticity of the incident wave and incident flux associated with Fig. 5 are identical with the values used to compute the response exhibited in Fig. 3; however, the value of Y in Fig. 5 is closer to electron cyclotron resonance (Y = 0.5). This closer proximity to cyclotron resonance results in a much higher final steady-state temperature. Although the total incident flux associated with Fig. 6 ($\bar{F} = 60$) is 50% greater than the incident flux associated with Fig. 5 ($\bar{F} = 40$), the final temperature is lower because the flux in the right-hand mode associated with Fig. 6 is lower than the right-hand mode flux associated with Fig. 5. This highlights the effect of cyclotron

heating.

The total flux of Fig. 7 is equal to the tota. flux of Fig. 6 ($\bar{F} = 60$), but the right-hand mode flux of Fig. 7 is about three times the value used in the computations depicted in Fig. 6. The much higher final temperature of Fig. 7 illustrates the pronounced effect of electron cyclotron heating by the right-hand wave. The final temperature of Fig. 7 is sufficiently high to contract the time scale for density changes (τ) to the point where it becomes of the order τ_{EN}:

$$\tau \tilde{\approx} \tau_{EN} \quad .$$

Hence, the response depicted in Fig. 7 corresponds to case (2).

It should be brought out at this point that Eq. 37 does not describe the time-dependent response of the plasma for case (2), because $\bar{N}$ does not remain equal to one for all η. Instead, Eq. 31 for $\bar{T}(\mu, \eta)$ must be simultaneously integrated, step-by-step, with Eq. 34 for $\bar{N}(\mu, \eta)$.

The temperature response illustrated in Figs. 8 and 9 with $Y = 0.8$ corresponds to case (2). The ellipticity of the incident wave and total flux of Fig. 8 are identical to the values used in computing the response illustrated in Figs. 5 and 3. However, the value of normalized cyclotron frequency corresponding to Fig. 8 is 0.8, so that the proximity of the wave frequency to cyclotron resonance has resulted in a very high final temperature.

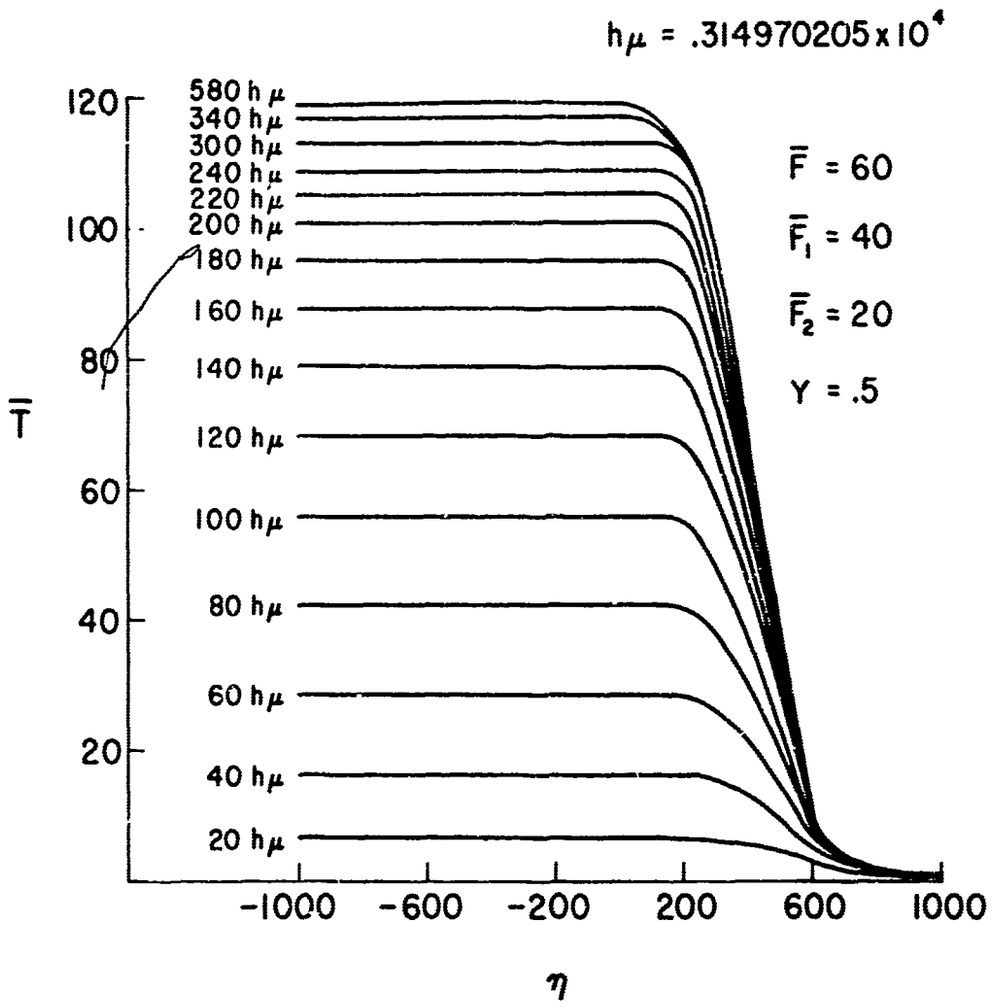


Fig. 7 T vs. η

$\bar{F} = 60$, $\bar{F}_1 = 40$, $\bar{F}_2 = 20$, $Y = 0.5$

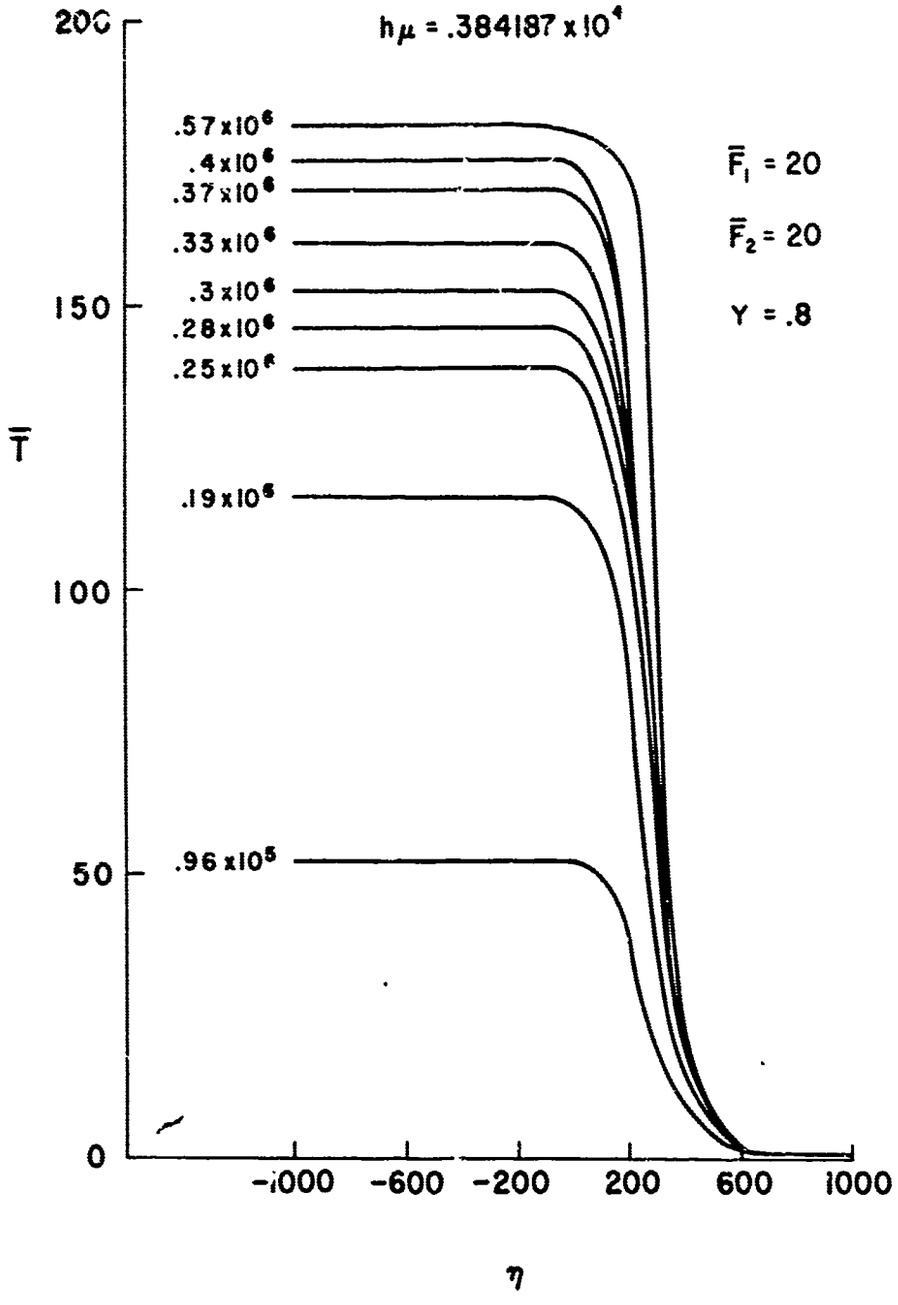


Fig. 8 $\bar{T}$ vs. η

$\bar{F} = 40$, $\bar{F}_1 = 20$, $\bar{F}_2 = 20$, $Y = 0.8$

The degree of cyclotron heating depicted in Figs. 8 and 9 has been sufficient to contract τ to the extent that it has become of the order of τ_{EN}. The total flux and value of Y associated with Fig. 9 are equal to the corresponding quantities of Fig. 10, but in Fig. 9, $\bar{F}_2 = 0$; whereas in Fig. 10, $\bar{F}_1 = 0$.

Figs. 11 through 14 all correspond to the case where $Y > 1$ and $\left(\omega_{p_o}/\omega_o\right)^2 < 1$, so that these figures refer to region six of the Clemmow-Mullaly-Allis diagram. Examination of Figs. 11 through 14 reveals that for the same ellipticity of incident wave and same value of incident flux, the final value of $\bar{T}$ decreases as Y increases above one. In particular, Figs. 13 and 14 show that the heating of the electron gas by the elliptically polarized microwave field becomes more uniform throughout the profile as Y increases above one. Fig. 15 is a plot of the final steady-state temperature at $\eta = -1000$ for $\bar{F}_1 = \bar{F}_2 = 20$ vs. normalized cyclotron frequency. This figure reveals the efficacy of electron cyclotron heating. Calculations have been performed for the case $\bar{F} = 60$ and $Y = 10$, but these calculations are not plotted because there is essentially no change in electron temperature. This is due to the inability of the EM wave to effectively heat the electrons when they are very tightly bound to the magnetic field lines at very high magnetic field strengths.

Stroboscopic pictures of the electron density changes as a function of

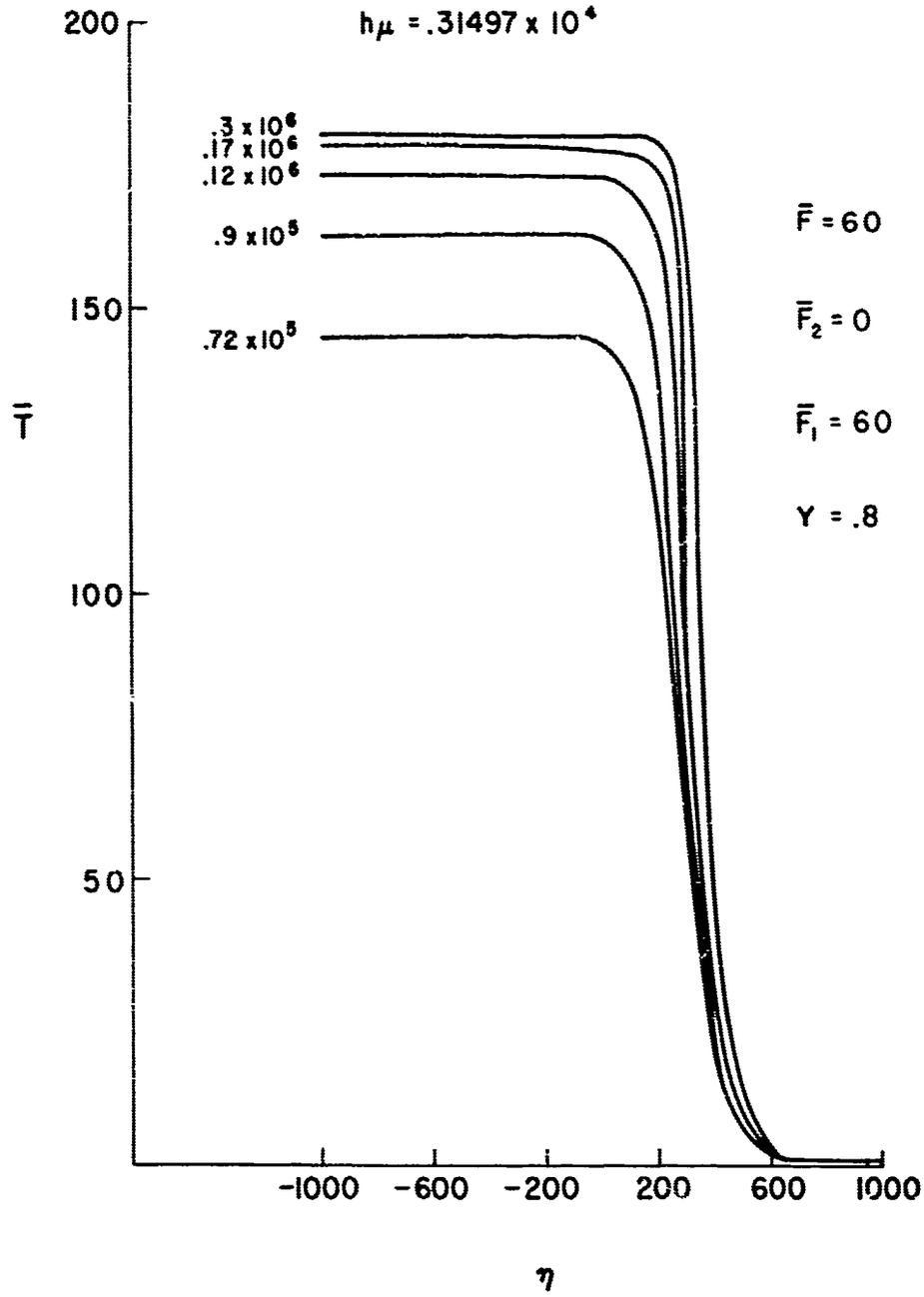


Fig. 9 $\bar{T}$ vs. η

$\bar{F} = 60$, $\bar{F}_1 = 60$, $\bar{F}_2 = 0$, $Y = 0.8$

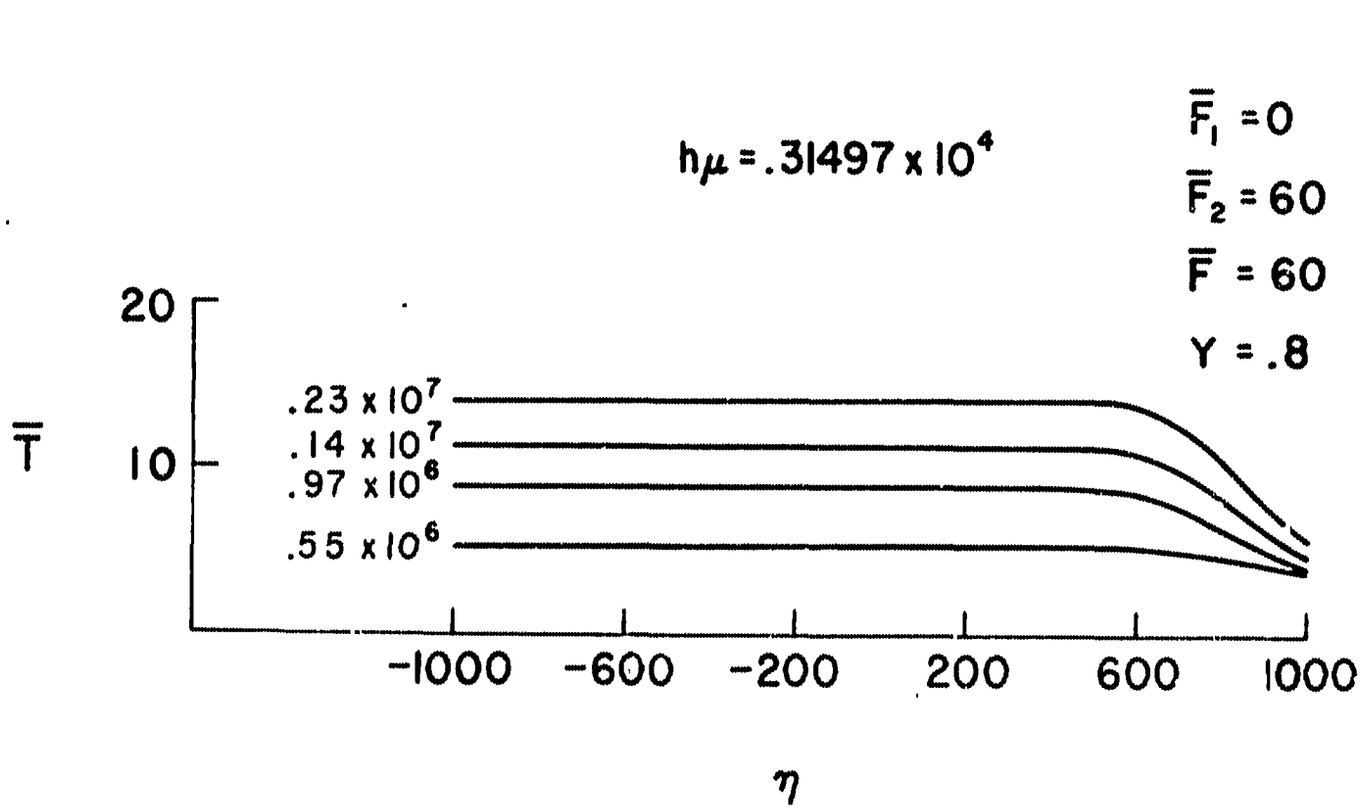


Fig. 10 $\bar{T}$ vs. η

$\bar{F} = 60$, $\bar{F}_1 = 0$, $\bar{F}_2 = 60$, $Y = 0.8$

position η for various values of $\bar{F}_1$, $\bar{F}_2$ and Y are represented in Figs. 16 through 24. These changes in electron density occur on a time scale of the order $\tau = 1/\nu_p = 1/\nu_i$. Eqs. 34 and 35 have been integrated numerically for $\bar{N}$ by choosing h_μ the temporal increment step size to equal a small fraction $\left(\frac{1}{100}\right)$ of $\left[1/\bar{\nu}_p\right]_{MIN}$. The quantity $\left[1/\bar{\nu}_p\right]_{MIN}$ is the smallest time scale for density changes for a particular pr[illegible] esponding to fixed values of $\bar{F}_1$, $\bar{F}_2$ and Y. The quantity $\left[1/\bar{\nu}_p\right]_{MIN}$ is the value of $\left(1/\bar{\nu}_p\right)$ at $\eta = -\eta_o$ and maximum, steady-state temperature. Figs. 16, 18, 21 and 23 all correspond to the same values for the quantities $\bar{F}_1$ and $\bar{F}_2$; only the value of Y differs. Figs. 16, 18 and 23 all exhibit the same general shape of the electron density profile as a function of time. Figs. 16, 18 and 23 correspond to case (1) where $\tau >> \tau_{EN}$. The general behavior of the electron density time-dependent response may be explained on the basis of the relative dilation and contraction of the time scale for density changes τ as a function of μ and η. In general, τ decreases rapidly as $\bar{T}$ increases.

Examination of Figs. 16, 17, 18, 19, 20, 23 and 24 reveals that for a particular time increment μ to $\mu + h_\mu$, the change in electron density decreases as η increases. This is due to the dilation of τ as $\bar{T}$ drops due to the wave attenuation as it propagates into the plasma. There is a great similarity in the behavior of the electron density response to the EM wave for the cases depicted in Figs. 16, 17, 18, 19, 20, 23 and 24. The

feature that distinguishes these figures from one another is the stroboscopic rate, that is, the value of the temporal increment step size h_μ changes. It should be noted that h_μ becomes shorter when: (a) the incident flux in the right-hand mode is increased when $\bar{F}$ and Y are held constant, or (b) Y approaches one (cyclotron resonance) when $\bar{F}_1$ and $\bar{F}_2$ are held constant.

The proximity of the wave frequency to cyclotron resonance (Y = 0.8) depicted in Figs. 21 and 22 has resulted in large values of $\bar{T}$ with a consequent sharp contraction of the time scale for density changes τ when $\eta < 0$. The quantity τ is contracted to the extent that it becomes the same order as τ_{EN} (case (2)). The feature that distinguishes Figs. 21 and 22 from the other figures of electron density changes is the alteration of the shape of the profile such that the density buildup in the vicinity of $\eta = 200$ is rapid enough to cause the incident flux to be quickly and effectively blocked from points further downstream ($\eta > 200$). This blocking of the incident flux causes $\bar{T}$ to decrease at points further downstream ($\eta > 200$) so that τ is greatly dilated. The large dilation of τ produces very minute changes in N_e for future successive time increments. Calculations have been performed for N_e vs η as a function of μ for $\bar{F} = 60$ and Y = 10. However, when Y = 10, the EM wave is so inefficient in heating the electrons that τ becomes an enormous number. Hence, there is essentially no electron density buildup on practical time scales.

Calculations were performed to determine the error incurred in using a finite (but small) increment step size in time and position when integrating the equations for $\bar{N}$ and $\bar{T}$. Using a value of $\left(\frac{1}{200}\right)\left[1/G\bar{\nu}\right]_{MIN}$ instead of $\left(\frac{1}{100}\right)\left[1/G\bar{\nu}\right]_{MIN}$ for h_μ in calculating $\bar{T}$ for $Y = 0.5$ and $\bar{F} = 40$ resulted in discrepancies of less than about 1%. Using a value of $\left(\frac{1}{200}\right)\left[1/\bar{\nu}_p\right]_{MIN}$ instead of $\left(\frac{1}{100}\right)\left[1/\bar{\nu}_p\right]_{MIN}$ for h_μ is calculating $\bar{N}$ for $Y = 0.5$ and $\bar{F} = 40$ resulted in relative errors of less than about 5%.

It should be emphasized at this point that the effects of particle diffusion and heat conduction within the electron gas have been neglected, but can be included in the analysis by a numerical relaxation procedure. The computations of the small frequency shifts of the right-hand and left-hand modes may be accomplished by finite difference techniques using Eqs. 14.1 and 14.2. These computations will be attempted in a future paper. The primary differences in the time-dependent temperature and density response of the magneto-plasma as contrasted with the isotropic plasma lie in the drastic contraction of the temperature time scale and density time scale near cyclotron resonance. It should be brought out that very close to cyclotron resonance, the plasma does not remain temperate, that is, the phase velocity of the right-hand wave approaches the thermal speed of the electrons. In this situation, effects such as heat conduction and collisionless cyclotron damping will become important.

The physical processes set forth in this paper have applicability to the

study of high-temperature shock waves in a magnetic field subjected to moderate power rf irradiation. The time-dependent response of rf irradiated shock waves for the isotropic case has been observed experimentally in a shock tube waveguide (Bethke et al[14]) and there has been qualitative agreement with theoretical calculations.

REFERENCES

1. King, J. I. F., The Dynamic Shielding Response of an Irradiated Plasma, RADC-TDR-62-48A, Feb. 1962.
2. Papa, R. J., Can. Jour. Phys. 43, 38 (1965).
3. Stix, T. H., The Theory of Plasma Waves, McGraw-Hill (1962).
4. Allis, W. P., S. J. Buchsbaum and A. Bers, Waves in Anisotropic Plasmas, M. I. T. Press (1963).
5. Holt, E. H., and R. E. Haskell, Foundations of Plasma Dynamics, New York: The Macmillan Co. (1965).
6. Westfold, K. C., Australian J. Sci. Res., 2, (Ser. A): 169, 1949.
7. Papa, R. J., Radio Frequency Propagation Through an Inhomogeneous, Magneto-Active, Nonlinear Plasma Medium, AFCRL-64-756 (Sept 1964).
8. Papa, R. J., Plane Wave Propagation in a Nonlinear, Inhomogeneous, Time-Dependent Plasma Medium, AFCRL-65-51 (Jan. 1965).
9. Poeverlein, H., Phys. Rev. 128, 956 (1962).
10. Johnston, T. W., Waves in Warm Quiescent Plasma, RCA Research Report 7-801, 12 (June 1961).
11. Papa, R. J., Phys. Fluids, 8, 1408 (1965).
12. Papa, R. J., The Nonlinear Interaction of an Electromagnetic Wave with a Time-Dependent Plasma Medium, AFCRL-64-250 (April 1964).
13. Sharofsky, I. P., Can. Jour. Phys. 39, (1961).
14. Bethke, G. W., Frohman, E. D., and Ruess, A. D., Phys. Fluids, 6, 593 (1963).

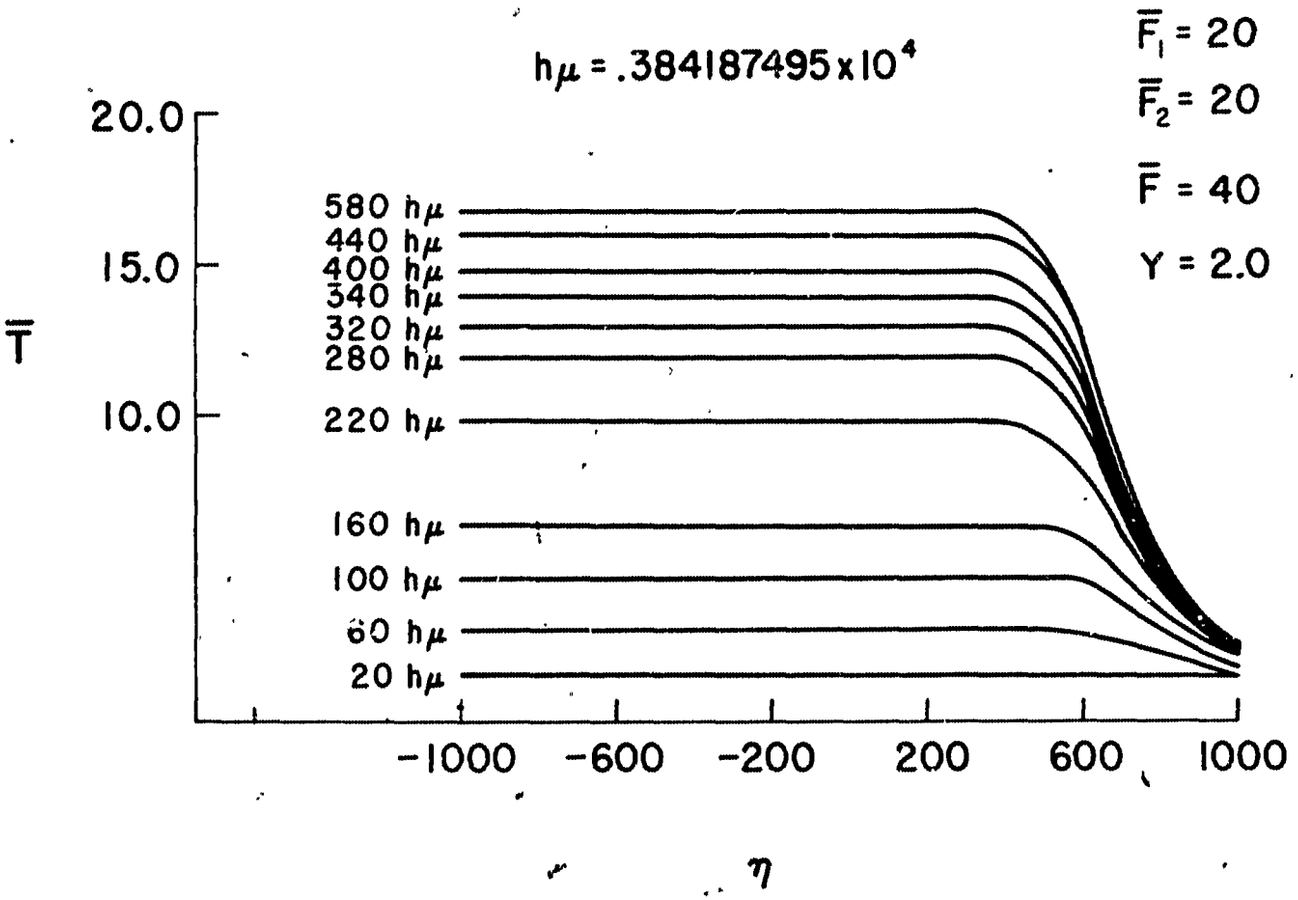


Fig. 11 ° $\bar{T}$ vs. η

$\bar{F} = 40$, $\bar{F}_1 = 20$, $\bar{F}_2 = 20$, $Y = 2.0$

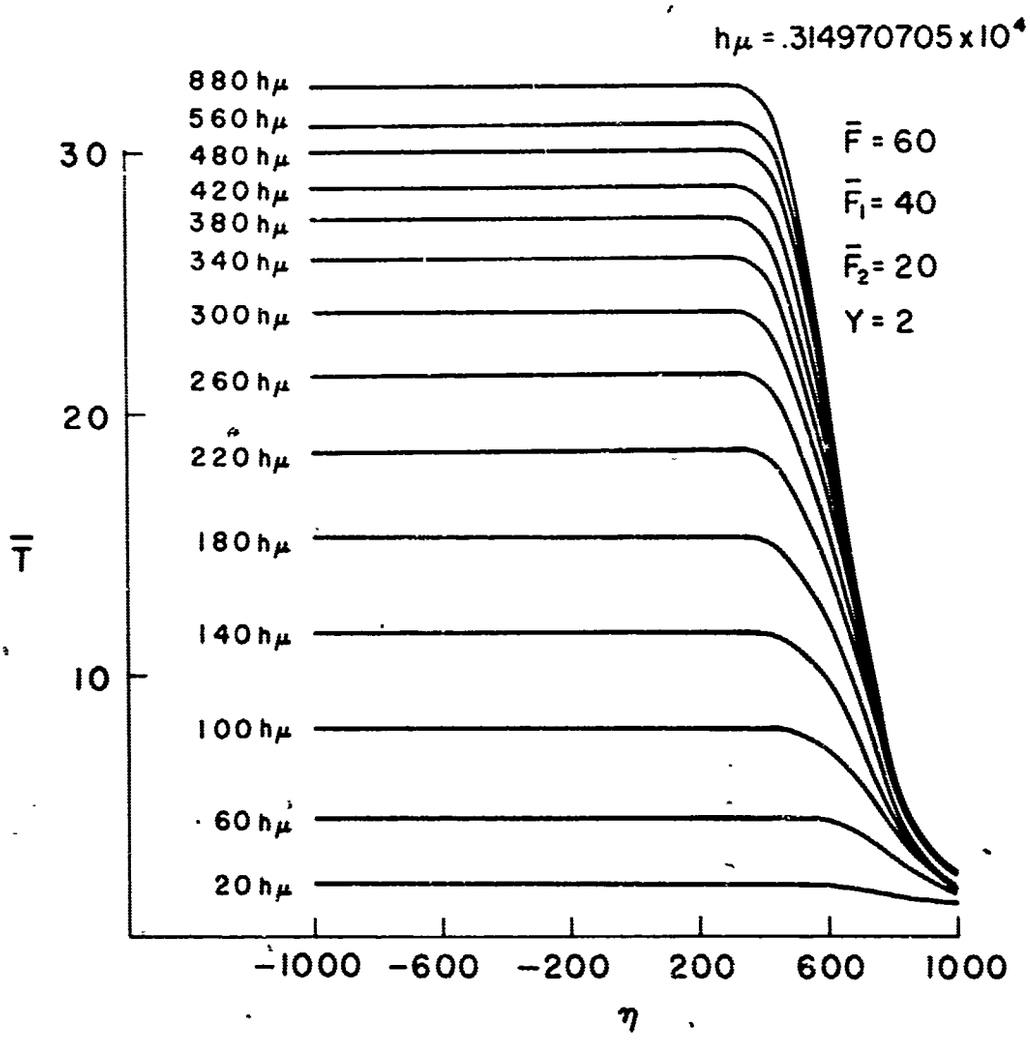


Fig. 12 $\bar{T}$ vs. η

$\bar{F} = 60$, $\bar{F}_1 = 40$, $\bar{F}_2 = 20$, $Y = 2.0$

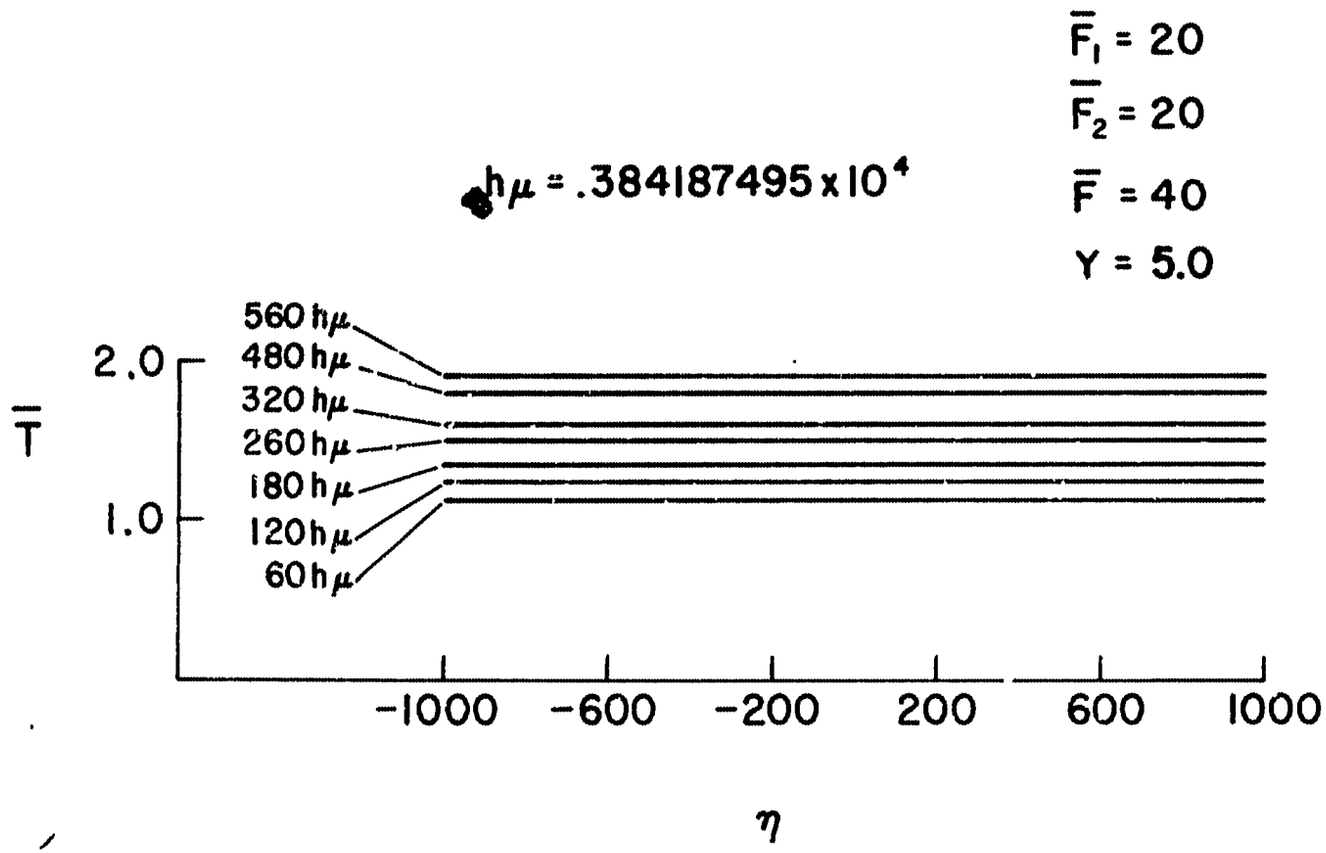


Fig. 13 $\bar{T}$ vs η

$\bar{F} = 40$, $\bar{F}_1 = 20$, $\bar{F}_2 = 20$, $Y = 5.0$

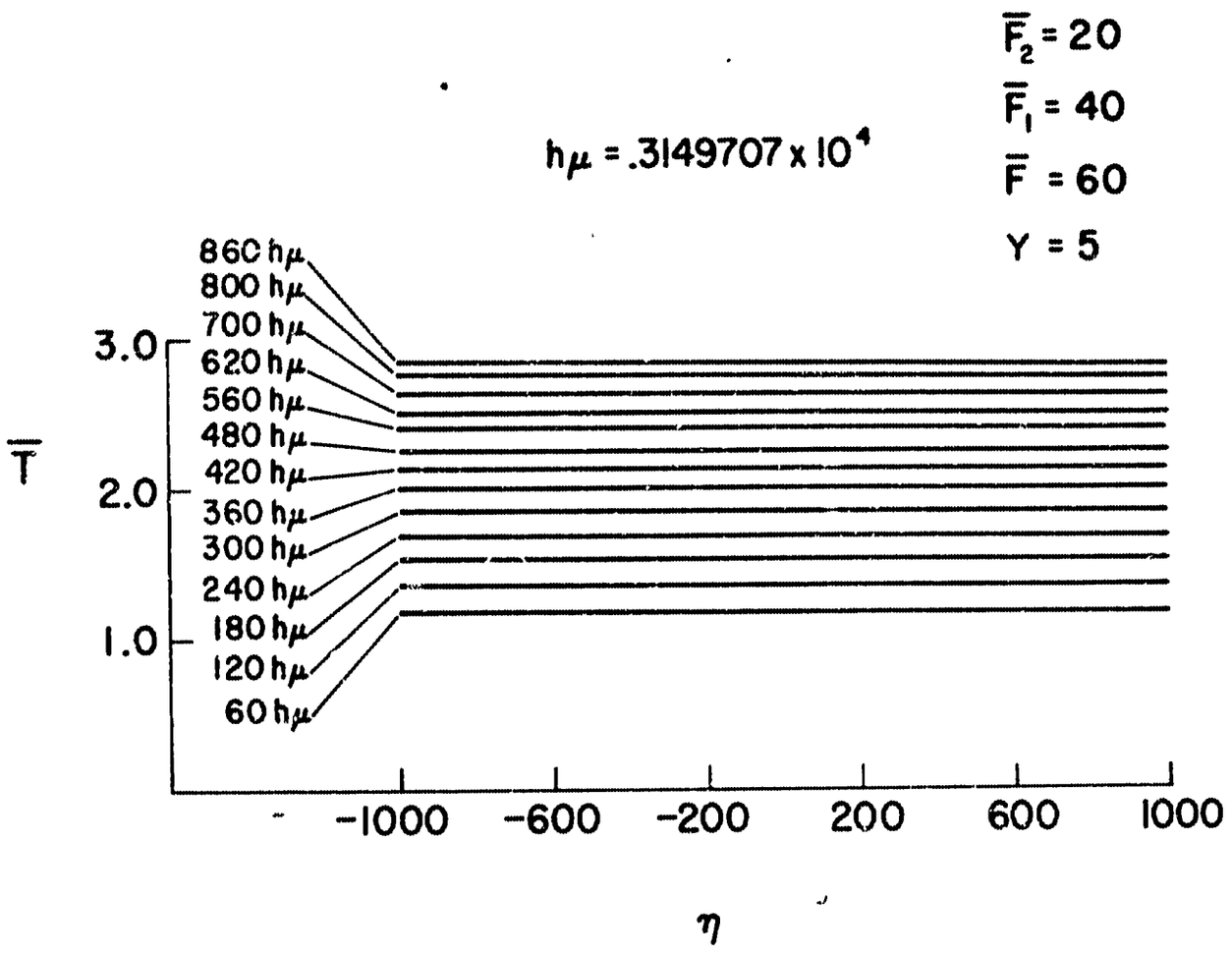


Fig. 14 $\bar{T}$ vs. η

$\bar{F} = 60$, $\bar{F}_1 = 40$, $\bar{F}_2 = 20$, Y = 5.0

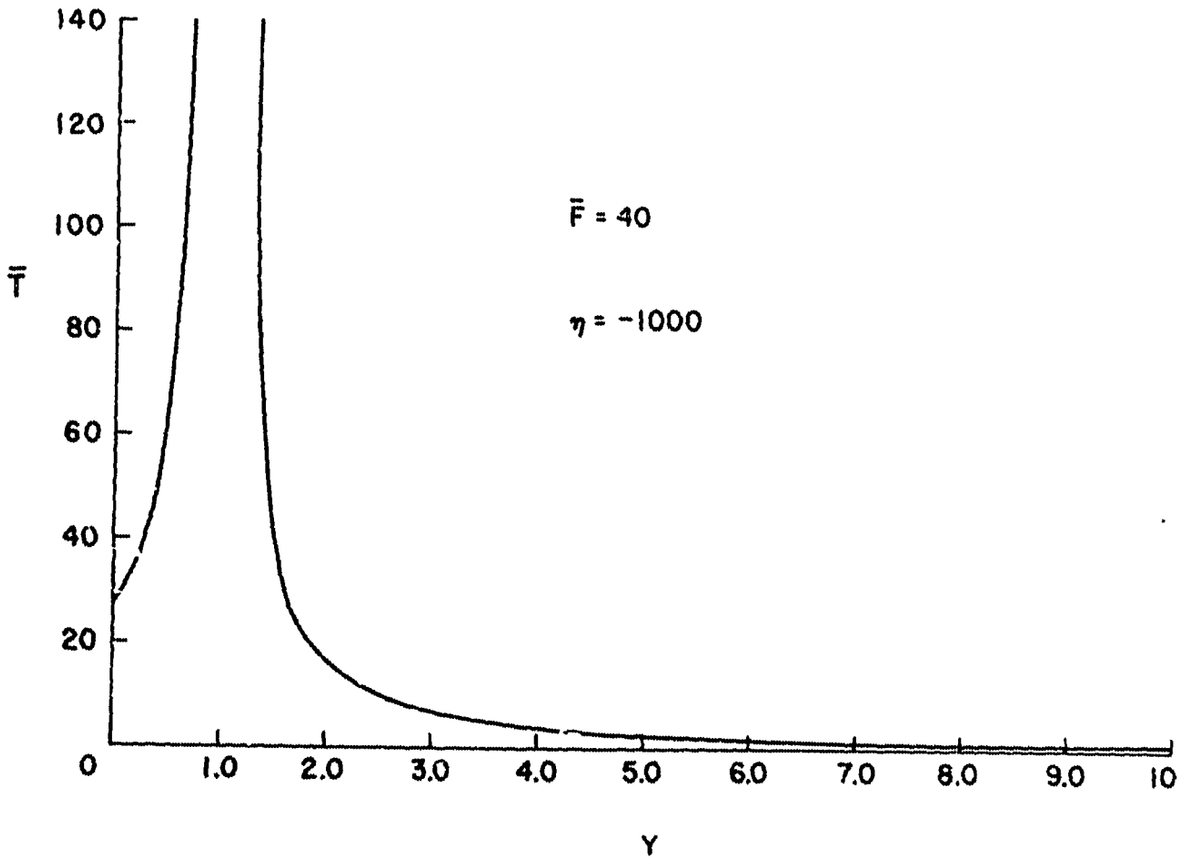


Fig. 15 $\bar{T}_s$ vs. Y

$\bar{F}$ = 40, η = -1000

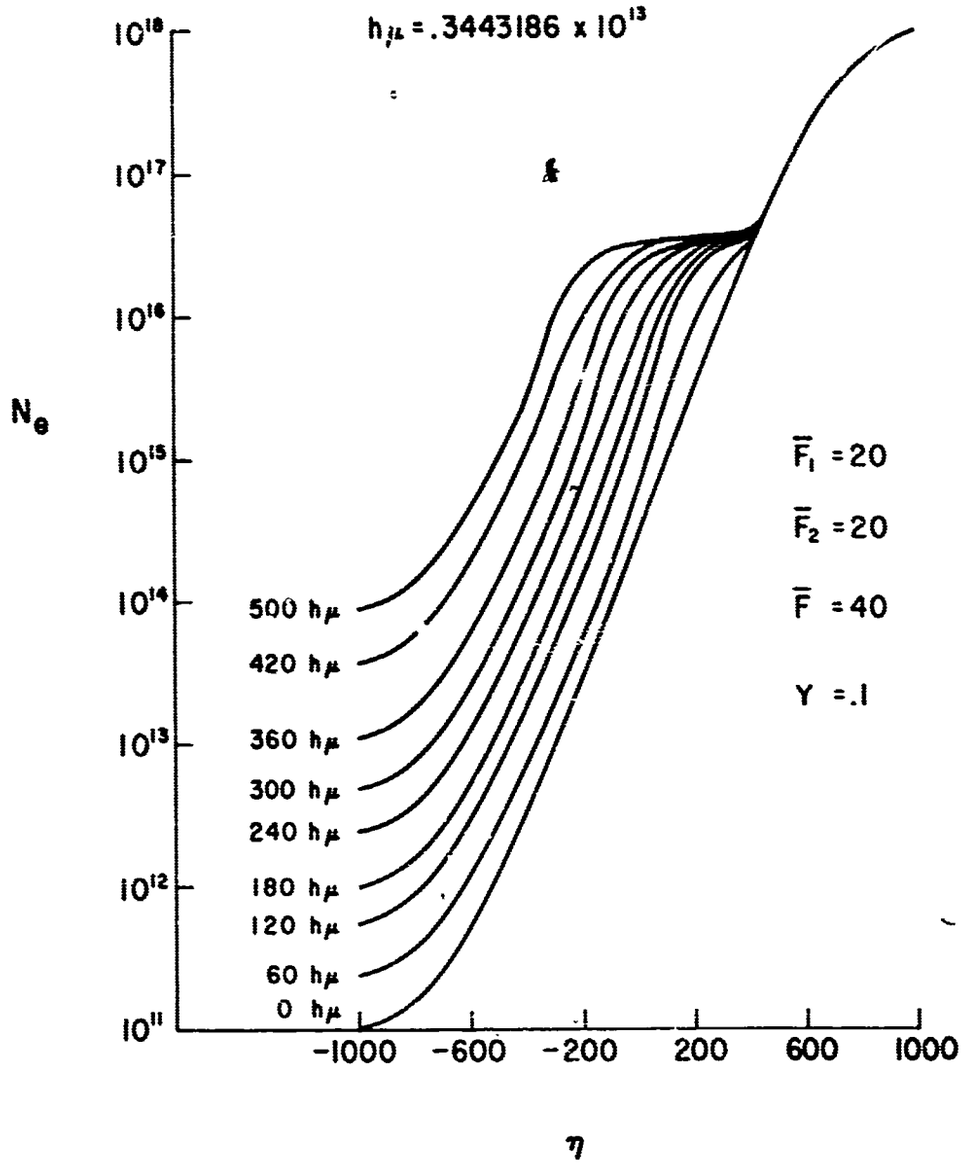


Fig. 16 N_e vs. η

$\bar{F} = 40$, $\bar{F}_1 = 20$, $\bar{F}_2 = 20$, Y = 0.1

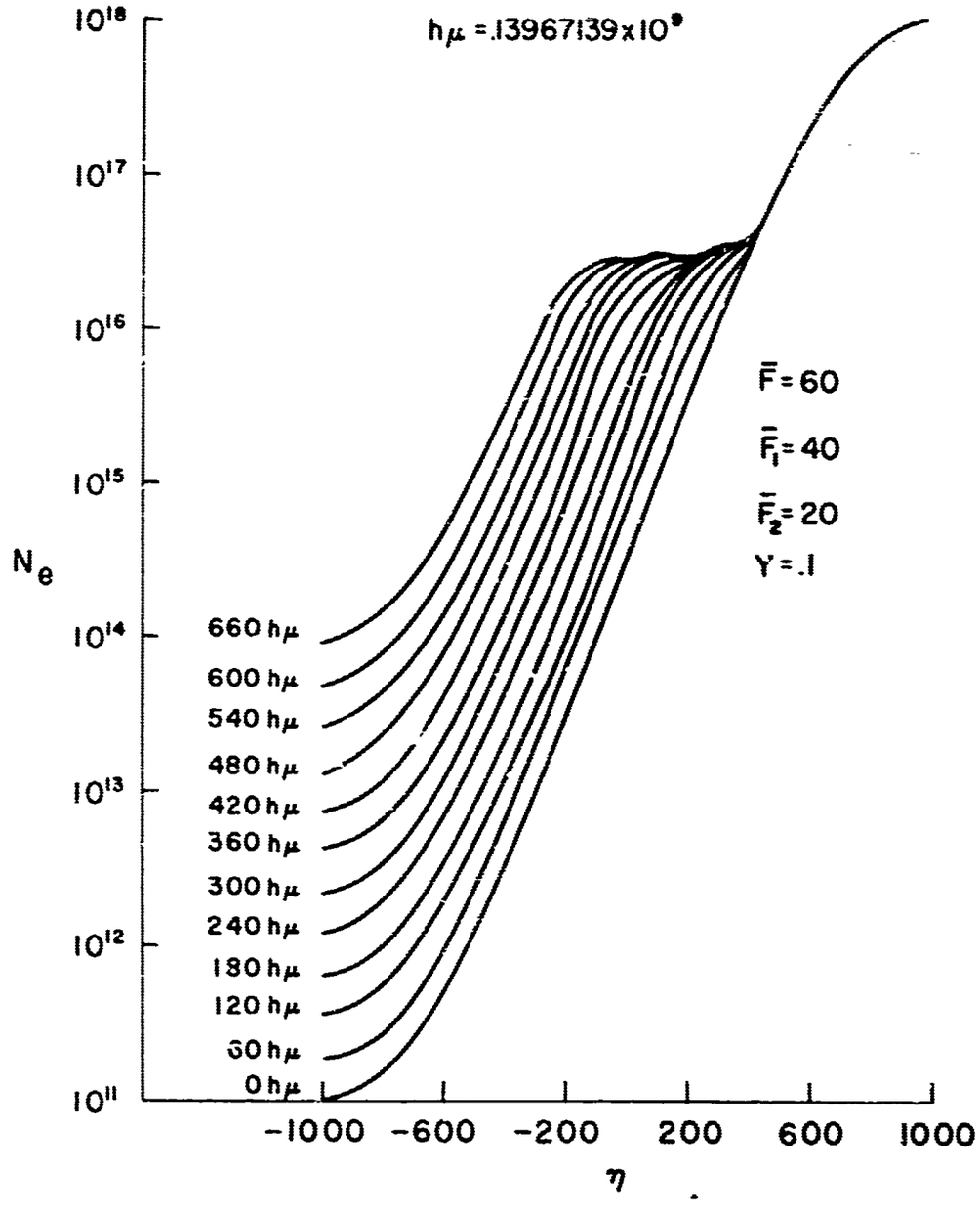


Fig. 17 N_e vs. η

$\bar{F} = 60$, $\bar{F}_1 = 40$, $\bar{F}_2 = 20$, $Y = 0.1$

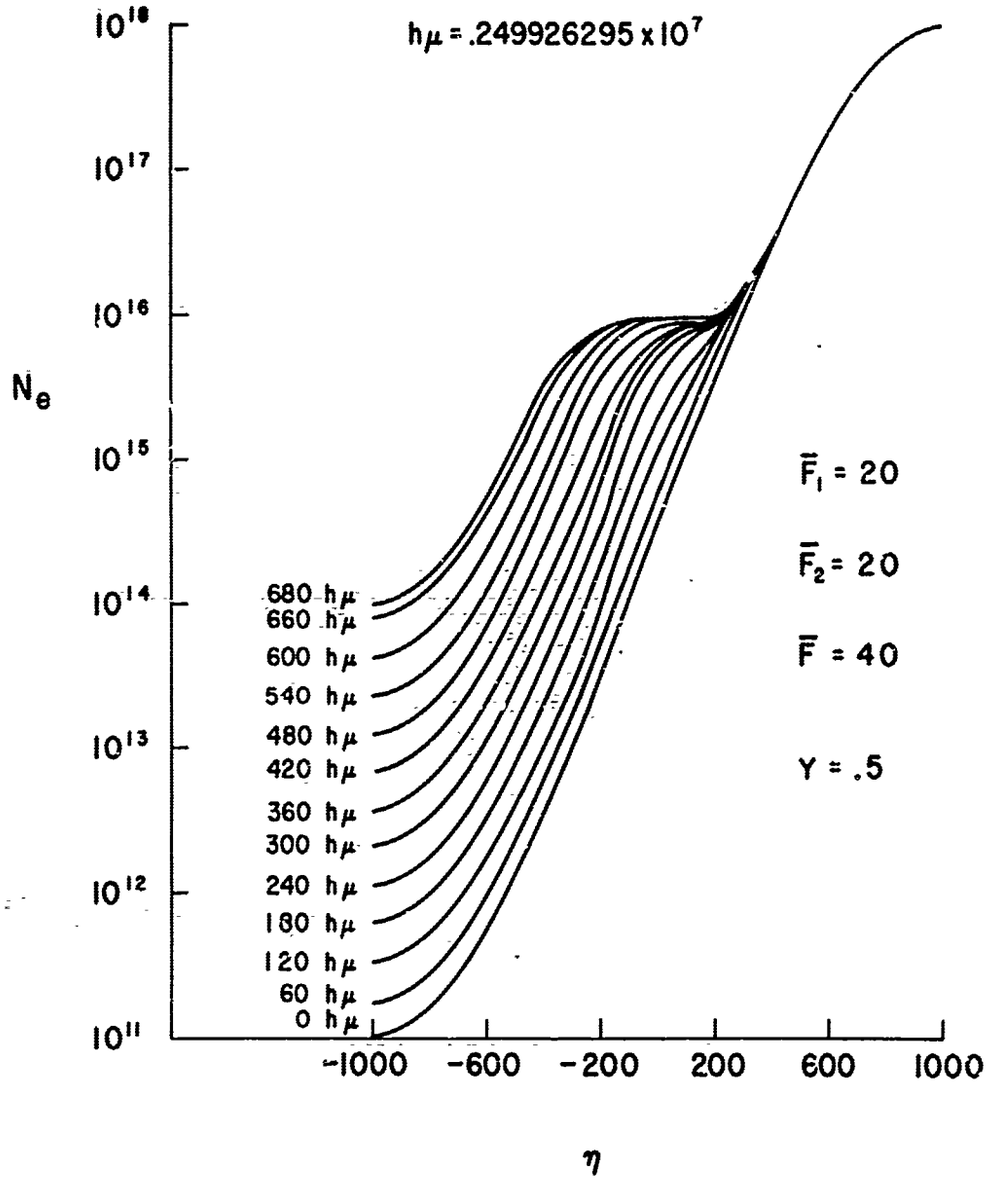


Fig. 18 N_e vs. η

$\bar{F} = 40$, $\bar{F}_1 = 20$, $\bar{F}_2 = 20$, $Y = 0.5$

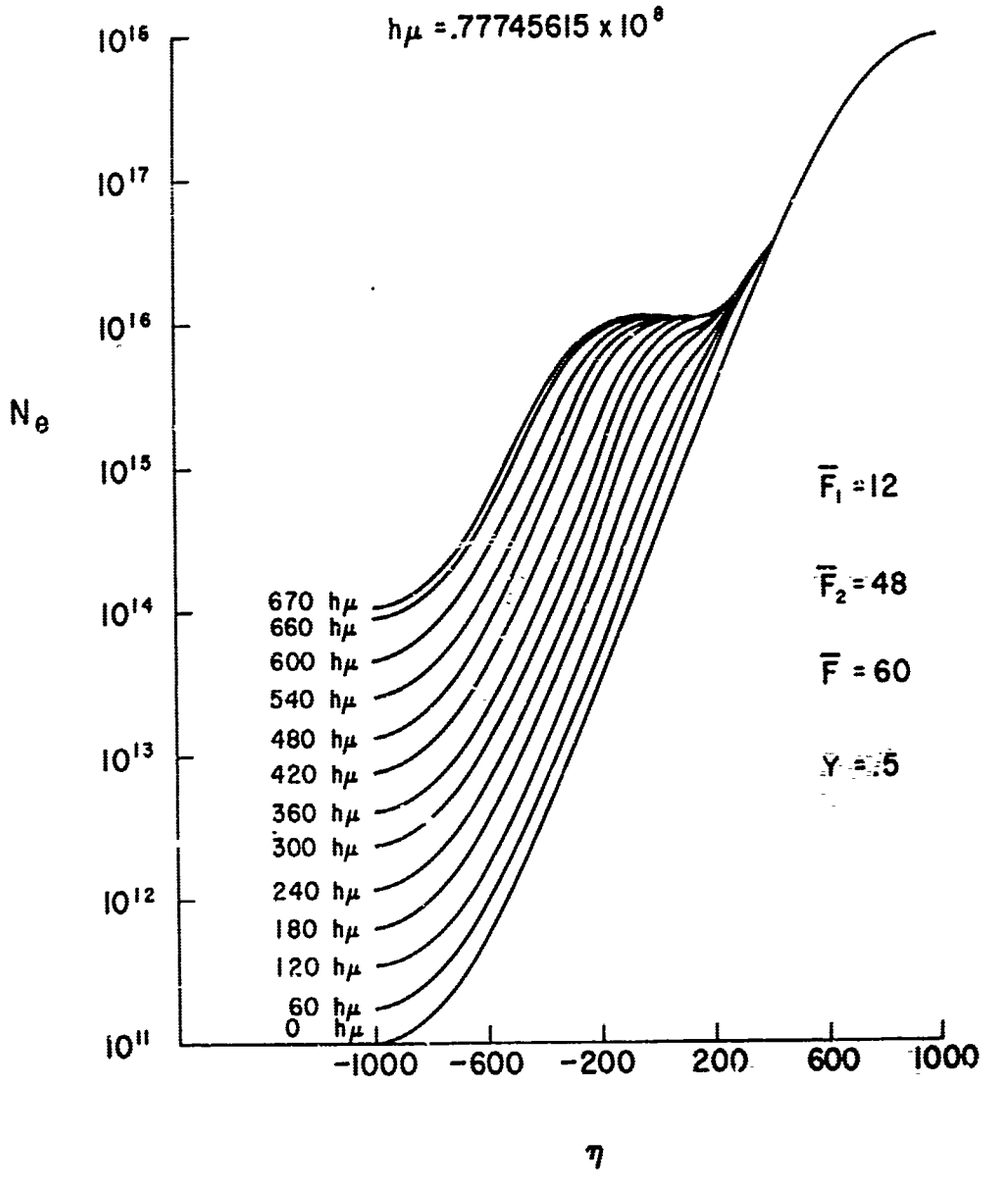


Fig. 19 N_e vs. η

$\bar{F} = 60$, $\bar{F}_1 = 12$, $\bar{F}_2 = 48$, $Y = 0.5$

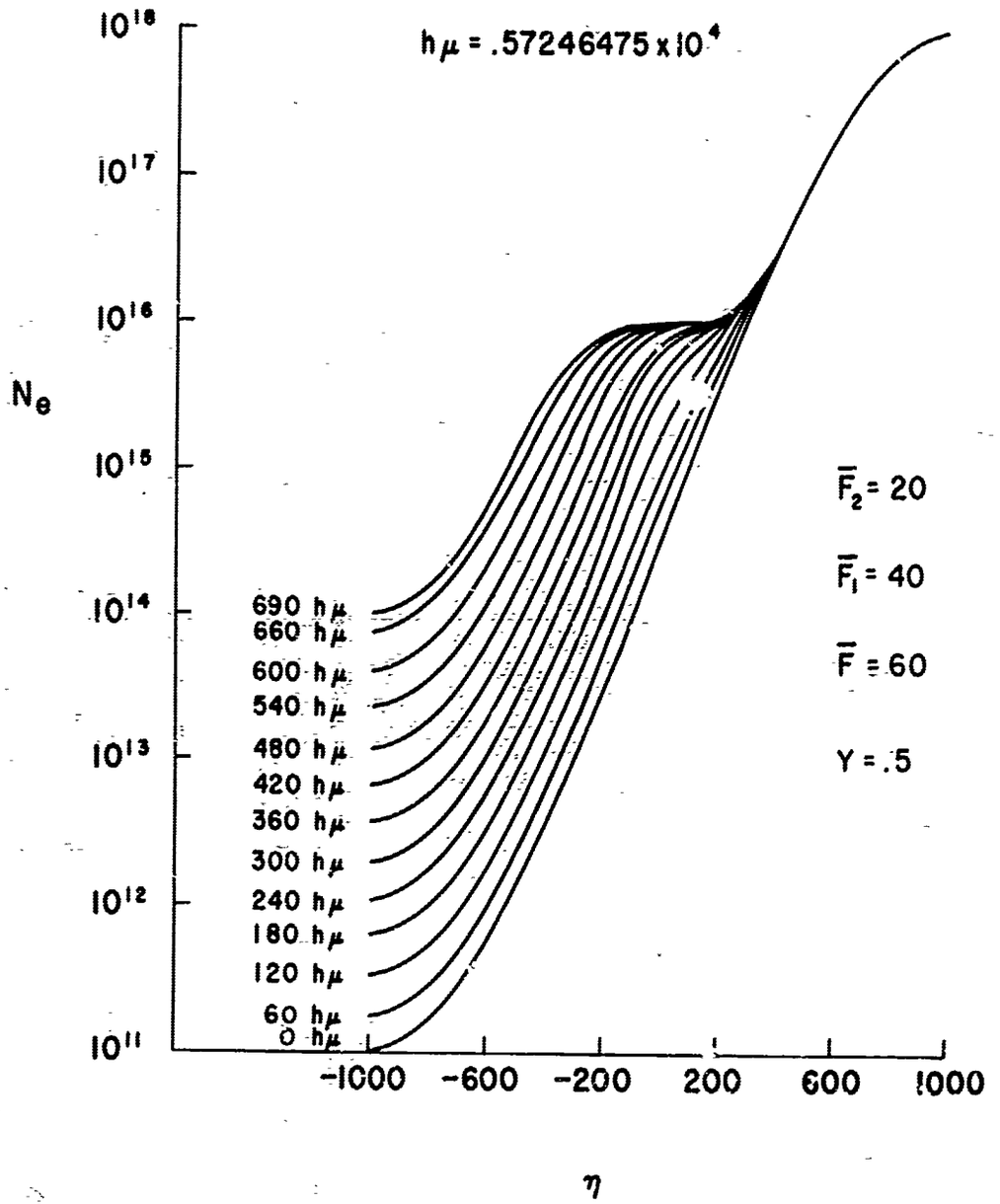


Fig. 20 N_e vs η

$\bar{F} = 60$, $\bar{F}_1 = 40$, $\bar{F}_2 = 20$, $Y = 0.5$

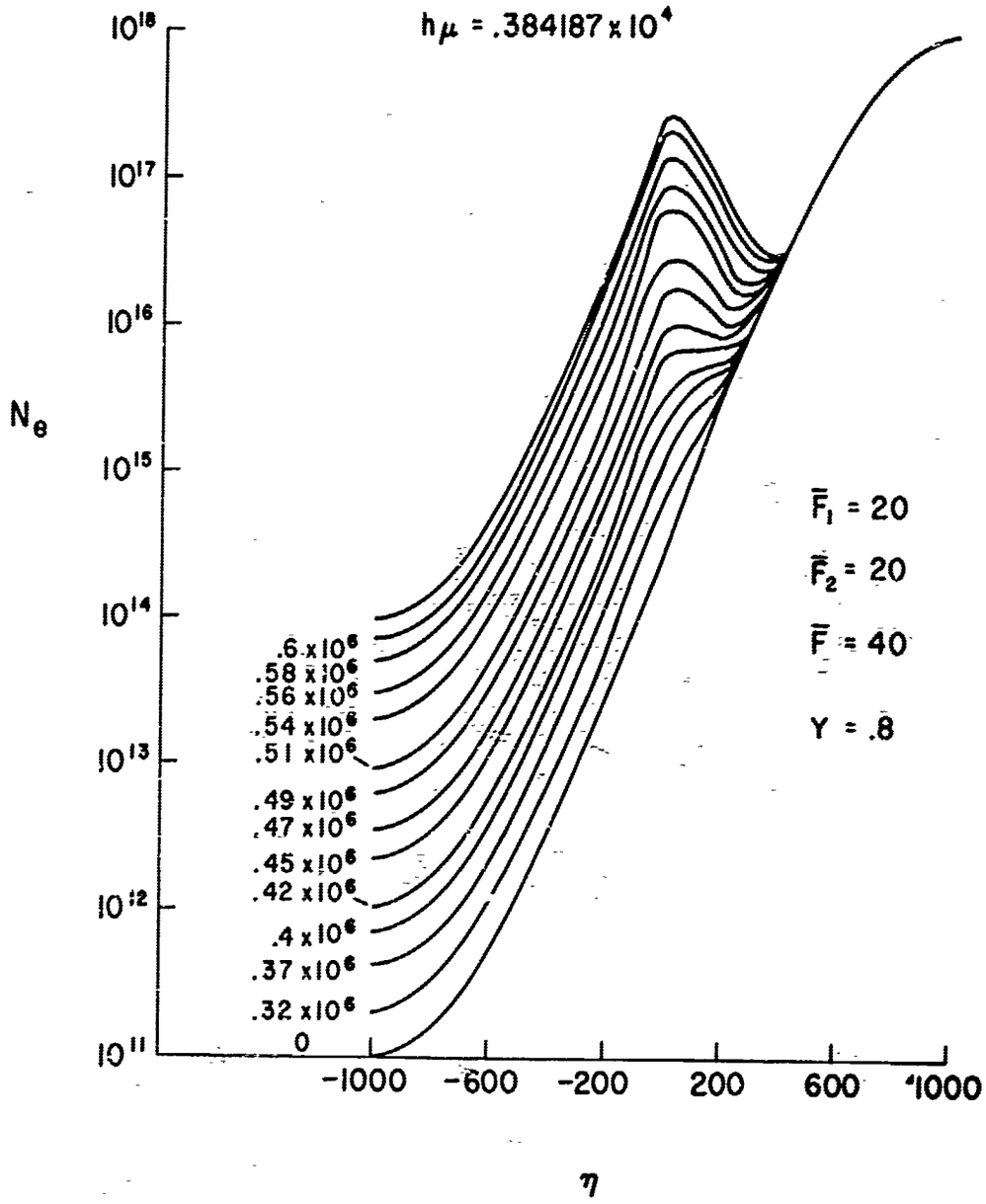


Fig. 21 N_e vs η

$\bar{F} = 40$, $\bar{F}_1 = 20$, $\bar{F}_2 = 20$, $Y = 0.8$

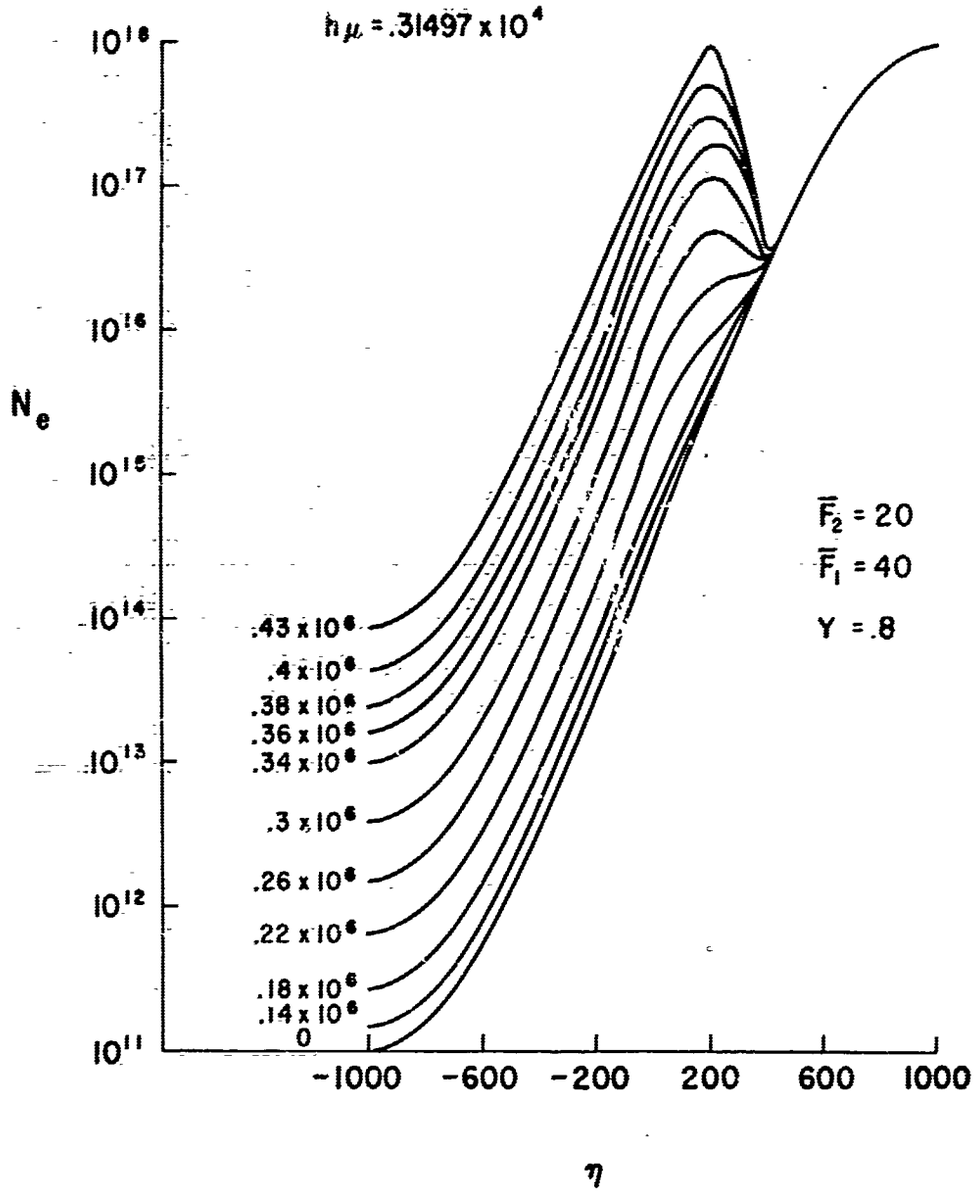


Fig. 22 N_e vs η

$\bar{F} = 60$, $\bar{F}_1 = 40$, $\bar{F}_2 = 20$, $Y = 0.8$

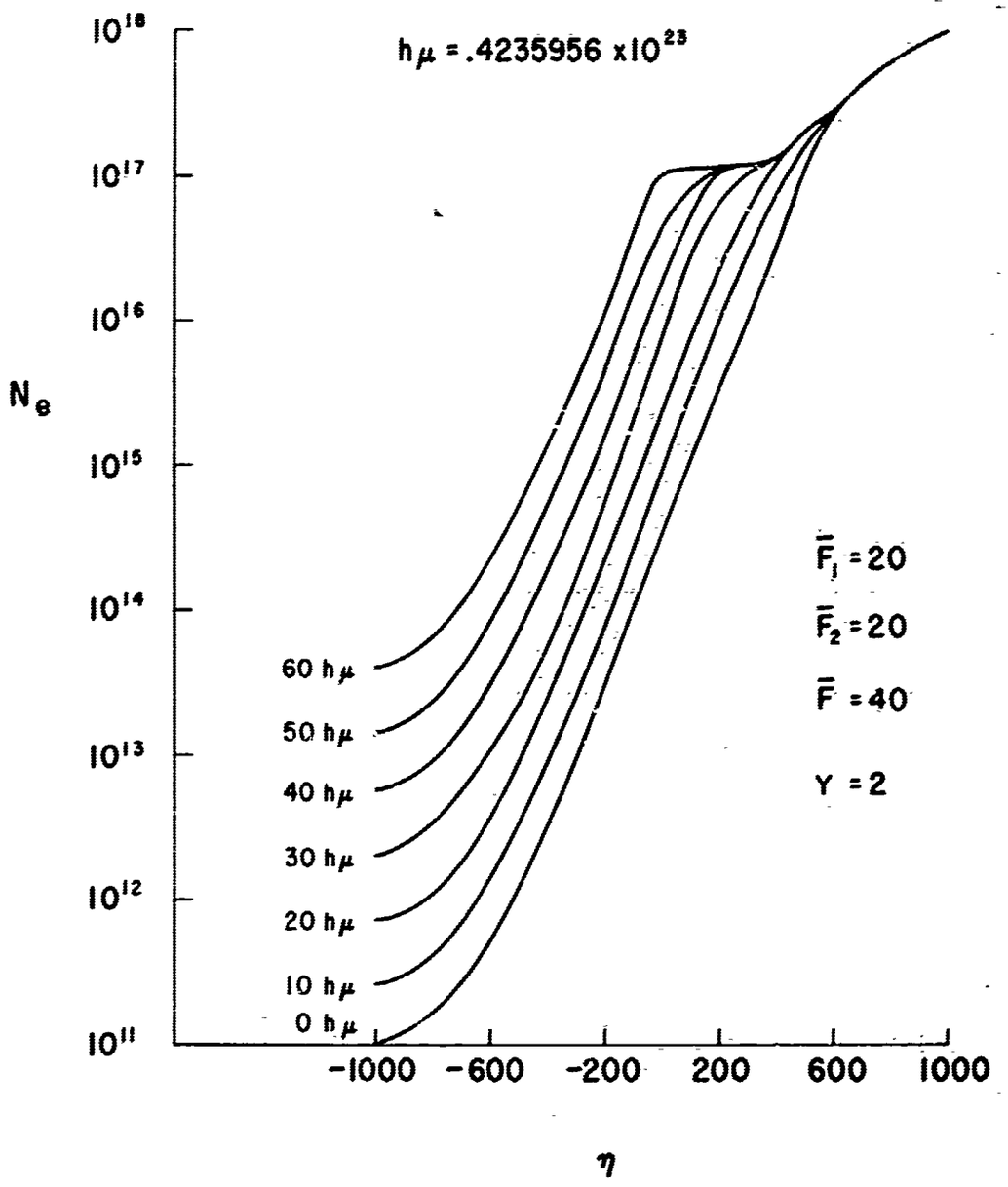


Fig. 23 N_e vs η

$\bar{F} = 40$, $\bar{F}_1 = 20$, $\bar{F}_2 = 20$, Y = 2.0

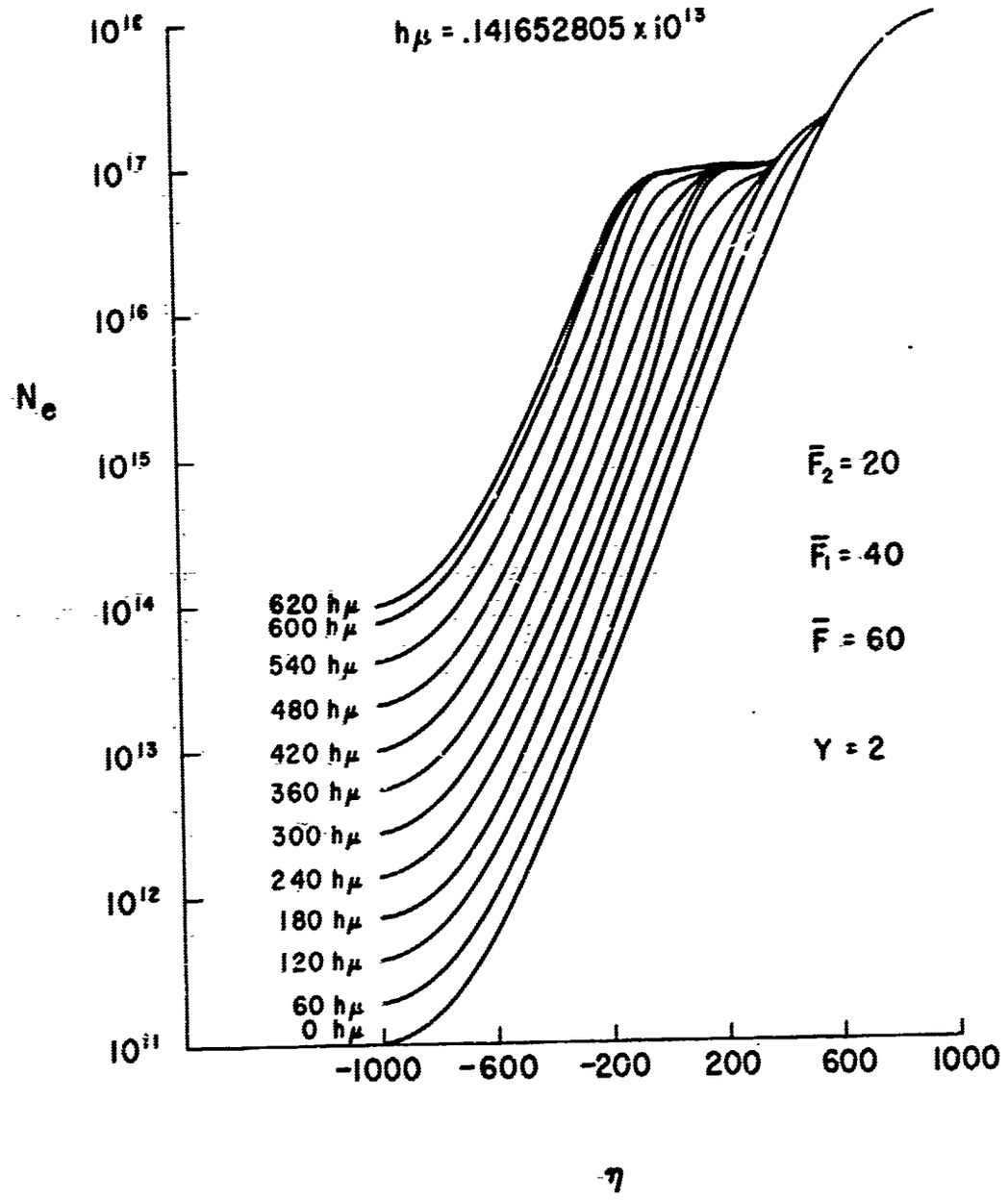


Fig. 24 N_e vs η

$\bar{F} = 60$, $\bar{F}_1 = 40$, $\bar{F}_2 = 20$, $Y = 2.0$

VII. EFFECTS OF RE-ENTRY AND SPACE ENVIRONMENTS ON ANTENNA BREAKDOWN

by

J. B. Chown, W. C. Taylor, E. F. Vance
J. E. Nanevicz, and T. Morita

Stanford Research Institute
Menlo Park, California

ABSTRACT

When an antenna is remote from a plasma through which it radiates, the effects of the plasma upon the power transmitted beyond it are determined essentially by the RF frequency in addition to the plasma frequency and collision frequency (as functions of position). In many missile/space applications, however, the antenna is either adjacent to or immersed in a plasma, and the ability to radiate power beyond the plasma depends upon many additional parameters, such as antenna configurations, size, material, and power, and upon the RF ionization rates, electron attachment rates, and diffusion properties of the plasma.

This paper reports both theoretical and experimental studies conducted to determine the quantitative effects of these parameters in three

The work reported was sponsored by Air Force Cambridge Research Laboratories.

main areas of practical interest. The first was the power-independent case in which an existing plasma (e.g., the re-entry sheath) in the antenna near fields alters its impedance and far-field radiation characteristics by (1) dissipating energy normally stored in near fields and (2) redistributing near fields and surface currents, in addition to the usual wave attenuation. Decreases in far-field radiation exceeding 10 dB were measured due to the near-field effects alone at plasma frequencies less than critical.

The second problem considered was voltage breakdown when the thermal plasma density is near or beyond critical. As the initial plasma increases in density, the breakdown process appears to become less abrupt and the threshold for nonlinear effects is lowered. However, the general conclusion is that a certain maximum level is reached beyond which the power transmitted beyond the antenna is independent of the power delivered to the antenna, due to the increased ionization produced by the RF.

Finally, consideration was given to voltage breakdown by the multipactor discharge mechanism which occurs in many RF structures when the electron mean free path becomes large compared with the structural dimensions. For high-Q systems, power levels of less than 10 watts can produce such discharges. Since most of the electron energy is dissipated on the antenna surface each half cycle, the power dissipated in the discharge depends on the frequency. Although multipactor discharge does not require the presence of gas molecules for its existence, the loss mechanisms and the threshold power levels are affected by the presence of a plasma.

I INTRODUCTION

In the design of antennas for use in space and on hypersonic re-entry vehicles, the effect of the plasma surrounding the vehicle must be considered. In addition to the problems encountered by telemetry and beacon systems, added interest is due to ECM as a penetration aid and to the use of RF probes for diagnostic purposes.

This paper is concerned with certain problem areas that arise due to the close interaction between the fields of the antenna and a nearby ionized medium. This interaction due to proximity of radiator and medium requires consideration of parameters that are not involved in the usual RF-plasma interaction. For example, the power-handling capability of an antenna radiating high power through an ablating dielectric surface of a hypersonic vehicle depends upon the RF fields created in the flow medium as well as electron production and loss rates in both the pure gas shock layer and ablator-contaminated boundary layer.

Two classes of problems to be discussed are in the usual gas discharge pressure regime where the electron mean free path in the gas is smaller than the dimensions of the antenna. They are: (1) the case for antennas operating at low power when existing plasma in the near fields dissipates power, changes antenna impedance, and alters the far-field radiation characteristics, and (2) the extension of the weak-field problem to strong-field regimes when the plasma is altered by RF ionization and electron heating.

Attempts to radiate high RF power from a re-entering missile will experience a combination of these two classes of effects, and this combination is understood even less than the separate phenomena as discussed above. However, according to the experimental evidence at hand, if the fields are sufficient to produce breakdown, and the thermal plasma alone is relatively thin, the major portion of the losses in total radiated power can be predicted as if ordinary breakdown were the only phenomenon acting.

A third problem area to be discussed lies in the lower pressure regime where the mean free path exceeds the antenna dimensions. Under this condition, multipactor or electron emission, resonance-controlled discharges can occur, resulting in reduction of radiated signal. The presence of the plasma due to the ionosphere may enhance the possibility of such a discharge.

II NEAR-FIELD EFFECTS

When a weak electromagnetic wave propagates through a plasma, the attenuation per unit length can be rather simply calculated on the basis of the conventional attenuation constant, α, which is a function of the wave frequency only in addition to the plasma properties. Similarly, when such a wave is incident upon a plasma-space interface, the reflection of the wave can be calculated using the wave frequency in addition to the plasma properties, and these two types of losses in a propagating wave are the only ones to be considered in many cases. In addition to these, however, i. a second class of RF losses, applicable to weak signals, due to the proximity of dissipative and/or reactive plasmas to these near-fields. There are three main effects: (1) Those electric near-fields which in free space are purely reactive become dissipative to some extent because they induce shunting currents in the conductive plasma, with ohmic losses resulting; (2) the field components contributing to the radiation are altered, hence the pattern is modified; (3) the altering of near-fields and currents is seen at the antenna input terminals as a change in overall impedance of the antenna, with attendant matching problems. Depending upon the type of antenna and the nature and extent of the plasma, any of these three effects could result in severe losses of power radiated, either totally or in a desired direction.

A measure of the near-field dissipation losses has been obtained by deriving the efficiency for an antenna immersed in a homogeneous plasma. The power radiated to a far-field distance r is proportional to $R_p e^{-2\alpha r}$,

where R_p is a function of the antenna dimensions and plasma properties but is not a function of r and α is the attenuation coefficient of the plasma. The total power dissipated by the antenna is proportional to $Re(Z_p)$ where Z_p is the antenna impedance in plasma. The efficiency is then the ratio

$$\eta = \left[\frac{R_p}{Re(Z_p)}\right] e^{-2\alpha r} = \eta_p e^{-2\alpha r} \quad . \qquad (1)$$

The exponential factor in Eq. (1) is the usual attenuation for propagating over a distance r. Thus η_p is a figure of merit for power dissipated in the near-fields. Figure 1 gives a graph of η_p derived for short dipoles and loops as a function of the plasma frequency ω_p normalized by ω, for ratios of collision to the RF frequency (ν/ω) of 1 and 0.1. The dipole length and the loop diameter were both chosen for this figure to be 1/10 wavelength, and the thickness of each to be 1/100 wavelength. Also plotted in Fig. 1 is the attenuation per wavelength of travel, $e^{-2\alpha\lambda_p}$, where λ_p is the RF wavelength in the plasma. The importance of the near-field losses compared with the ordinary attenuation factor in the region $(\omega_p/\omega)^2 \lesssim 1$ is demonstrated by Fig. 1. For values of ω_p/ω less than unity, the effect of the near-field loss predominates over the attenuation loss in the propagating wave for the electric dipole with the large reactive near field. For the loop, the stored energy is mostly in the magnetic field and hence the near-field loss is lower.

Figure 2 shows measurement of the efficiency of a dipole in a plasma formed by a sodium-seeded hydrocarbon flames, compared with the predicted efficiency. An integration over the nonuniform plasma in the flame was used to obtain the exponential attenuation factor, and the measured plasma properties at the dipole tip were used for the prediction of η_p shown in Fig. 2.

III BREAKDOWN THEORY

In the extreme case of nonlinearity in either intially ionized or un-ionized gases, the electric fields are strong enough to produce additional

ionization in the gas. The resulting breakdown proceeds catastrophically until the electron density is high enough that the plasma thus formed limits, by attenuation and reflection, the strength of the RF fields penetrating the plasma. Such limiting does not occur until the plasma frequency exceeds the wave frequency. Although the details and the extent of the propagation within the resulting plasma are not well understood, tests have shown that the plasma will grow to a thickness such that the fields penetrating beyond it are just below the levels required to maintain a discharge under the existing local conditions of pressure, frequency, etc. When the initial plasma density about an antenna is such that $\omega_p \gtrsim \omega$, the electron density in the plasma does not increase precipitously, but transitions gradually into the nonlinear regime when the RF fields are made strong enough to add to the ionization.

A solution to the problem of predicting threshold power levels for breakdown due to RF ionization of room temperature air can be obtained by the use of empirical data in connection with the electron continuity equation.[1,2,3] Equating the electron production and loss rates gives a relationship for the ionization rate required to overcome the various losses, resulting in a discharge in the high-field regions. However, the hypersonic environment complicates the predicting problem because:

(1) The empirical data are for the most part not available for high-temperature pure air or ablation-contaminated air.

(2) The heated layers of gas are nonuniform in temperature, gas density, and electron density.

(3) The velocity of the flowing gas provides an additional loss mechanism for electrons in the high-field regions.

The steady-state electron continuity equation with velocity effect excluded is

$$\nu_i n = \nu_a n - \nabla^2 Dn \qquad (2)$$

where n is the electron density, ν_i is the RF ionization rate, ν_a is the

attachment rate, and D is the appropriate diffusion coefficient. In re-entry situations, all of the parameters in Eq. (2) may be functions of position because of nonuniform gas conditions.

The neglect of recombination in Eq. (2) restricts its validity to describing electron densities below the levels where recombination is an important loss process. Since there is considerable uncertainty in the recombination coefficient for air, especially at high temperatures, it is difficult to determine the lower limit of electron density above which recombination is important. It has been predicted to be anywhere from 10^9 to 10^{12} cm^{-3} or greater.

In principle, Eq. (2) can be solved for n as a function of position, using appropriate boundary conditions for the geometry of the problem. This solution of Eq. (2) will provide a relationship giving the level of the ionization rate required to barely offset the electron loss rates. Call this particular level ν_o. When an unlimited time is available for the build-up of electron density, an infinitesimal increase of ν_i over ν_o will be sufficient to produce a discharge, where "discharge" is usually defined as an indefinite increase in n. However, an unlimited time is not available for the case when the flow sweeps the gas out of the region of exposure to the RF. Consequently, the rate ν_i obtained from Eq. (2) will produce only an infinitesimal increase in the initial electron density in the flow during any finite available time. In practice, for breakdown to be recognized, some critical electron density level n_c must be attained, where n_c is usually much greater than the initial density. In addition, transit time over the RF aperture may be less than 10^{-5} seconds. Consequently, the ionization rate required to increase n to n_c during the exposure time, t, will be greater[4] than ν_o.

To a first approximation, the electron density growth in time at a given position is given by

$$n = n_o e^{\nu_e t} \tag{3}$$

where n_o is the initial density, and ν_e, the local excess of the ionization rate over the loss rate, is assumed to be constant during the time interval of interest. For simple configurations, the steady-state loss rates can be obtained from the solution of Eq. (2) as the sum of separate terms in the form $(\nu_a + D/\Lambda)^2$ where Λ is the effective diffusion length and depends on the configuration. A particularly simple example of diffusion length is that for a discharge between intinite parallel plates with separation d, giving $\Lambda = d/\pi$.

It is approximately true that the losses determined by the steady-state solution are valid for the entire time interval of interest, giving

$$\nu_e = \nu_i - \nu_a - D/\Lambda^2 \quad . \tag{4}$$

To determine the ionization rate required to increase n from n_o to n_c in an exposure time τ, ν_e in Eq. (4) is substituted into Eq. (3). Then, using $n = n_c$ and $t = \tau$, solving explicitly for ν_i gives

$$\nu_i = \nu_a + D/\Lambda^2 + \frac{\ln(n_c/n_o)}{\tau} \quad . \tag{5}$$

Since $\nu_o = \nu_a + D/\Lambda^2$ the excess of ν_i over ν_o required for attaining n_c during the finite interval τ is given by the last term in Eq. (5). This term can be used to evaluate the effect of any limited exposure time--for example, when the RF is pulsed for a duration τ. If the solution occurs where the exposure is limited by both RF pulsing and flow, the value of τ used in Eq. (5) would be either the RF pulse width or the flow transit time, whichever is smaller.

In Eq. (5), ν_i, ν_a and D are all functions of gas density. This usually results in some loss processes being more important than others, depending upon the atmospheric gas density, and in there being a range of gas density where breakdown is produced with a minimum RF power. When the gas density is lower than at the minimum breakdown power level, the important loss term in Eq. (5) is usually the diffusion term, D/Λ^2. The

diffusion coefficient D, besides being a function of gas density, also depends on the electron density. At very low n, the electrons diffuse freely out of the high field regions, independently of the heavier positive ions. But as n increases, the Debye shielding length becomes small and the electron mobility is reduced because of the space-charge fields acting upon it. This is called ambipolar diffusion in the limit of $n \gg (kT/4\pi e^2 L^2)$, where k is Boltzmann's constant, T is the temperature, e is the electronic charge, and L is the characteristic scale length for spatial gradients in n. Plasma surrounding re-entry vehicles will often have electron densities sufficient to make the diffusion ambipolar. For ambipolar diffusion, D is 1/40th the free diffusion value. Consequently, when diffusion is the only important loss mechanism, the breakdown power may be reduced significantly in the presence of plasma. The resulting reduction in RF power threshold is illustrated by Fig. 3, showing the power required for breakdown of an L-band slot antenna, for the two limits of free and ambipolar diffusion, as a function of collision frequency. It is seen from Fig. 3 that this reduction is especially important at high altitudes (low collision frequencies).

The high nonuniform electron density around some re-entering vehicles complicates the important problem of determining whether the diffusion will be free or ambipolar, or essentially a combination of the two. Consider the case of a sharp-nosed body with only the hot boundary layer having n high enough that diffusion might be ambipolar. The requirement that diffusion in this layer be ambipolar is the Debye shielding length be much less than the scale factor for density gradients. If n in the boundary layer has an approximately cosinusoidal variation normal to the vehicle surface, this scale factor will be $L \approx \Delta/\pi$, where Δ is the layer thickness. Thus, for ambipolar diffusion, the maximum n in the layer must satisfy the inequality

$$\sqrt{n_{max}} \gg \frac{7\pi\sqrt{T_e}}{\Delta} \quad \text{(cgs)}$$

where T_e is the electron temperature. Let the ordinary diffusion length for this geometry with uniform gas and free diffusion be Λ_o. The question

of how the mode of diffusion in the boundary layer determines the overall diffusion losses depends generally on the relation of L to Λ_o. Obviously, if diffusion in the boundary layer is free, the entire diffusion process will be free regardless of L and Δ. But, if the boundary layer diffusion is ambipolar, two regimes arise:

Case 1--When $L \gtrsim \Lambda_o$, the diffusion will be dominated by the ambipolar boundary layer.

Case 2--When $L < \Lambda_o$, the overall process will still be essentially ambipolar until L gets to be much less than Λ_o because the diffusion velocity through the boundary layer is so slow. Now the time to diffuse a given distance is proportional to the square of the distance. Consequently, the limiting case, when diffusion through the ambipolar layer will be just as fast as the diffusion would have been with completely free diffusion, can be evaluated by taking the ratio of L to Λ_o as equal to the square root of the inverse ratio of the diffusion coefficients. That is, the ambipolar boundary layer is thin enough to be neglected when $\frac{L}{\Lambda_o} \leq \sqrt{\frac{1}{40}}$ or, since $L = \Delta/\pi$, when $\Delta \gtrsim \frac{\Lambda_o}{2}$.

For example, consider the case of a slender cone re-entry vehicle at an altitude of 200,000 feet with velocity = 22,000 FPS. At a distance one foot back from the vertex on an 8-degree half-angle cone, $\Delta \approx 1$ cm. If the near-breakdown electron temperature is taken to correspond to 4 ev, the criterion for completely ambipolar diffusion in this layer will be that $n \gg 2 \times 10^7$ cm^{-3}. According to recent non-equilibrium predictions for such a flow field,[5] n will not be this great. Thus, breakdown at this altitude would be controlled by free diffusion, or be in the transition regime. If it should occur, however, that n is indeed high enough for the boundary layer alone to be completely ambipolar, it is important to estimate whether Δ is small enough that the diffusion from the entire ionizing field outside the boundary layer would still be essentially free. Typically, the effective

diffusion length of a half-wave slot will be $\Lambda_o \approx h/2\pi$, where h is the effective slot height (dimension parallel to the electric field in the slot.) According to Case 2 above, Δ is small enough to be neglected when $\Delta \lesssim \frac{\Lambda_o}{2}$. For this particular example, then, it can be neglected if the slot antenna height satisfies the relation $h \gtrsim 4\pi\Delta = 12.5$ cm.

The ionization and attachment rates, ν_i and ν_a, are measured as a function of pressure and field as net production rate, $\nu_{net} = \nu_i - \nu_a$. When normalized by the average electron collision frequency, ν, ν_{net} for room temperature gases has been measured as a universal empirical function of E_e/ν, where $E_e = E\nu/(\nu^2 + \omega^2)^{\frac{1}{2}}$, E is the rms field strength and ω the RF radian frequency. The net ionization rate is shown in Fig. 4 for air, with ν replaced by the pressure p. The sharp threshold of ν_{net}/ν at low values of E_e/ν is the important feature determining breakdown thresholds in the limit of high ν when diffusion losses are low. This can be seen on the right-hand side of Fig. 3 where the diffusion effect is disappearing as ν increases.

The effect of velocity on the breakdown power level of a 2-inch slot antenna has been calculated and is shown in Fig. 5. The ambient electron density in the flow, n_o, was assumed to be such that $\omega_p < 0.1\omega$ for the purpose of the calculation. Since the field decreases away from the aperture surface, while the flow velocity increases, it seems appropriate to choose a velocity less than the free-stream value in calculating the effect on the breakdown power level.

As can be seen in Fig. 5, the velocity effect becomes important in the vicinity of the minimum power-handling level and approaches a fixed value as the collision frequency increases and the altitude decreases. For example, at a gas velocity of 16 kft/sec (approximately 2/3 of the assumed 24 kft/sec free-stream velocity), the power required to produce breakdown increases 3 dB at the minimum and approaches a constant value of about 5 dB on the high-pressure side of the minimum.

The effect of velocity on antenna breakdown is presently being studied experimentally in a 12-inch-diameter shock tube at the Stanford Research Institute. It is expected that information concerning ionization rates in elevated-temperature air will also be obtained during the measurement program.

IV EXPERIMENTAL INVESTIGATION

In order to investigate the effects of a plasma, such as those experienced during re-entry, in the vicinity of antennas, a 14-MHz RF plasma jet that could supply a continuous source of pure hot gases was developed. The facility offers promise also as a tool for determining some of the presently unknown basic data for elevated temperature air.

A. Experimental Measurements

The initial breakdown experiments accomplished in the plasma jet facility concerned the performance of a 2-by-5-inch L-band slot antenna previously measured in a plasma environment created by a seeded ethylene oxygen flame.[6]

The flow from the plasma jet was shaped into a slab-like configuration by the use of a quartz circular-to-rectangular transition section as illustrated in Fig. 6. The resulting flow over the antenna face was nearly homogeneous over a width of 2-1/2 to 3 inches, covering the high-field region of the slot. Typical profiles of the electron density in the direction normal to the face at its center are shown in Fig. 7, with a profile along the same axis of the electric field (without plasma) as determined by a small dipole probe. These electron density profiles are similar to those that may be encountered during actual re-entry of a hypersonic missile in the altitude range of 150,000 to 200,000 feet.

The 1.1-GHz (L-band) RF power was delivered to the slot antenna as indicated in Fig. 6. Due to the proximity of the 14-MHz tank circuit the HF fields were sufficient to produce a glow discharge in the vicinity of the L-band slot antenna. In order to insure that the L-band measurements

were performed when the plasma over the antenna surface was essentially in thermal equilibrium, the 14-MHz power was turned off periodically for 80 μsec. L-band pulses of 8-μsec duration were applied to the antenna near the end of the HF off period. Since the plasma flows for a distance of only 1 to 2 cm during the "off" time, the neutral gas properties in front of the antenna are essentially unaffected.

Peak L-band power up to about 1500 watts was deliverable to the antenna. The collection of saturation ion current on iridium wire probes was used to spatially resolve the electron density within a factor of about two over a very large dynamic range. This technique was previously developed and checked with both a microwave interferometer and shock-tube data.[7,8] These measurements were made prior to, during, and after the microwave pulse. Previous experience indicated that because of field distortion by the probe, the measurements made during the pulse were less accurate than the others. In addition, when the microwave power was too low to induce added ionization, the probes were used to measure changes in the electron temperature, the saturation ion current being proportional to the square root of the electron temperature.

Fig. 8(a) shows typical oscillograph traces comparing the time-resolved power received by the monitoring antenna (the lower trace) with the power incident upon the transmitting slot (the upper trace). The incident power level for this figure is seen to be great enough to induce attenuation that increases during the pulse. The weak-signal attenuation due to the thermal plasma was determined to be 1.8 dB by observation of a received, low-level signal with the plasma jet on, then off. The initial electron density, n_0, was near the critical level, n_{crit}, for this measurement.

Fig. 8(b) shows a series of oscillograph traces similar to those of Fig. 8(a), where incident power was varied from trace to trace. The decrease of signal transmitted at the end of the pulse for high powers is typical for pressures less than 0.5 torr. Fig. 8(c) shows a contrasting behavior in this regard, typical for pressures higher than about 2 torr, where the power "saturates" but does not decrease.

A compilation of the power transmitted beyond the plasma at the end of the pulse is shown in Fig. 9 as a function of the delivered power for five different pressures. The absolute level of power radiated beyond the plasma was established by assuming that the power received by the monitoring antenna located on a line normal to the slot aperture was always proportional to the total power transmitted beyond the plasma. The constant of proportionality is determined under no-plasma, weak-signal conditions. The weak-signal plasma attenuation was determined to be 1.8 db for all pressures except for 0.17 torr, when it was 3 dB. This attenuation is shown on the curves as a constant separation between input and radiated levels at low-input levels. The net power delivered to the transmitting antenna was determined from the incident power monitored by a calibrated meter, the reflected power level, and a measure of the losses in the transmission line from the meter to the antenna. Reflection losses caused by the thermal plasma over the antenna face were always less than 1/2 dB. The results at high pressure shown in Fig. 9 are seen to be quite similar to the results of the same type of tests with the same antenna in sodium-seeded hydrocarbon flames, shown in Fig. 10. There, the pressure was a constant throughout the tests, but n was varied by varying the seeding. The collision frequency, which was a function of both the gas constituents and temperature, besides the pressure, appears to have fallen between the plasma jet results for 2.0 and 4.5 torr.

The initial electron density for Figs. 8(a), 8(b), and 8(c) was near critical or greater. When the power becomes high enough to produce additional attenuation it is seen, from these figures, to start at essentially the beginning of the trace. This would be expected, since fields just high enough to produce any additional electrons in plasma will produce additional attenuation immediately. This is contrasted with the case shown in Fig. 8(d), where the initial electron density was only 1/8 critical. A period of 6 μsec after the ionization was initiated was required at this power level before the electron density was increased to an attenuating level (approximately critical, since the

collision frequency ν is much less than the radian frequency ω).

Oscillograph traces like those of Fig. 8(d) give a measure of ν_i when n_o is known if diffusion losses are negligible ($\nu_i = 3.5 \times 10^5$ for this case). Initial comparison of the hot-air results with the standard cold-air data does not indicate that ν_i varies greatly with temperature below about 2000°K. Preparations are being made for measuring the temperature and density in these experiments to allow precise calculation of ν_i for various temperatures.

The nonuniformities in ν, n_o, and E appear to have interesting effects during the 8-μsec pulse at the lower pressures. The traces in Fig. 8(b) that show increasing attenuation give evidence that ionization proceeded seperately in at least two discrete strata. Each distinct discontinuity of slope in the transmitted signal probably resulted when the density in a given stratum reached the critical level. At pressures higher than 2.0 torr, the maximum ionization rate occurs where the collision frequency is minimum--i.e., at the hottest part of the slab. However, at pressures lower than 1 torr, there would likely be two strata, one outside the hottest part of the slab and one inside, where the collision frequency, combined with the electric field at each stratum, results in faster net electron production rates than at the temperature maximum. Even so, these rates may not be equal, and in addition, they may not start at the same n_0, so that n reaches n_{crit} at slightly different times.

B. Interpretation of Results

The initial tests performed in the plasma jet repeated breakdown power level measurements on a 2-by-5-inch X-band slot previously measured in a plasma environment provided by a seeded ethylene oxygen flame burning at low pressure.[6] Comparison of the two sets of data showed that the breakdown levels in the two plasma environs were essentially the same, indicating that the ionization rates in the two media were similar. Thus it appears that one can use plasmas created by both techniques to

determine the effect of re-entry environment on antenna performance.

Evaluation of the experiments reported here leads to some practical conclusions from a general engineering viewpoint:

(1) Whereas in cold air, nonlinear interaction is not observed unless power input levels are high enough to produce abrupt and precipitous transmission losses, in a hot plasma the nonlinear interaction phenomena may result in transmitted signal reduction starting at levels 10 dB or more below those for cold air. The threshold for serious losses will be about 6 dB below the cold-air levels as in the case of any ambipolar diffusion-controlled breakdown.

(2) When $\nu \gtrsim \omega$, there appears to be little variation of transmitted signal with input power, once nonlinear ionization thresholds are exceeded (from Fig. 9). This result agrees with earlier tests made in sodium-seeded hydrocarbon flames. However, when $\nu < \omega$, the ultimate power level transmitted is lower than the threshold level as input power is increased, and an optimum input level appears warranted for this condition.

(3) When input power exceeds threshold for nonlinear attenuation by 10 dB or more, the variation of transmitted power with pressure is similar to that previously observed with cold-air breakdown--i.e., the transmitted power decreases as pressure decreases. This behavior has been observed over pressure ranges that go as low as that required for $\nu = 0.1\omega$.

V MULTIPACTOR DISCHARGES

In the exo-atmosphere, the power-handling capability of radiating systems may be affected by multipacting voltage breakdown.

Under high-vacuum conditions when the electron mean free path is large compared to the dimension of the RF structure, ordinary gas discharges are not normally a problem. Under such conditions, however,

multipactor or secondary emission-controlled discharges can occur on RF equipment. RF breakdown voltage for parallel plates is illustrated in Fig. 11 for pressures ranging from a few hundred microns Hg, where gas processes predominate. Multipacting breakdown is very dependent on the geometry of the structure. However, in the presence of a plasma medium such as the ionosphere, it appears that multipacting can occur in geometries that normally would not support it.

The multipactor discharge is dependent upon secondary electrons produced at one electrode being accelerated across the electrode gap in a half period (or an odd multiple of a half period) of the RF wave, whereupon they strike the electrode and produce new secondary electrons to be accelerated back across the gap during the next half period.[9] Since a dc field in the electrode gap will tend to upset the synchronism between the electron transits and the RF field, or cause most of the electrons in the gap to be collected by the positive electrode, the application of a dc bias may be considered an appropriate means of preventing multipactor discharges. Theoretical[10] and experimental data indicate the gap can be biased until the discharge fails to occur, but bias voltages of the order of the upper RF breakdown voltage are required. Furthermore, below cutoff the bias voltage serves merely to establish a new one-sided multipactor discharge mode at the positive electrode.[11,12]

Experiments have been conducted with electrically small discone antenna configurations. Fig. 12 shows contours of multipactor discharge initiation voltage (rms volts) at 57 Mc for cone angles ranging from 90° to 60°. For angles less than 60°, the discharge voltages were so erratic that smooth contours could not be obtained, and for cone angles less 30° no discharges were observed. However, when ambient ionization was introduced by producing a small auxiliary discharge at VHF in the vacuum chamber, multipactor discharges occurred for all cone angles of 15° or

greater, and the discone discharge continued even after the VHF discharge was stopped. After the VHF discharge had been extinguished, the discone voltage was reduced until the discone discharge became extinguished. The rms voltages at which the discone discharges extinguish are shown in Fig. 13. These extinguish voltages may be taken as an indication of the voltage at which multipactor discharge occurs in the presence of ambient ionization, since, once established, the discharge provides its own ionization.

Since most of the energy the electron gains from the RF field during its transit across the electrode gap is dissipated when it strikes the electrode, the power absorbed by the discharge is a function of the RF frequency of the discharge--i.e., the number of electron impacts per second and the number of electrons participating in the discharge is of the order of 10^7 per cm^2 of discharge cross section and the energy dissipated by each electron is about 100 ev. Thus the power dissipated in the discharge is 2 fnW or 3.2×10^{-10} f watts/cm^2. The power dissipated in a discharge of reasonable size is thus small compared to the power dissipated in a gas discharge. The multipactor discharge can effectively detune high-Q circuits, however, and produce sufficient heating to melt soft solder joints. It should also be noted that although the power density appears to increase with frequency, in configurations such as the discone antenna the area of the discharge is proportional to the inverse square of the frequency, so that the dissipated power may actually decrease with increasing frequency.

It is concluded, therefore, that the possibility of multipactor discharge should be considered in the design of high-Q RF transmission lines, cavities, and antennas for use on space vehicles. Particular care is required for vehicles operating in ambient ionization such as exists in the earth's ionosphere.

VI ANTENNA DESIGN CONSIDERATIONS

In the design of antennas for use on reentry vehicles where a severe low-pressure plasma environment is to be encountered, there are several design techniques and considerations that will enhance the antenna performance.

In general, the use of narrow-band (high-Q) antennas is undesirable for reentry vehicles. High-Q antennas are characterized by the fact that there is a large amount of stored energy near the antenna in comparison with the energy radiated per cycle. This means that the field will be quite high in the vicinity of the antenna. The high-Q antenna is undesirable for several reasons--one is that the high fields imply a low power-handling capability, another is that the impedance of a high-Q antenna will be more sensitive to the presence of the plasma environment. Reactive fields, upon immersion in a plasma, become dissipative, providing another means of absorbing the RF power.

Another factor that must be considered in the design of antennas for high power is that the antenna feed system can also create high reactive fields adjacent to the antenna, with associated undesirable effects. As an illustration, measurements of the aperture field of a T-fed slot revealed a field 6 dB higher than for the same slot fed by a waveguide for the same power radiated.

Two possible ways to increase the power-handling capability of antennas in the plasma medium are: (1) alter the antenna field configuration, and (2) modify the environment over the antenna. In order to increase the power that can be radiated from a given aperture, the amplitude of the field per unit power in the aperture must be reduced. This could be accomplished, for example, by increasing the size of the antenna aperture. Unfortunately, space requirements on the reentry vehicle usually preclude carrying this approach very far. Another possible method is to put over the antenna a dielectric cover sufficiently thick that the large reactive field of the antenna can be kept from interacting with the plasma.

The data in Fig. 14 give an example of the possible improvements that can be obtained by this approach for a horn and a slot antenna. The two antenna apertures considered lie in a large ground plane and are centered in a hemispherical, negligibly thin radome that is surrounded by the low-pressure region. The effect of the radome radius on the breakdown power is plotted. The radome reduced the field intensity at the surface where the RF energy enters the medium, which is at low pressure compared to the power densities in the plane of the apertures. Therefore, at a fixed pressure and frequency, more total power can leave the antenna aperture without causing breakdown as the radome radius is increased.

The field in the aperture of the horn is predominantly a propagating field that does not decay as rapidly normal to the aperture as the field normal to the aperture of the smaller antenna. Therefore, the presence of a radome within a wavelength of the aperture will increase the power-handling level of the smaller antenna by a larger factor than will the horn antenna. These data (Fig. 14) show that a radome radius equal to the smaller slot height (0.32) will add 7.4 dB to its power-handling level. The data also show that a radome of any size will improve the smaller antenna more. It can also be seen in Fig. 14 that for a radome of radius λ or more, the smaller antenna can radiate higher power because it is less directive than the horn. For instance, the horn will produce higher intensities on axis than the smaller antenna, and will therefore break down 3.5 dB below it, where this number is comparable to the ratio of directivities.

Increasing the aperture to reduce the field introduces problems that may not have previously been encountered--e.g., as the aperture gets larger, it becomes more difficult to control the phase and amplitude of the field to ensure the proper pattern. Thus, the antenna pattern becomes more susceptible to the plasma environment existing over the surface. Since dielectric windows over the antennas may also function as ablative

heat shields and their thicknesses may change with time, the pattern-control problem is further complicated.

Another solution is to reduce the electron density to the point where the diffusion rate will always be free instead of ambipolar. Perhaps the best chance for attaining this in practice is by vehicle design, using sharp-nosed conical bodies.[5] For example, in reentry, this could effect a delay in the production of sufficient electron density to produce ambipolar diffusion until the gas density is so high that breakdown probability is reduced due to the high-pressure limitation. Other possible methods being investigated include the injection of liquids[13-15] and gases[16] to cool the boundary layer or increase the gas density adjacent to the antenna, injection of chemicals to recombine or attach the electrons,[17] and the use of electric fields to sweep out the electrons. The use of an electric field, however, does not appear to be feasible due to the sheath effect. The use of a magnetic field to obtain a propagating mode does not appear feasible because of the high collision frequency that would be encountered in the altitude range of interest.[18]

Still another possible technique to control the breakdown power level is to use the effect of gas density increase on the electron-loss mechanism. The minimum breakdown power level occurs when the RF angular frequency, ω, is approximately equal to the collision frequency, ν. Thus, when $\nu < \omega$ and the principal electron loss mechanism is diffusion, the collision frequency and consequently the pressure should be reduced to increase the breakdown power level. Conversely, when $\nu > \omega$, the gas density should be increased to increase the breakdown level. Some measure of control of the gas density can be obtained by selecting the location of the antenna on the vehicle. For ECM application the highest jamming power is required at the lower altitudes where $\nu > \omega$; placing of the antenna on the fore-cone of a cone-cylinder-flare shaped vehicle, for example, would provide a location where the gas density would be increased as early as possible during the reentry regime. Thus, recovery from

breakdown power limitations in reentry would be accomplished at as high an altitude as possible.

In the case of multipacting breakdown, there are three principal means of increasing the power-handling capability of the antenna. First, the use of a pressurized radome over the antenna appears to be the simplest solution for preventing breakdown. This technique is applicable for gas as well as multipacting discharges. Design consideration for this technique is well known and by increasing the radome size, the power-handling capacity can be raised to any desired level. Secondly, the use of dc biasing voltage for inhibiting is possible. However, the value of voltage required will be sensitive to the geometry, and care must be taken that a dc voltage breakdown will not be initiated. Thirdly, the use of titanium surfaces to discourage secondary emission from surfaces of antennas appears to be a possible method for discouraging multipacting breakdown.

REFERENCES

1. S. C. Brown, "High Frequency Gas Discharge Breakdown," Proc. IRE 39, 12, pp. 1493-1501 (December 1961).

2. L. Gould and L.W. Roberts, "Breakdown of Air at Microwave Frequencies," J. Appl. Phys. 27, 10, pp. 1162-1170 (October 1956).

3. J. Chown, W. Scharfman, and T. Morita, "Voltage Breakdown Characteristics of Microwave Antennas," Proc. IRE 47, 8, pp. 1331-1337 (August 1959).

4. D. Kelly and H. Margenau, "High Frequency Breakdown of Air," J. Appl. Phys. 31, 9, pp. 1617-1620 (September 1960).

5. A. J. Pallone, J. A. More, and J.P. Erdos, "Nonequilibrium, Nonsimilar Solutions of the Laminar Boundary Layer Equations," Contract AF 04(694)-239, Technical Memorandum RAD-TM-63-58, Avco Corporation, Wilmington, Massachusetts (November 1963).

6. J.B. Chown, "Effects of Reentry Environment on ECM Antenna System Performance", Final Report, SRI Project 4583, Sperry Gyroscope Co. P.O. 259160, Stanford Research Institute, Menlo Park, California (August 1964).

7. W.C. Taylor, "The Use of Ion Probes for Diagnosing Reentry Plasmas," Technical Report 11, SRI Project 3857, Contract SD-103, Stanford Research Institute, Menlo Park, California (July 1963).

8. W. E. Scharfman, "The Use of Langmuir Probes to Determine the Electron Density Surrounding Reentry Vehicles," Final Report, Contract NAS 1-3942, SRI Project 5034, Stanford Research Institute, Menlo Park, California (June 1965).

9. A. J. Hatch and H.B. Williams. J. Appl. Phys. 25, 4, pp. 417-423 (1954).

10. C. Milazzo, "Study of Multipactor Discharge in the Presence of a dc Bias," Technical Memo TM G1-15, General Electric Co., Palo Alto, California (13 March 1961).

11. E.F. Vance, J. Appl. Phys. 34, 11, pp. 3237-3242 (1963).

12. E.F. Vance and J.E. Nanevicz, "One-Sided Multipactor Discbarge Modes", Technical Report 75, SRI Project 3977, Contract AF 19(628)-325, Stanford Research Institute, Menlo Park, California (April 1963).

13. W.F. Cuddihy, I.F. Beckwith, and L.C.Schroeder, "RAM B2 Flight Test of a Method for Reducing Radio Attenuation During the Hypersonic Reentry," NASA TM X-902.

14. W.F. Cuddihy and J.K. Hughes, "Simulated Reentry Tests of a Method for Reducing Radio Blackout by Material Addition to the Ionized Flow-Field," NASA TM X-988.

15. "Proceedings of NASA Conference on Communicating Through Plasmas of Atmospheric Entry and Rocket Exhaust"(U), 14-15 January 1964, Langley Research Center, Langley Station, Hampton, Virginia SP-52, CONFIDENTIAL.

16. A.G. Hammitt, et al.. "Wake Cooling by Fluid Injection (U)," Proc. of AMRAC, Monterey, California (April 1963), SECRET.

17. Dwain F. Spencer, "An Evaluation of the Communication Blackout Problem for a Blunt Mars-Entry Capsule and a Potential Method for the Elimination of Blackout," Technical Report No. 32-594, Jet Propulsion Lab. (15 April 1964).

18. H. Rothman, et al., "Transmission Through an Ionized Medium in the Presence of a Strong Magnetic Field," Second Symposium on the Plasma Sheath, Boston, Massachusetts (April 1962).

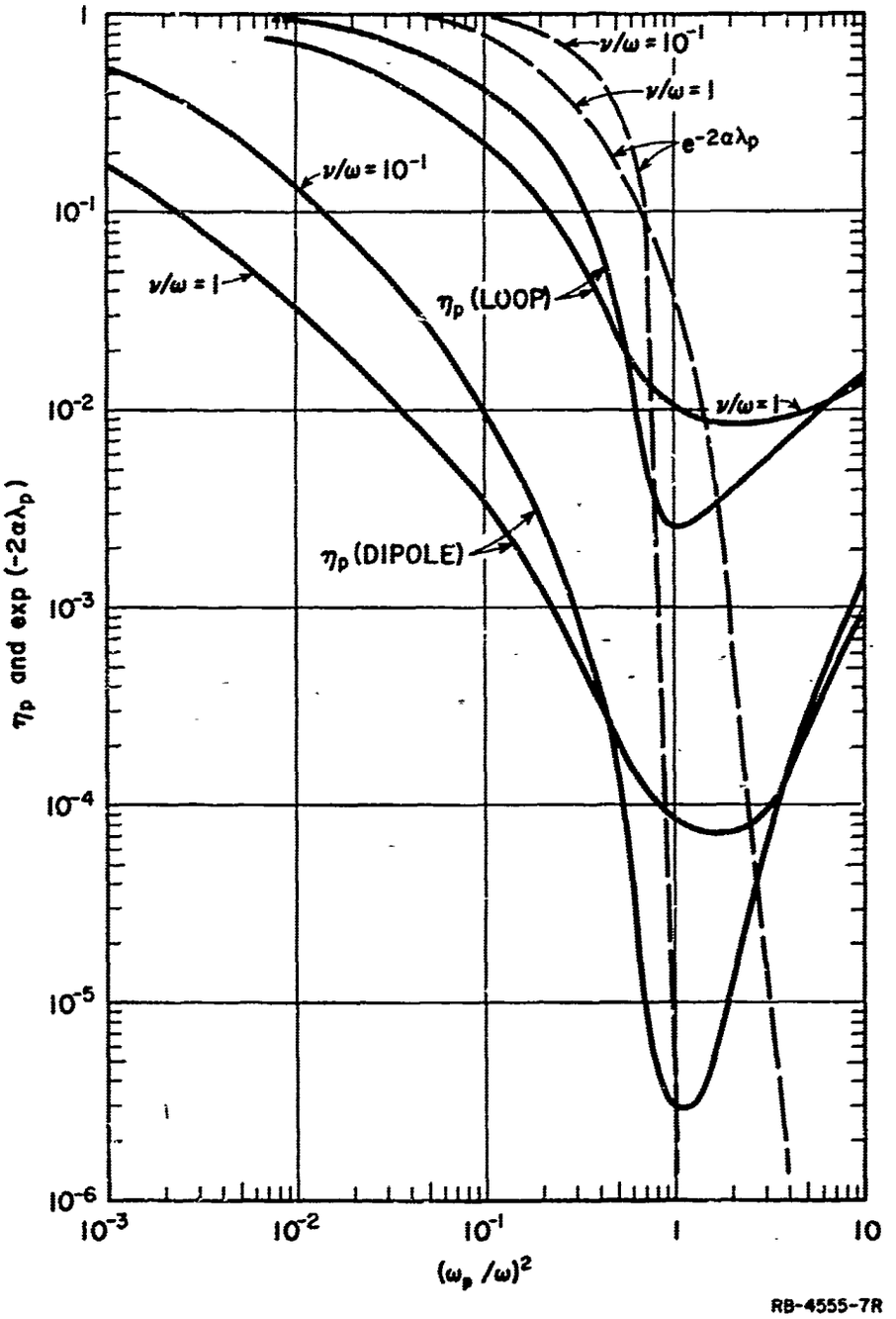


Fig. 1 Radiation Efficiency, η_p, and Propagation Losses, $\exp(-2\alpha\lambda_p)$, for a Wavelength Sphere, as a Function of Normalized Plasma Frequency

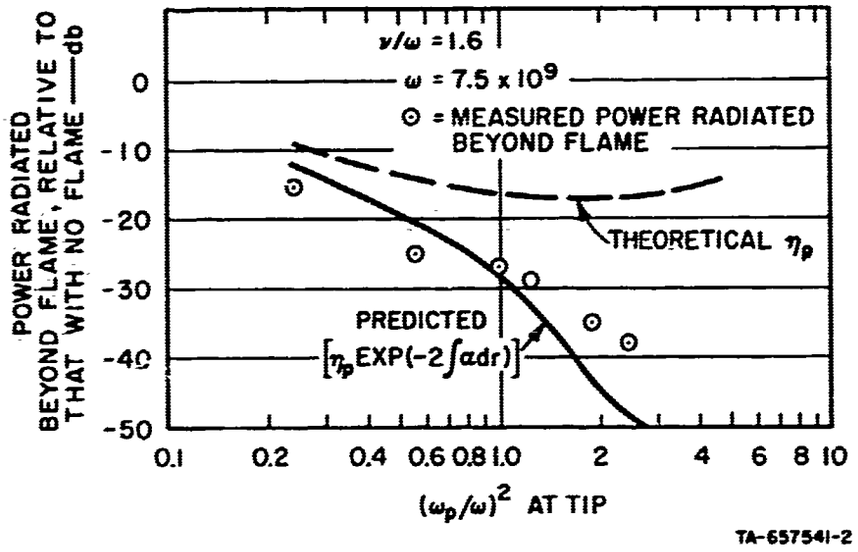


Fig. 2 Drop in Radiated Power Due to Flame Normalized to Constant Input-Dipole

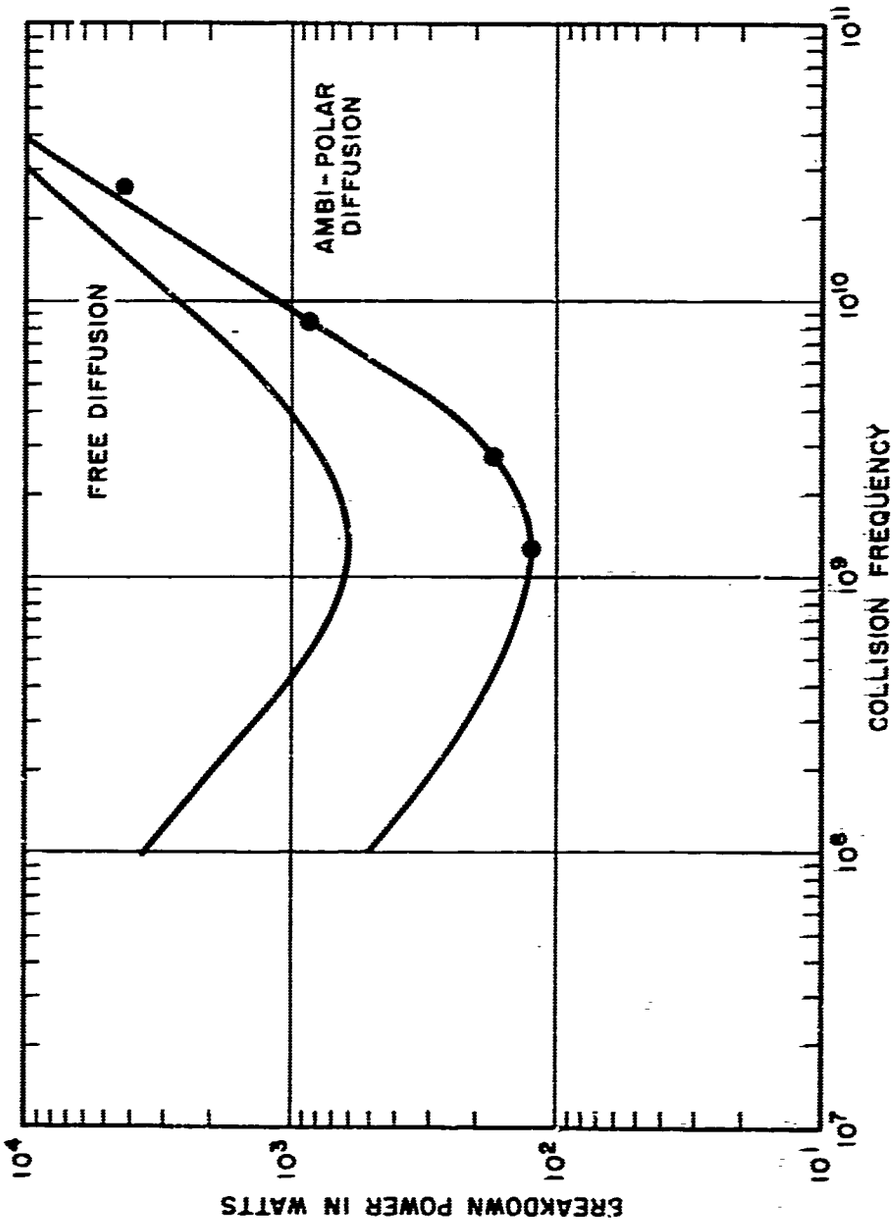


Fig. 3 Breakdown Characteristics of X-Band Slot Antenna

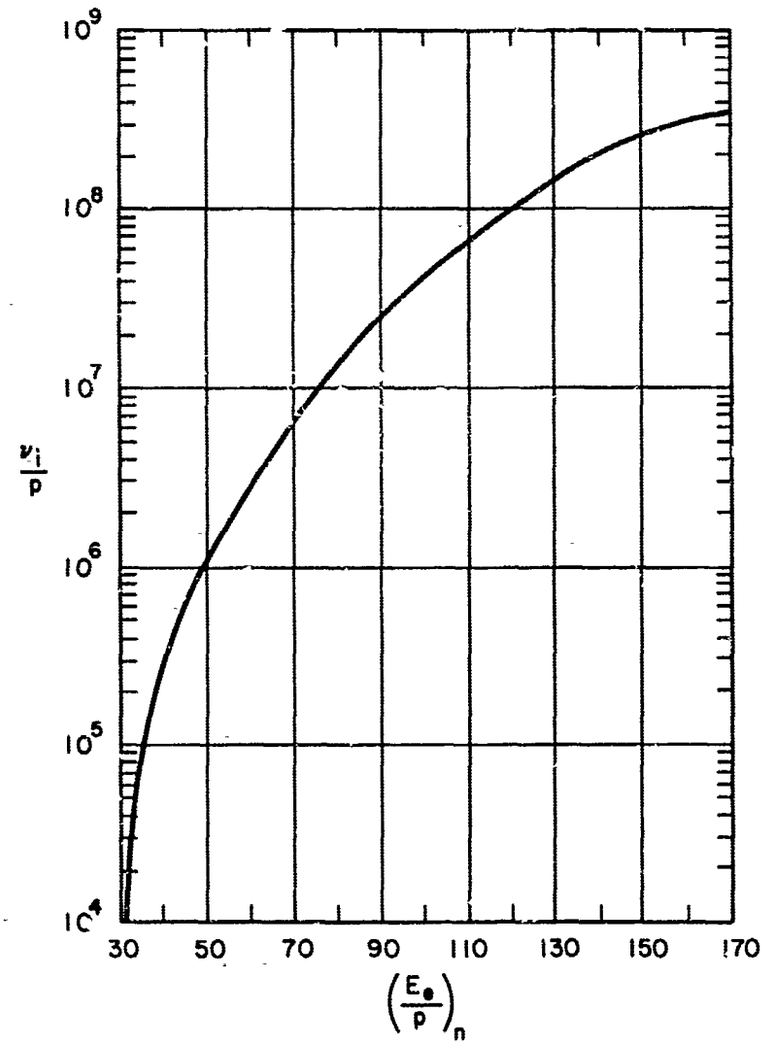


Fig. 4 (ν_i/p) as a Function of $(E_e/p)_n$ for Air

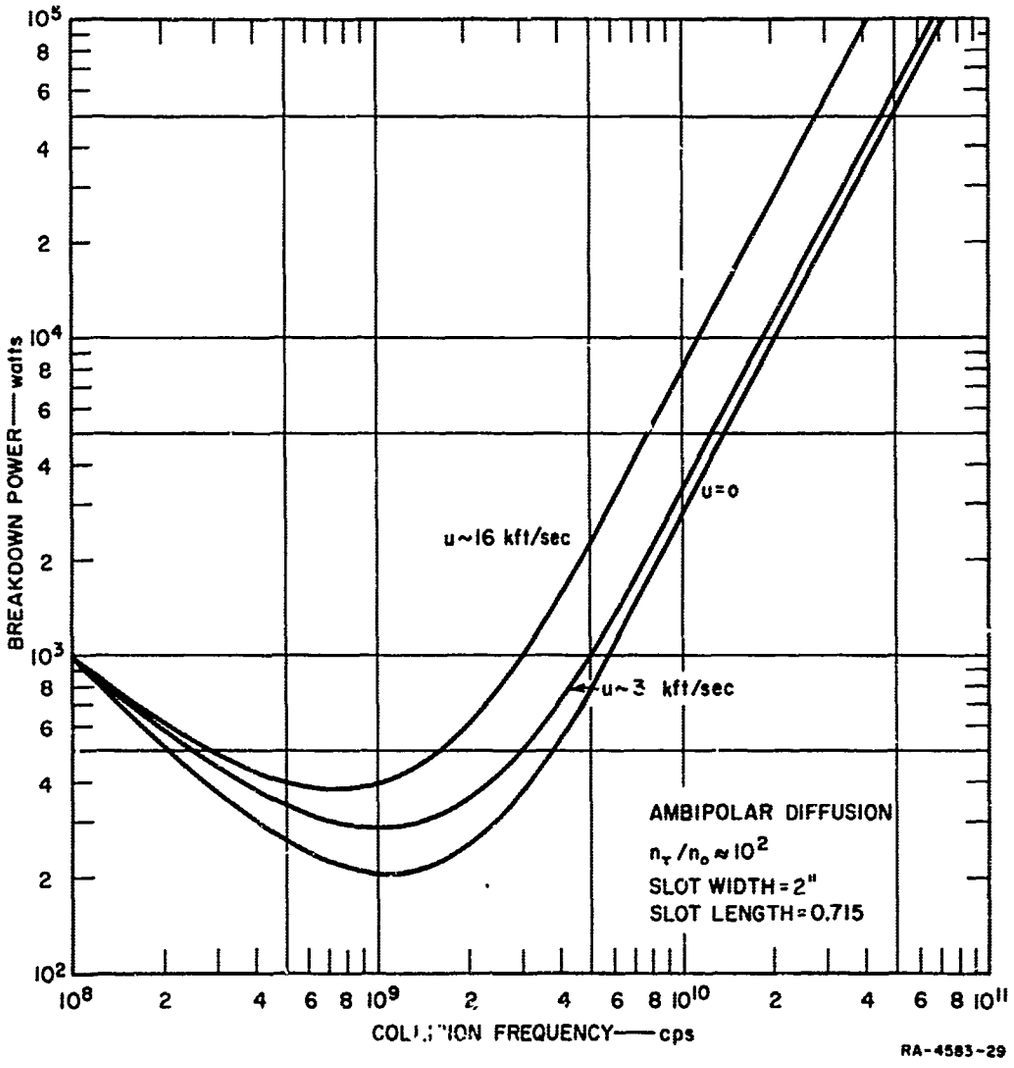


Fig. 5 Effect of Flow Velocity on 2-inch Slot Antenna at 1200 Mc

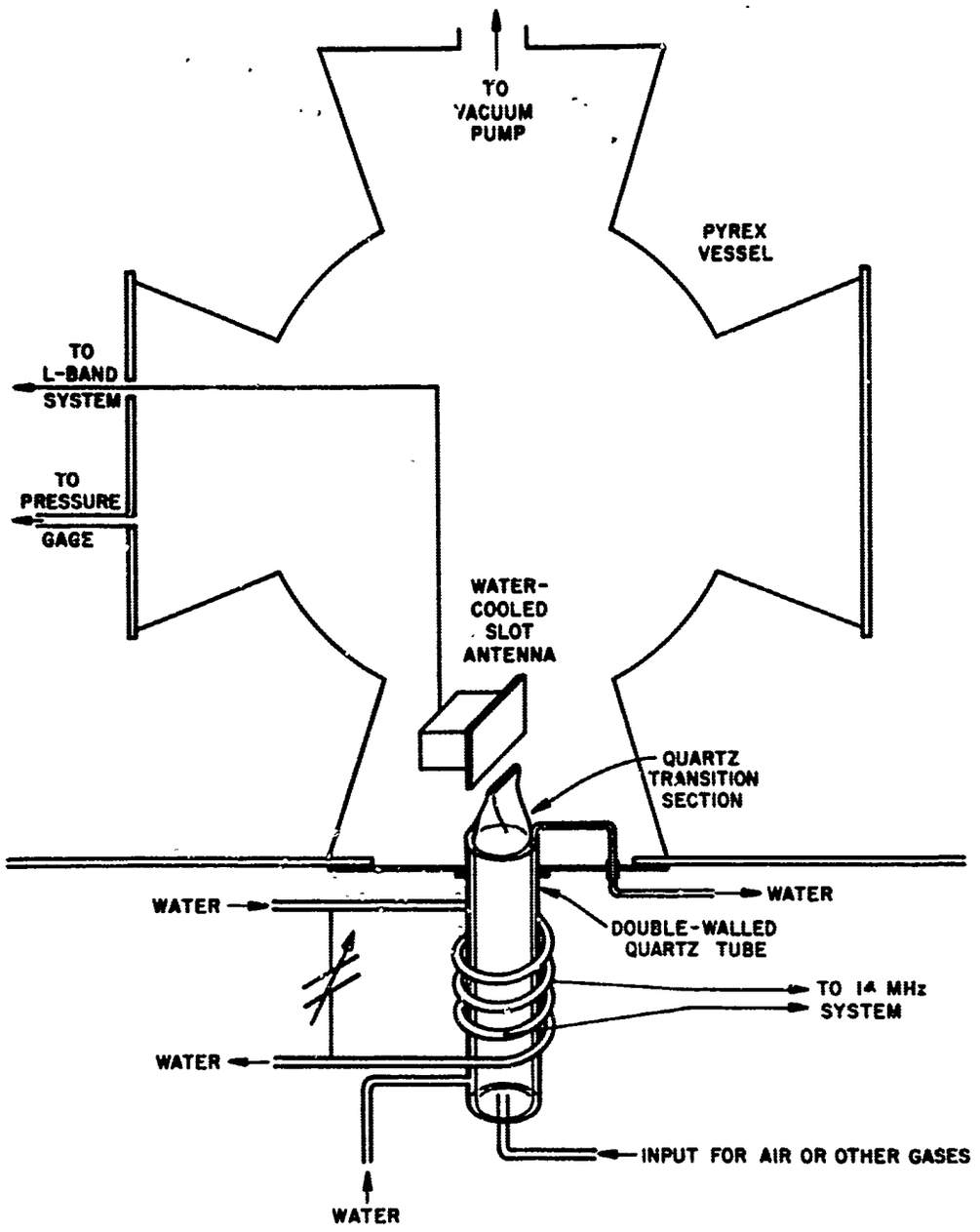


Fig. 6 Plasma Jet Systems, Providing Input Gas, Vacuum, and Water Cooling

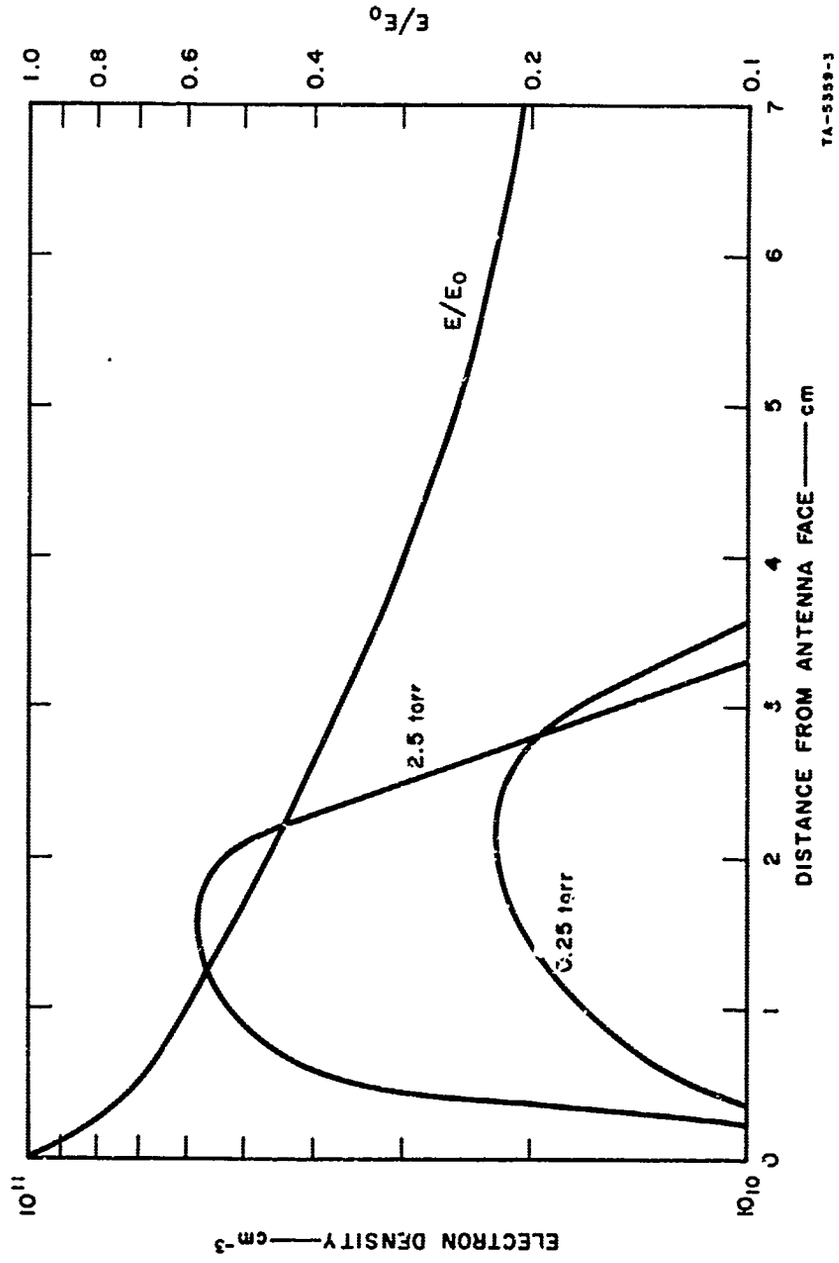


Fig. 7 Typical Profiles for Electron Density Along Normal to Antenna Face Compared with Electric Field (Without Plasma)

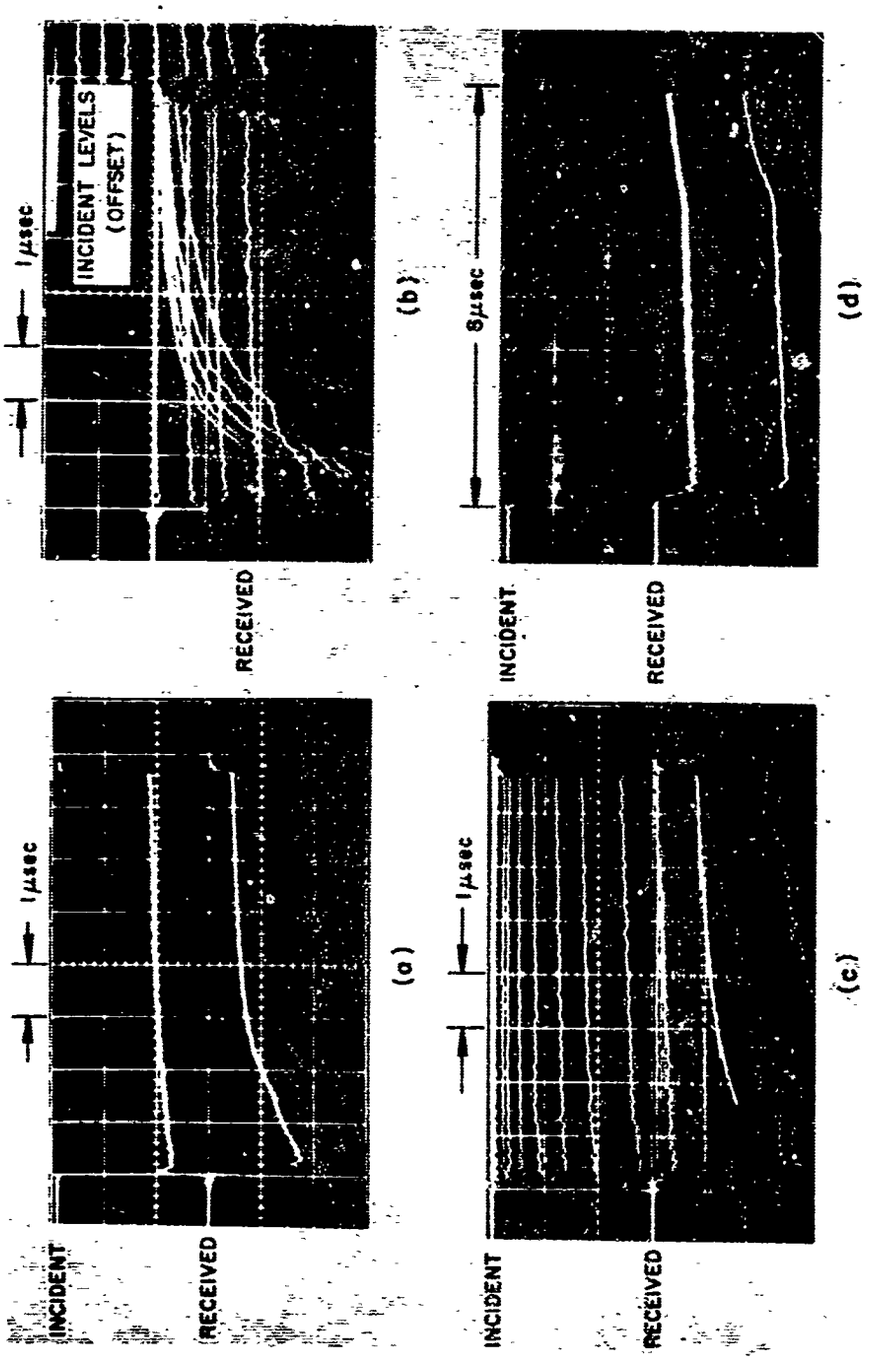


Fig. 8 Oscillograph Traces of Incident and Received L-Band Pulses

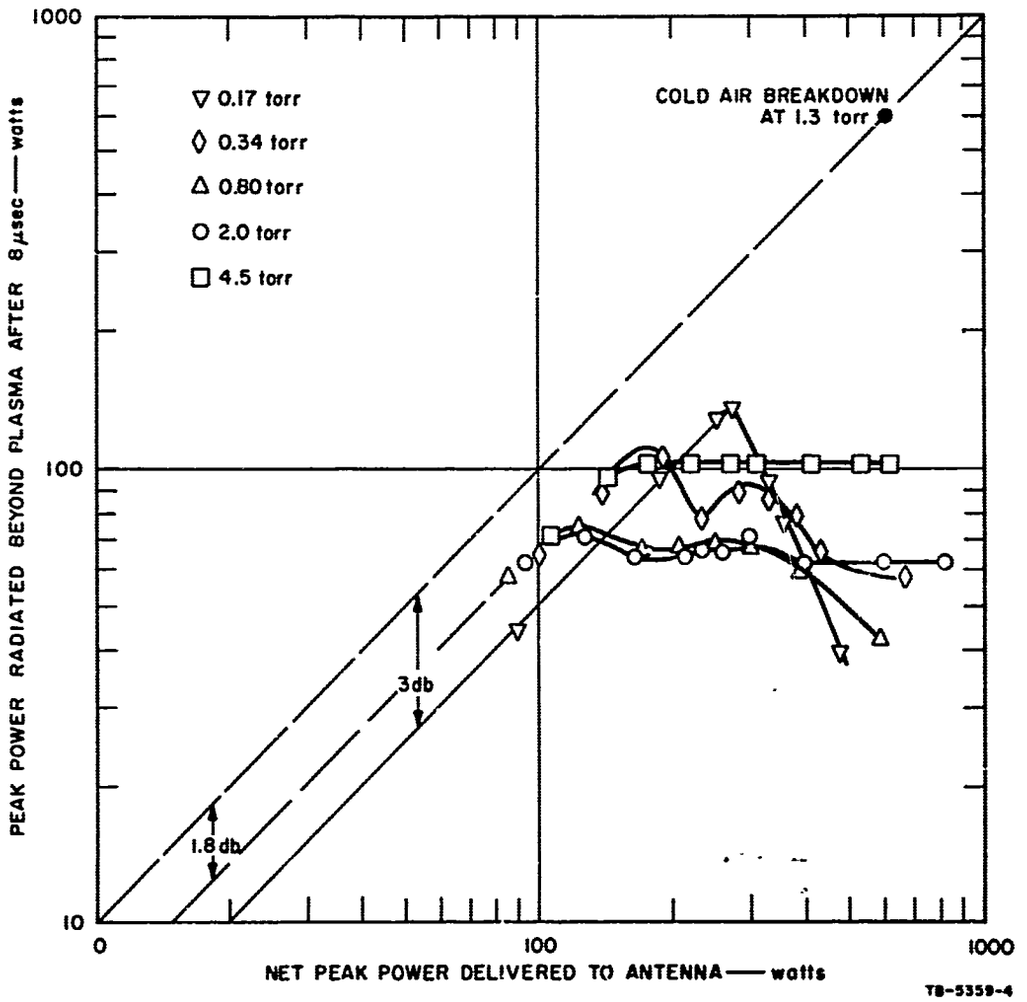


Fig. 9 Measured Power Transmitted Beyond Plasma as a Function of Antenna Input Power (Peak)

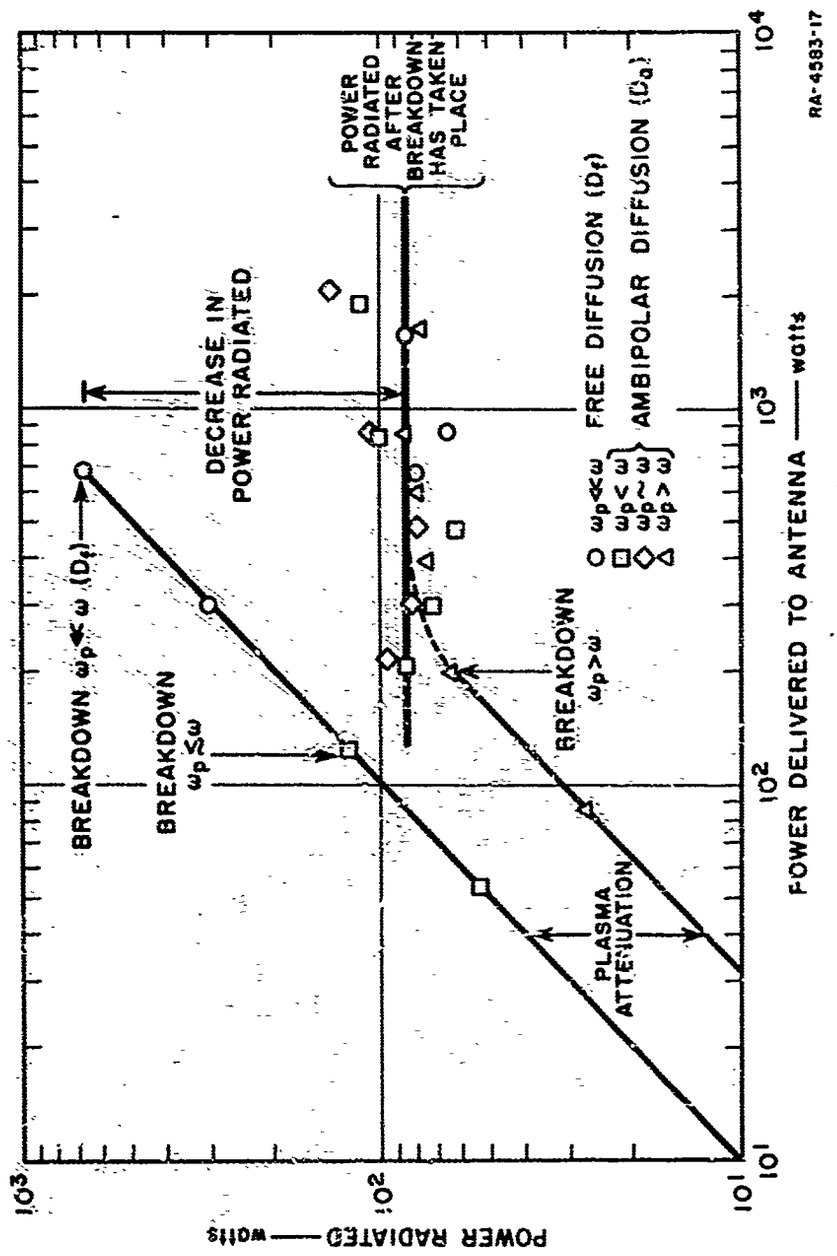


Fig. 10 Power Radiated Normal to an L-Band Slot Antenna for Various Ratios of ω_p/ω ($P_c \approx 1$ mmHg)

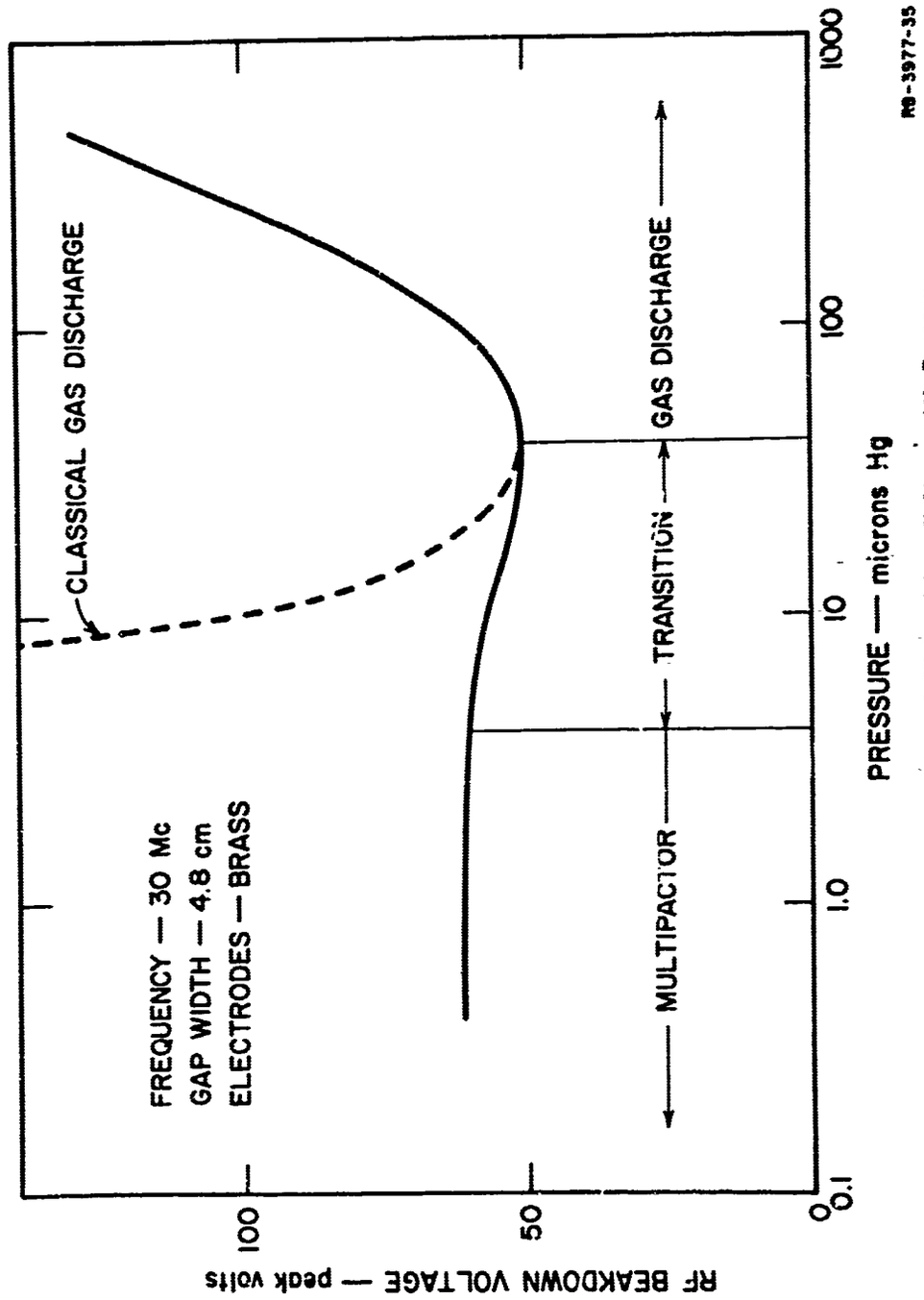


Fig. 11 Variation of RF Breakdown Voltage with Pressure

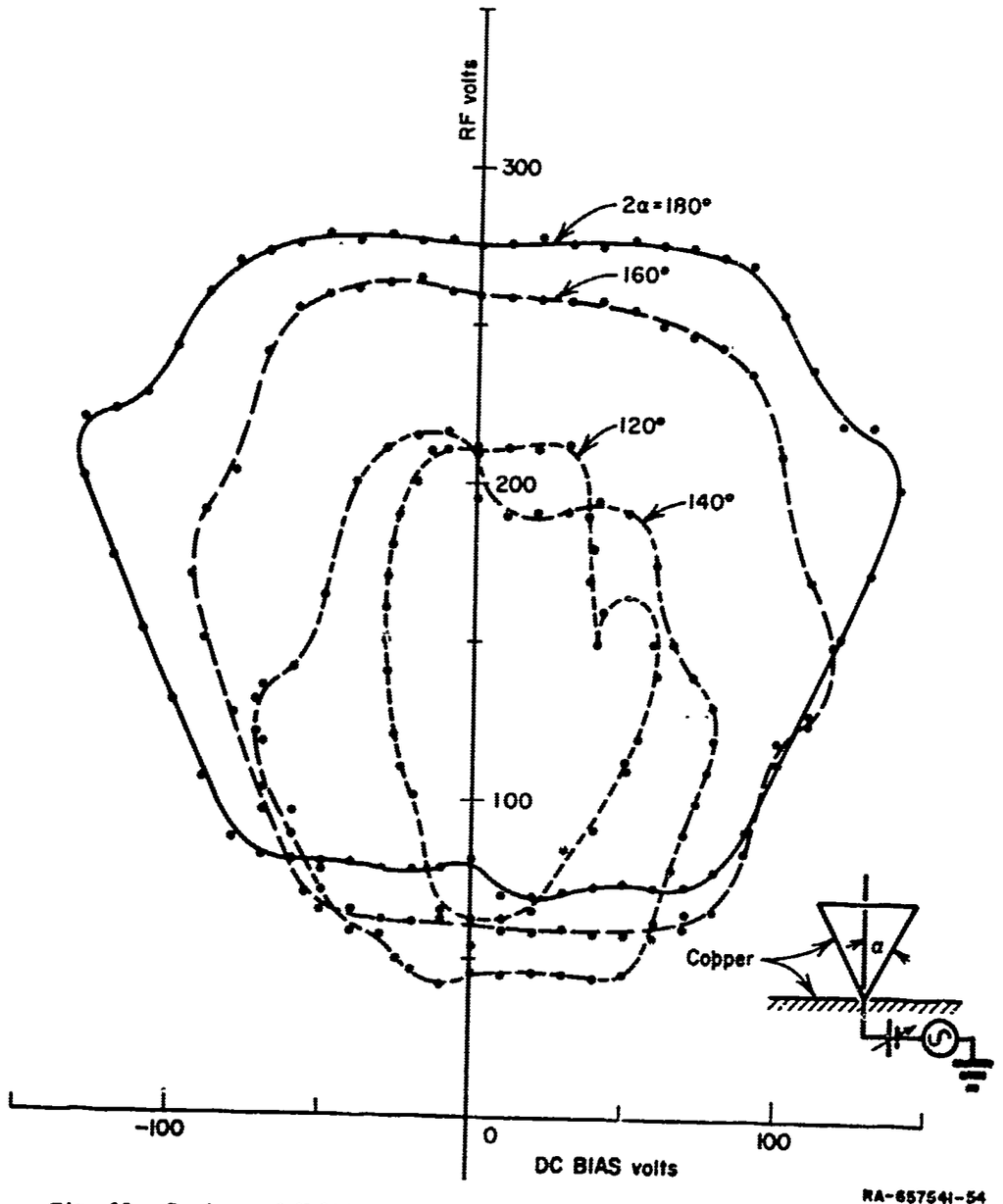


Fig. 12 Regions of Multipactor Discharge for Small Discone Antennas

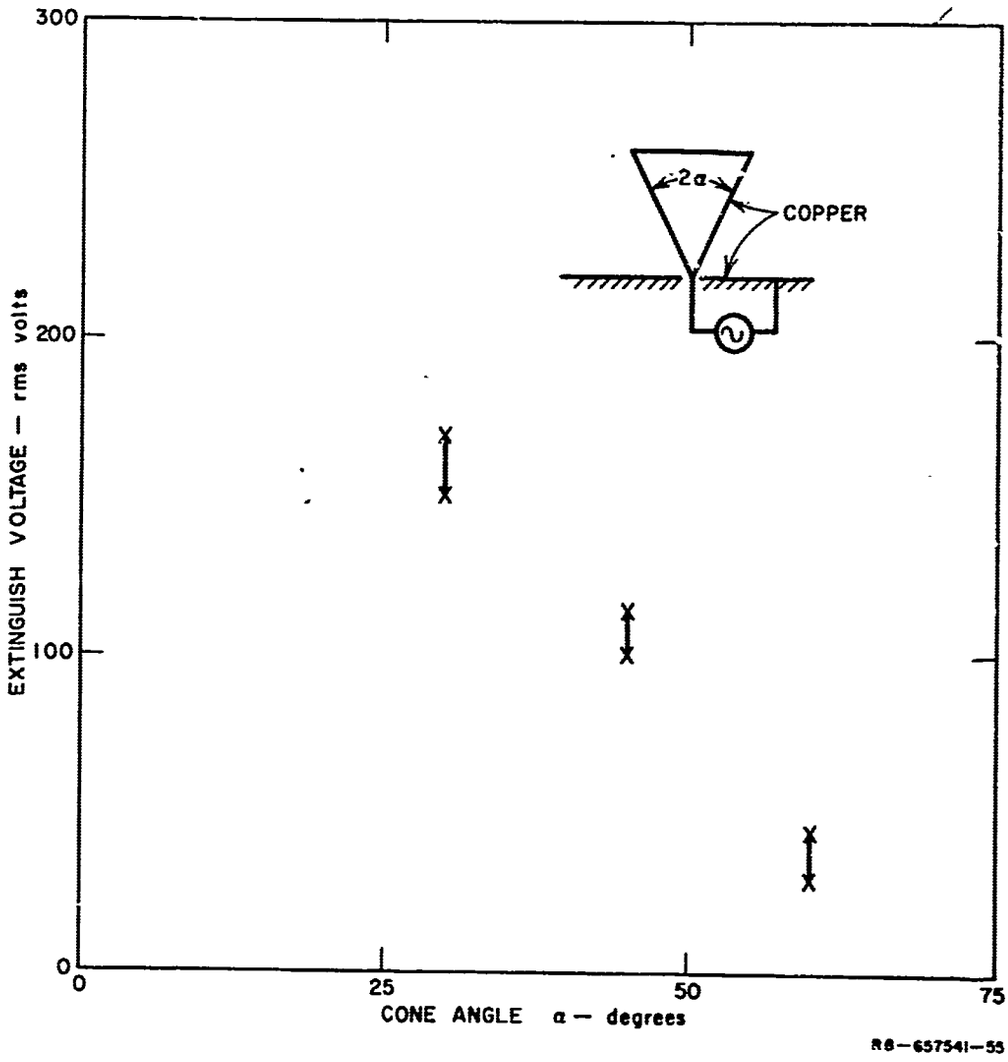


Fig. 13 Discharge Extinguish Voltage for Small Discone Antennas

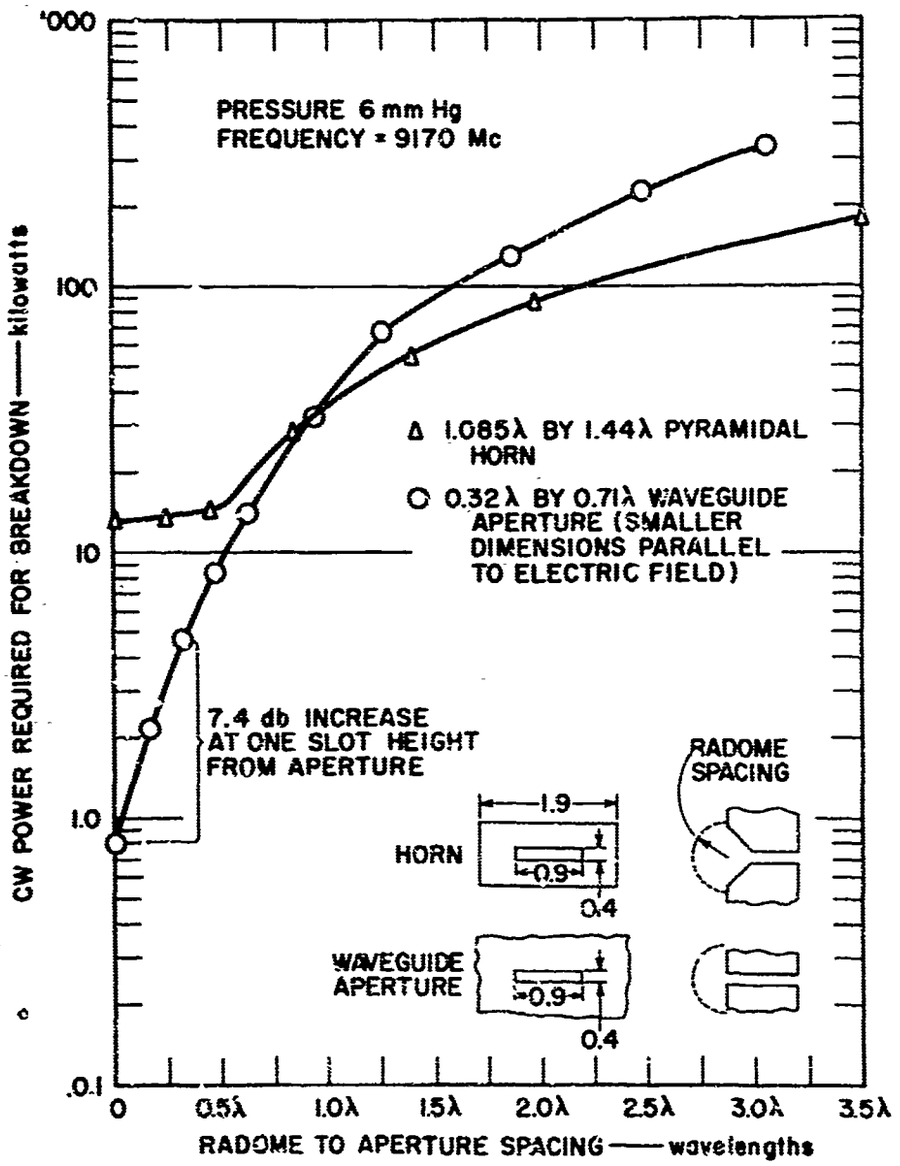


Fig. 14 Effect of Thin Spherical Radome on Power-Handling Capability of Slot Antenna and Pyramidal Horn

TP-122 November 1965

VIII. A MATHEMATICAL MODEL FOR PREDICTING RF INTERFERENCE EFFECTS IN ROCKET EXHAUST PLUMES*

H. S. Pergament and H. F. Calcote

AeroChem Research Laboratories, Inc.
Princeton, New Jersey
a subsidiary of Ritter Pfaudler Corporation

ABSTRACT

A systematic procedure for developing electron density and collision frequency contours (necessary input to rf interference calculations) in solid and liquid propellant rocket exhausts is developed. It is shown that there is no formal difficulty in constructing the required contours over altitudes ranging from sea level to near-vacuum conditions. The accuracy of these contours is shown to depend on a knowledge of fundamental reaction rate and turbulent mixing data, as well as a realistic treatment of coupling inviscid and viscous flows with afterburning. Examples are given for typical solid and liquid propellant systems in order to give a "feel" for the important parameters. It is concluded that many comparisons between the theoretical calculations and in-flight and sea level data must be made to develop a high confidence level in the prediction technique.

INTRODUCTION

The title of this paper could mislead the reader into expecting a neat, closed form solution to the problem of predicting rf interference effects in rocket exhausts. Unfortunately, this type of solution is not possible. However, a systematic approach to the problem is possible in which a number of individual mathematical models (or analyses) are developed and properly put together to give the desired result. The emphasis in this paper, therefore, is on the systematic approach and the type of individual analyses which must be utilized to obtain a solution. We will concentrate here on the gas dynamic, thermodynamic, and chemical kinetic aspects of the problem and will not discuss the electromagnetic wave interactions with the exhaust plasma. The latter analysis is discussed in another paper in this Symposium.[1] As much as possible, during the following discussion, we will indicate the present state of the art in making the necessary calculations.

---

* Presented at the Third Symposium on the Plasma Sheath, Plasma Electromagnetics of Hypersonic Flight, Hanscom Field, Bedford, Massachusetts, 21-23 September 1965.

In order to fix ideas, consider the sketch of the ascending plume shown in Fig. 1. The low-altitude plume is characterized by the typical shock diamond pattern, while at the intermediate altitudes the familiar Mach disc configuration is observed. At extreme altitudes, the Mach disc is translated many exit radii downstream, so that it does not even appear in the figure;* finally, in the near-vacuum condition, the plume actually bends back in front of the vehicle. The problem we are treating here concerns the prediction of electron density and collision frequency contours throughout the exhaust plume at all combinations of altitude and flight velocity, with the following parameters as given input data:† propellant composition, chamber pressure, nozzle configuration, vehicle velocity and altitude, signal frequency, and aspect angle. These contours are necessary input data to the calculation of interference effects (attenuation, reflection, refraction, and phase shift) with a given rf path entering the plume.‡

Analysis of exhaust plume interference must begin by considering the propellant combustion products in the chamber, follow their reaction as they flow from the combustion chamber to the nozzle exit plane, and then treat the subsequent expansion of the rocket exhaust products downstream of the exit plane. This paper divides naturally into two parts, i.e., determination of the plasma properties at the nozzle exit plane and in the exhaust plume. In order to illustrate the procedure, calculations have been made for typical liquid and solid propellant systems. The purpose is to bring out the essential features of the model rather than make a direct comparison of the two systems or compute detailed electron density and collision frequency contours for a specific system. In this manner, we hope to give the reader a "feel" for the magnitude of the important parameters and their expected influence on rf interference.

EXHAUST NOZZLE EXIT PLANE ANALYSIS

A block diagram of the analysis required to calculate rf interference effects at the exhaust nozzle exit plane is shown in Fig. 2. This step-by-step procedure determines nozzle exit plane properties--starting with a chemical analysis of a propellant sample for low ionization potential metal impurities, usually limited to alkali metals. Along with the propellant composition and chamber pressure, these impurity data serve as input to a thermochemical equilibrium calculation of the combustion chamber properties. The electrons produced by thermal ionization of impurities, as well as the combustion products in the chamber, are thus accounted for. The chemi-ionization

---

* At these altitudes, the size of the rocket becomes negligible compared to the size of the plume.

† These parameters are usually given information for a specific propellant/missile system.

‡ It is clear from Fig. 1 that the angle of the rf path with respect to the vehicle axis will be a significant parameter in this calculation; this specifies the regions of the plume traversed by the signal.

box in Fig. 2 is dotted because, in almost all cases, chemi-ionization is unimportant when compared to the contribution of the total electron concentration made by thermal ionization. Even so, the results of both thermal and chemi-ionization analyses are used as input to the nozzle expansion process. Equilibrium, frozen, and chemical kinetic (nonequilibrium) solutions for the nozzle flow properties are then obtained in order to determine the exit plane values which are important as initial conditions for the plume analysis. Electron density and collision frequency are used to compute exit plane radar attenuation, which can subsequently be compared with exit plane measurements. This indicates the accuracy of the model to this point. Modifications to the theoretical treatment might be made to effect agreement with experimental results and, therefore, give a higher confidence level to nozzle exit plane calculations for future systems. To date, modifications have been unnecessary because the agreement has always been as good as the experimental data.

COMBUSTION CHAMBER

Thermal Ionization. The compositions of some typical solid propellants are shown in Table I which compares a composite with a composite double-base propellant. The large amount of ammonium perchlorate in the composite system is the cause of higher impurity levels, since impurity analyses have shown ammonium perchlorate to be very "dirty."

Measurements of alkali metal impurities in solid propellants are performed at AeroChem by burning a sample of the propellant in a combustion bomb, absorbing the products in water, and analyzing the solution by flame photometry.[2] It is possible to measure the impurity content of the propellant to $\pm$ 10%, which is satisfactory because the electron concentration is proportional to approximately the square root of alkali metal content. The impurity levels for the solid propellants shown in Table I are representative for these types of systems and it is therefore interesting to note the contrast between the solids and the typical liquid fuels shown in Table II.

From the data in Tables I and II we are in a position to determine thermochemical equilibrium combustion chamber properties and the subsequent thermal ionization levels in the chamber. For this purpose, a standard thermochemical equilibrium program is utilized[3-5] and the adiabatic flame temperature and complete neutral and charged species composition determined. Specific calculations have been made for the composite solid propellant at typical chamber conditions and the N_2O_4/Aerozine-50* propellant system for chamber conditions duplicating those existing in the Lunar Excursion Module (LEM) descent engine. The results are shown in Tables III and IV, respectively.

Regarding the solid system (Table III) it is interesting to note that, although calcium is the largest impurity, the dominant positive ions are potassium and sodium. The dominant calcium-containing species is $CaCl_2$, which is thermodynamically favored over, e.g., CaOH and CaCl. The strong effects of attachment to chlorine are evident

* Aerozine-50 contains 50% UDMH-50% Hydrazine by weight.

by comparing the ratio of negative ion to electron concentration (2 orders of magnitude). Comparing the above findings with the results for the liquid propellant system (Table IV), we note that, although the chamber pressure and temperature are somewhat different, the electrons are now the dominant negative species, being an order of magnitude larger than the OH^- concentration. In view of the large difference in impurity levels between the liquid and solid systems, it might be surprising that the electron mole fraction is larger in the liquid propellant combustion chamber. The above results clearly indicate the importance of attachment and the larger electron affinity of Cl over OH.*

The compositions shown in Tables III and IV are used as input data to an analysis of flow properties in the exhaust nozzle, but we must first consider the possible contribution of chemi-ionization to the electron concentration in the combustion chamber.

Chemi-Ionization. In each propellant system the electrons produced via chemi-ionization should be compared with the thermal ionization level calculated by the above procedure. A typical reaction producing chemi-ions in both liquid and solid propellant systems is $CH + O \rightarrow CHO^+ + e^-$. It would be possible to calculate the electrons produced by this reaction if we had some means of determining the concentration of CH free radicals. The oxygen atom concentration is not a serious problem, and the reaction rate coefficient has been estimated.[6] Unfortunately, we do not have sufficient confidence in the neutral reaction rate coefficients which lead to CH production to calculate the CH concentration from chemical kinetic considerations. However, we can measure the amount of chemi-ionization in the chamber for a given propellant system.

The LEM descent engine propellant system was analyzed at conditions simulating those in the combustion chamber.[7] A Langmuir probe was used to measure ion currents and the results interpreted in terms of the total positive ion concentration in the chamber; the measurements therefore included electrons produced by both thermal and chemi-ionization. The measured electron mole fraction was $1.2 \pm 1 \times 10^{-7}$, which compared favorably with the thermal equilibrium value of 3.4×10^{-7} (Table IV). Since the predicted and measured values were so close, we concluded that the effect of chemi-ionization in the LEM descent engine combustion chamber was negligible, the difference in predicted and measured values being due to the uncertainty in the impurity concentration in the fuel and the degree to which the chamber conditions were simulated by the experiment.

Laboratory measurements in typical solid propellant systems have also demonstrated that thermal ionization dominates in the chamber. This would be expected considering the high impurity content in solid propellant systems and the rapidity at which equilibrium is approached at the high pressures and temperatures prevailing in the chamber.

---

* The electron affinity of Cl is 3.61 eV, while the electron affinity of OH is 1.78 eV.

TP-122

NONEQUILIBRIUM NOZZLE FLOW

The nozzle configurations used for the ensuing calculations are shown in Figs. 3 and 4. The solid propellant nozzle is conical and corresponds to a perfectly expanded nozzle at an ambient pressure of approximately 0.3 atm. The flow properties are assumed to be one-dimensional, which is reasonable for conical nozzles. The nozzle used for the LEM descent engine is bell-shaped and has strong radial gradients at any given axial location.

The two limiting conditions for the determination of flow properties and composition in the nozzles are: (a) frozen and (b) shifting equilibrium expansion processes. Both are isentropic expansions--the former assumes a frozen composition at the chamber conditions; the latter assumes that local thermochemical equilibrium can be maintained at each point in the expansion process. These calculations are easily made with the same type of digital program utilized for calculating specific impulse.[3-5] The results for the two systems considered in this paper are shown in Tables III and IV, and some of the important points* are:

1. The shifting equilibrium variation of the major stable neutral species concentrations is quite small for both systems.

2. For the solid system, the exhaust contains approximately 20 wt % aluminum oxide particles.

3. The difference between frozen and shifting equilibrium exit plane values for the charged species is quite large for both systems, indicating that chemical kinetic effects must be considered. (The frozen values, of course, will be the same as the chamber values.)

4. The effects of electron attachment for a shifting equilibrium expansion are even greater at the exit plane than in the chamber for the solid propellant system.

5. The difference between frozen and shifting equilibrium temperature and velocity is seen to be relatively small for both systems.

The formal procedure for integrating the one-dimensional, nonequilibrium equations has been extensively studied.[8,9] The most convenient method is one which specifies, as input data, the pressure distribution along a given streamline in the nozzle, and the initial conditions. For the conical nozzle, the pressure is assumed to be uniform radially† but, for the bell-shaped nozzle, the streamline distribution must

---

* A direct comparison between these systems at the exit plane should not be made because of the widely different pressures.

† Therefore, it would be equally useful to prescribe the area distribution as input.

first be determined before the pressure gradients can be calculated. This is accomplished by utilizing a method of characteristics procedure[18] for either equilibrium or frozen flow, since the streamline locations and corresponding pressure distributions are relatively insensitive to chemical kinetics.* Figure 5 shows the pressure distribution in the conical nozzle and indicates the small difference between equilibrium and frozen flow, while Fig. 6 gives the pressure distribution for a few streamlines in the LEM descent engine nozzle. It is obvious that one-dimensional considerations would not suffice for the bell-shaped nozzle.

Although the equations describing nonequilibrium nozzle flow are straightforward, certain numerical problems arise in performing the integration. These problems concern starting the integration from an equilibrium condition in the chamber at high pressure. The initial expansion closely follows shifting equilibrium and thus requires very small integration steps for numerical stability. These steps can be so small as to make the computer time required to obtain a solution prohibitively large. In order to bypass this problem, various numerical techniques have been suggested.[10,11] A procedure adopted at AeroChem[7] utilizes the thermochemical equilibrium results when the expansion process is, in fact, close to equilibrium.† Then, when the flow starts to deviate significantly from equilibrium (as determined by a deviation criterion), the nonequilibrium calculations are initiated.‡ This procedure cannot give results which are exactly correct, but they will be sufficiently accurate for most purposes. Using the method described in Ref. 7, the time required to complete a given nozzle calculation on an IBM 7094 computer is approximately one hour for the propellant systems considered here.

Chemical Reactions and Rate Constants. Computation of the nonequilibrium flow properties depends upon utilizing a suitable group of chemical reactions for the expanding combustion products, as well as obtaining reasonable values of the corresponding rate constants. A list of pertinent reactions which can be used to describe the nonequilibrium exhaust nozzle flow of the solid and liquid propellant combustion products is given in Table V. Not all the reactions are equally important for a given system, and many of the rate constants are not known to within an order of magnitude.§ The most important reactions are, by definition, those which can influence the electron concentration at the nozzle exit plane--both directly and indirectly. The direct reactions are obvious; these include electron attachment, binary and three-body recombination reactions. The neutral species reactions which influence the Cl and OH concentrations are also of obvious importance.

---

* This feature is convenient because it effectively uncouples the chemical kinetics from the inviscid flow.

† This procedure is used because a thermochemical equilibrium digital program runs considerably faster than a nonequilibrium program.

‡ In effect, this method serves to avoid the problem of using the nonequilibrium analysis when the flow is close to shifting equilibrium.

§ More detailed information on the source of the rate data and the probable accuracy is given in Ref. 12.

Once the most important reactions have been determined, it is possible and, in fact, desirable to vary the rate constants over the range of uncertainty of their values. In this manner, one can discover exactly which rate constants most strongly influence the results. The accuracy to which these rate constants are known will determine the accuracy of the final result. The rate constants which are most needed to increase the accuracy of the nozzle flow calculations are the electron attachment and binary recombination reactions. Both sets of reactions play a major role in determining the exit plane electron density, and are simultaneously quite difficult to estimate with any level of confidence.

Nozzle Exit Plane Results. The chemical reactions and rate constants listed in Table V and the pressure distributions shown in Figs. 5 and 6 have been used as input to the nonequilibrium program. Figure 7 shows the electron mole fraction distribution in both solid and liquid propellant nozzles. One can see that, for the solid propellant system, the electrons stay close to their equilibrium values throughout most of the expansion. This is primarily the result of the high pressure in the nozzle and, to a lesser extent, the specific charged species composition.

An interesting contrast is observed in the liquid propellant nozzle, where the kinetic value at the nozzle exit plane is only about a factor of 2 less than the chamber value. Here, the chamber pressure is considerably lower, and the rapid nozzle expansion causes the electrons to break away from equilibrium near the throat. It should be cautioned that, although we are treating typical solid and liquid propellant systems here, we hesitate to draw generalities from these results. Each propellant system must be and--as just discussed--can be treated separately in order to determine the properties at the nozzle exit plane.

In solid propellant systems containing large amounts of aluminum, such as the composite propellant considered here, one must consider several possible effects due to the presence of aluminum oxide particles in the exhaust. Such particles may affect the electron concentration by thermal emission or attachment of electrons, and enhancement of the rates of ion-electron recombination. Whether electrons are emitted or attached will depend upon temperature and electron concentration and can be calculated with procedures developed by Soo and Dimick.[13] In the present system, attachment prevails, and one must consider the possibility of enhanced recombination.

The effective rate constants for the enhanced recombination process are calculated on the basis that the particle maintains a negative charge due to more rapid diffusion of electrons to the particle than positive ions. Positive ions then diffuse to the particle and, on striking it, remove an electron in a two-body process. Such enhanced rates, when compared with three-body recombination, become more significant at the higher altitudes (lower pressures) and can be formally included in the nonequilibrium analysis.

An ablating nozzle or chamber liner must also be considered for its possible effect on electron concentration at the exit plane. These liners typically contain large amounts of sodium impurity which can be thermally ionized by the high temperatures in the nozzle boundary layer. This can result in a thin sheath of high electron density which,

when issuing from the nozzle, can expand along the plume boundary increasing rf interference effects. Estimates of nozzle boundary layer electron densities have been made by Kryzcki.[14]

RF Attenuation and Collision Frequency. The absorption of an rf beam passing through the exhaust can be computed from the following approximate equation,* valid for a wide range of signal frequency, plasma frequency, and collision frequency.†

$$a = 1.17 \frac{n_e}{\nu_e} \left[\left(\frac{\omega}{\nu_e}\right)^2 + 1 \right]^{-1} \text{ db/in} \qquad (1)$$

The collision frequency is dominated by electron-neutral collisions and can be computed from the following equation:

$$\nu_e = n\bar{c}_e \sum X_i Q_i \qquad (2)$$

Equation (2) can alternately be expressed as

$$\nu_e = 4.57\,(10^{27})\, pT^{-1/2} \sum X_i Q_i \text{ sec}^{-1} \qquad (2a)$$

where p is in atm, T in $^{\circ}$K, and Q_i in cm^2.

Electron-neutral collision cross sections for a number of species commonly found in rocket exhausts have been compiled by Molmud.[16] For those polar compounds not found in Ref. 16, the analysis of Altshuler[17] is used. The average cross section is dominated, in many systems, by electron collisions with polar molecules, such as H_2O and HCl. Since the mole fraction of these neutral species at the nozzle exit plane can be computed fairly accurately and the cross sections are reasonably well known, the collision frequency calculation is sufficiently accurate.‡ Thus, if agreement between predicted and measured exit plane attenuation is not obtained, the electron density is probably in error.

Comparison with Experiments. It is reasonable to consider checking the mathematical model at the nozzle exit plane by comparing predicted and experimental values. This is more important at high-altitude (non-afterburning) flight conditions than at low altitudes. At extreme altitudes the electron concentration achieves peak values at the

---

* The same parameters employed in Eq. (1) to calculate attenuation are required to calculate reflection, refraction, and phase shift.

† The more exact attenuation equation is listed in, e.g., Ref. 15.

‡ At exit plane pressures of 1 atm, ν_e is of the order of 10^{11} sec^{-1}.

nozzle exit plane and then decays throughout the exhaust (except for the possibility of shock ionization, in which case the electron concentration increases rapidly through the shock and then decays downstream).

Radar attenuation measurements have been made for many propellant systems at the nozzle exit plane.* Agreement between predicted and measured values can give a high confidence level to the procedure described in Fig. 2. It should be stressed here that agreement does not necessarily indicate that the reaction rate constants used in the analysis were correct; reactions for which incorrect rate constants were employed may have been unimportant in the particular calculation or, because of the number of rate constants involved, the errors may have canceled out. In any case, agreement adds confidence to the overall procedure, starting with the chemical analysis for alkali metal impurities. Certainly, if agreement is not obtained (and the measurements are known to be good), then one should review the rate constants that have been used in the nonequilibrium nozzle flow program and try to systematically adjust these to obtain agreement. It is always possible, of course, that agreement is fortuitous and that some other combination of rate constants would give the measured result; this can only be learned from experience with a number of different types of propellant systems.

EXHAUST PLUME ANALYSIS

The block diagram in Fig. 3 gives some perspective into the types of analyses needed to analytically determine electron density and collision frequency contours in the exhaust plume. The first step is to compute the complete inviscid flow, usually by combining the method of characteristics with the oblique shock equations,[18-22] including a determination of exhaust plume streamlines. Here, as in the nozzle flow, we can compute the electron decay along individual streamlines--given the pressure distribution and the initial conditions at the nozzle exit plane. Some data from these inviscid calculations are used as input to the mixing and afterburning study; the pressure distribution along the inviscid jet boundary is especially important.

The mixing and afterburning calculations can be carried out simultaneously by methods to be described in a subsequent section. If the altitude is high enough, no ignition will take place, and a purely "frozen" mixing situation exists. At lower altitudes, the combustibles in the exhaust (typically, carbon monoxide, hydrogen, and solid carbon) will react with the oxygen in the air to increase the exhaust plume temperature and give rise to thermal ionization of the alkali metals. Chemi-ionization

* C, X, and K-band frequencies have (typically) been used; most of the data are found in the classified literature.

may also take place in an afterburning exhaust; the reaction between hydrocarbons in the exhaust and atomic oxygen formed by dissociation of oxygen molecules will react to give chemi-ions. Unfortunately, the contribution of chemi-ionization to the total electron concentration in the exhaust cannot be confidently predicted at the present time.

The electron concentration and collision frequency, as calculated from the viscous and inviscid flows, must then be combined. One of the major weaknesses in this analysis is the superposition of the two different types of flows. As we shall see later, this superposition is especially poor at low altitudes, whereas, for the high-altitude plume, the assumptions employed are more reasonable. Once the complete electron density and collision frequency contours are obtained, the rf interference effects can be computed by presently available analyses (see, e.g., Ref. 1).

INVISCID FLOW (WITH SHOCK STRUCTURE)

The method of characteristics has been used for many years to compute the inviscid exhaust plume structure.* Typically, these calculations were made for a constant specific heat ratio in the exhaust and were combined with oblique shock equations to give properties behind the shocks. Detailed explanations of the method of characteristics analysis used for exhaust plumes, as well as corresponding computer programs, may be found in Refs. 19 to 22.

Low Altitude. The limit of the low-altitude plume is the sea level case. Calculations of the exhaust plume structure for the composite solid propellant nozzle shown in Fig. 3 have been made at sea level with no external flow. Constant pressure contours are shown in Fig. 9 up to two shock diamonds (or reflections from the axis). Although this is a perfectly expanded nozzle, i.e., exit plane pressure equals ambient pressure, the obliquity of the supersonic flow leaving the nozzle causes the resulting shock structure. We can also note the rapid decay of pressure from the nozzle exit plane to the first shock diamond and the consequent overshoot in pressure behind the shock. An interesting point about this structure is that it shows the exhaust of a perfectly expanded conical nozzle to have strong axial and radial pressure gradients.

At higher altitudes, the exhaust plume structure changes to the familiar Mach disc pattern.† Figure 10 shows the constant pressure profiles in the exhaust of a contoured nozzle, with uniform exit plane properties, at an altitude of 100 kft. This figure was constructed from the results of D'Attorre and Harshbarger,[24] who thoroughly investigated the flow in the vicinity of the Mach disc. They applied the triple-point

---

* We limit our discussion to the single-nozzle exhaust plume here. A method of characteristics solution for multiple nozzles has not yet been developed, although work on this problem is now in progress, see e.g., Ref. 23.

† Actually, the Mach disc also exists at sea level, but the diameter is so small that the shock pattern resembles the diamond shape. As the altitude increases, the diameter of the Mach disc increases and is thus more readily observed.

criterion[25] along with the method of characteristics in order to locate the disc; this is an advance over the earlier work of Adamson and Nicholls[26] and Eastman and Radtke.[27] In addition, Ref. 28 gives some very useful curves for locating the Mach disc.

The extreme case of increasing altitude is that of exhausting into a vacuum; for this case there are no shocks in the exhaust. We draw on our analysis of the LEM descent engine[7] to describe the exhaust plume structure. Method of characteristics calculations have been made for the nozzle shown in Fig. 4 exhausting into a vacuum, and the results are given in Fig. 11. Since the major neutral species are nearly frozen at their exit plane values (the equivalent of constant γ flow), all constant property profiles (pressure, Mach number, and temperature) are equivalent. The profiles shown in Fig. 11 are typical of the exhaust from a bell-shaped nozzle with highly non-uniform exit plane profiles.

SHOCK IONIZATION

Some effect on the electron mole fraction can be expected when a streamline passes through a shock. There are two extreme cases: Either the electron mole fraction remains frozen at its upstream value, or it can attain a value consistent with a local thermochemical equilibrium condition behind the shock. The "frozen" increase in electron density through a shock, of course, is proportional to the gas density increase. The equilibrium electron density can be computed from the temperature and pressure behind the shock. Calculations have been made for the approximate temperature and pressure conditions existing behind shocks in the sea level exhaust shown in Fig. 9. The alkali metal impurities in the exhaust are equal to those originally in the composite solid propellant system. The resulting equilibrium values of electron density as a function of temperature are shown in Fig. 12; these should be compared with the exit plane and combustion chamber electron density shown in Table III.

CHEMICAL KINETICS IN INVISCID PLUME

In order to determine the effects of chemical kinetics* (electron recombination and attachment) in the exhaust, we utilize the same technique previously employed for the bell-shaped nozzle, i.e., the pressure distribution along exhaust plume streamlines, as determined from the method of characteristics, is used as input to the non-equilibrium digital program. For simplicity, consider the pressure distribution along the axis streamlines for the exhaust plumes shown in Figs. 9 through 11; these are plotted in Fig. 13.† For the low-altitude plume, the continuous compression and subsequent shock ionization must be treated relatively near the exit plane, while the plume at 100 kft shows a pressure decrease of four orders of magnitude before the Mach disc is reached. For this case, the pressure behind the Mach disc approaches

---

* The assumption that all major neutral species remain frozen in the exhaust is a good one.

† A comparison of the pressure distributions has no real meaning due to the widely different exit plane and ambient conditions.

ambient--as postulated by Adamson and Nicholls.[26]

For the two propellant systems considered in this paper, the electron density is approximately frozen in the nozzle (Fig. 7); therefore the electron density in the exhaust will be proportional to the gas density.* Each system must be considered individually, however, to determine the inviscid exhaust plume electron density.

MIXING AND AFTERBURNING PHENOMENA†

In order to cover the complete range of mixing and afterburning phenomena which exists as a given rocket increases in altitude, two types of analyses must be utilized. First, at high altitudes where the plume boundaries are highly curved (Fig. 14a), a two-dimensional program is necessary which uses as input the pressure distribution along the inviscid boundary and uses coordinates which are normal and tangential to the boundary. Both internal and external boundary conditions are determined from the inviscid calculations just discussed. Clearly, problems arise when the inner jet boundary reaches the axis (Fig. 14a); in that case, the coordinate system must be changed from two-dimensional to axisymmetric.

At low altitudes, where the plume boundary is nearly horizontal, the mixing rates are sufficiently high to cause the inner boundary to reach the axis within a few nozzle exit radii downstream of the exit plane‡ (Fig. 14b). It is therefore more desirable to utilize an axisymmetric mixing and afterburning analysis, using as input the nozzle exit plane and free stream properties.

The equations describing the mixing and afterburning process are written below for the case of turbulent mixing. The equations are taken to be identical to the corresponding equations for laminar flow with mean turbulent quantities replacing their steady laminar counterparts, the transport quantities replaced by their phenomenological counterparts, and with the turbulent Prandtl number and all Lewis numbers equal to unity.§[29,30]

Conservation of Momentum

$$\rho u\, u_x + \rho v u_y = - p_x + \frac{1}{y^j} \left(\varepsilon \rho y^j u_y \right)_y \qquad (3)$$

---

* This is only true up to the first shock for the low-altitude plume. No specific calculations have been made in this paper for the electron mole fraction decay downstream of the multiple shocks, although the procedure has been outlined.

† The analysis in this section neglects the possible effect of the shock structure on the mixing and afterburning regions.

‡ This would be the case, for example, in a sea level plume.

§ If laminar mixing were considered, the same equations could be used by including, for example, Sutherland's Law for molecular viscosity.

Conservation of Energy

$$\rho u H_x + \rho v H_y = \frac{1}{y^j} (\varepsilon \rho y^j H_y)_y \tag{4}$$

Global Conservation of Mass

$$(\rho u)_x + \frac{1}{y^j} (\rho v y^j)_y = 0 \tag{5}$$

Conservation of Species

$$\rho u (Y_i)_x + \rho v (Y_i)_y = \dot{w}_i + \frac{1}{y^j} [\varepsilon \rho y^j (Y_i)_y]_y \tag{6}$$

where $j = 0$ for two-dimensional flow and $j = 1$ for axisymmetric flow.

We define an element mass fraction by

$$\tilde{Y}_k = \sum_i \frac{m_k}{m_i} Y_i \tag{7}$$

This leads to the following equation for conservation of elements:

Conservation of Elements

$$\rho u (\tilde{Y}_k)_x + \rho u (\tilde{Y}_k)_y = \frac{1}{y^j} [\varepsilon \rho y^j (\tilde{Y}_k)_y]_y \tag{8}$$

The only difference in the calculations for two-dimensional and axisymmetric flow are the boundary and initial conditions for Eqs. (3) to (8). In the two-dimensional case, flow conditions must be specified at the outer and inner edges of the mixing region, where only the external flow conditions are required for axisymmetric flow. In both analyses, the pressure is assumed to be uniform in the y direction. This is a more reasonable assumption for the high-altitude, two-dimensional case than for low altitudes; as seen in Fig. 9, the strong radial gradients make this assumption somewhat questionable.

A digital program has formally been developed which can solve Eqs. (3) to (8), including the effects of finite rate chemistry. This, of course, requires a chemical reaction mechanism for the neutral and charged species in the exhaust in order to specify the $\dot{w}_i$ required for the integration of Eq. (6). In order to obtain solutions, the equations were transformed to the von-Mises plane,[30,31] i.e., $(x, y) \rightarrow (x, \Psi)$ and a standard finite difference procedure[32] used for the numerical integration. Unfortunately, we have not yet been able to obtain useable results from this program for the mixing and afterburning regions of typical solid and liquid propellant exhausts. However, preliminary computer runs with carbon monoxide-hydrogen jets exhausting into air show that, at altitudes below 100 kft (ambient pressure less than approximately 0.01

atm), the computational time on an IBM 7094 computer is prohibitive. This implies that the afterburning process is so rapid that the assumption of local thermochemical equilibrium in the afterburning exhaust is probably a good one.

Surprisingly, it is somewhat more difficult to develop an equilibrium program for the rocket exhaust than a nonequilibrium program. Although both programs are quite similar to those used extensively in analyzing hypersonic wakes,[31] there is a significant difference involving determination of the thermodynamic properties. Mollier diagrams presently exist for dissociated air and are relatively simple to employ in computational techniques. The description of thermodynamic properties in an afterburning exhaust, however, requires specification of a considerable amount of data for a multitude of species. While this is formally no problem, the computational time is increased by such an amount as to make the equilibrium calculations impractical.*

When thermochemical equilibrium in an afterburning exhaust is a reasonable assumption (usually at low altitudes), a simplified procedure has been developed which can yield solutions with relatively little computer expense. This approximate method involves utilization of a frozen mixing analysis† (i.e., $\dot{w}_i = 0$ in Eq. (6)) and a separate thermochemical equilibrium program which uses as input the results of the frozen mixing analysis. The rationale for this procedure is as follows: The only requirements for a thermochemical equilibrium solution are the element mass fractions, static enthalpy, and pressure. We note from Eqs. (3) to (7) that (for constant pressure flow‡) the enthalpy and element mass fractions are functions of velocity only--as determined from the boundary conditions. Now, $u(x, y)$ can be computed from the frozen mixing analysis; giving $h(x, y)$ and $\tilde{Y}_i(x, y)$. These data can then be used as input to the thermochemical program and the afterburning temperature and thermal ionization level determined. This method is obviously approximate because it assumes that the velocity distribution is identical for both frozen and equilibrium flow. However, how bad an assumption is this? Consider Eq. (3). Only the difference in density between frozen and equilibrium flow can influence the velocity distribution. However, for the same pressure,

$$\frac{\rho_{eq}}{\rho_f} = \frac{T_f}{T_{eq}} \frac{W_{eq}}{W_f} \tag{8}$$

---

* Such a program can be developed and used, but one must expect large computer costs.

† For typical rocket exhausts, this program can give the complete flow field up to 100 nozzle exit radii downstream from the exit plane in approximately 5 minutes' IBM 7094 computer time.

‡ The pressure along the jet boundary is relatively constant at low altitudes and Mach numbers ($1 < M_\infty < 3$).

Since $T_{eq} > T_f$ and $W_{eq} > W_f$, there is a good possibility that $\rho_{eq} \approx \rho_f$, which would justify the approximate equilibrium procedure. Each system must be considered separately in estimating the accuracy of this method, which has been used extensively to make afterburning predictions at flight conditions where thermochemical equilibrium is a reasonable assumption.*

In applying this approximate procedure,† it is convenient to use an independent variable for the thermochemical calculations which reflects the "degree" of afterburning. We have selected the frozen oxygen/hydrogen mole fraction ratio (β) as this parameter. With some manipulation of Eqs. (3) to (6), we can express h and $\tilde{Y}_i$ as a function of β. The determination of electron density contours is therefore made in three steps: (1) contours of constant β are found in the frozen exhaust, (2) electron density is computed as a function of β, and (3) the above results are combined to give the required contours. Figure 15 gives the electron density contours in the sea level afterburning exhaust of the composite solid propellant system (the corresponding values of β are shown on the curve).

It is evident that these results depend upon the eddy diffusivity "model" selected and the corresponding phenomenological description of the turbulent mixing process. Other "models" could yield different results for the spatial distribution of electron density. Comparisons with experiments are therefore necessary to give confidence in the validity of these theoretical calculations.

CHEMI-IONIZATION IN AFTERBURNING EXHAUSTS

In the liquid propellant system considered here, there is no problem with afterburning due to the lack of oxygen in the external environment. In the solid propellant example, thermal ionization exceeds the chemi-ionization value which would be anticipated by comparison with a comparable laboratory flame of the afterburning mixture.‡

Because of the difficulty in obtaining a realistic estimate of the CH free radical concentration, it is impossible, at this time, to make accurate <u>a priori</u> predictions of the significance of chemi-ionization in producing electrons in afterburning exhausts. Thus far, this problem has not had to be faced in a practical sense, because

---

* No comparisons with experimental data are yet available to test the validity of the method. The predictions, made by AeroChem, appear in the classified literature.

† The turbulent eddy diffusivity "model" of Ting-Libby[30] is used in making the calculations.

‡ assuming any reasonable concentration of unburned hydrocarbon from the propellant.

preliminary evaluations have indicated chemi-ionization to be less significant than thermal ionization. Nevertheless, this is one of the more significant problems in limiting the accuracy of model studies and should receive more attention in the future.

There are several ways to obtain limiting values which can be applied in any given situation. Since it was already pointed out that chemi-ions are produced by the reaction of hydrocarbon fragments with oxygen atoms, the application of a few rational assumptions can be used to derive a maximum concentration of such fragments in the exhaust. For example, in a motor for which carbon particles are predicted thermodynamically, but not observed, solid carbon can be left out of the thermochemical nozzle calculation so it will show up in the form of hydrocarbons. For a number of laboratory systems[6] it has been observed that about one electron is produced for every 10^6 hydrocarbon molecules reacted. Application of this observation can then be used to estimate an electron concentration. When this concentration is less than the computed thermal ionization value, chemi-ionization can be neglected. When this is not the case, other (more realistic) procedures will have to be developed and applied to the particular system being investigated.

ELECTRON DENSITY AND COLLISION FREQUENCY CONTOURS

All the separate analyses described previously (and outlined in Fig. 8) produce electron density and collision frequency contours in the exhaust plume. Clearly, the inviscid flow regions, including shocks and chemical kinetics, can be analyzed separately from the mixing and afterburning regions and then "patched together." As discussed through this paper, the high-altitude case can be treated in a straightforward manner, whereas at low altitudes the interaction of the inviscid and viscous flows is likely to be strong. There are no presently available techniques for treating these strong interactions from first principles, and approximate superposition techniques must therefore be utilized. The type of procedure employed depends upon that region of the exhaust for which the greatest degree of accuracy is required, i.e., what is the rf path through the plume? If it passes directly through the afterburning region, care must be exercised in constructing the contours in that region; the same reasoning applies if the rf path goes through the strong part of the shock structure. A sketch of electron density contours in a low-altitude plume superimposing the effects of afterburning, inviscid flow, and shocks is given in Fig. 16.

The above remarks obviously refer to a pragmatic solution to the coupled problem. Considerably more theoretical effort is required in this area to achieve completely satisfying results.

CONCLUSIONS

The problem of predicting electron density and col' ion frequency contours in a rocket exhaust is well formulated, i.e., a systematic procedure can be utilized to give the required contours from a knowledge of fundamental propellant/missile system parameters. An examination of this procedure shows that there are four major areas of study which must be investigated further before more reliable predictions can be made:

1. More accurate reaction rate data and description of the turbulent mixing process with chemical reactions (i.e., eddy diffusivity "model").

2. More sophisticated analytical techniques for treating the interaction between the mixing anf afterburning regions, inviscid flow, and shock structure.

3. A means of theoretically treating chemi-ionization in afterburning exhausts from first principles.

4. Comparisons between good rf interference data (either in-flight or ground tests) and theoretical predictions.* If possible, techniques which measure point values of electron concentration in a rocket exhaust should be used. This is obviously a more direct method of checking the theory.

---

* It is implicit here that differences between theory and measurements will not be due to inaccuracies in the electromagnetic analysis.

REFERENCES

1. G. Hasserjian, "Interaction of Electromagnetic Waves with the Exhaust Flame of Launch Vehicles," Paper presented at the Third Symposium on the Plasma Sheath, Boston, Mass. (September 22, 1965).

2. H. H. Willard, L. L. Merrit and J. A. Dean, "Flame Photometry," Instrumental Methods of Analysis, D. Van Nostrand Co., Inc., Princeton, N.J., 1948, Chap. 8.

3. H. N. Browne and M. M. Williams, "The Theoretical Computation of Equilibrium Compositions, Thermodynamic Properties and Performance Characteristics of Propellant Systems," NOTS TP 2434, NAVWEPS Report No. 7043, DDC AD 246 591 (June 1960).

4. S. A. Greene and H. J. Vale, "The Aerospace Corporation Computer Programs for the Solution of Multielement Chemical Equilibria," Report No. TDR 69(2240-51) TR-2, DDC AD 282 658 (June 1962).

5. S. Gordon and F. J. Zeleznik, "A General IBM 704 or 7090 Computer Program for Computation of Chemical Equilibrium Compositions, Rocket Performance and Chapman-Jouget Detonations," NASA Report No. TN D-1737 (October 1963).

6. H. F. Calcote, "Ionization in Hydrocarbon Flames," AeroChem TP-119, August 1965; presented at the 26th Meeting of Propulsion and Energetics Panel, AGARD, Pisa, Italy (September 6-9, 1965). (to be published)

7. W. J. Miller and H. S. Pergament, "Radar Interference Effects in the LEM Descent Engine Exhaust Plume," Final Report, AeroChem TP-118 (July 1965).

8. J. A. Lordi and R. E. Mates, "Nonequilibrium Expansions of High-Enthalpy Air Flows," Aerospace Research Laboratories Report No. ARL 64-206, DDC AD 610 320 (November 1964).

9. G. Emmanuel and W. G. Vincenti, "Method of Calculation of the One-Dimensional Nonequilibrium Flow of a General Gas-Mixture Through a Hypersonic Nozzle," Arnold Engineering Development Center, Report No. AEDC TDR-62-131 (June 1962).

10. G. Moretti, "A New Technique for the Numerical Analysis of Nonequilibrium Flows," AIAA J., vol. 3, pp. 223-229 (1965).

11. C. E. Treanor, "A Method for the Numerical Integration of Coupled Differential Equations with Greatly Different Time Constants," Cornell Aeronautical Laboratory, Inc., CAL AG-1729-A-4 (December 1963).

12. D. E. Jensen and S. C. Kurzius, "Rate Constants for Calculations on Rocket Exhausts Containing Alkali Metals," AeroChem TP-149 (March 1967).

13. S. L. Soo and R. C. Dimick, "Interaction of Solid Particles with an Ionized Gas," Tenth Symposium (International) on Combustion, The Combustion Institute, 1965, pp. 699-707.

14. L. J. Krzycki, "Electrical Properties of Rocket Nozzle Boundary Layers," AIAA J. vol. 3 pp. 558-560 (1965).

15. W. W. Balwanz, "Interaction Between Electromagnetic Waves and Flames," Part VI: Theoretical Plots of Absorption, Phase Shift and Reflection," U.S. Naval Research Laboratory, NRL Report 5388 (September 1959).

16. P. Molmud, "The Electrical Conductivity of Weakly Ionized Gases," Space Technology Laboratory, Inc., Report No. 6120-J-757-RU-000, DDC AD 289 012, BSD-TDR-62-234 (October 1962).

17. S. Altshuler, "Theory of Low-Energy Electron Scattering by Polar Molecules," Phys. Rev., vol. 107, p. 114 (1957).

18. A. Ferri, Elements of Aerodynamics of Supersonic Flows, The Macmillan Co., New York, 1949.

19. D. W. Eastman and L. P. Radtke, "Two-Dimensional or Axially Symmetric Real Gas Flows by the Method of Characteristics, Part III: A Summary of Results from the IBM 7090 Program for Calculating the Flow Field of a Supersonic Jet," Boeing Co., D-2-10599 (1962).

20. E. S. Love, C. E. Grigsby, L. P. Lee and M. J. Woodling, "Experimental and Theoretical Studies of Axisymmetric Free Jets," NASA Technical Report R-6 (1959).

21. M. M. Moe and B. A. Troesch, "The Computation of Jet Flows with Shocks," Space Technology Laboratories, Inc., TR-59-0000-00661, DDC AD 418 769 (May 1959).

22. A. R. Vick, E. H. Andrews, J. S. Dennard and C. B. Craidon, "Comparisons of Experimental Free-Jet Boundaries with Theoretical Results Obtained with the Method of Characteristics," NASA TN D-2327 (June 1964).

23. H. Yoshihara and R. Magnus, "Multi-Rocket Exhaust Plumes," General Dynamics/Astronautics, GDA-ERR-AN 544 (September 1964).

24. L. D'Atorre and F. Harshbarger, "Further Experimental and Theoretical Studies of Underexpanded Jets Near the Mach Disc," General Dynamics/Astronautics, GDA-DBE 64-041, DDC AD 444 088 (July 1964).

25. L. Howarth, ed., Modern Developments in Fluid Dynamics - High Speed Flow, Clarendon Press, London, 1956, vol. I, chap. IV.

26. T. C. Adamson, Jr. and J. A. Nichools, "On the Structure of Jets from Highly Underexpanded Nozzles into Still Air," J. AeroSpace Sci., vol. 26, pp. 16-24 (1959).

27. D. W. Eastman and L. P. Radtke, "Location of the Normal Shock Wave in the Exhaust Plume of a Jet," AIAA J., vol. 1, pp. 918-919 (1963).

28. L. D'Attorre and F. Harshbarger, "Experimental and Theoretical Studies of Underexpanded Jets Near the Mach Disc," General Dynamics/Astronautics, GDA-DBE 64-008, DDC AD 436 014; Appendix, DDC AD 343 015 (February 1964).

29. H. Schlicting, Boundary Layer Theory, Pergamon Press, New York, 1955, chap. XXIII.

30. P.A. Libby, "Theoretical Analysis of Turbulent Mixing of Reactive Gases with Application to Supersonic Combustion of Hydrogen," ARS J., vol. 32, pp. 388-396 (1962).

31. S.L. Zeiberg and G.D. Bleich, "Finite Difference Calculation of Hypersonic Wakes," AIAA J., vol. 2, pp. 1396-1402 (1964).

32. R.D. Richtmyer, Difference Methods for Initial Value Problems, Interscience Publishers, New York, 1957, chaps. 1, 4, and 6.

33. D.R. Stull, ed., JANAF Interim Thermochemical Tables, Dow Chemical Co., Midland, Mich., 1960.

34. E.A. Moelwyne-Hughes, Physical Chemistry, Pergamon Press, New York, 1961, 2nd ed.

35. L.K. O'Brian and B. Brown, "A Survey of Ionization Potentials of Combustion Products," APL Working Group on Thermochem., Proc. of 2nd Meeting, Vol I, August 1964, pp. 1-12.

36. D. E. Rosner, "Ionization in Rocket Exhaust Plumes," AeroChem TP-85. April, 1964.

NOMENCLATURE

a	attenuation, db/in
$\bar{c}_e$	mean thermal electron velocity
h	static enthalpy
H	stagnation enthalpy, $h + u^2/2$
$\dot{m}$	nozzle mass flow
m_i	mass of species i
m_k	mass of element k
M_∞	free stream (vehicle) Mach number
n	number density of mixture
n_e	electron density, cc^{-1}
p	static pressure
Q_i	electron-neutral collision cross section
T	static temperature
u	velocity in x direction
v	velocity in y direction
$\dot{w}_i$	net rate of production of species i
W	molecular weight of mixture
x	coordinate in axial direction (or parallel to inviscid jet boundary for 2-dimensional mixing)
X_i	mole fraction of species i
y	normal coordinate (Fig. 14)
Y_i	mass fraction of species i
$\tilde{Y}_k$	element mass fraction (Eq. (7))

Greek Symbols

β	oxygen/hydrogen mole fraction ratio, X_{O_2}/X_{H_2}
γ	specific heat ratio
ε	eddy diffusivity
ν_e	electron-neutral collision frequency, sec^{-1}
ρ	density
Ψ	stream function, defined from $\Psi\Psi_y = \rho uy$ and $\Psi\Psi_x = \rho vy$
ω	signal frequency, sec^{-1}

NOMENCLATURE (cont'd)

Subscripts

eq	equilibrium value
f	frozen value
$( )_{\substack{x \\ y}}$	partial differentiation with respect to x or y
j	nozzle exit plane value
∞	free stream value

Table I - Typical Solid Propellant Compositions and Impurities

Composition, wt.%	Composite--Double-Base	Composite
Ammonium Perchlorate	21	79
Aluminum	4	9
Binders	8	12
Double-Base	67	-
Impurities, ppm		
Na	50	100
K	20	40
Li	10	30
Ca	100	300

Table II - Typical Liquid Propellant Fuels and Impurities

Impurity, ppm	UDMH[a]	Hydrazine	Mixed Hydrazines[b]
Na	3	1	<0.7
K	1	0.2	1
Li	1	0.2	<0.5
Ca	<0.1	<0.1	2

[a] unsymmetrical Dimethyl Hydrazine

[b] contains Monomethyl Hydrazine and Hydrazine

TP-122

Table III - Thermochemical Equilibrium Properties in Typical Composite Solid Propellant Exhaust Nozzle

	Chamber	Exit Plane
Pressure, psia	700	14.7
Temperature, °K		
Equilibrium	3270	2020
Frozen	3270	1780
Velocity, fps		
Equilibrium	----	8020
Frozen	----	7840
Composition, mole fraction[b]		
Major Neutral Species		
CO	1.8(-1)[c]	1.7(-1)
CO_2	4.2(-2)	6.0(-2)
HCl	1.6(-1)	1.8(-1)
H_2	1.5(-1)	1.7(-1)
H_2O	2.8(-1)	2.8(-1)
N_2	9.0(-2)	9.2(-2)
OH	1.4(-2)	1.3(-4)
H	1.9(-2)	7.0(-4)
Al_2O_3[a]	4.7(-2)(ℓ)	5.0(-2)(s)
Minor Neutral Species		
O_2	7.5(-4)	2.7(-7)
O	1.0(-3)	3.8(-7)
N	3.0(-6)	3.3(-10)
NO	1.3(-3)	3.3(-6)
Ca	5.4(-8)	1.0(-10)
$CaCl_2$	2.2(-4)	2.3(-4)
Na	4.8(-6)	3.9(-7)
NaCl	9.6(-5)	1.2(-4)
NaOH	1.0(-5)	1.0(-6)
K	5.0(-7)	3.3(-8)
KCl	2.3(-5)	3.0(-5)
KOH	5.7(-7)	2.8(-8)
Li	6.8(-7)	1.1(-8)
LiCl	9.9(-5)	1.1(-4)
LiOH	6.3(-6)	5.5(-7)
Cl	1.3(-2)	5.9(-4)
Cl_2	3.8(-5)	5.6(-7)

Table III (cont'd)

Charged Species		
e^-	7.9(-8)	1.7(-10)
Cl^-	8.6(-6)	1.8(-7)
Ca^+	4.3(-9)	7.2(-14)
Na^+	3.0(-6)	1.9(-8)
K^+	5.4(-6)	1.6(-7)
Li^+	1.3(-7)	1.2(-10)
Al^+	8.5(-8)	<1(-14)
NO^+	2.1(-10)	<1(-14)
Electron Density, cc^{-1}		
Equilibrium	8.4(12)	6.0(8)
Frozen	8.4(12)	3.2(11)

[a] Since Al_2O_3 exists as particles in the nozzle, a more meaningful quantity is the mass fraction which, for this system, is about 0.20.

[b] Shifting equilibrium.

[c] Numbers in parenthesis refer to power of 10, e.g., (-8) is equivalent to 10^{-8}.

TP-122

Table IV - Thermochemical Equilibrium Properties in LEM Descent Engine Exhaust Nozzle, O/F Ratio = 1.6

	Chamber	Exit Plane	
		Lip	Centerline
Pressure, psia	110	0.34	0.037
Temperature, °K			
Equilibrium	3060	1170	740
Frozen	3060	890	575
Velocity, fps			
Equilibrium	----	10200	10900
Frozen	----	9620	10200
Composition, Mole Fraction[b]			
Major Neutral Species			
H	2.6(-2)	2.0(-7)	3.0(-12)
CO	9.8(-2)	5.1(-2)	1.2(-2)
CO_2	3.4(-2)	8.5(-2)	1.2(-1)
OH	2.4(-2)	2.1(-9)	a
H_2	1.4(-1)	1.8(-1)	2.2(-1)
H_2O	3.5(-1)	3.5(-1)	3.0(-1)
N_2	3.2(-1)	3.4(-1)	3.4(-1)
Minor Neutral Species			
O	2.7(-3)	a	a
O_2	2.8(-3)	a	a
N	4.3(-6)	a	a
NO	3.8(-3)	1(-10)	a
K	5.4(-8)	6.2(-8)	4.1(-9)
Na	4.0(-7)	2.9(-8)	2.1(-10)
Li	4.8(-7)	8.2(-10)	a
KOH	3.9(-8)	2.9(-7)	3.7(-7)
NaOH	5.6(-7)	1.0(-6)	1.1(-6)
LiOH	3.5(-6)	4.1(-6)	2.0(-7)
Charged Species			
ϵ^-	3.4(-7)	a	a
OH^-	3.9(-8)	a	a
K^+	2.5(-7)	a	a
Na^+	9.0(-8)	a	a
Li^+	4.1(-8)	a	a
NO^+	1.0(-10)	a	a

[a] Denotes <1 (-14).

[b] Shifting equilibrium

Table V - Chemical Reactions and Rate Constants for Typical Solid and Liquid Propellant Combustion Products[a, b]

Reaction	Forward Rate Constant[c, d]

NEUTRAL SPECIES

Chain-Carrying Binary Reactions

1. $OH + H_2 \rightleftarrows H_2O + H$	k_1	$= 4 \times 10^{-11} \exp(-5,500/RT)$
2. $OH + OH \rightleftarrows H_2O + O$	k_2	$= 1 \times 10^{-11} \exp(-1,000/RT)$
3. $O + H_2 \rightleftarrows OH + H$	k_3	$= 3 \times 10^{-11} \exp(-8,200/RT)$
4. $H + O_2 \rightleftarrows OH + O$	k_4	$= 3 \times 10^{-10} \exp(-16,500/RT)$
5. $OH + CO \rightleftarrows CO_2 + H$	k_5	$= 5 \times 10^{-13} \exp(-600/RT)$
6. $N + OH \rightleftarrows NO + H$	k_6	$= 2 \times 10^{-11}$
7. $N + NO \rightleftarrows N_2 + O$	k_7	$= 3 \times 10^{-11}$
8. $N + O_2 \rightleftarrows NO + O$	k_8	$= 7 \times 10^{-12} \exp(-6,500/RT)$
9. $H + Cl_2 \rightleftarrows HCl + Cl$	k_9	$= 7 \times 10^{-10} \exp(-3,000/RT)$
10. $Cl + H_2 \rightleftarrows HCl + H$	k_{10}	$= 1.5 \times 10^{-10} \exp(-5,600/RT)$
11. $Cl + H_2O \rightleftarrows HCl + OH$	k_{11}	$= 5 \times 10^{-11} \exp(-19,000/RT)$
12. $Cl + OH \rightleftarrows HCl + O$	k_{12}	$= 3 \times 10^{-11} \exp(-5,000/RT)$

Salt-Forming Binary Reactions

13. $Li + H_2O \rightleftarrows LiOH + H$	k_{13}	$= 3 \times 10^{-11} \exp(-20,000/RT)$
14. $Na + H_2O \rightleftarrows NaOH + H$	k_{14}	$= 3 \times 10^{-11} \exp(-44,000/RT)$
15. $K + H_2O \rightleftarrows KOH + H$	k_{15}	$= 3 \times 10^{-11} \exp(-40,000/RT)$
16. $Li + HCl \rightleftarrows LiCl + H$	k_{16}	$= 3 \times 10^{-10}$
17. $Na + HCl \rightleftarrows NaCl + H$	k_{17}	$= 3 \times 10^{-10} \exp(-5,000/RT)$
18. $K + HCl \rightleftarrows KCl + H$	k_{18}	$= 3 \times 10^{-10}$

Ternary Termination Reactions

19. $H + H + M \rightleftarrows H_2 + M$	k_{19}	$= 1 \times 10^{-29}/T$
20. $H + O + M \rightleftarrows OH + M$	k_{20}	$= 1 \times 10^{-29}/T$
21. $H + OH + M \rightleftarrows H_2O + M$	k_{21}	$= 1 \times 10^{-28}/T$
22. $O + O + M \rightleftarrows O_2 + M$	k_{22}	$= 1 \times 10^{-29}/T$
23. $O + CO + M \rightleftarrows CO_2 + M$	k_{23}	$= (5 \times 10^{-29}/T) \exp(-4,000/RT)$
24. $N + N + M \rightleftarrows N_2 + M$	k_{24}	$= 1 \times 10^{-29}/T$
25. $N + O + M \rightleftarrows NO + M$	k_{25}	$= 3 \times 10^{-30}/T$
26. $Cl + H + M \rightleftarrows HCl + M$	k_{26}	$= 3 \times 10^{-29}/T$
27. $Cl + Cl + M \rightleftarrows Cl_2 + M$	k_{27}	$= 3 \times 10^{-29}/T$

Table V (cont'd)

Ternary Salt-Forming Reactions

28.	$Li + OH + M \rightleftarrows LiOH + M$	k_{28}	$= 3 \times 10^{-28}/T$
29.	$Na + OH + M \rightleftarrows NaOH + M$	k_{29}	$= 3 \times 10^{-28}/T$
30.	$K + OH + M \rightleftarrows KOH + M$	k_{30}	$= 3 \times 10^{-28}/T$
31.	$Li + Cl + M \rightleftarrows LiCl + M$	k_{31}	$= 1 \times 10^{-28}/T$
32.	$Na + Cl + M \rightleftarrows NaCl + M$	k_{32}	$= 1 \times 10^{-28}/T$
33.	$K + Cl + M \rightleftarrows KCl + M$	k_{33}	$= 1 \times 10^{-28}/T$

CHARGED SPECIES

Attachment Reactions

34.	$e^- + OH + M \rightleftarrows OH^- + M$	k_{34}	$= 3 \times 10^{-30}$
35.	$e^- + Cl + M \rightleftarrows Cl^- + M$	k_{35}	$= 3 \times 10^{-30}$
36.	$e^- + HCl \rightleftarrows Cl^- + H$	k_{36}	$= 1 \times 10^{-10} \exp(-20,000/RT)$

Ternary Recombination Reactions

37.	$Li^+ + e^- + M \rightleftarrows Li + M$	k_{37}	$= 2 \times 10^{-20}/T^2$
38.	$Na^+ + e^- + M \rightleftarrows Na + M$	k_{38}	$= 1.5 \times 10^{-20}/T^2$
39.	$K^+ + e^- + M \rightleftarrows K + M$	k_{39}	$= 2 \times 10^{-22}/T^{1.5}$

Binary Recombination Reactions

40.	$NO^+ + e^- \rightleftarrows N + O$	k_{40}	$= 1 \times 10^{-4}/T$
41.	$Li^+ + OH^- \rightleftarrows Li + OH$	k_{41}	$= 1 \times 10^{-7}/T^{0.5}$
42.	$Na^+ + OH^- \rightleftarrows Na + OH$	k_{42}	$= 1 \times 10^{-7}/T^{0.5}$
43.	$K^+ + OH^- \rightleftarrows K + OH$	k_{43}	$= 1 \times 10^{-7}/T^{0.5}$
44.	$Li^+ + Cl^- \rightleftarrows Li + Cl$	k_{44}	$= 2 \times 10^{-7}/T^{0.5}$
45.	$Na^+ + Cl^- \rightleftarrows Na + Cl$	k_{45}	$= 2 \times 10^{-7}/T^{9.5}$
46.	$K^+ + Cl^- \rightleftarrows K + Cl$	k_{46}	$= 1 \times 10^{-8}/T^{0.5}$
47.	$NO^+ + Cl^- \rightleftarrows NO + Cl$	k_{47}	$= 1 \times 10^{-6}/T^{0.5}$

Table V (cont'd)

Charge Transfer Reactions

48. $Li^+ + Na$	$\rightleftarrows$ $Na^+ + Li$	k_{48}	$= 3 \times 10^{-10}$
49. $Li^+ + K$	$\rightleftarrows$ $K^+ + Li$	k_{49}	$= 3 \times 10^{-10}$
50. $Na^+ + K$	$\rightleftarrows$ $K^+ + Na$	k_{50}	$= 3 \times 10^{-10}$
51. $NO^+ + Li$	$\rightleftarrows$ $Li^+ + NO$	k_{51}	$= 7 \times 10^{-10}$
52. $NO^+ + Na$	$\rightleftarrows$ $Na^+ + NO$	k_{52}	$= 4 \times 10^{-10}$
53. $NO^+ + K$	$\rightleftarrows$ $K^+ + NO$	k_{53}	$= 5 \times 10^{-10}$
54. $OH^- + Cl$	$\rightleftarrows$ $Cl^- + OH$	k_{54}	$= 9 \times 10^{-10}$

[a] This list of reactions and rate constants was compiled by S. C. Kurzius and D. E. Jensen at AeroChem[12].

[b] Refers to combustion products in Tables III and IV; compounds containing Al and Ca have not been included since they have a negligible effect on the exit plane electron density.

[c] Rate constant units are: binary reactions, cc molecule^{-1} sec^{-1}; ternary reactions, cc^2 molecule^{-2} sec^{-1}. T is the local static temperature in ^{o}K; R is the universal gas constant in gm cal • gm mole^{-1} ^{o}K^{-1}.

[d] Reverse reactions are implicitly included in the mechanism. Their rate constants, k_r, are calculated from the relation $k_r = k_f/K$, where k_f is the forward rate constant and K the equilibrium constant. K for most neutral species can be readily calculated from the generally reliable JANAF tables.[33] In other instances, particularly for the charged species, recourse must still be made directly to thermochemical data (or estimates) and statistical mechanical treatments (see, e.g., Refs. 34 and 35.)

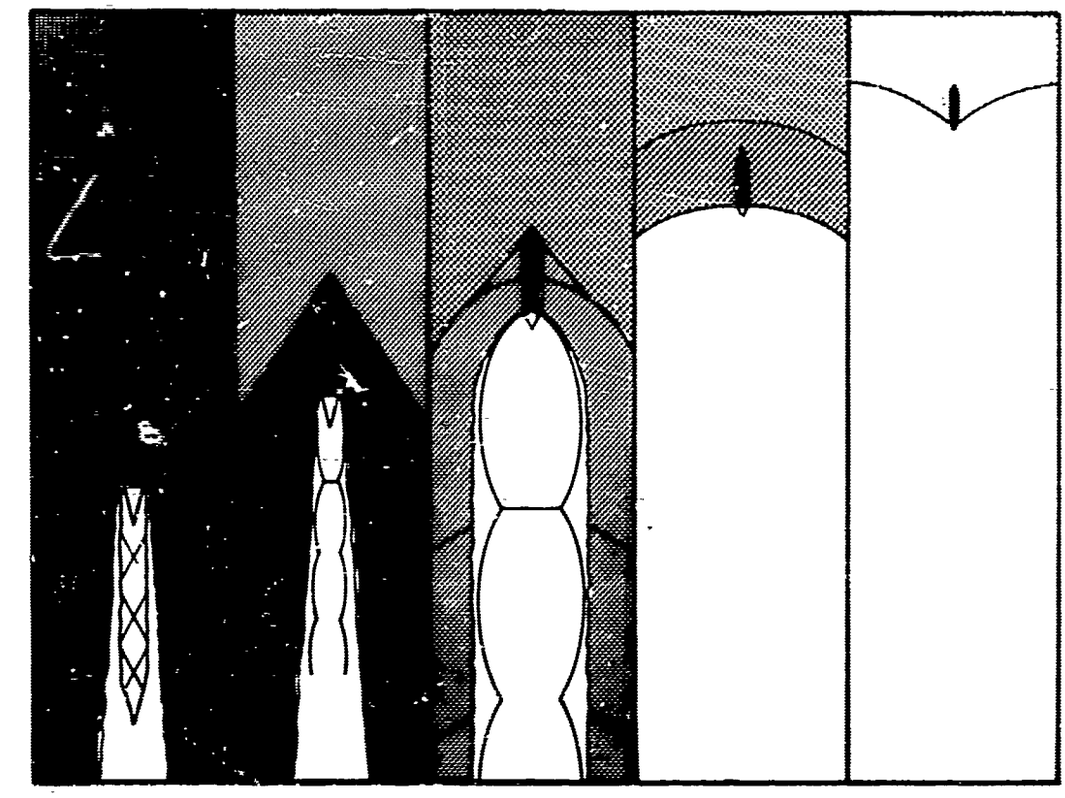


Figure 1. Ascending rocket exhaust plume from sea level to near-vacuum.
(taken from Ref. 36)

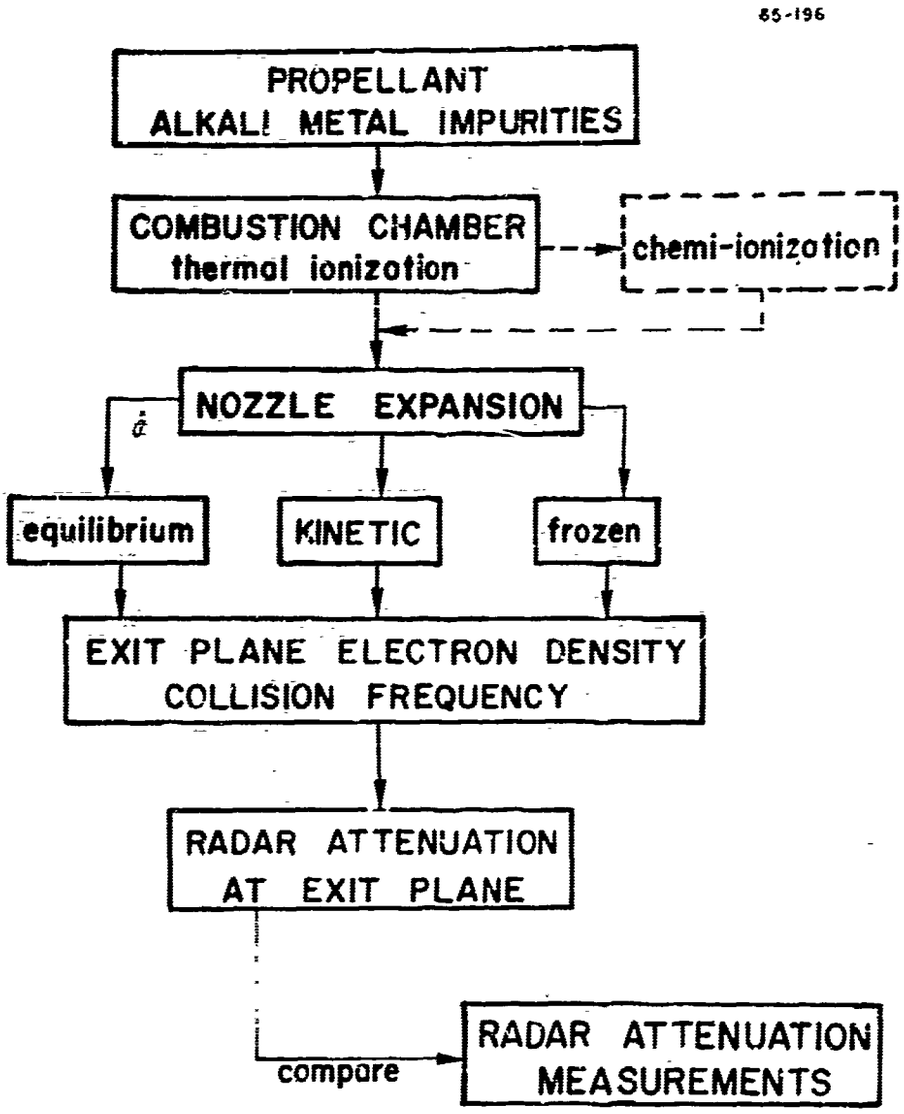


Figure 2. Procedure for determining nozzle exit plane radar attenuation.

65-110

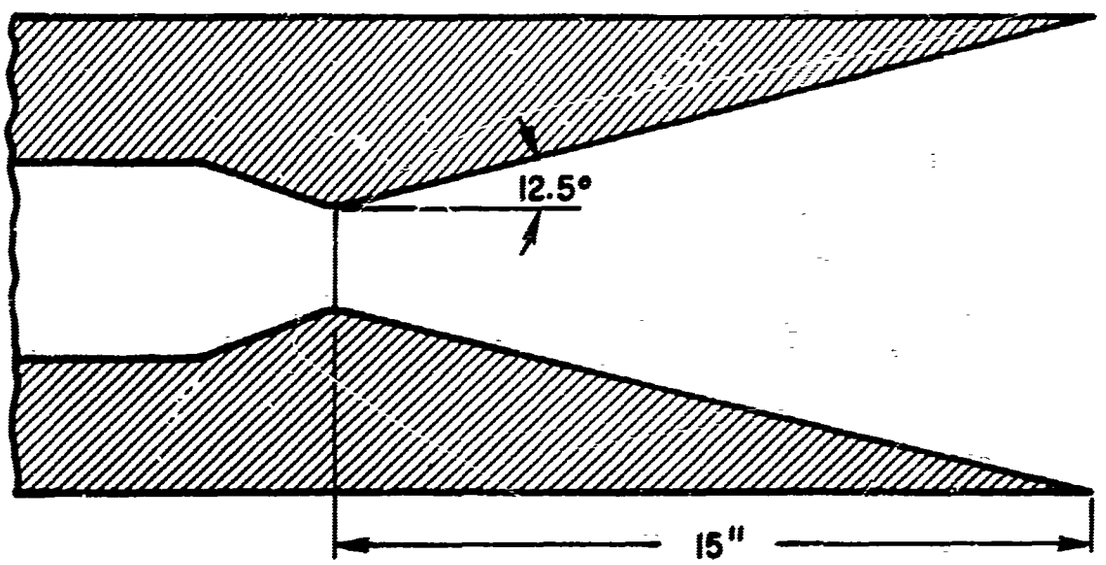


Figure 3. Composite solid propellant exhaust nozzle configuration.

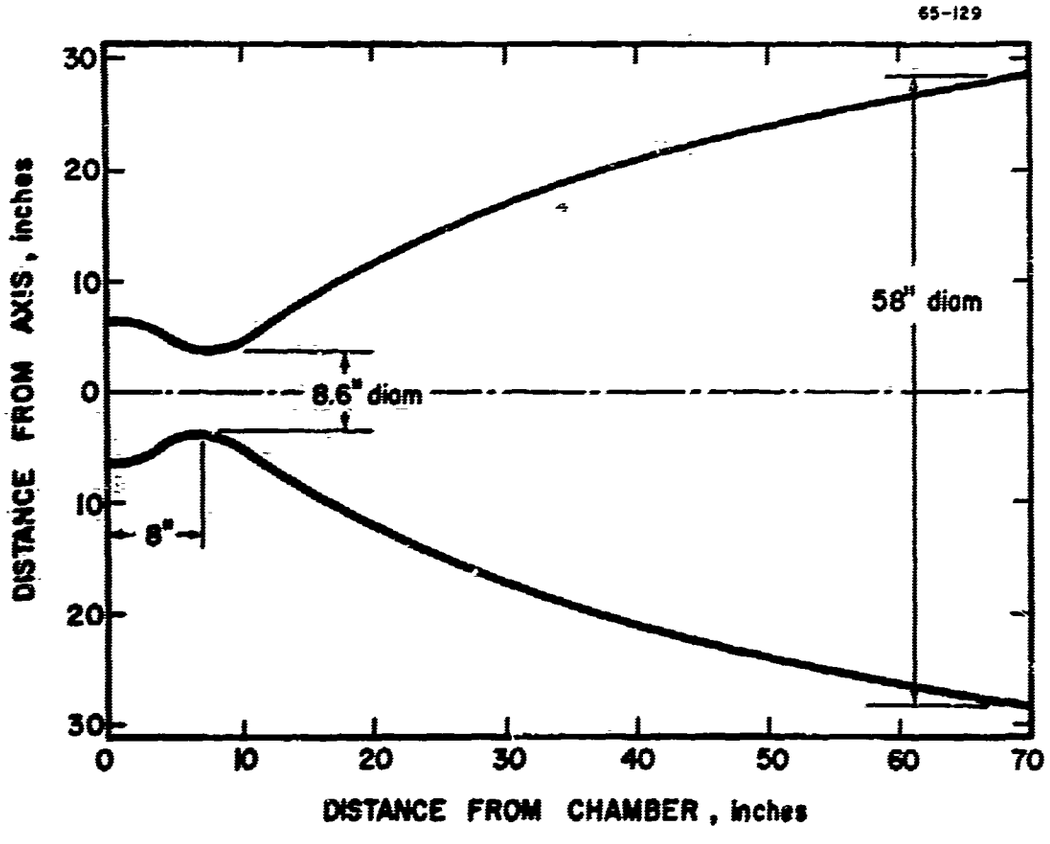


Figure 4. LEM descent engine exhaust nozzle.

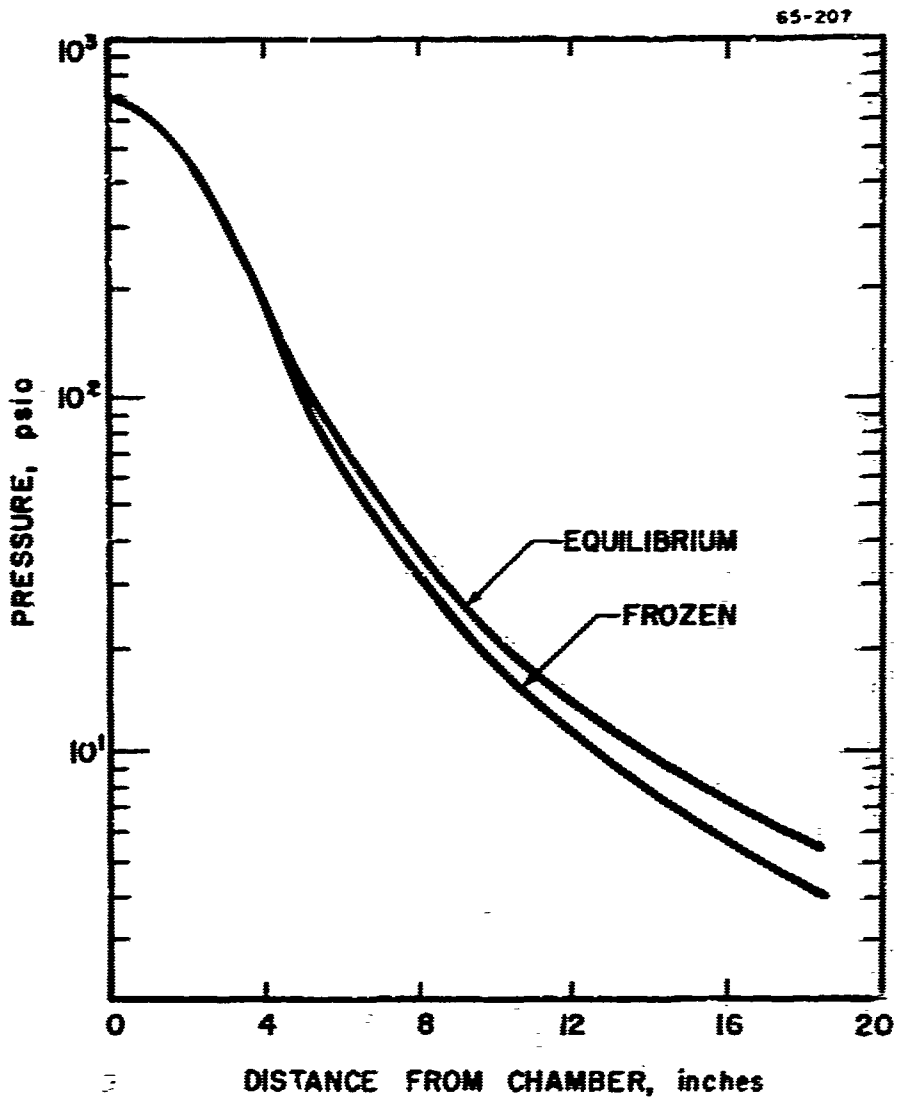


Figure 5. Pressure distribution in composite solid propellant exhaust nozzle (Fig. 3).

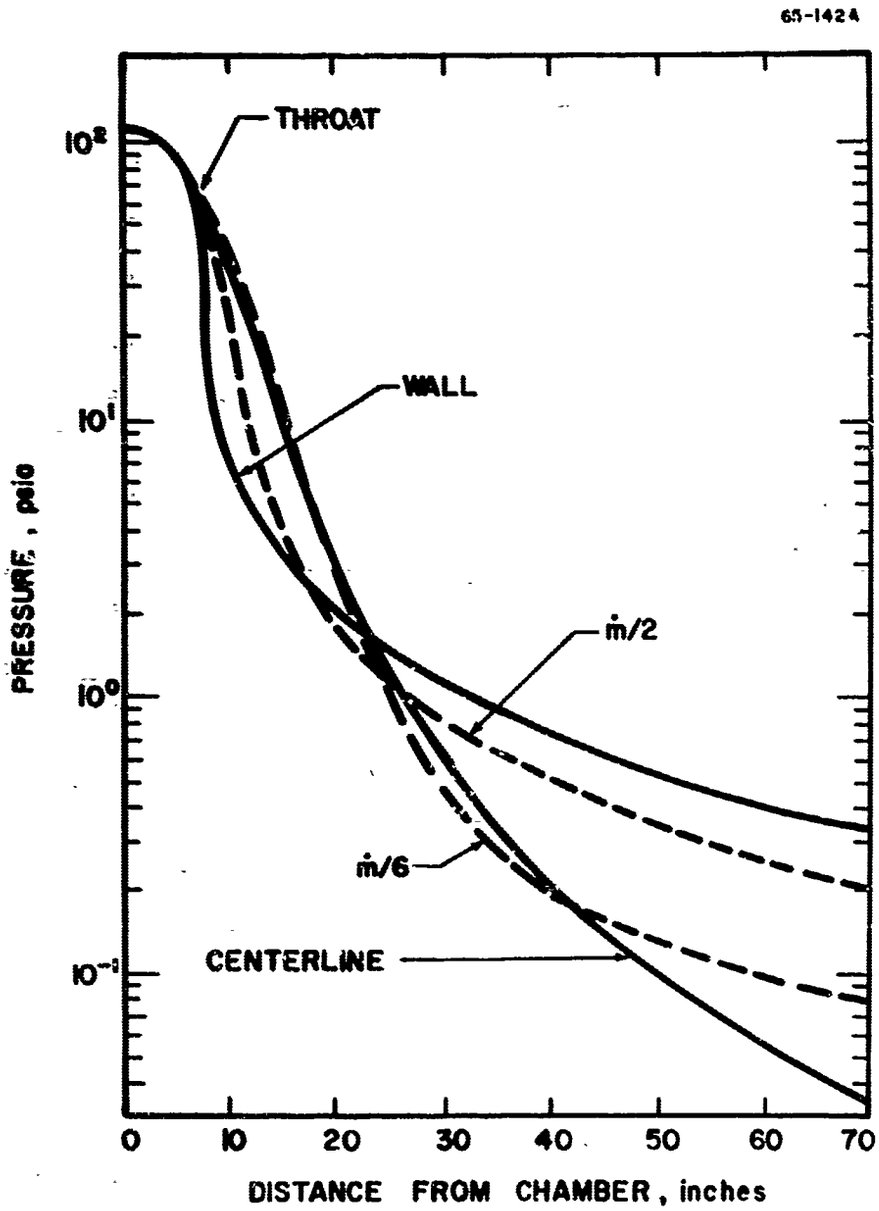


Figure 6. Pressure distribution in LEM descent engine exhaust nozzle (Fig. 4).

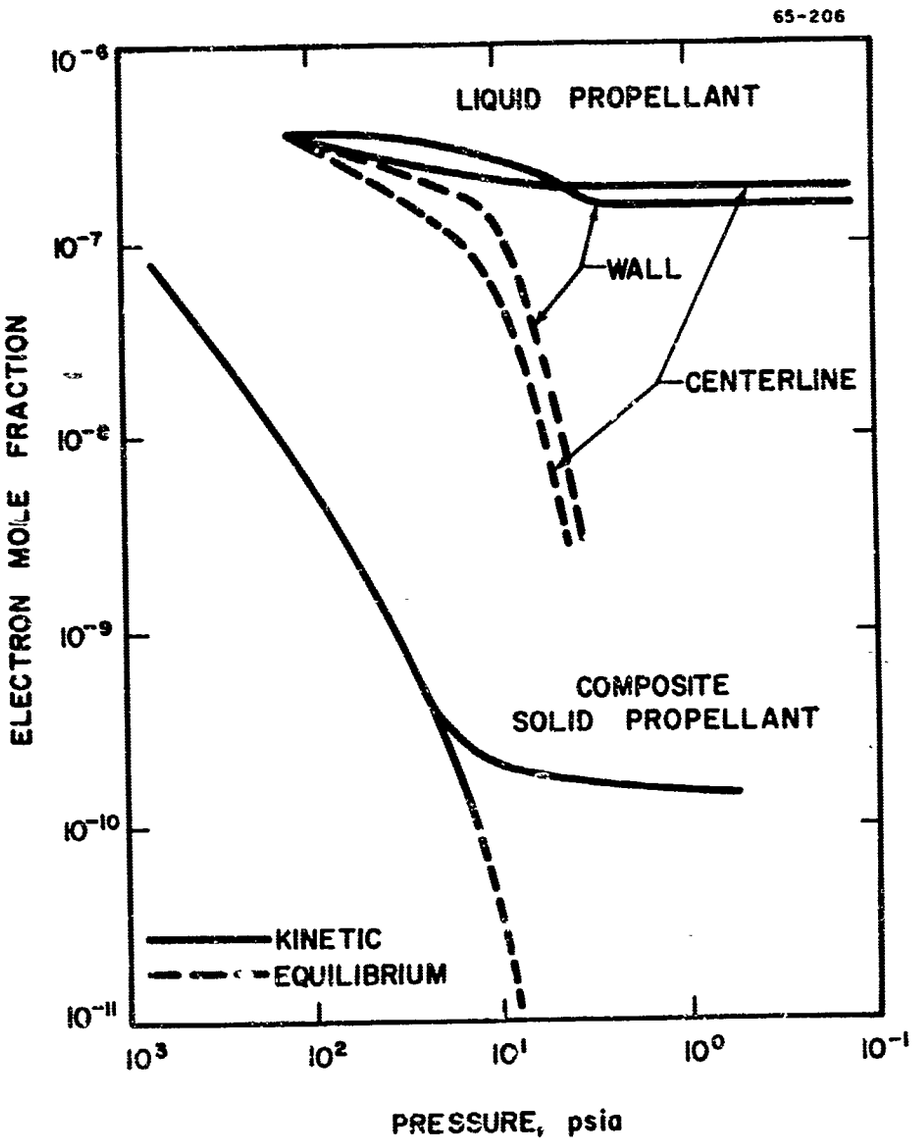


Figure 7. Electron mole fraction distribution in solid and liquid propellant exhaust nozzles.

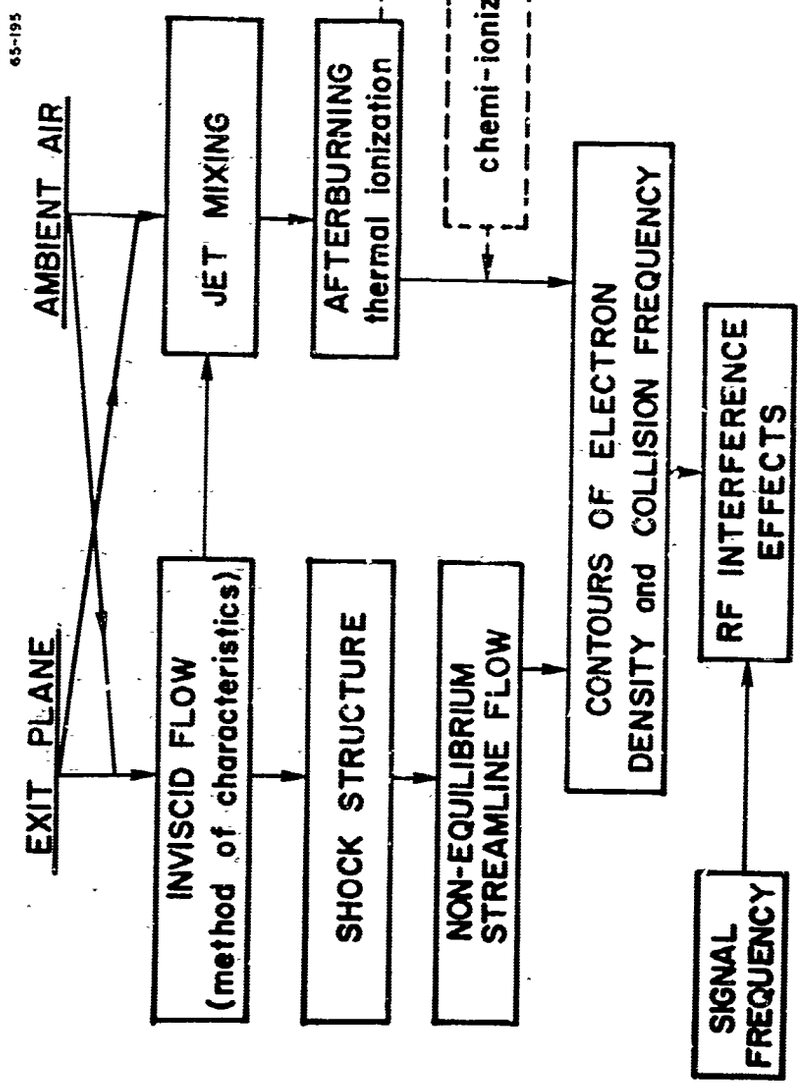


Figure 8. Procedure for determining exhaust plume rf interference.

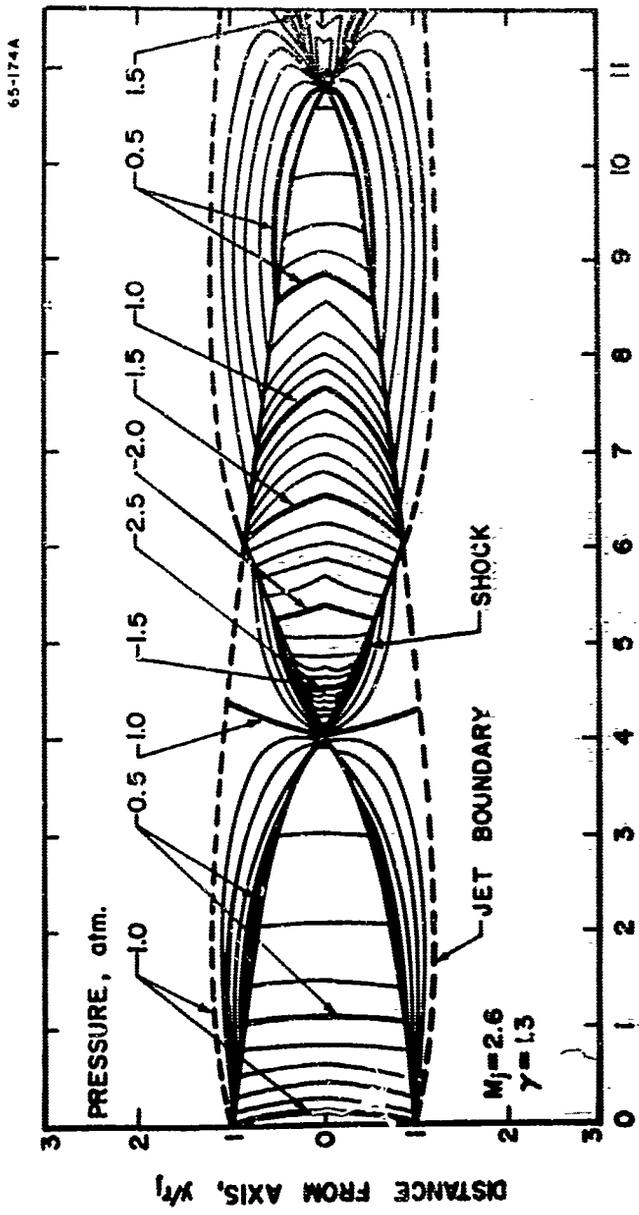


Figure 9. Constant pressure contours in sea level exhaust plume of solid propellant nozzle (Fig. 3).

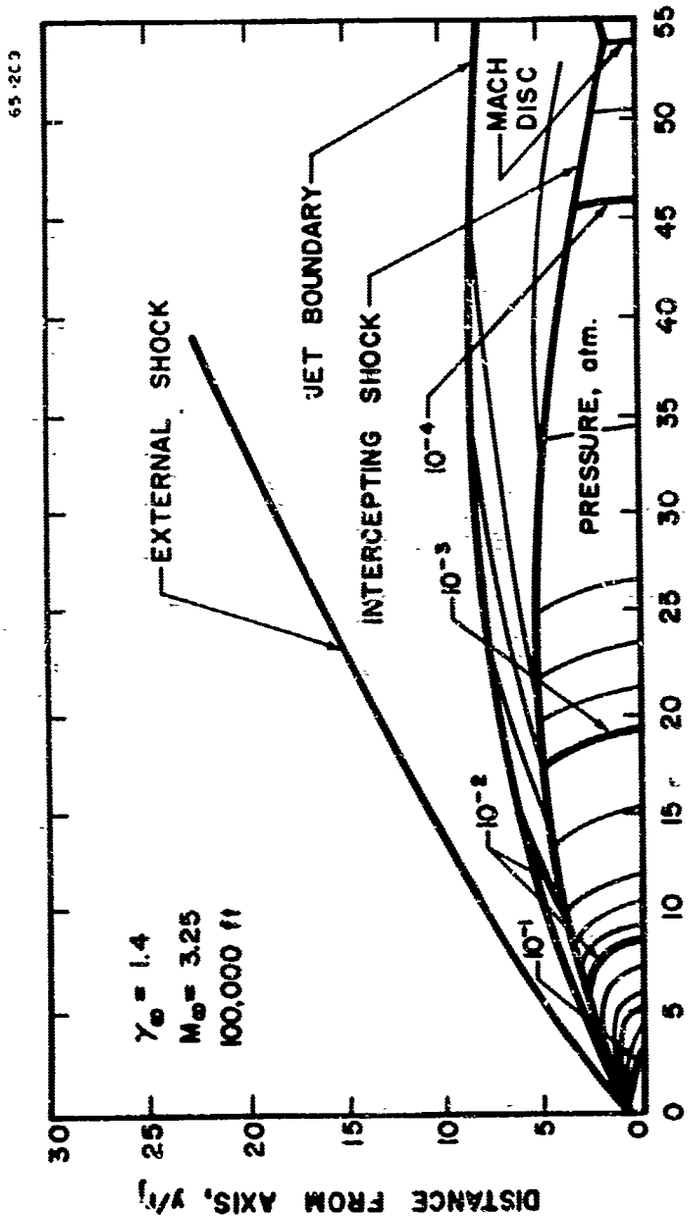


Figure 10. Constant pressure contours at intermediate altitude (after D'Attorre and Harshbarger[24]). Uniform nozzle exit plane properties, $\gamma = 1.22$.

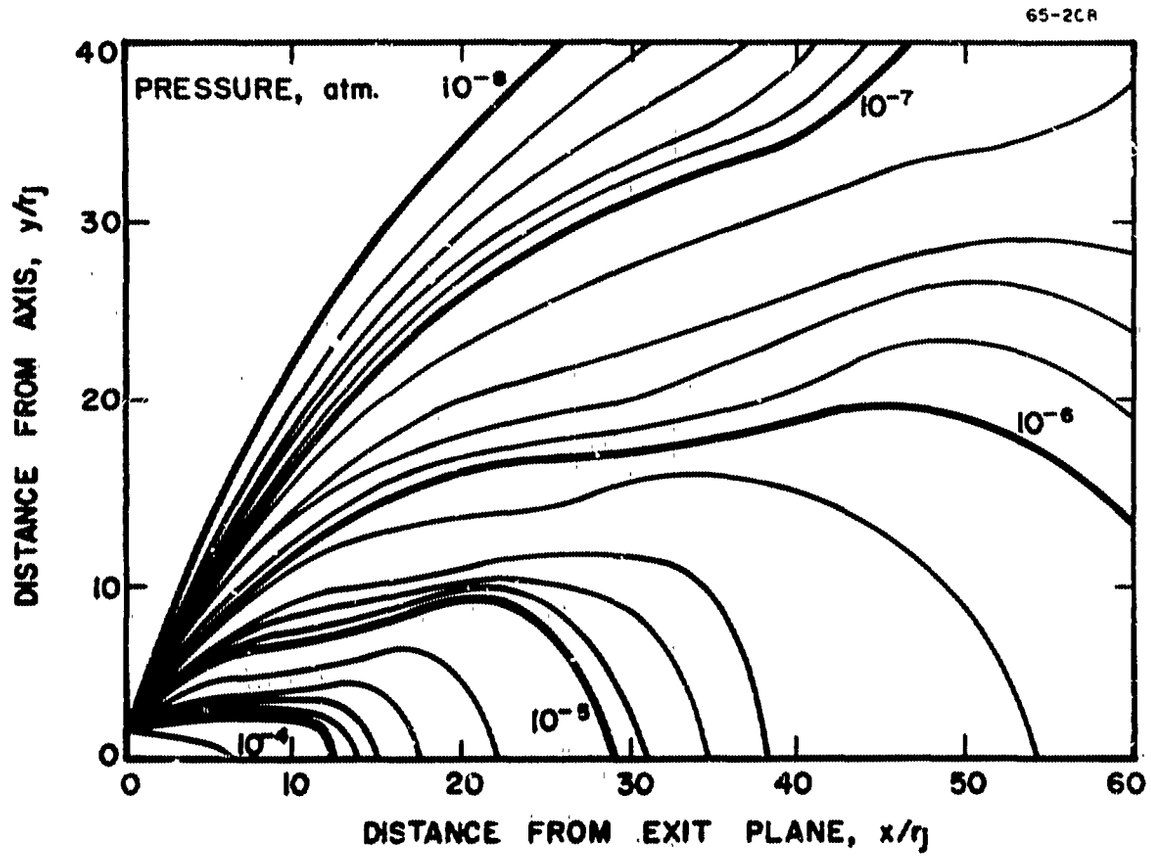


Figure 11. Constant pressure contours in vacuum exhaust plume of the LEM descent engine.

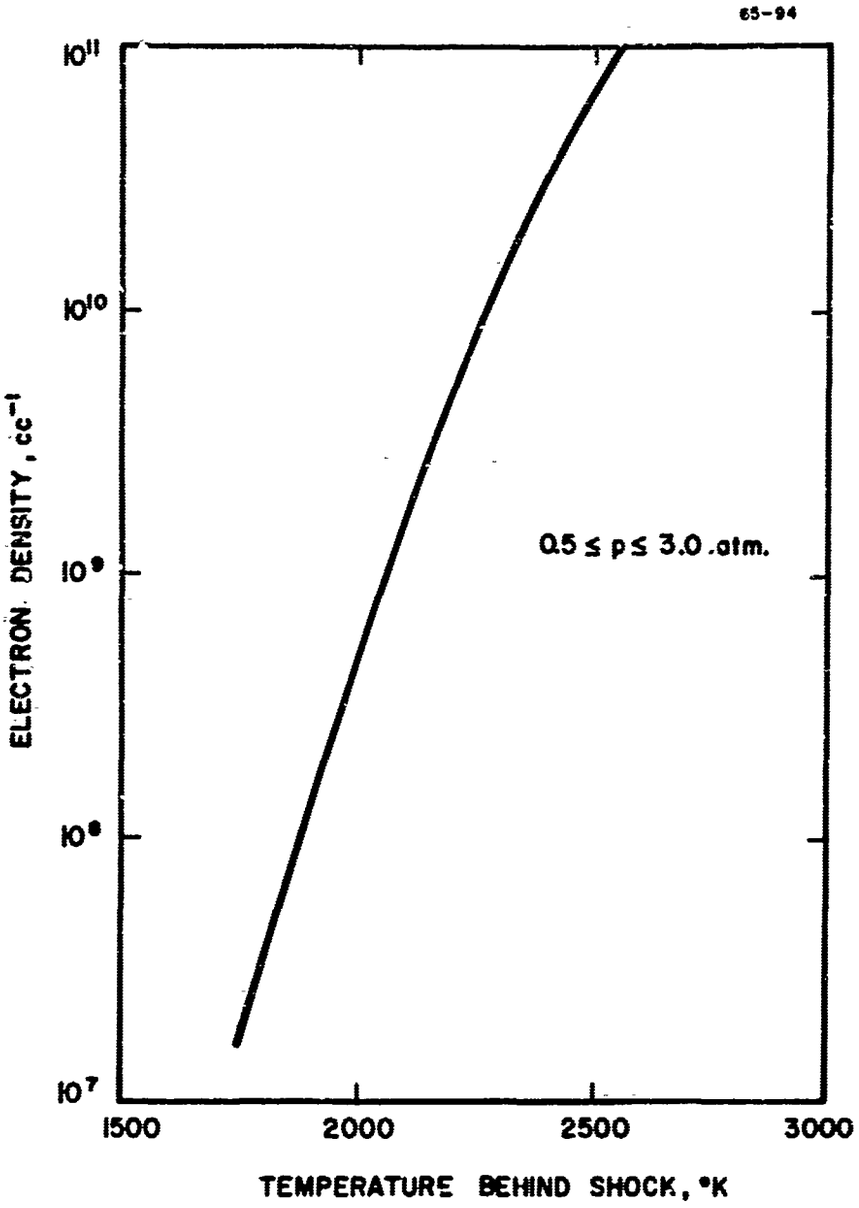


Figure 12. Shock ionization in the solid propellant exhaust plume. Thermochemical equilibrium behind shock-impurities from Table I.

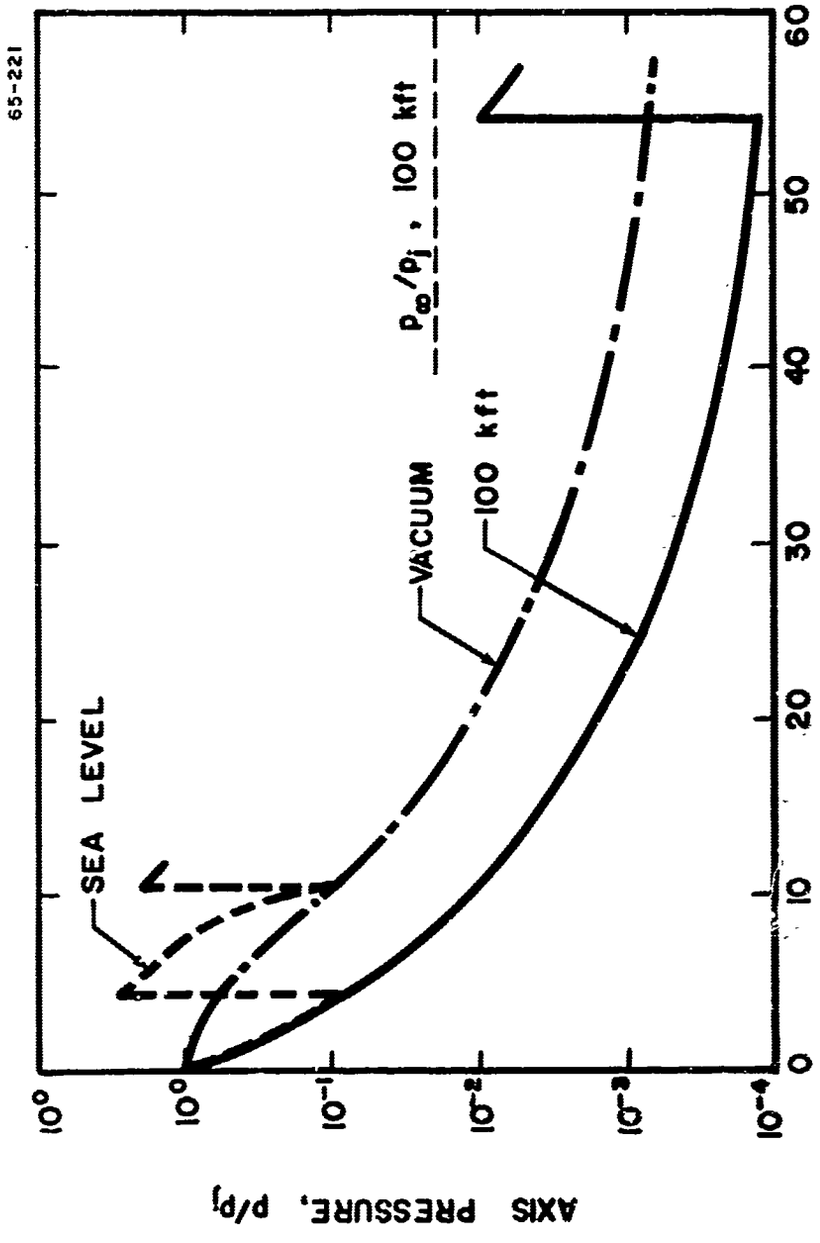


Figure 13. Axis pressure distributions for low, intermediate, and high altitude exhausts. Low altitude (Fig. 9), 100 kft (Fig. 10), vacuum (Fig. 11).

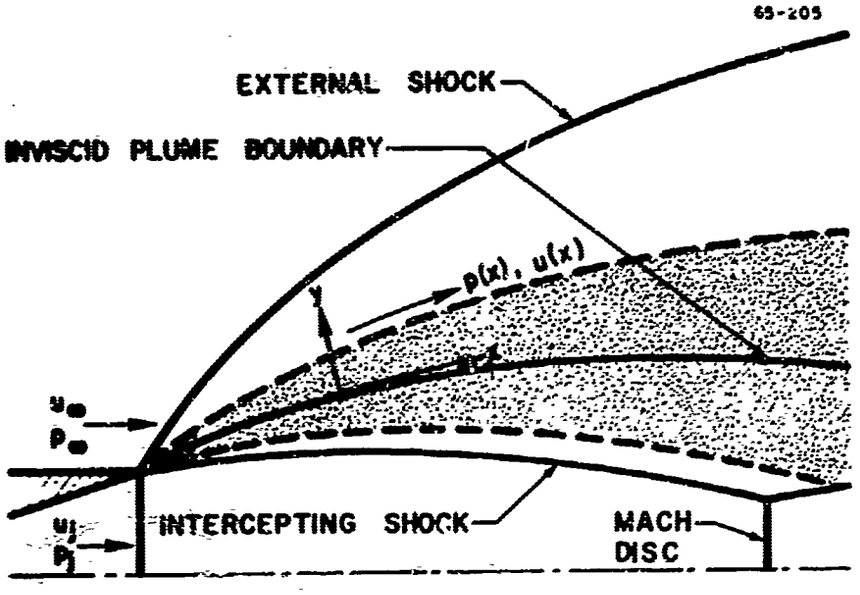


Figure 14a Two-dimensional mixing and afterburning. $p_j/p_\infty \gg 1$

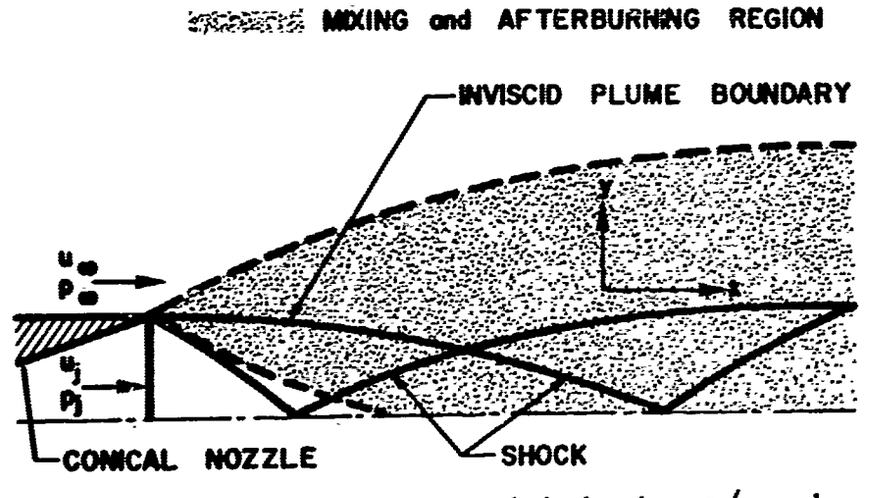


Figure 14b Axisymmetric mixing and afterburning. $p_j/p_\infty \approx 1$

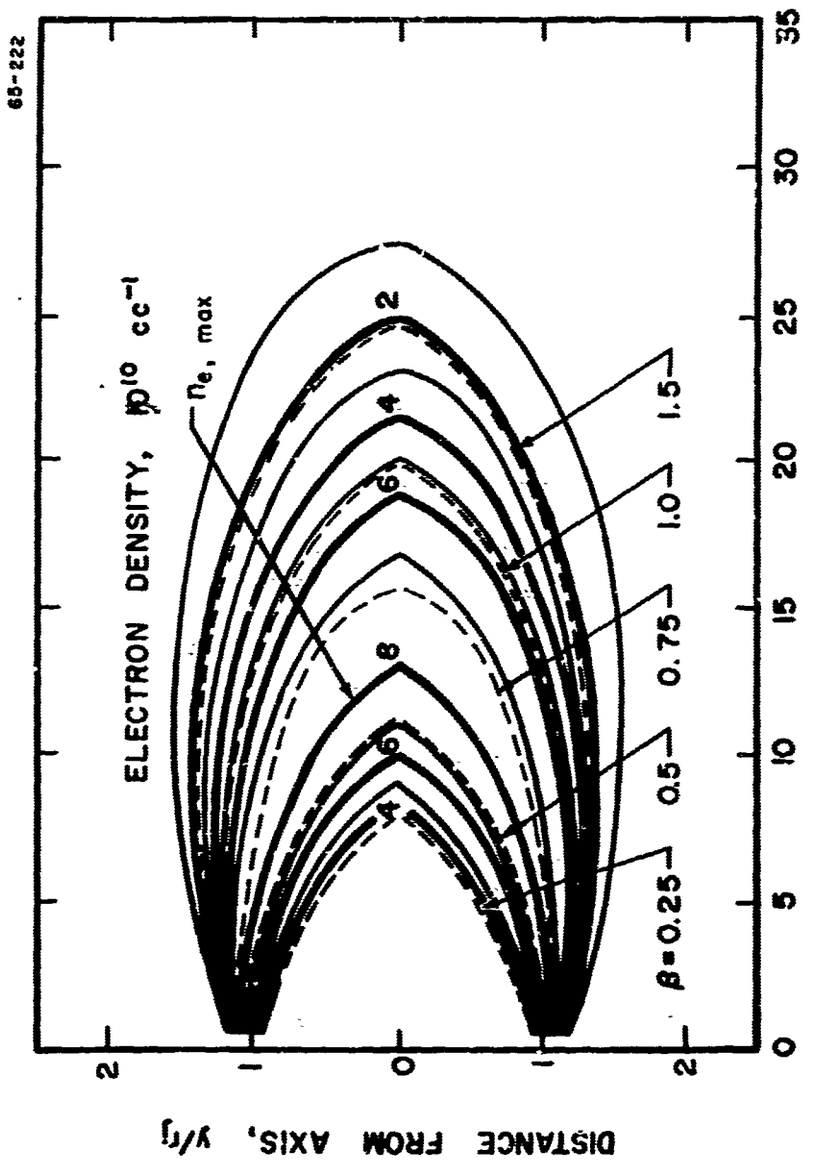


Figure 15 Constant electron density contours in sea level afterburning exhaust. Composite solid propellant system (Tables I and III).

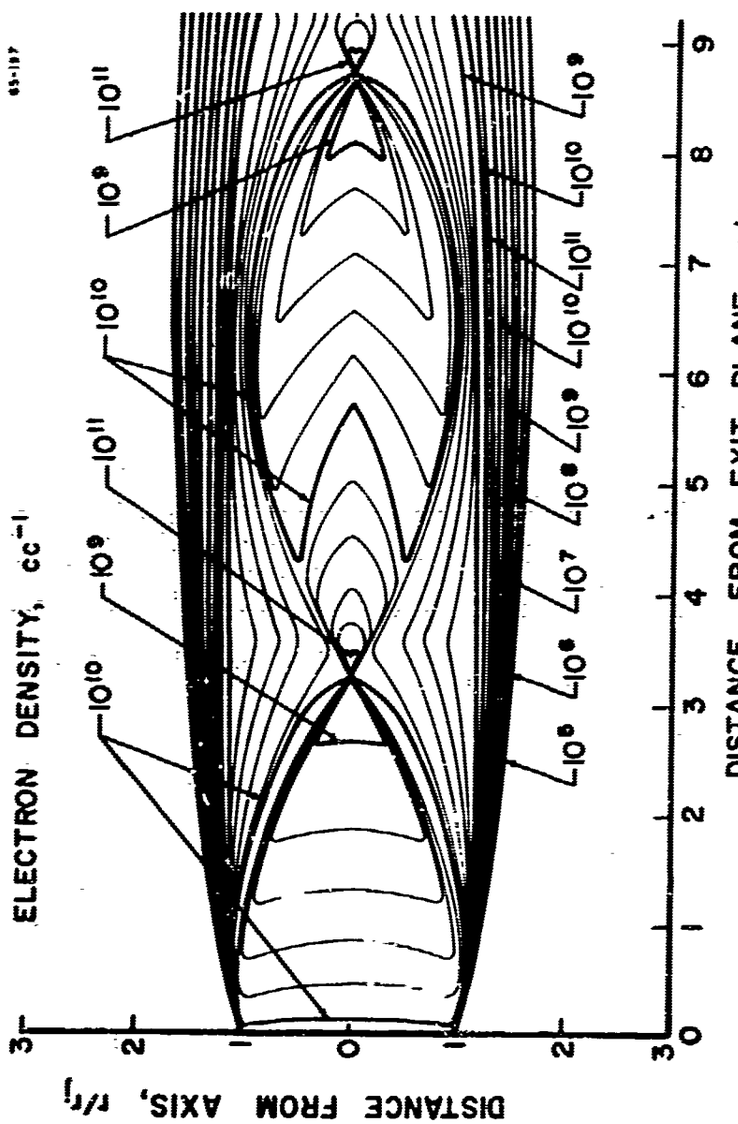


Figure 16. Electron density contours in a low altitude exhaust plume. Sketch showing superposition of afterburning, inviscid flow, and shock structure.

Unclassified
Security Classification

DOCUMENT CONTROL DATA - R&D

(Security classification of title, body of abstract and indexing annotation must be entered when the overall report is classified)

1. ORIGINATING ACTIVITY *(Corporate author)*
Hq AFCRL, OAR (CRD)
United States Air Force
Bedford, Massachusetts 01730

2a. REPORT SECURITY CLASSIFICATION
Unclassified

2b. GROUP
-

3. REPORT TITLE Proceedings of the Third Symposium on the Plasma Sheath–Plasma Electromagnetics of Hypersonic Flight: Volume II. Electrical Properties of Shock-Ionized Flow Fields

4. DESCRIPTIVE NOTES *(Type of report and inclusive dates)*
Proceedings of Symposium

5. AUTHOR(S) *(Last name, first name, initial)*
Rotman, W., Moore, H., Papa, R., Lennon, J.

6. REPORT DATE	7a. TOTAL NO. OF PAGES	7b. NO. OF REFS
May 1967	356	115

8a. CONTRACT OR GRANT NO.

b. PROJECT AND TASK NO. 4642, all tasks

c. DOD ELEMENT 62405394

d. DOD SUBELEMENT 681000

9a. ORIGINATOR'S REPORT NUMBER(S)
AFCRL-67-0280 (Volume II)
Special Reports No. 64 (II)

9b. OTHER REPORT NO(S) *(Any other numbers that may be assigned this report)*
AFCRL-67-0280 (Volume II)

10. AVAILABILITY/LIMITATION NOTICES
[redacted]

11. SUPPLEMENTARY NOTES
-

12. SPONSORING MILITARY ACTIVITY
Hq AFCRL, OAR (CRD)
United States Air Force
Bedford, Massachusetts 01730

13. ABSTRACT

This volume is a collection of the unclassified papers presented at the Third Symposium on the Plasma Sheath—Plasma Electromagnetics of Hypersonic Flight. This symposium consisted of the review of progress in reentry communication studies during the three year period since the prior meeting. The program of this symposium on plasma electromagnetics of hypersonic flight involves a wide range of scientific disciplines, including electromagnetics, aerodynamics, aerothermochemistry, plasma dynamics, electronics, and high-temperature phenomena. The papers were selected to explore as many of these facets of research, including the results of laboratory, flight, and system tests, as time permitted.

DD FORM 1 JAN 64 1473

Unclassified
Security Classification

Unclassified
Security Classification

14. KEY WORDS	LINK A		LINK B		LINK C	
	ROLE	WT	ROLE	WT	ROLE	WT
Plasma Electromagnetics Hypersonic-Flight Reentry Communications						

INSTRUCTIONS

1. ORIGINATING ACTIVITY: Enter the name and address of the contractor, subcontractor, grantee, Department of Defense activity or other organization *(corporate author)* issuing the report.

2a. REPORT SECURITY CLASSIFICATION: Enter the overall security classification of the report. Indicate whether "Restricted Data" is included. Marking is to be in accordance with appropriate security regulations.

2b. GROUP: Automatic downgrading is specified in DoD Directive 5200.10 and Armed Forces Industrial Manual. Enter the group number. Also, when applicable, show that optional markings have been used for Group 3 and Group 4 as authorized.

3. REPORT TITLE: Enter the complete report title in all capital letters. Titles in all cases should be unclassified. If a meaningful title cannot be selected without classification, show title classification in all capitals in parenthesis immediately following the title.

4. DESCRIPTIVE NOTES: If appropriate, enter the type of report, e.g., interim, progress, summary, annual, or final. Give the inclusive dates when a specific reporting period is covered.

5. AUTHOR(S): Enter the name(s) of author(s) as shown on or in the report. Enter last name, first name, middle initial. If military, show rank and branch of service. The name of the principal author is an absolute minimum requirement.

6. REPORT DATE: Enter the date of the report as day, month, year, or month, year. If more than one date appears on the report, use date of publication.

7a. TOTAL NUMBER OF PAGES: The total page count should follow normal pagination procedures, i.e., enter the number of pages containing information.

7b. NUMBER OF REFERENCES: Enter the total number of references cited in the report.

8a. CONTRACT OR GRANT NUMBER: If appropriate, enter the applicable number of the contract or grant under which the report was written.

8b, 8c, & 8d. PROJECT NUMBER: Enter the appropriate military department identification, such as project number, subproject number, system numbers, task number, etc.

9a. ORIGINATOR'S REPORT NUMBER(S): Enter the official report number by which the document will be identified and controlled by the originating activity. This number must be unique to this report.

9b. OTHER REPORT NUMBER(S): If the report has been assigned any other report numbers *(either by the originator or by the sponsor)*, also enter this number(s).

10. AVAILABILITY/LIMITATION NOTICES: Enter any limitations on further dissemination of the report, other than those imposed by security classification, using standard statements such as:

(1) "Qualified requesters may obtain copies of this report from DDC."

(2) "Foreign announcement and dissemination of this report by DDC is not authorized."

(3) "U. S. Government agencies may obtain copies of this report directly from DDC. Other qualified DDC users shall request through _____."

(4) "U. S. military agencies may obtain copies of this report directly from DDC. Other qualified users shall request through _____."

(5) "All distribution of this report is controlled. Qualified DDC users shall request through _____."

If the report has been furnished to the Office of Technical Services, Department of Commerce, for sale to the public, indicate this fact and enter the price, if known.

11. SUPPLEMENTARY NOTES: Use for additional explanatory notes.

12. SPONSORING MILITARY ACTIVITY: Enter the name of the departmental project office or laboratory sponsoring *(paying for)* the research and development. Include address.

13. ABSTRACT: Enter an abstract giving a brief and factual summary of the document indicative of the report, even though it may also appear elsewhere in the body of the technical report. If additional space is required, a continuation sheet shall be attached.

It is highly desirable that the abstract of classified reports be unclassified. Each paragraph of the abstract shall end with an indication of the military security classification of the information in the paragraph, represented as *(TS), (S), (C), or (U).*

There is no limitation on the length of the abstract. However, the suggested length is from 150 to 225 words.

14. KEY WORDS: Key words are technically meaningful terms or short phrases that characterize a report and may be used as index entries for cataloging the report. Key words must be selected so that no security classification is required. Identifiers, such as equipment model designation, trade name, military project code name, geographic location, may be used as key words but will be followed by an indication of technical context. The assignment of links, rules, and weights is optional.

Unclassified
Security Classification